Multidimensional sorting of microparticles in electrically switchable dielectrophoretic filters

Vom Fachbereich Produktionstechnik
der
UNIVERSITÄT BREMEN

zur Erlangung des Grades
Doktor der Ingenieurwissenschaften (Dr.-Ing.)
genehmigte

Dissertation
von
M.Sc. Laura Weirauch

1. Gutachter:	Prof. Dr.-Ing. Jorg Thöming (Universität Bremen)
2. Gutachterin:	Prof. Dr.-Ing. Jeanette Hussong (Technische Universität Darmstadt)
Tag der mündlichen Prüfung	02.10.2023

Zusammenfassung

Die Sortierung von Nano- und Submikrometerpartikeln nach Größe, Form und Leitfähigkeit ist ein industriell hoch relevantes, aber in Teilen ungelöstes Problem. Partikelsysteme mit spezifischen Eigenschaften sind für zahlreiche Anwendungen, zum Beispiel für Hochtechnologieprodukte wie Photovoltaikzellen oder Komponenten für Energiespeicher, erforderlich. Klassische Trennverfahren stoßen jedoch im Submikrobereich an ihre Grenzen oder sind ökonomisch oder ökologisch nicht tragbar. Zudem existieren kaum Verfahren, die eine Trennung von Partikeln anhand mehrerer Eigenschaften in einem Separator möglich machen. Eine Trenntechnik, welche vor allem im bioanalytischen Bereich Anwendung findet und ein hohes Potenzial für die Lösung solcher Probleme bietet, basiert auf der dielektrophoretischen Kraft. Dielektrophorese ist die Bewegung von polarisierbaren Partikeln in einem inhomogenen elektrischen Feld. Die dielektrophoretische Kraft kann verwendet werden, um Partikel im Nano- und Mikrometerbereich an Oberflächen von Elektroden oder Filtermedien rückzuhalten. Die Poren der Filter können hierbei mehrere Größenordnungen größer sein als die abzuscheidenden Partikel, was die Strukturen hochpermeabel macht. Eine Besonderheit ist, dass die dielektrophoretische Kraft sowohl in ihrer Amplitude als auch in ihrer Richtung durch Anpassung der Stärke und Frequenz des verwendeten elektrischen Feldes steuerbar ist. Für die Nutzung ist keine Markierung oder Veränderung der Partikel notwendig und in zahlreichen Studien konnte die hohe Selektivität von auf Dielektrophorese basierenden Verfahren gezeigt werden.

Ein bisher nicht untersuchter Bereich ist, ob Dielektrophorese eine Sortierung von Mikropartikeln anhand mehrerer Eigenschaften in einem Durchlauf eines Filters ermöglicht. Ziel dieser Arbeit ist es, das Potential von Dielektrophorese in diesem Bereich anhand eines Modellpartikelsystems zu untersuchen. Im Gegensatz zu der in der Literatur verbreiteten Verwendung von mikrofluidischen Aufbauten soll hier ein einfach skalierbarer Aufbau realisiert werden, um relevant für den Einsatz für technische Partikel zu sein. Eine Skalierbarkeit und das Erreichen von industriell relevanten Volumenströmen konnte bereits zuvor in dielektrophoretischen Filtern aus porösen Schwämmen oder Kugelschüttungen gezeigt werden. Diese weisen jedoch eine im Hinblick auf mehrdimensionale Sortierungen eingeschränkte Selektivität auf. In der vorliegenden Arbeit wird daher der Einsatz von regelmäßigen Filterstrukturen überprüft.

In dieser Arbeit wurde zunächst ein Modellpartikelsystem konzipiert und hergestellt, das die Untersuchung einer Sortierung nach mehreren Eigenschaften er-

möglicht. Drei Partikelarten wurden untersucht. Die erste Partikelart, sphärische Polystyrol-Mikropartikel, dient gleichzeitig als Basis für die anderen Partikel. Hieraus wurden durch eine Goldbeschichtung leitfähige, aber kaum in ihrer Größe und Dichte veränderte Partikel hergestellt. Durch einen Streckprozess konnten die Basispartikel in eine ellipsoide Geometrie verformt werden, ebenfalls ohne ihr Volumen zu verändern. Somit unterscheiden sich die Partikel jeweils nur in einer einzigen Eigenschaft, wodurch die Komplexität reduziert wird. Die Trennbarkeit der Basispartikel und deren Modifikationen wurde zunächst mit etablierten dielektrophoretischen Methoden in Mikrokanälen überprüft. Anschließend wurde die Trennbarkeit in einem neu entwickelten und skalierbaren Filter untersucht und mit den Ergebnissen eines Mikrokanals verglichen. Es konnten ähnliche Trenneffizienzen bei einem um drei Zehnerpotenzen höheren Volumenstrom (120 mL h^{-1} vs. 0.1 mL h^{-1}) erzielt werden. Zudem weist der Prototyp eine gesteigerte Selektivität im Vergleich zu bestehenden skalierbaren dielektrophoretischen Aufbauten aus der Literatur auf, was für die mehrdimensionale Sortierung entscheidend ist. Um mehrere Partikeleigenschaften in einem Filterdurchlauf zu adressieren, wurde das Konzept einer selektiven Remobilisierung auf den skalierbaren Filter übertragen. Schließlich wurde ein Partikelgemisch nach Partikelgröße, -form und -beschichtung mit einer Kombination aus selektiver Abscheidung und selektiver Remobilisierung erfolgreich sortiert. Hierfür wurde die Frequenz des elektrischen Feldes schrittweise erhöht, was zu einer selektiven Richtungsänderung der dielektrophoretischen Kraft und Ablösung von der Filterstruktur führt und so eine Trennung ermöglicht.

Die Ergebnisse dieser Arbeit zeigen, dass eine mehrdimensionale Sortierung in dielektrophoretischen Filtern möglich ist und erweitern das Verständnis zu Remobilisierungsvorgängen von dielektrophoretischen Filterstrukturen. Zusätzlich konnte gezeigt werden, dass der Einsatz von regulären Filterstrukturen die Selektivität von dielektrophoretischen Filtern erhöht. Die gleichzeitige Skalierbarkeit des Ansatzes bietet zukünftig die Möglichkeit, die Einsetzbarkeit auf komplexere und industriell relevante Trennprobleme zu erweitern.

Abstract

The sorting of nano- and sub-microparticles according to size, shape and conductivity is an industrially highly relevant but in parts unsolved problem. Particle systems with specific properties are required for numerous applications, for example for high-tech products such as photovoltaic cells or components for energy storage. However, classical separation processes reach their limits in the sub-micrometer range or are not economically or ecologically operable. Additionally, very few processes exist that enable the separation of particles based on multiple particle properties in one separator. One separation technique, which is currently mainly used in the bioanalytical field and offers a high potential for solving such problems, is based on the dielectrophoretic force. Dielectrophoresis is the movement of polarizable particles in an inhomogeneous electric field. This dielectrophoretic force can be used to retain nano- and micrometer-sized particles by moving them out of a fluid flow to the surfaces of electrodes or highly permeable filter media. The pores of the filters can be several orders of magnitude larger than the particles that are to be separated, which makes the structures highly permeable. A special feature is that the force is controllable in both its magnitude and direction by adjusting the strength and frequency of the electric field used. No labeling or modification of the particles is required, and numerous studies have demonstrated the high selectivity of dielectrophoresis-based methods.

An area that has not previously been investigated is whether dielectrophoresis facilitates the sorting of microparticles based on multiple properties in one pass of a filter. This thesis aims to investigate the potential of dielectrophoresis in this field using a model particle system. In contrast to the widespread use of microfluidic setups in the literature, an easily scalable setup is to be realized here in order to be relevant for the processing of non-biological particles. Scalability and achievement of industrially relevant volumetric flow rates have been previously demonstrated in dielectrophoretic filters made of porous sponges or packed beds. However, these show limited selectivity with respect to multidimensional sorting. In the context of this work, therefore, the use of regular filter structures is examined.

In this thesis, a model particle system was first conceptualized and produced to facilitate the investigation of sorting based on several properties. Three particle types were investigated. The first particle type, spherical polystyrene microparticles, also serves as the basis for the other particles. Out of these, particles that were conductive but hardly changed in size and density were produced by a gold-coating process. Through a stretching method, the base particles could be deformed into an ellipsoidal

geometry, also without changing their volume. Thus, the particles each differ in only a single property, reducing complexity of the investigation. The separability of the base particles and their modifications was first tested in microchannels using established dielectrophoretic methods. Subsequently, the separability was examined in a scalable filter prototype, which had been developed within the context of this work, and compared to the separation efficiencies of one microchannel approach. Similar separation efficiencies could be achieved at a three orders of magnitude higher flow rate (120 mL h^{-1} vs. 0.1 mL h^{-1}). In addition, the prototype shows an increased selectivity compared to existing scalable dielectrophoretic setups presented in the literature, which is crucial for multidimensional sorting. In order to address several particle properties in one filter run, the concept of selective remobilization was transferred to the scalable filter. Finally, a mixture of particles was successfully sorted based on their particle size, shape, and coating with a combination of selective trapping and selective remobilization. For this purpose, the frequency of the electric field was increased stepwise, resulting in a selective change of direction of the dielectrophoretic force and detachment from the filter structure, and thus allowing separation.

The results of this work show that multidimensional sorting in dielectrophoretic filters is possible and extend the understanding of remobilization processes of dielectrophoretic filter structures. In addition, it was shown that the use of regular filter structures increases the selectivity of dielectrophoretic filters. The scalability of the approach offers the possibility to extend the applicability to more complex and industrially relevant separation problems in the future.

Danksagung

Diese Arbeit wurde am Zentrum für Umweltforschung und nachhaltige Technologien (UFT) der Universität Bremen verfasst. Die Inhalte sind Ergebnisse aus dem Projekt „Hochpermeabler, schaltbarer Filter zur Form- und Eigenschaftssortierung dispergierter Submikropartikel“, welches im Rahmen des SPPs 2045 von der Deutschen Forschungsgemeinschaft (DFG) finanziert wurde (TH 893/20-1 und TH 893/20-2). An dieser Stelle möchte ich mich besonders bei Prof. Dr.-Ing. Jorg Thöming bedanken, der nicht nur diese Arbeit ermöglicht, betreut und begutachtet hat, sondern mir auch über die gesamte Zeit stets mit kritischen und hilfreichen Anregungen zur Seite stand. Ich danke Prof. Dr.-Ing. Jeanette Hussong dafür, dass sie sich sofort bereit erklärt hat, als zweite Gutachterin meiner Arbeit zu fungieren, und dass sie sich die Zeit genommen hat, diese zu lesen und zu begutachten.

Michael Baune und Georg Pesch möchte ich ebenfalls für die hervorragende Betreuung danken. Michael hatte immer eine Idee, auch wenn ich dachte, alles mögliche bereits ausprobiert zu haben und Georg hat mit seiner Arbeit das Fundament für diese Dissertation gelegt und stets motivierende Worte gefunden. Ich möchte allen derzeitigen und ehemaligen Mitgliedern der Arbeitsgruppe chemische Verfahrenstechnik dafür danken, jederzeit ein offenes Ohr in wissenschaftlichen wie auch nicht-wissenschaftlichen Fragen gehabt zu haben. Auch abseits der Arbeit, ob auf Seminarfahren, Konferenzen oder bei sportlichen Aktivitäten, habe ich die gemeinsame Zeit genossen. Besonders möchte ich meinem Bürokollegen Jasper Giesler danken. Ich bin sehr froh, diesen langen und teils anstrengenden Weg nicht alleine gegangen zu sein und dankbar, dass er mir immer mit wertvollem Rat und aufmunternden Worten zur Seite gestanden hat. Ebenfalls möchte ich ihm danken, dass er sich die Zeit genommen hat, diese Arbeit Korrektur zu lesen.

Denise Meyerhoff und Andrey Guzev möchte ich für ihre Unterstützung im Labor danken und dafür, dass sie sich nie beschwerten, auch wenn lange Zeit nur die gleichen Aufgaben im Labor anstanden. Ich danke meinen Eltern, die es mir ermöglicht haben, eine solch gute Ausbildung zu erhalten und ohne deren Unterstützung ich nicht da wäre, wo ich jetzt bin. Meiner Schwester Sarah Weirauch möchte ich ebenfalls für ihren Beistand danken und dafür, dass sie sich selbst zum x-ten Mal einen Probevortrag vorstellen ließ. Zuletzt möchte ich Susanne Müller nicht nur für das sorgfältige Korrekturlesen dieser Arbeit danken, sondern auch für die emotionale Unterstützung während meiner Promotionszeit und in den vielen Jahren davor.

List of publications

Laura Weirauch, Malte Lorenz, Nicole Hill, Blanca H. Lapizco-Encinas, Michael Baune, Georg R. Pesch, and Jorg Thöming. „Material-Selective Separation of Mixed Microparticles via Insulator-Based Dielectrophoresis“. *Biomicrofluidics* 13.6 (2019), p. 064112

Laura Weirauch, Jasper Giesler, Michael Baune, Georg R. Pesch, and Jorg Thöming. „Shape-Selective Remobilization of Microparticles in a Mesh-Based DEP Filter at High Throughput“. *Separation and Purification Technology* 300 (2022), p. 121792

Contents

1 Introduction

Although separation processes have been indispensable unit operations in a wide range of applications for ages, continuous development and improvement is crucial to increase sustainability or to enable the separation of certain components at all. In particular, the importance of the recycling of valuable materials has increased in recent years, as resources are finite, extraction processes become economically or environmentally unsustainable, or the disposal of composites is problematic for the environment. At the same time, there is also an increasing demand for highly specific particle systems with narrow property distributions for applications such as solar cells [Cho17] or energy storage components [Pre12]. Especially in the lower micrometer and nanometer particle-size range, the sorting according to properties such as size, shape, and material is a highly relevant topic with still unsolved problems. Some separation tasks in this size range are the recycling of valuable components from waste such as the dust fraction of electronic scrap [Soh12; Tun12], the selection of metallic or semiconducting nanotubes e.g. for sensors or thin film materials [Wal14; Rab17], or cell separation for analytics and diagnostics [Gas14; Shi13]. As particle size decreases, numerous conventional techniques loose efficiency due to equally decreasing selectivity and reach their limits below 10 μm [Wil15, p. 429]. For example, the selectivity of density-based separation techniques, such as gravitational field-flow fractionation or centrifugation, in terms of multidimensionality is low in the submicron range because particle size and shape are coupled with density [Con17]. However, the sorting of particles based on multiple properties is becoming increasingly relevant. In synthesis of particles, for instance, the result often shows variations in size, shape, or properties like conductivity. The subsequent classification according to size is quite established, but according to shape it is still challenging in the microscale [Beh18]. So far, complex multidimensional separations can only be realized by using label-based separation methods, which require rather complicated preparations, or by combining multiple label-free techniques, e.g. on a single microfluidic chip [Wu21].

A basis for separation techniques suitable for use in this size range and which are able to address multiple particle properties is dielectrophoresis (DEP). DEP is the movement of polarizable particles in an inhomogeneous electric field. Among other things, DEP can be used to retain particles in structures. Separation techniques based on DEP are label-free, non-invasive, and highly selective [Reg11], making them a promising alternative to established separation methods. The direction and strength of the DEP force and therefore also whether particles are retained, is dependent on particle and medium properties but also on characteristics of the electric field like the applied voltage and frequency. Consequently, the direction of a particle's

movement due to DEP can, under certain conditions, be changed by altering the frequency of the applied electric field. The suitability of DEP processes has already been demonstrated for numerous particle or cell systems. However, to the author's knowledge, DEP has not yet been used for simultaneous sorting based on multiple properties in one pass of the filter. Especially the possibility of flexible and fast change of the DEP force offers a high potential for such complex tasks.

In the recent past, DEP has mostly been applied in the bio-medical/-technological field [Pet10], where the focus is on high selectivity rather than high throughputs. Thus, microfluidic systems that can process sample volumes in the microliter to milliliter range are commonly used [Mar22]. The main hurdle to a broader use of DEP is considered to be the limited throughputs at high selectivity. Goals of current research are therefore to improve the selectivity, flexibility, and scalability of dielectrophoretic manipulation methods [Liu19; Gho23], or the realization of portable systems [Zho21; Guo22]. The difficulty of scaling DEP processes is based on the inherent physics, as the force is influenced by the gradient of the squared electric field. Consequently, the force decreases exponentially with the distance from the electrodes [Wan98], which limits the overall scale of the device.

There are a few approaches to overcome this limitation. One is the use of electrically insulating packed beds or porous structures between widely spaced electrodes in macroscopic devices to create field inhomogeneities. This was realized quite early in some patents [Obe77; Cri77a] and, among a few, taken up by our group [Pes18b; Lor20]. The porous structures scatter the electric field instead of acting as a mechanical filter, thus functioning as a highly permeable, electrically switchable DEP filter. High separation efficiencies at increased throughputs compared to microchannels (540 mL h^{-1} vs. mostly less than 0.1 mL h^{-1}) and first successes in selective particle trapping have already been demonstrated [Lor21]. The drawback of this concept is that such devices are unlikely to reach the selectivity of state-of-the-art microfluidic DEP or electrokinetic separators [Pes21]. Due to the irregular structure, the predictability of the local field inhomogeneities is limited, which makes multidimensional sorting difficult.

This work aims to develop a scalable DEP filter concept using regular field disturbing structures to increase selectivity. It is to be examined to what extent a multidimensional separation of particles is feasible by this approach. In the context of this thesis, multidimensional separation or sorting is considered as a classification of particles on the basis of multiple properties by passing through a filter once. Separation of particles with multidimensionally distributed properties is conceivable and is to be investigated in the future, but is not part of this work.

This thesis is structured as follows: First, a summary of fundamentals required to understand the mechanisms and possibilities of DEP is presented (chapter 2). Then, a literature survey of important concepts and applications is given to put this work in the context of past and current research (chapter 3). Chapter 4 summarizes the goals of and approaches taken in this work. Chapters 5 and 6 contain results

of investigations published by the author (and co-workers). Chapter 5 describes the selection, generation, and validation of a model system suitable for the study of a multidimensional separation in DEP filters, whereas chapter 6 presents the development and validation of a scalable prototyp of a DEP filter with regular structures. Chapter 7 uses the findings from the previous two chapters to implement a multidimensional separation. Parts of this chapter have already been published. The thesis concludes with a summarizing discussion and an outlook in chapter 8. Further details on the experiments and additional findings throughout this work can be found in the appendix.

2 Fundamentals: Moving particles in electric fields

This chapter summarizes fundamentals that are crucial to understand the movement of particles due to dielectrophoresis. For electrokinetic phenomena in general, it is necessary to consider the interconnection of fluid dynamics, mass transport, and electrostatics [Mas06, p. xvii]. Therefore, most of the following pages cover the basic theory; the busy reader might skip this part until Sec. 2.2. The chapter starts with electrostatic and electrodynamic fundamentals, introduces the dielectrophoretic force, then describes other forces and phenomena influencing the particle movement in dielectrophoretic devices, and ends with DEP trapping conditions. The main focus is on the polarization of particles and their motion in aqueous solutions since, in this work, only these suspension media are used and particular effects are associated with them.

2.1 Electrostatics and electrodynamics

Electrostatics describe interactions of stationary charges and static electric fields, while electrodynamics also take the movement of charge into account [Kir10, p. 97]. In this chapter fundamentals of electrostatic and electrodynamic effects are described, ranging from the definition of charges, electric fields and potentials, over the dipole formation in free space, to the polarization of spherical and non-spherical dielectric particles in aqueous mediums.

2.1.1 Electric charges, fields and potentials

Electric charge is a basic property of matter and can be carried by subatomic particles. The charge q can be negative (carried by electrons) or positive (carried by protons) [Pur13, p. 3]. Charges of equal sign repel each other and attract charge of unequal sign. The height of a charge is an integer multiple of the elementary charge $e = 1.602 \times 10^{-19}$ C, which is called charge quantization. [Mor03, p. 15] Charges can be distinguished into free and bound charges depending on their mobility. Free charges are mobile and can travel large distances compared to an atomic length scale. Examples are electrons in metals or ions in solutions [Kir10, p. 97]. Bound charges can only move approximately atomic distances and are held in proximity to an opposite charge of equal magnitude. Examples are bound ions in solid crystals or the atomic nucleus and its associated electron cloud [Kir10, p. 97]. For an isolated body, the total charge Q_e (sum of i single charges) is constant [Mas06, p. 33], $Q_\mathrm{e} = \sum q_i =$ constant, which is called charge conservation.

Every charged object generates an electric field $\vec{E}$ in its surroundings. The electric field around a negative charge points radially inwards to the charge, and for a

positive charge in the opposite direction. $\vec{E}$ is a vector field , and it can be visualized by the representative concept of field lines (Fig. 2.1 a). The direction of the field can be depicted by the course and its strength by the density of the lines. A second

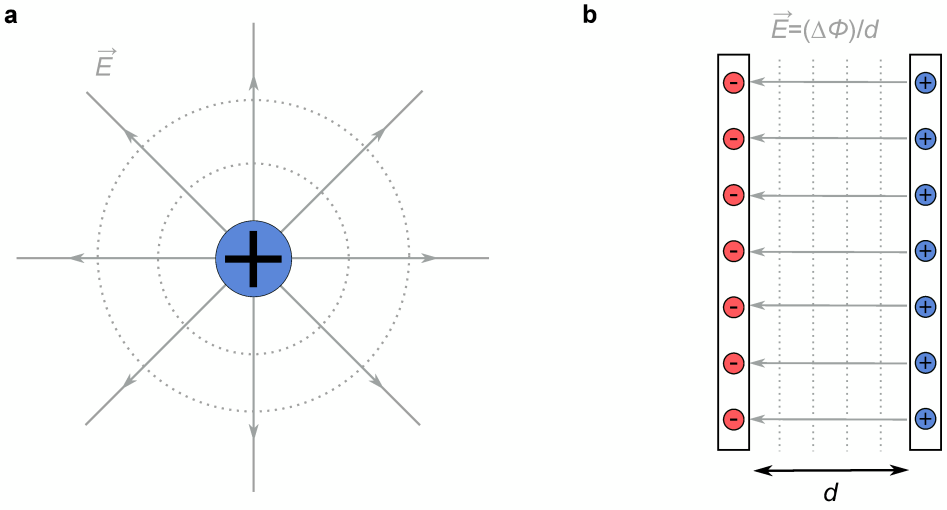

Fig. 2.1.: a) Electric field $\vec{E}$ (arrows) around a charge Q_e with lines of equal potential (equipotentials, dotted line) (based on Ref. [Mor03, p. 16]). b) Electric field between two parallel plate electrodes with distance d (based on Ref. [Pet17a, p. 32]).

point charge placed into this field will experience an electric force $\vec{F}_e = \vec{E}Q_\mathrm{e}$ with the electric field strength of the original field and charge of the placed charge [Kir10, p. 97]. This force is also given by Coulomb's law

$$\vec{F}_\mathrm{e} = k_e \frac{Q_{\mathrm{e},1} Q_{\mathrm{e},2}}{d^2} \tag{2.1}$$

which considers the interacting between both charges ($Q_{\mathrm{e},1}$ and $Q_{\mathrm{e},2}$) and associated electric fields in free space [Mas06, p. 34]. Here, k_e is the Coulomb constant ($k_e = \frac{1}{4\pi\varepsilon_0} \approx 8.988 \times 10^9\ \mathrm{N\ m^2\ C^{-2}}$) with the permittivity of the free space $\varepsilon_0 = 8.85 \times 10^{-12}\ \mathrm{C\ (V\ m)^{-1}}$ and the distance d between the charges $Q_{\mathrm{e},1}$ and $Q_{\mathrm{e},2}$. In case of multiple charges, the principle of superposition states that the total electric field is a sum of the effects of the individual charges.[Mor03, pp. 15-16]

Moving a charge within a field requires a specific amount of work energy. This is defined as the electrical potential energy and is independent of the path taken. Dividing this value by the charge itself leads to the electric potential ϕ of the electric field in volt. The potential is a scalar quantity and indicates how a charge $Q_{\mathrm{e},i}$ at a certain distance is effected by the electric field of the charge $Q_{\mathrm{e},1}$ [Mur11]. The electric potential and electric field are related via [Mor03, p. 16]

$$\vec{E} = -\nabla\phi\ . \tag{2.2}$$

The symbol ∇ is the nabla operator, which denotes the gradient of the scalar/vector field to which it is applied. The gradient gives the direction and magnitude of the maximum rate of change [Kir10, p. 426]. The potential is zero 'infinitely' far away from another charge [Pet17a, p. 90]. The difference between the potentials of two separated points is called voltage.

To give an example, the voltage between two parallel plate electrodes is defined as the difference of the applied potentials $U = \Delta\phi$. The magnitude of the electric field for this example is the voltage (potential difference) divided by the distance between the electrodes d [Mas06, p. 54],

$$E = \frac{U}{d} = \frac{\phi_1 - \phi_2}{d} \,, \tag{2.3}$$

if the field is uniform, not time-varying, and neglecting effects at the plate edges (Fig. 2.1 b) [Pet17a, p. 32]. The electric field is the same at every point, which is called homogeneous.

2.1.2 Gauss's law, Poisson's and Laplace's equation

Another definition of the electric field is given by Gauss's law, which in its differential form relates the electric field to the volume electric charge density ρ

$$\nabla \cdot \vec{E} = \frac{\rho}{\varepsilon_0} \,. \tag{2.4}$$

The volume electric charge density is the quantity of charge per unit volume at any point in a volume V [Mor03, p. 17], where $Q_\mathrm{e} = \int_V \rho dV$ [Mas06, p. 44]. $(\nabla\cdot)$ is the divergence of the electric field giving the net flux of the field at a point in space [Kir10, p. 427]. This basically means that if more positive than negative charges are in a volume, they act as sources of the electric field, whereas more negative charges act as sinks [Pet17a, p. 64].

Replacing $\vec{E}$ in Gauss's law with Eq. 2.2 gives Poisson's equation

$$\nabla^2\phi = -\frac{\rho}{\varepsilon_0} \,. \tag{2.5}$$

In many cases the charge density within a body is zero, which leads to (the so-called) Laplace's equation $\nabla^2\phi = 0$. Both equations are only valid for electrostatics and describe the electric field in free space [Mas06, p. 51]. In common applications and also in the case of dielectrophoresis, the electric field does not propagate in free space. The differences to electric fields in media like dielectrics will be discussed in Sec. 2.1.4.

2.1.3 Dipoles

This section is mainly based on Refs. [Mor03, pp. 18-20] and [Kir10, pp. 108, 109]. A system of two opposite charges with the same magnitude and opposite sign

separated by an infinitesimal distance is called dipole (Fig. 2.2 a). On the charges acts a dipole moment $\vec{p}$ which is pointing from negative to positive charge

$$\vec{p} = Q_\mathrm{e}\vec{d} \tag{2.6}$$

with a vector distance $\vec{d}$ between the charges and the magnitude of the charges Q_e (Fig. 2.2 b). The charge separation can be permanent or induced by an interaction with an electric field. For example, the charge distribution of a small particle exposed to an electric field can in many cases be approximated as a point-dipole [Mor03, p. 38]. This will be further discussed in Sec. 2.1.7.

In a time-independent electric field the force on a dipole is given by

$$\vec{F}_\mathrm{e} = (\vec{p} \cdot \nabla)\vec{E} \,. \tag{2.7}$$

From this it can be concluded that there will be no force on the dipole unless it is exposed to a non-uniform electric field. The net force couple acting on the dipole also gives rise to a torque $\vec{T}_\mathrm{e}$

$$\vec{T}_\mathrm{e} = \vec{p} \times \vec{E} \tag{2.8}$$

that aligns the dipole parallel to the electric field, regardless if it is uniform or non-uniform [Jon95, p. 8](Fig. 2.2 c). As $\times$ is the cross product of the two force vectors, the torque becomes zero if the two forces are parallel. In all other cases it results in a third vector perpendicular to the plane created by the two force vectors.

In order to calculate suitable approximations for both the force and torque on a dipole, finding a 'good' expression for $\vec{p}$ is crucial. This will be discussed in Sec. 2.1.7.

2.1.4 Polarization of dielectrics

An electric field interacts with a material in contrast to free space. A dielectric material contains charges which polarize when exposed to an electric field. Polarization means the separation of charges within the material, for example by generating an induced dipole. In a dielectric, the charges are bound and can only move short distances. Thus, the material is a poor conductor (ideal dielectric with a conductivity $\sigma = 0$) [Pet17a, p. 49].

The polarizability of a dielectric is dependent on the permittivity of the material ε. While the conductivity of a material defines how well charges can move through a material (depending on the amount of free and mobile charges), the permittivity indicates how well a material can store energy by (bound) charge separation in or accumulation at the interfaces of the system [Mor03, p. 6]. Usually, the permittivity of a material is given in relation to that of a free space $\varepsilon = \varepsilon_\mathrm{r}\varepsilon_0$ with the relative permittivity ε_r. In matter, the effects of a source charge can be divided into two parts: (a) the polarization of the medium, and (b) the residual electric field that is not canceled by the polarization of the medium. The dielectric constant of a medium indicates how much smaller the electric field of a source charge is in the medium

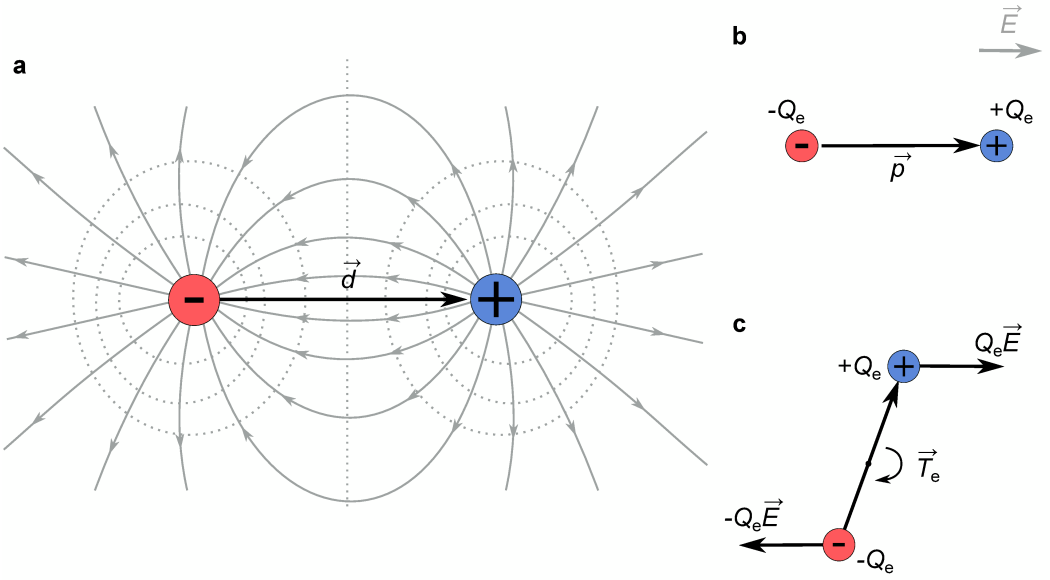

Fig. 2.2.: a) Generated electric field of a dipole consisting of a negative and positive charge which are separated by a vector distance $\vec{d}$ (based on Ref. [Mor03, p. 18]). b) A dipole with the dipole moment $\vec{p}$ aligned parallel to an imposed electric field. c) If the dipole moment is not parallel to the electric field, a torque will act on the dipole and will align it (based on Ref. [Jon95, Ch. 2.1])

compared to free space. An ion in water causes polar water molecules to orient themselves in response to the electric field caused by the ion itself. The attractive force on a negative ion will be smaller than that which it would experience in free space. [Kir10, pp. 100, 101]

The basic equations given in Sec. 2.1.2 change if the charges are located in a dielectric instead of free space. For dielectic materials with a constant permittivity, ε_0 and ρ in Gauss's law (Eq. 2.4) and Poisson's equation (Eq. 2.5) are replaced by the permittivity of the material $\varepsilon = \varepsilon_\mathrm{r}\varepsilon_0$ and the free volumetric charge density ρ_f [Mas06, p. 58]. In Coulomb's law (Eq. 2.1) only ε_0 is replaced with ε. Thus, the force between two charges in a dielectric is reduced by a factor of ε_r compared to free space [Mas06, p. 60].

The following paragraph is mainly based on Ref. [Mor03, pp. 22-23]. There are multiple polarization mechanisms that contribute to the overall polarizability of an object. The first mechanism is *electronic polarization*, which is present in all materials. The electron cloud in an atom moves slightly with respect to its positive nucleus when an electric field is applied. A dipole moment is formed between the displaced center of negative and positive charge. The net polarization due to this mechanism is the sum of the dipole moments for a unit volume. The second mechanism, *atomic polarization*, occurs in molecules with polar bonds and is based on a displacement of the atoms' nuclei with respect to one another. The applied field causes the polar bond to stretch, which creates an additional dipole moment. Similarly, the *ionic polarization* mechanism works for ionic bonds of crystalline solids [Pet17a, pp. 148-

150]. Furthermore, dielectric materials can be classified into polar and non-polar on the basis of the presence of permanent dipoles. Polar dielectrics like water contain permanent dipoles and will be polarized by the orientation of these dipoles. This is called *orientational polarization*. The last mechanism, *(Maxwell-Wagner) interfacial polarization*, considers long-range charge transport and is not a material property as such. Charges accumulate at inhomogeneous spots, like the interface between two dielectrics, when a current flows across the interface. If

$$\frac{\sigma_1}{j\omega}\vec{E}_{\mathrm{n1}} - \frac{\sigma_2}{j\omega}\vec{E}_{\mathrm{n2}} \neq \varepsilon_2\vec{E}_{\mathrm{n2}} - \varepsilon_1\vec{E}_{\mathrm{n1}} \tag{2.9}$$

'residual' free charges appear at the boundary [Pet17a, p. 115] as the materials on both sides respond differently to the electric field. $\vec{E}_{\mathrm{n}i}$ are the normal components of the electric field pointing from dielectric (1) to dielectric (2). This mechanism is dependent of the effective surface of the interface and also dependent on its shape (see Sec. 2.1.8).

2.1.5 Electric currents

In electrodynamics the movement of charges and the current they carry are described. A current can only flow if charges are separated and is thus driven by a voltage between two points [Mas06, p. 52]. In general, two kinds of currents, ohmic and displacement currents, can be distinguished [Kir10, p. 114]. The movement of free charge, for example that of ions in the bulk medium or electrons in a conductor, is called ohmic currents. Ohm's law describes this movement of free charge relative to the fluid. The electric current density $\vec{J}$ is given by

$$\vec{J} = \sigma\vec{E}. \tag{2.10}$$

The ohmic flux dominates in many cases over charge transport by fluid convection or net diffusion of ions [Kir10, p. 110].

The motion of bound charges is called displacement current $\vec{D}$ [Kir10, p. 114]

$$\vec{D} = \varepsilon\frac{d\vec{E}}{dt}. \tag{2.11}$$

In this case, the current is proportional to the permittivity of the medium and the time derivative (rate of change) of the electric field $\frac{d\vec{E}}{dt}$.

2.1.6 Non-ideal dielectrics

The behavior of a real dielectric in an electric field is influenced by different energy dissipation mechanisms. In this case, electrical energy is converted into another form of energy, e.g., thermal energy. There are two components of loss, one due to a frequency dependency of the permittivity (dielectric loss) and one due to a finite conductivity of non-ideal dielectrics (ohmic loss).

The dielectric loss results from the fact that the polarization of a material cannot change instantaneously when the electric field changes. In contrast to the response in free space, there will be a dependency of the applied frequency on the permittivity. This phenomenon is also called dielectric dispersion. Each of the polarization mechanisms has an individual frequency response (Fig. 2.3 a) and a specific relaxation time τ. This time is needed to achieve maximum polarization and thus follow the electric field. At low frequencies, the maximum polarization of the contributing polarization mechanisms is achieved. Above the characteristic relaxation frequency of one or multiple polarization processes, there will be an incomplete polarization or no response to the field at all at very high frequencies. As $\varepsilon(\omega)$ is the sum of the contributions of the single polarization processes, this results in a gradual drop of the permittivity with increasing frequency, and the dominating polarization mechanism may change (Fig. 2.3 a). [Mor03, p. 27]

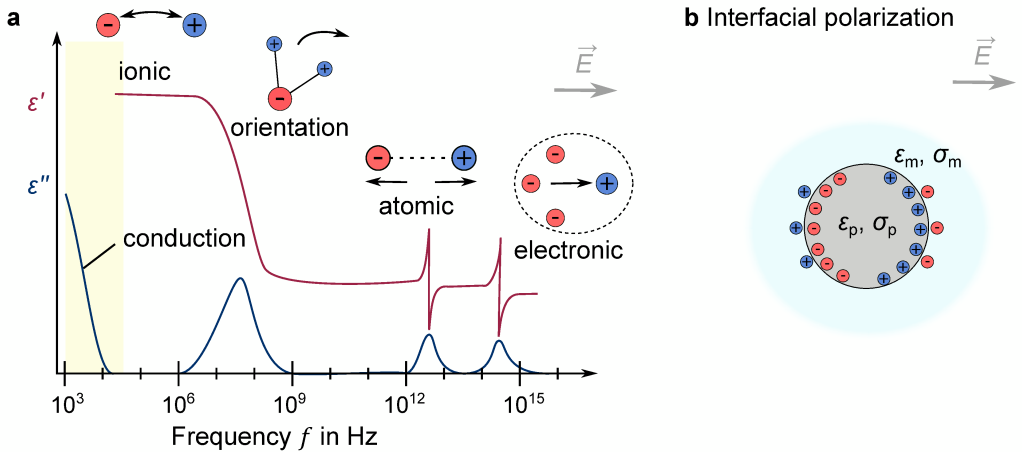

Fig. 2.3.: a) Variation of the real and imaginary part of the complex permittivity of dielectrics with the frequency of the applied electric field (based on Ref. [Pet17a, p. 164]). The dominant frequency range for each polarization mechanism is marked and the corresponding charge movement depicted. The yellow area marks the frequency range used in this work. b) Charge accumulation at the boundaries of a dielectric object called interfacial polarization. The dielectric properties of the object and the surrounding medium have to fulfill Eq. 2.9.

To describe the frequency dependent behavior, the material permittivity is treated as a complex function on the frequency or angular frequency $\omega = 2\pi f$. It can be written as $\tilde{\varepsilon}(\omega) = \varepsilon'(\omega) - j\varepsilon''(\omega)$ with the real part ε', imaginary part ε'', and imaginary unit j. The imaginary part (energy dissipation) passes through a maximum at those frequencies at which the permittivity is decreasing with ω [Kir10, p. 116]. At these points, maximum energy is dissipated [Mor03, p. 27]. The energy loss due to the displacement current W_ε is [Pet17a, p. 136]

$$W_\varepsilon = 0.5\omega\varepsilon_0\varepsilon''|\vec{E}|^2 \,. \tag{2.12}$$

The second loss is due to a finite conductivity of most dielectrics and the conductivity arising from a (small) amount of free charges in the material. The conductivity of a material leads to current conduction instead of conversion to dielectric polarization [Mor03, p. 28]. Similarly, the movement of free charge is not without loss and generates heat (called ohmic, resistance or Joule Heating). As the charges move through the material, they collide with other charges or atoms and convert kinetic energy into thermal energy. The energy loss W_σ per unit volume generated by an electric field due to a conduction current is given by [Pet17a, p. 136]

$$W_\sigma = 0.5\sigma|\vec{E}|^2. \tag{2.13}$$

Considering both losses, the complex permittivity can be written as [Sau85]

$$\tilde{\varepsilon} = \varepsilon'(\omega) - j(\varepsilon''(\omega) + \frac{\sigma}{\omega}) \; . \tag{2.14}$$

With increasing frequency, the dielectric loss increases and gets dominant [Pet17a, p. 136]. In this thesis, frequencies below the MHz range are used. At this range dielectric relaxation is negligible $\varepsilon' = \varepsilon_0\varepsilon_\mathrm{r} \neq f(\omega)$ and $\varepsilon'' = 0$ [Sau85]. The simplified form

$$\tilde{\varepsilon} = \varepsilon_0\varepsilon_\mathrm{r} - \frac{j\sigma}{\omega} \tag{2.15}$$

for the complex permittivity is used.

2.1.7 Polarization of spherical particles

In this section the knowledge of the previous sections is combined to describe the polarization of a spherical particle in an electric field. Due to the different dielectric properties of the particle and its surrounding medium, the interface will accumulate charges and will be polarized (Fig. 2.3 b). As different charges appear at either side of the particle, in some cases it can be approximated as a dipole. This approximation achieves good results if the scale of the non-uniformity of the electric field is large compared to the particle dimensions. However, to find an analytical expression is only possible for few, simple particle shapes, and in case the non-uniformity is in the same range as the dipole size, for example for large particles or when multiple dipoles interact with each other, the assumption can lead to an error [Jon95, p. 8]. Furthermore, the approximation is not capable of describing the behavior of a particle located exactly in the center of a negative DEP trap, where the dipole moment would be zero [Mor03, p. 44]. In these cases, higher-order multipolar moments (like of two charge pairs called quadrupole) need to be examined to describe the force on the particle [Jon79]. An approximation is possible via a multipole method [Was93; Jon96] or an 'accurate' [Zha17] calculation by means of the integration of the so-called Maxwell stress tensor over the particle surface [Wan97]. This has to be solved numerically and considers basically all electric force components in different coordinate directions acting on the particles

surface. However, the consideration of the Maxwell stress tensor has limitations as well. The method is not suitable for the evaluation of non-homogeneous particles, as only the particle's surface is considered. Zhao et al. [Zha17] propose a volumetric-integration method. Arbitrary particle shapes and material compositions as well as particle interactions and effects due to double layer formation (Sec. 2.1.10) can be considered, but the computational demands for both numerical methods are high (further read Refs. [Mas06, pp. 68-73; Nil11; Zha17]).

The particles used in this work are small and low particle concentrations are used. Therefore, the dipole approximation is assumed to describe the particle polarization sufficiently accurately. As explained in Sec. 2.1.1, the electric force on a dipole can be estimated by the dipole moment and gradient of the electric field (Eq. 2.7). Assuming a particle with the volume V and the effective polarizability $\tilde{\alpha}$, the effective dipole moment will be

$$\vec{p} = V\tilde{\alpha}\vec{E}\,. \tag{2.16}$$

The effective polarizability for a homogeneous dielectric spherical particle is given by [Mor03, p. 37]

$$\tilde{\alpha} = 3\epsilon_m \left(\frac{\tilde{\varepsilon}_\mathrm{p} - \tilde{\varepsilon}_\mathrm{m}}{\tilde{\varepsilon}_\mathrm{p} + 2\tilde{\varepsilon}_\mathrm{m}} \right) = 3\epsilon_m \tilde{f}_\mathrm{CM} \tag{2.17}$$

in which the fraction is usually summarized as the so-called Clausius-Mossotti (CM) factor $\tilde{f}_\mathrm{CM}$. Here, $\tilde{\varepsilon}_\mathrm{p}$ is the complex permittivity of the particle (index p), and $\tilde{\varepsilon}_\mathrm{m}$ is that of the surrounding medium (index m). The real part of the $\tilde{f}_\mathrm{CM}$

$$\mathrm{Re}(\tilde{f}_\mathrm{CM}) = \mathrm{Re}\left(\frac{\tilde{\varepsilon}_\mathrm{p} - \tilde{\varepsilon}_\mathrm{m}}{\tilde{\varepsilon}_\mathrm{p} + 2\tilde{\varepsilon}_\mathrm{m}} \right) \tag{2.18}$$

determines the strength of the effective polarization and is bound between the values -0.5 and 1 for a spherical particle. The complex part induces a torque on a particle, as the dipole moment is not in phase with the changing electric field [Kir10, pp. 386, 387]. If the CM factor is positive, the effective dipole moment points toward regions of high electric field strength; if the CM factor is negative, the effective dipole moment points against to this direction [Pet17a, p. 120]. In the following, the tilde is omitted in the spelling of the real part of the CM factors.

2.1.8 Polarization of non-spherical particles

It was already shown that the dipole moment of a particle in an electric field is influenced by the particle's and medium's complex permittivity and by the particle's radius cubed. But the particle shape also has a major impact on its polarization. For non-spherical particles, the induced polarization can usually only be determined by numerical calculation. One geometry that can be used to approximate the shape of a variety of particles and cells, but still has an analytical approximation of the dipole moment, is an ellipsoid [Pes21]. In the special case that the major and minor semiaxes are all identical, one receives again the characteristics of a sphere. For

a prolate ellipsoid the particle is rotationally symmetric about the longer, major axis $a_1 \geq a_2 = a_3$ (see Fig. 2.4), for an oblate ellipsoid about the minor axis. The

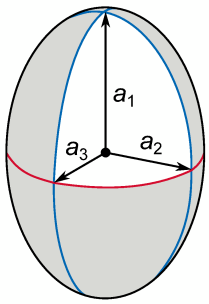

Fig. 2.4.: Prolate ellipsoid with major axis a_1, and minor axes a_2, a_3.

effective polarizability $\alpha_i = 3\varepsilon_\mathrm{m}\tilde{f}_{\mathrm{CM,i}}$ and CM factor are different for each axis a_i in the case of an ellipsoid. The real part of the CM factor is given by

$$\mathrm{Re}(f_{\mathrm{CM},i}) = \mathrm{Re}\left(\frac{\tilde{\varepsilon}_{\mathrm{p},a_i} - \tilde{\varepsilon}_\mathrm{m}}{3(\tilde{\varepsilon}_\mathrm{m} + (\tilde{\varepsilon}_{\mathrm{p},a_i} - \tilde{\varepsilon}_\mathrm{m})L_{a_i})}\right), \tag{2.19}$$

with the depolarization factor L_{a_i} [Kir10, p. 384; Poh78]. The depolarization factor quantifies the reduction of the electric field inside the polarized particle relative to the external field caused by induced polarization charges on the particle's surface [Pet17a, p. 117]. For each axis it is defined as

$$L_{a_i} = \frac{1}{2}a_1a_2a_3\int_0^\infty \frac{1}{(s+a_i^2)B}\,ds \tag{2.20}$$

with $B = \sqrt{(s+a_1^2)+(s+a_2^2)+(s+a_3^2)}$ and the arbitary distance for integration s [Mor03, p. 39]. The dipole moment can be calculated analogously to Eq. 2.16 with $\vec{p}_i = 3\varepsilon_\mathrm{m}\tilde{f}_{\mathrm{CM},i}\vec{E}_i$ with the electric field component in direction of the different axis $\vec{E}_i$. The sum of the depolarization factor components is one. Therefore, a sphere with the radii $a_1 = a_2 = a_3 = r_\mathrm{p}$ has a depolarization factor of $L_{a_1} = \frac{1}{3}$, which results in the very same Eq. 2.18 for the CM factor.

The orientation of the ellipsoid in the electric field caused by a torque (Eq. 2.31 in Sec. 2.2) depends on the CM factors of the individual axes. The axis with the highest CM factor aligns in direction of the electric field [Jon95; Tor18], as this alignment corresponds to a minimization of potential energy [Pet17a, p. 14]. For the case that the major axis of a prolate ellipsoid is aligned parallel to the electric field, the depolarization factor (Eq. 2.20) can be approximated by [Kir10, p. 385]

$$L_{a_1} = \frac{a_2^2}{2a_1^2\delta^3}\left[\ln\left(\frac{1+\delta}{1-\delta}\right) - 2\delta\right] \tag{2.21}$$

with the eccentricity $\delta = \sqrt{1 - \left(\frac{a_2}{a_1}\right)^2}$ [Mor97].

2.1.9 Electrical double layer formation

Many dielectrophoretic processes are performed in an aqueous solution. The polarization at the interfaces plays a major role in the frequency range under consideration. The same applies to the medium-side interface. An aqueous solution usually contains dissolved substances in the form of dissociated ions and can thus be called an electrolyte. While pure water is a poor conductor, ions are mobile (free charge carries) and make solutions conductive [Mas06, p. 71]. However, these ions can be of various types and quantities. At any charged interface in an aqueous solution, such as a particle surface or an electrode, ions together with aligned water molecules form a thin layer. This layer is called electrical double layer (EDL). Its properties influence the electrokinetic behavior of particles especially of sub-micrometer size [Mor03, p. 82] and can also give rise to a fluid motion in channels called electroosmosis (Sec. 2.3.5). There are many different (partly sequential) models to describe the properties of EDLs, e.g. Refs. [Hel53; Gou10; Cha13; Ste24; Kor07], starting with the first mention of EDL by Helmholtz [Hel53]. In this thesis, the Gouy-Chapman model with the modifications of Stern will be described and used. For simplification, the attachment of water molecules in form of a hydrate shell around ions is not considered. This shell consists of aligned water dipoles screening the charge of the single ions and thus keeping the solution stable [Mor03, p. 85].

The surface net charge of the particle creates a local electrostatic surface potential ϕ_0. This potential attracts ions of the opposite charge (counterions) and repels ions with the same charge (co-ions). Near the surface the counterions are bound to the surface referred to as Stern layer and screen the potential linearly (Fig. 2.5). In the subsequent layer, counterions can still be found in greater numbers than co-ions, but the ions are no longer rigidly bound [Mor03, p. 98]. The ions experience a balance between electrostatic attraction and diffusion [Baz11a, p. 229]. This layer is called diffuse layer and the potential decreases exponentially over it. With increasing distance the ions can move more freely. A part of the diffuse layer will therefore be sheared off if tangential stress is applied. The electric potential at this shear plane can be measured experimentally and is called zeta potential ζ [Mor03, p. 98].

A characteristic length scale for the double layer thickness was defined by Debye and Hückel [Deb23] in which the potential falls to $1/e$ of its maximum value. The Debye length λ_D or reciprocal Debye-Hückel parameter κ^{-1} is given by

$$\lambda_D = \kappa^{-1} = \sqrt{\frac{\varepsilon_0 \varepsilon_\mathrm{r} k_\mathrm{B} T}{2 z^2 e^2 n_0}} \tag{2.22}$$

with the Boltzmann constant k_B, temperature T, ion valence z, elementary charge e, and number concentration of ions n_0 without an electric field (or in bulk) [Mas06,

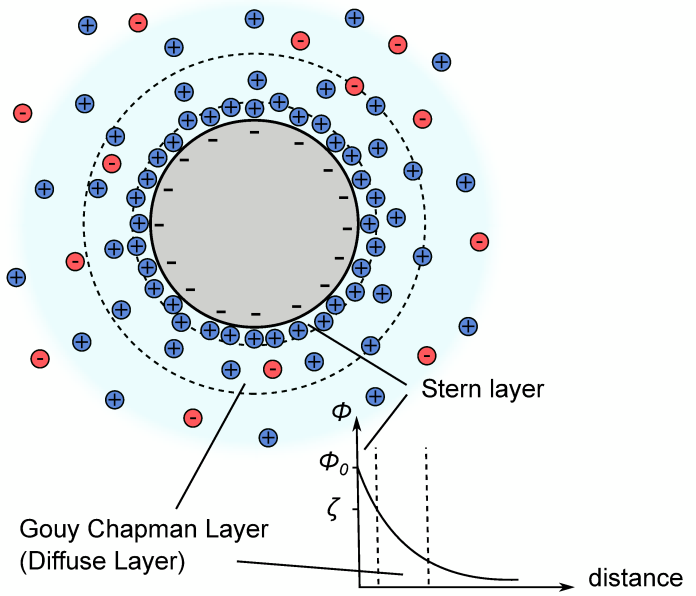

Fig. 2.5.: Electric double layer regarding Gouy-Chapman-Stern model. For simplicity, the hydrate shell around the ions is not shown (based on Ref. [Mor03, p. 92]).

p. 114]. Typically the Debye length is in the range of a few nm [Kir10, p. 145]. As becomes obvious in Eq. 2.22, there is a great dependence on the electrolyte properties. In particular, the pH value of the solution strongly influences the Debye length and the zeta potential, as this value specifies the presence of H^+ ions. The pH further leads to the dissociation of acidic or basic surface groups [Mas06, p. 106].

The surface charge of a particle can arise, among others, from the dissociation of chemical surface groups, or adsorption of ions or molecules like surfactants. An overview of other mechanisms that lead to a charged surface can be found for example in Ref. [Mas06, pp. 106, 107]. Polystyrene (PS) particles used in this thesis usually show a negative surface charge at a wide pH range caused by carboxylic acid (carboxyl, COOH) or sulfate ester (SO_4H) groups on the surface [Inc16; Inc18]. In comparison to the radius of the microparticles, the double layer thickness can be quite large and heavily influence the behavior of the particle polarization [Mor03, p. 82], which will be explained in the next section.

2.1.10 Contribution of the double-layer polarization

To determine the complex permittivity of a dielectric particle, it was found that the particle conductivity is underestimated if only the conductivity of the bulk material is considered [Gre99]. For example, non-conducting particles like polystyrene would usually be less polarizable than aqueous solutions almost independent of the frequency of the applied field. But up to a certain medium conductivity, the particles have a positive Clausius-Mossotti factor at low frequencies [Gre99]. A suspended particle in an electrolyte with a surface charge attracts ions from the solution, which form an electrical double layer (Sec. 2.1.9). The double layer around the particle polarizes and contributes to the overall polarizability of the particle. One model

to describe this behavior is the Maxwell-Wagner-O'Konski (MWO) model. For a suspended dielectric microparticle, the particle conductivity can be calculated as a sum of its bulk conductivity $\sigma_{\mathrm{p,bulk}}$ and a surface conductance term, K_{S} [OKo60]. For a sphere, the effective particle conductivity is given by

$$\sigma_{\mathrm{p}} = \sigma_{\mathrm{p,bulk}} + \sigma_{\mathrm{p,surface}} = \sigma_{\mathrm{p,bulk}} + \frac{2K_{\mathrm{S}}}{r} \,. \tag{2.23}$$

For a prolate ellipsoidal particle with the dimensions $a_i \geq a_j = a_k$, Ref. [OKo60] derived

$$\sigma_{\mathrm{p},a_i} = \sigma_{\mathrm{p,bulk}} + \frac{(a_j + a_k)K_{\mathrm{S}}}{a_j a_k} = \sigma_{\mathrm{p,bulk}} + \frac{2K_{\mathrm{S}}}{a_j} \,. \tag{2.24}$$

If $\sigma_{\mathrm{p,bulk}}$ is very small, like for polystyrene, the contribution of the bulk material is negligible compared to the surface conductivity [Gre99; Erm05]. The K_{S} value can further be splitted into one contribution of the Stern and one of the diffuse layer. The Stern layer conductance $K_{\mathrm{S}}^{\mathrm{S}}$ is assumed to be 1 nS almost independent of the particle's and medium's properties in many studies [Hug99; Erm05]. The diffuse layer conductance $K_{\mathrm{S}}^{\mathrm{D}}$, in contrast, increases with increasing medium conductivity and zeta potential of the particle as the thickness of the layer decreases. The MWO model is only valid in case of a thin double layer $\kappa r >> 1$ and at sufficiently high frequencies. At low frequency, the surface conductance is reduced compared to the MWO model predicted value. There is enough time for the full formation of the double layer and its polarization. The dipole will be effectively reduced by ion diffusion between the bulk and the concentrated regions at the surface as well as diffusion along the surface of the particle. The charge cloud around the particle is no longer symmetrical. The reduction of the surface conductance is described by the theory of Dukhin and Shilov (DS model). Furthermore, in case the EDL is large compared to the particle, the electrophoretic motion of the particle will alter the polarizability of the EDL [Zha11]. This is especially the case for nanoparticles and very diluted electrolytes [Mor03, p. 125]. For small particles at low conductivities, the effect of the EDL is more prominent, as the volume of the EDL increases with the square of the particle radius, while the volume of the particle itself increases with its cube [Gas02]. The MWO and DS models cannot sufficiently describe the polarization for thick EDLs, as the actual structure and ion distribution inside the double layer is not considered [Zha17]. For nearly all frequencies and EDL thicknesses, numerical solving of the Poisson-Nernst-Planck equations [Zha09; Zha11] or a modified version [Baz11b; Ali18] leads to a good description of the ion concentration around particles exposed to electric fields. The volumetric integration method developed by Zhao et al. [Zha17] is also suitable for EDLs with arbitrary thicknesses.

For the particle sizes and conductivities in this work, the EDL is small compared to the particle size. In addition, the frequencies used are large enough for the effect of ion diffusion to be negligible [Erm05; Zha11]. Therefore, the particle conductivity is modeled using Eq. (2.24) without considering the contribution of the diffuse layer.

For conductive particles such as metals, it has generally been shown for a wide range of frequencies that they are more polarizable than water [Hon11a; Fan06]. In case of very low AC and DC currents, negative CM factors are observed, at least for conductively coated and uncharged particles [Gar12; Ren11; Ram16]. One possible reason for this could be that the formation of a double layer may also affect the polarizability of conductive particles in an aqueous solution. Below the double layer charging frequency, the double layer is completely formed and thus screens the induced charge of the particle. The conductive particle appears to be non-conducting and less polarizable than the surrounding medium. Its CM factor is negative. Above the frequency, the double layer can not or not completely shield the charges, and the conducting particle behaves as expected and is more polarizable than most surrounding media. [Ren11] García-Sánchez [Gar12] propose that the real part of the CM factor can be described by

$$\mathrm{Re}(f_{\mathrm{CM}}) = \frac{\Omega - 2}{\Omega + 4} \tag{2.25}$$

with the dimensionless frequency $\Omega = \omega\varepsilon_{\mathrm{m}}\kappa r/\sigma_{\mathrm{m}}$ using the Debye-Hückel approximation.

2.2 Dielectrophoresis

Dielectrophoresis is a movement resulting from the polarization of an object and its surrounding medium in an inhomogeneous electric field [Poh51]. In comparison to electrophoresis, no net-surface charges of the objects are necessary and alternating voltage fields also lead to a net movement [Kir10, p. 373]. A polarizable particle which is placed in an electric field will form a dipole (or multipole), while staying electrically neutral in total (see Sec. 2.1.7). A Coulomb force acts on these separate charges, which does not lead to a net movement in a homogeneous electric field, as the force on each pole of the induced dipole is equal and opposite (Fig. 2.6 a). In the case of an inhomogeneous electric field, on the other hand, the force induces a particle movement [Mor03, p. 50] (Fig. 2.6 b and c). The amplitude and also the direction of the dielectrophoretic force depends on several properties of the particle and the medium.

Using the dipole approximation, the force is given by

$$\vec{F}_{\mathrm{DEP}} = (\vec{p} \cdot \nabla)\vec{E} \tag{2.26}$$

with induced dipole moment $\vec{p} = V\tilde{\alpha}\vec{E}$. The time-averaged DEP force is [Mor03, p. 53]

$$\langle \vec{F}_{\mathrm{DEP}} \rangle = \frac{1}{2} V \mathrm{Re}(\tilde{\alpha}(\vec{E} \cdot \nabla)\vec{E}). \tag{2.27}$$

Assuming that the field is irrotational ($\nabla \times \vec{E} = 0$), the field factor can be rewritten $(\vec{E} \cdot \nabla)\vec{E} = \frac{1}{2}\nabla|\vec{E}^2| = \frac{1}{2}\nabla E^2$ [Pet17a, p. 41], which leads to the notation

$$\langle \vec{F}_{\mathrm{DEP}} \rangle = \frac{1}{4} V \mathrm{Re}(\tilde{\alpha}) \nabla E^2 \tag{2.28}$$

of the DEP force. For a spherical particle, the effective polarizability from Eq. 2.17 gives [Mor03, p. 52]

$$\langle \vec{F}_{\mathrm{DEP}} \rangle = \pi \varepsilon_{\mathrm{m}} r^3 \mathrm{Re}(f_{\mathrm{CM}}) \nabla E^2 \, . \tag{2.29}$$

Note that the medium permittivity outside the CM factor is not complex [Jon95, p. 18]. When using DC fields, or $\mathrm{V_{rms}\ m^{-1}}$ instead of $\mathrm{V\ m^{-1}}$ for the amplitude E of the electric field, there will be a factor 2 in Eq. 2.29 [Mor03, p. 52].

For a prolate ellipsoidal particle with $a_1 \geq a_2 = a_3$, the time-averaged DEP force for each axis i is [Poh78]

$$\langle \vec{F}_{\mathrm{DEP,pr},i} \rangle = \pi a_1 a_2^2 \varepsilon_{\mathrm{m}} \mathrm{Re}(f_{\mathrm{CM},i}) \nabla E^2 \, . \tag{2.30}$$

The direction and amplitude of the DEP force depend on the difference in the complex permittivity of the particle and that of the medium. If a particle is more polarizable than its surrounding medium, it moves towards regions of highest field strength termed positive dielectrophoresis (pDEP, Fig. 2.6 c). If a particle is less polarizable than the medium, it moves away from the regions of high field strength termed negative dielectrophoresis (nDEP, Fig. 2.6 b). [Mor03, p. 53]

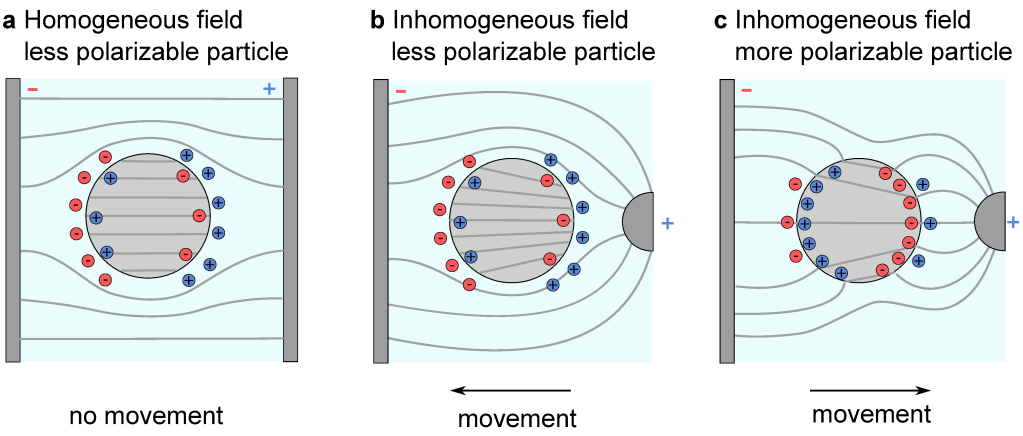

Fig. 2.6.: Direction of particle movement in a) a homogeneous electric field, b) inhomogeneous electric field for a less polarizable particle than the surrounding medium and c) inhomogeneous electric field for a more polarizable particle than the surrounding medium (based on Ref. [Mor03, p. 10]).

Eqs. 2.29 and 2.30 describe the DEP behavior in most cases quite accurately. Note, however, that their limitations have to be kept in mind. The particles are simplified as point dipoles and their volumetric polarization and its effects on the electric field are not taken into account [Zha17].

2.2.1 Rotation and orientation

Dielectrophoretic forces can not only cause translational motions of particles but also rotational ones. The rotation of a particle is caused by an orientational torque for non-spherical particle shapes and inhomogeneous particles, or by a rotational torque for all types of particles [Jon95, p. 110]. The last case occurs in AC rotational fields. A torque arises when the induced dipole cannot keep up with the change of the electric field and thus the dipole moment does not point in the same direction as the electric field. In this case, the imaginary part of the CM factor (loss) is linearly involved in the torque [Mor03, pp. 55, 56]. The rotational behavior of particles can be used to study their dielectric properties referred to as electrorotation [Jon95, p. 92]. In the following, this kind of rotation will not be considered further, because no rotational fields are involved. For non-spherical particles like ellipsoids, however, it is crucial to consider the orientation in the electric field. The torque on an homogeneous ellipsoid is given by

$$\vec{T} = \frac{4}{3}\pi a_1 a_2 a_3 (\varepsilon_\mathrm{p} - \varepsilon_\mathrm{m}) \vec{E}_\mathrm{body} \times \vec{E}_0 \tag{2.31}$$

with the initial field $\vec{E}_0$ and the resultant field inside the body $\vec{E}_\mathrm{body}$ [Str07, p. 216]. The axis with the highest polarizability and accordingly highest CM factor aligns with the direction of the electric field. Here, the magnitude of the CM factor is decisive; the sign only determines the positioning (field maxima/field minima) in the electric field [Tor18].

2.2.2 Frequency dependence of polarization

For an ideal dielectric particle (uncharged, uniform) and medium, there is no influence of the frequency of the applied electric field on the polarizability [Kir10, p. 374]. A dielectric particle with loss, however, shows a frequency dependency. According to the particle and medium properties, as well as the particle shape, characteristic curves of the Clausius-Mossotti factor over the frequency result. In the limit of very low frequencies the CM factor becomes

$$\mathrm{Re}(f_\mathrm{CM}) = \frac{\sigma_\mathrm{p} - \sigma_\mathrm{m}}{\sigma_\mathrm{p} + 2\sigma_\mathrm{m}} \tag{2.32}$$

as $\omega \to 0$ [Pet17a, p. 258]. At the high frequencies limit, the permittivity of the particle and medium dominate the real part of the CM factor

$$\mathrm{Re}(f_\mathrm{CM}) = \frac{\varepsilon_\mathrm{p} - \varepsilon_\mathrm{m}}{\varepsilon_\mathrm{p} + 2\varepsilon_\mathrm{m}} \,. \tag{2.33}$$

At the Maxwell-Wagner relaxation frequency $f_\mathrm{MW} = 1/(2\pi)(\varepsilon_\mathrm{p} + 2\varepsilon_\mathrm{m})/(\sigma_\mathrm{p} + 2\sigma_\mathrm{m})$, the imaginary part of the CM factor is at its maximum. Below the MHz range, the particles show just one dispersion due to the interfacial polarization mechanism [Gre99].

For a spherical particle like polystyrene in a very low conductive medium, the real part of the CM factor is positive at low frequencies and the particle shows pDEP [Gre99] (Fig. 2.7). At the crossover frequency f_{CO} (at which $\mathrm{Re}(f_{\mathrm{CM}}) = 0$) it experiences no DEP force, and at high frequencies nDEP. This is typical the response of a semiconducting material with $\sigma_{\mathrm{p}} > \sigma_{\mathrm{m}}$ and $\varepsilon_{\mathrm{p}} << \varepsilon_{\mathrm{m}}$. Although the bulk material of PS is insulating, the particles behaves like a semiconductor in low conductive aqueous media due to the contribution of the double layer.

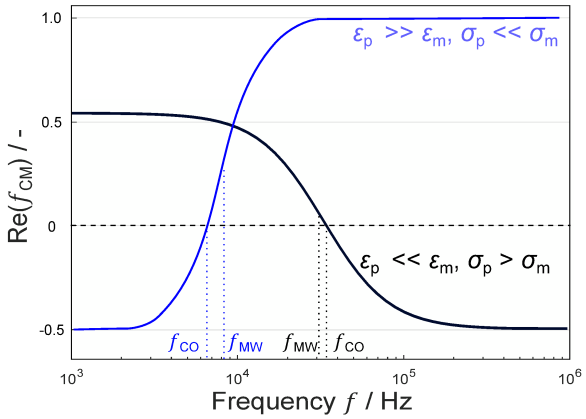

Fig. 2.7.: Clausius-Mossotti factor for a dielectric sphere with $\sigma_{\mathrm{p}} > \sigma_{\mathrm{m}}$ and $\varepsilon_{\mathrm{p}} << \varepsilon_{\mathrm{m}}$ (black) and a dielectric sphere with $\sigma_{\mathrm{p}} << \sigma_{\mathrm{m}}$ and $\varepsilon_{\mathrm{p}} >> \varepsilon_{\mathrm{m}}$ (blue) (based on Ref. [Mor03, p. 39]). For both cases the crossover frequency and Maxwell-Wagner relaxation frequency are shown with dotted lines. A polystyrene microparticle follows the black curve in ultrapure water ($\sigma_{\mathrm{m}} = 1$ µS cm^{-1}) as its effective particle conductivity is about $\sigma_{\mathrm{p}} = 10$ µS cm^{-1} assuming a surface conductivity of around 1 nS.

For ellipsoidal particles, the CM factor for each axis is also a function of the frequency. The alignment of the particle is therefore frequency dependent as well [Tor18].

2.3 Other forces and phenomena causing particle or fluid motion

Besides dielectrophoresis, numerous other deterministic but also stochastic forces act on a particle during dielectrophoretic separation processes. In this chapter, different forces and phenomena are described which can cause or influence the fluid as well as the particle movement. Classical forces such as inertia, gravitation, and diffusion are discussed, as well as further electrokinetic effects such as electroosmosis, electrophoresis, and electrothermal fluid motion. A classification of the expected strength of the various effects is provided. The aim of this chapter is to give an overview of when which forces have a large influence on the particle motion. Based on this knowledge, for example, the selection of the experimental parameters can be derived or it can be determined which forces can be neglected in a model for the description of the particle motion.

2.3.1 Hydrodynamic forces

A moving particle or a particle placed in a moving fluid experiences a force due to viscous drag. To calculate the forces on a particle in a medium moving relative to it, a model of fluid motion is needed. The flow of Newtonian fluids, like air and water, can be described by the Navier-Stokes equations. The equations are based on the law of conservation of momentum for a continuous medium. Newtonian means that the viscosity of the fluid is constant for a constant temperature and thus independent on the shear rate. For an incompressible fluid (e.g., water, not applicable for air) with a uniform mass density ρ_m the equation is given in differential form by

$$\rho_\mathrm{m}\frac{\partial\vec{u}}{\partial t} + \rho_\mathrm{m}(\vec{u}\cdot\nabla)\vec{u} = -\nabla p + \eta_\mathrm{m}\nabla^2\vec{u} + \vec{f} \tag{2.34}$$

with the pressure p, viscosity of the medium η_m and applied body force $\vec{f}$ (force per unit volume) [Mor03, pp. 66, 67].

In its dimensionless form, there will be a factor characterizing the contribution of the viscous and the inertial term called Reynold's number

$$Re = \frac{\rho_\mathrm{m} u_0 l_0}{\eta_\mathrm{m}} \ . \tag{2.35}$$

Here, l_0 is a characteristic length scale (e.g., the channel radius) and u_0 the velocity of the fluid. If the Reynold's number is low ($Re << 1$), the viscous term $\eta_\mathrm{m}\nabla^2\vec{u}$ dominates the fluid dynamics in Eq. 2.34. For high Reynolds numbers ($Re >> 1$) the inertial term $\rho_\mathrm{m}(\vec{u}\cdot\nabla)\vec{u}$ (net momentum convected out of the control volume) dominates. Solving the Navier-Stokes equation with appropriate boundary conditions gives the fluid velocity arising from a certain body force. [Mor03, p. 67] Analytical solutions are only possible for a few very simple systems. For more complex systems, a numerical solution is necessary or the solving of a simplified version valid for specific limits [Kir10, p. 178].

An example is the Stokes flow for low Reynolds numbers. A fluid flow with a low Reynolds number is in the laminar flow regime. The flow follows streamlines, is free of turbulances and steady at steady boundary conditions. In small channel geometries this is the most common regime. For example, in a microchannel typical Reynolds numbers of 0.1 to 0.01 are reached [Mor03, p. 67]. Therefore the flow is in the viscous fluid limit where $\rho_\mathrm{m}(\vec{u}\cdot\nabla)\vec{u} = 0$ and is dominated by viscose forces [Kir10, p. 178].

Microsystems can be externally driven (pressure-driven by a pump) or by an electric field. For a pressure-driven flow in a pipe, the steady state form is a Poiseuille flow [Kir10, p. 46]. After a certain entry length the steady state is established and results in a parabolic flow profile typical for laminar flows with the mean velocity given by

$$\bar{u} = \frac{h^2 p_0}{3\eta_\mathrm{m} l_0} \tag{2.36}$$

for a rectangular channel cross section with a much greater width than height [Mor03, pp. 67-69].

A common boundary condition for the Navier-Stokes equation is the no-slip boundary condition. For a motionless wall the tangential velocity directly at the wall is defined to be zero $u_\mathrm{t} = 0$. This condition is compatible with findings of macroscale flows as well as the majority of micro- and nanoscale flows [Kir10, p. 30]. But it can fail, for example, for a water flow in a channel with hydrophobic walls [Kir10, p. 35] or in case of electroosmotic flow at the channel walls. These cases can be described by the Navier slip model. The tangential velocity at the wall is proportional to the normal derivative of the velocity

$$u_\mathrm{t} = b \frac{\partial u_\mathrm{t}}{\partial n}\bigg|_\mathrm{wall} . \tag{2.37}$$

The constant b is called the slip length. Typical values are in the order of 1 nm [Kir10, p. 31]. In Sec. 2.3.5 and 2.3.7 the influence of electroosmotic flow will be discussed in more detail.

Unbound Stokes flows like the flow around immersed solid objects with a simple geometry like spheres or prolate ellipsoids are commonly not solved purely numerically [Kir10, p. 182]. If the surrounding fluid velocity and, if necessary, other fields that exert a force on a particle are known, e.g., numerically determined, the resulting particle velocity can be estimated using analytical equations. Solving the Stokes equation for the case of a particle moving relative to the fluid (velocity $\vec{v}_\mathrm{rel}$) leads to the viscous drag force $\vec{F}_\mathrm{drag} = -f_\mathrm{P}\vec{v}_\mathrm{rel}$ on the particle [Mor03, p. 76]. In this case, a non-slip boundary condition is used. f_P is the friction factor which depends on particle size, shape (see overview in Tab. 2.1), and surface characteristics. During acceleration caused by a deterministic force there can be higher drag forces. At a constant applied force, Newton's second law is

$$m\frac{d\vec{v}}{dt} = \vec{F} + \vec{F}_\mathrm{drag} = \vec{F} - f_\mathrm{P}(\vec{v} - \vec{u}) \tag{2.38}$$

with mass of particle m, particle velocity $\vec{v}$, and fluid velocity $\vec{u}$. After the acceleration time $\tau_\mathrm{a} = m/f_\mathrm{P}$ the terminal velocity of the particle

$$\vec{v}_\mathrm{T} = \frac{\vec{F}}{f_\mathrm{P}} + \vec{u} \tag{2.39}$$

is reached. A microparticle will reach this steady state quickly. Ignoring Brownian motion and Buoyancy, the particle velocity due to an applied dielectrophoretic force gets

$$\vec{v}_\mathrm{T} = \frac{V\mathrm{Re}(\tilde{\alpha})\nabla|\vec{E}|^2}{4f_\mathrm{P}} + \vec{u} \tag{2.40}$$

with volume V and dielectrophoretic mobility $\mu_{\mathrm{DEP}} = \frac{V\mathrm{Re}(\tilde{\alpha})}{4f_{\mathrm{P}}}$. [Mor03, pp. 76-78] Using the CM factor instead of α gives:

$$\mu_{\mathrm{DEP}} = \frac{3V\varepsilon_{\mathrm{m}}\mathrm{Re}(\tilde{f}_{\mathrm{CM}})}{4f_{\mathrm{P}}} \,. \tag{2.41}$$

Tab. 2.1.: Translational friction factors for different particle shapes [Mor03, p. 77].

Particle	**Friction factor**
Sphere $a_1 = a_2 = a_3 = r$	$f_{\mathrm{P}} = 6\pi\eta_{\mathrm{m}}r$
Prolate ellipsoid $a_1 >> a_2 = a_3$ random orientation	$\langle f_{\mathrm{P}} \rangle = \frac{6\pi\eta_{\mathrm{m}}a_1}{\ln(2a_1/a_2)}$

2.3.2 Gravity

This paragraph is mainly based on Ref. [Mor03, pp. 165, 166]. Differences in mass density $\Delta m = V(\rho_{\mathrm{m,p}} - \rho_{\mathrm{m,m}})$ between a particle $\mathrm{m,p}$ and the medium $\mathrm{m,m}$ can give rise to a buoyancy or gravitational force on the particle. Here, V is the volume of the particle. The direction depends on the sign of the mass density difference and is given by

$$\vec{F}_{\mathrm{Buoyancy}} = \Delta m\vec{g} \,. \tag{2.42}$$

Here, $\vec{g}$ is the acceleration due to gravity ($9.81\ \mathrm{m\ s^{-2}}$). For sedimentation of a particle, the gravitational force balances with Stoke's drag force. For a spherical particle in a Newtonian fluid, this leads to a terminal sedimentation velocity of

$$|\vec{v}| = \frac{\Delta m|\vec{g}|}{6\pi\eta_{\mathrm{m}}r} \,. \tag{2.43}$$

In many cases, where sub micrometer particles are involved, gravitation can be neglected. But with increasing particle size and density of the considered particles, it can achieve relevant orders of magnitude. For example, a 500 nm polystyrene particle has a sedimentation velocity of around 7 nm $\mathrm{s^{-1}}$, while a 4.5 µm particle can reach 539 nm $\mathrm{s^{-1}}$. However, diffusion of particles can be dominant compared to gravity when it leads to concentration gradients (see Sec. 2.3.4). The gravitational force can also act on density differences within a medium caused, for example, by temperature differences. This can lead to thermal fluid motions, which will be discussed in Sec. 2.3.9.

2.3.3 Brownian motion

As particle dimensions become smaller, their motion is increasingly influenced by random collisions with surrounding molecules [Fri00, p. 30]. This so-called Brownian motion does not lead to a net unidirectional movement in average, but the root mean square of the displacement of particles is not zero [Mor03, p. 166]. The origin of the motion is thermal energy causing molecules to vibrate. The mean

square displacement with time t is given by $\bar{x}^2 = 2Dt$ [Fri00, p. 30]. The coefficient of diffusion D for a particle can be described by the Stokes-Einstein relation

$$D = \frac{k_\mathrm{B}T}{f_\mathrm{P}} \tag{2.44}$$

with Boltzmann's constant k_B, temperature T, and friction factor f_P [Kir10, p. 191].

For small particles, this random motion can exceed deterministic forces like DEP and must be overcome in order to keep particles trapped. The maximum value of the resulting force (index therm) can be approximated by

$$F_\mathrm{therm} \approx \frac{k_\mathrm{B}T}{2r} \ . \tag{2.45}$$

The DEP force and thermal force therefore scale with a ratio to the fourth power of the particle radius [Zhe03]. Accordingly, DEP forces can be expected to significantly dominate over Brownian motion for particles larger than around 500 nm [Mor03, p. 4].

2.3.4 Diffusion

During trapping, a concentration gradient of particles will be build up either at places of low (nDEP) or high field gradients (pDEP). The concentration gradient leads to a directed motion from high to low particle concentration, which is known as diffusion. The driving mechanism is again Brownian motion. When particles are concentrated by DEP in certain areas, the net particle movement due to diffusion is in opposite direction than the DEP flux leading to a concentration profile. However, when a high DEP force is present, the particles are immobilized at the trapping spots and the concentration near the wall/electrode seems to be reduced, which makes diffusion and DEP act in the same direction [Mor03, p. 187]. In any case the particles will redistribute due to diffusion when the field is switched off, and they will be flushed out of the channel by drag force [Pet17a, p. 353]. The transport equation (diffusion and convection) in steady state is given by

$$\vec{u} \cdot \nabla c = D\nabla^2 c \tag{2.46}$$

with the particle concentration c, assuming that the diffusion coefficient is constant and not influenced by surrounding particles [Mas06, p. 471].

2.3.5 Electroosmosis

Electroosmosis (EO) is a common phenomenon in DC electrokinetics and is used, for example, to transport media through microchannels. As explained in Sec. 2.1.9, a double layer is formed when a charged surface is introduced into an electrolyte. Unlike the solution in the bulk, the EDL is not electroneutral and has a net volumetric free charge density. When an electric field has a tangential component with respect to the surface, an electric force acts on these charges of the EDL, moving the ions

and corresponding hydrate shell along the surface. This also sets the surrounding medium in motion via viscous drag. Directly at the surface, the velocity is assumed to be zero because the charges are bound. At the shear layer (slip plain), the fluid motion is maximum and beyond that, fluid molecules are entrained by viscous shear forces (see Fig. 2.8 a). [Mor03, p. 106; Kir10, p. 135] The velocity in x-direction u_x along the surface depends on medium permittivity, zeta potential of the surface ζ_{wall}, and viscosity of the medium η_{m} and is linearly proportional to the electric field tangential to the wall $\vec{E}_t$ just outside the EDL. For thin EDLs (with a thickness small compared to characteristic length of the channel h, $\kappa h >> 1$) and low wall zeta potentials, the velocity in the bulk can be calculated with the Helmholtz–Smoluchowski equation [Kir10, p. 136]

$$u_x = -\frac{\zeta_{\mathrm{wall}}\varepsilon_{\mathrm{m}}}{\eta_{\mathrm{m}}}\vec{E}_t = \mu_{\mathrm{EO}}\vec{E}_t \,. \tag{2.47}$$

The first term can be summarized as the electroosmotic mobility μ_{EO}. The fluid in the bulk seems to slip at the wall and flows in a plug [Mas06, p. 257]. Analytical

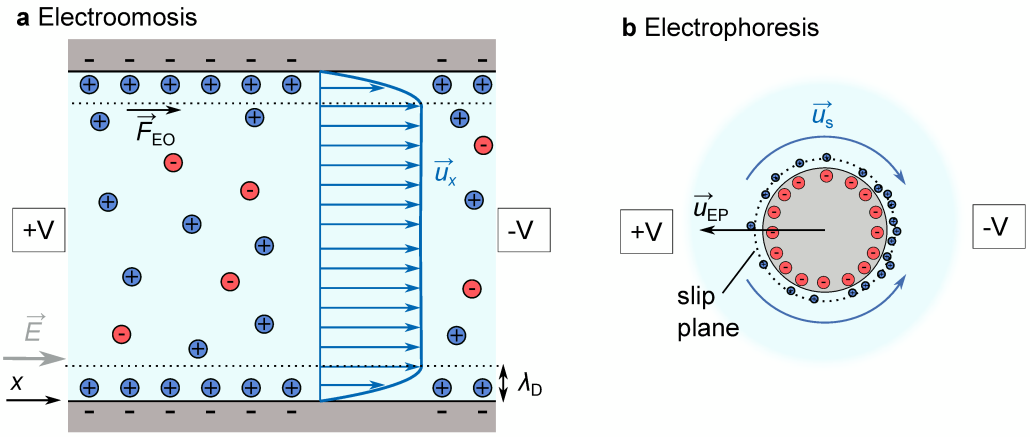

Fig. 2.8.: Linear electrokintetic effects. a) Double layer formation on negatively charged channel walls and resulting electroosmosis flow (based on Ref. [Kir10, p. 132]). b) Electrophoresis of a negatively charged dielectric particle (based on Ref. [Kir10, p. 290]).

solutions for other cases (thick DL or high zeta potential) for which the assumptions are not valid can be found, e.g., in Ref. [Mas06, Ch. 8]. If only the bulk velocity is of interest, Eq. 2.47 can be used as an effective slip boundary condition to solve the Navier-Stokes equation with no source term and using Laplace's equation to get the electric field [Kir10, p. 137].

In an AC field, the time-averaged force for a channel like the one in Fig. 2.8 a is zero. On the other hand, there will be AC electroosmotic (ACEO) phenomena in different geometries. If the electric field is inhomogeneous, e.g., in setups with interdigital electrodes at the channel bottom, this can result in a non-zero time-average local fluid motion. The voltage applied to the electrode gives rise to an

electric field with the tangential component $\vec{E}_\mathrm{t}$ outside the double layer, which acts on the induced charge on each electrode surface. When the potential of the electrodes changes, the sign of the induced charge changes, but the direction of the force and thus fluid movement stays the same as the electric field also changes direction [Mor03, p. 108]. In a closed channel, circulating fluid rolls result (Fig. 2.9 a), which can push particles away from regions of high electric strength. The magnitude of the velocity is frequency dependent. At very low and high frequencies either the potential across the suspending medium or across the double layer is zero (induced charges cannot form), resulting in $\vec{E}_\mathrm{t} = 0$ and no fluid movement. Only at medium frequencies between 10 Hz and 10 kHz there will be relevant AC electroosmosis [Mor03, p. 148] with a time-average velocity [Mor03, p. 109]

$$\langle u_x \rangle = \frac{1}{2}\mathrm{Re}\left(\frac{\varepsilon_\mathrm{m}\kappa\phi_\mathrm{D}}{\eta_\mathrm{m}\kappa}\vec{E}_\mathrm{t}^{*}\right) . \tag{2.48}$$

Here, κ is the reciprocal Debye length, $\vec{E}_\mathrm{t}^{*}$ the complex conjugated of the tangential electric field, and ϕ_D the potential at the diffuse layer. As the velocity is dependent on the EDL thickness, the magnitude of the flow decreases with rising medium conductivity. On the other hand, the frequency at which the maximum velocity is reached increases at higher medium conductivities [Mor03, p. 140]. It should be noted, that in the DEP setups used in this work, no influence of ACEO is to be expected, since the electrodes are widely spaced.

2.3.6 Electrophoresis

The following paragraph is mainly based on Ref. [Mor03, pp. 123-125]. Unlike the dielectrophoretic force, electrophoresis acts exclusively on particles with a non-zero net charge. The Coulomb force on this charge $\vec{F}_\mathrm{EP} = Q_\mathrm{e}\vec{E}$ moves the particle. Electrophoresis also occurs in homogeneous electric fields because in this case, the electric field itself, rather than its gradient, is directly proportional to the force. Furthermore, unlike the DEP force, AC fields produce a time-averaged motion of zero due to the force's change in direction. An electrophoretic movement only occurs in DC fields. In an aqueous solution, the net charge of the particle is shielded by an EDL formation. Just as electroosmosis arises at a charged surface, an electroosmotic fluid flow occurs around the charged particles. For small particles, however, the condition is in the viscous limit and this results in a motion of the particle, while the fluid remains stationary (Fig. 2.8 b). The ion flow moves the particles in the same direction in which they would move without EDL in free space. However, the properties of the double layer which determine its polarization influence whether a particle moves faster or slower than in free space.

In order to select a suitable model to get the particle velocity of a sphere, again the product of a characteristic length, here the particle size (radius r), and the thickness of the double layer κ is considered as well as the magnitude of the zeta potential. For small zeta potentials and $\kappa r >> 1$, the double layer is thin and appears flat

on the scale of the Debye length (Helmholtz-Smoluchowski limit). Therefore, the planar theory like for electroosmosis is valid, giving the steady-state relative particle velocity

$$\vec{u}_{\mathrm{EP}} = \zeta_{\mathrm{p}} \frac{\varepsilon_{\mathrm{m}}}{\eta_{\mathrm{m}}} \vec{E}_0, \tag{2.49}$$

with the particle instead of the wall zeta potential ζ_{p} and the applied field $\vec{E}_0$ instead of the local field. The electrophoretic mobility μ_{EP} is equal to $-\mu_{\mathrm{EO}}$ and the particle will move instead of the fluid [Mor03, p. 124]. Its movement is independent of its size and shape [Kir10, p. 285].

The estimation of the particle velocity gets more complex if the double layer is comparably thick $\kappa r << 1$ or the particle has a high surface potential. In both cases a coupling between the particle's EDL and the electric field must be taken into account. For thick double layers (as for nanometer particles), the ions in the EDL experience a variation of the local electric field, which must be considered (Hückel solution) [Kir10, p. 287]. Furthermore, Eq. 2.49 does not apply for particles with high zeta potentials. In this case, the presence of the double layer perturbs the bulk electric field, as ions are shifted within the double layer. The distorted double layer than counteracts the applied electric field and reduces the electrophoretic movement. How both cases can be taken into account, as well as models for arbitrary Debye lengths, can be found, e.g., in Refs. [Del07; Kir10, pp. 288-292; Mas06, pp. 303-324]. For conductive particles, the electric field is distorted by the EDL, leading to Hückel's model as for thick EDLs [Mas06, pp. 320-321]. The particles used in this work are assumed to meet the conditions for Eq. 2.49 being valid.

2.3.7 Induced-charge electroosmosis

Induced-charge electroosmosis (ICEO) is a term for electrokinetic effects, where an electric field acts on its own induced charges at polarizable (metallic or dielectric) surfaces [Baz04]. ACEO falls into this category, for which in particular the voltage of the electrodes induces charges in the medium. Further phenomena with the same fundamental physical process are travelling-wave electroosmosis and the hydrodynamic interaction among polarizable particles [Baz11a, p. 222]. In contrast to classical electroosmosis, no surface charge of the objects is necessary. Since the charges are induced by the field itself, it has a non-linear influence. ICEO phenomena were observed, for example, around dielectric particles [Gam86], and posts (Fig. 2.9 b) or sharp corners or constrictions in microchannels [Tha02; Yos06]. Some research groups use these effects purposefully for mixing [Baz04; Lev05] and transportation in microchannels [Squ04].

ICEO effects scale with the applied electric field squared and show a plateau in the frequency dependence around the reciprocal of the charge relaxation time of the electrolyte $(\sigma/(2\pi\varepsilon_{\mathrm{m}})$ [Cal21]. The maximum time-average slip velocity for an AC field is

$$v_{\mathrm{slip}}^{\mathrm{ICEO}} = \frac{\varepsilon_{\mathrm{dielec}}}{\eta_{\mathrm{m}}} \lambda_{\mathrm{D}} E_0^2 \tag{2.50}$$

where $\varepsilon_{\mathrm{dielec}}$ is the permittivity of the dielectric object [Cal21] (e.g. post or particle). Recent studies [Cal21; Fer21] show that fluid flows around charged dielectric obstacles attributed to ICEO may be caused by more dominant concentration polarization electroosmosis effects, which will be explained in the next section.

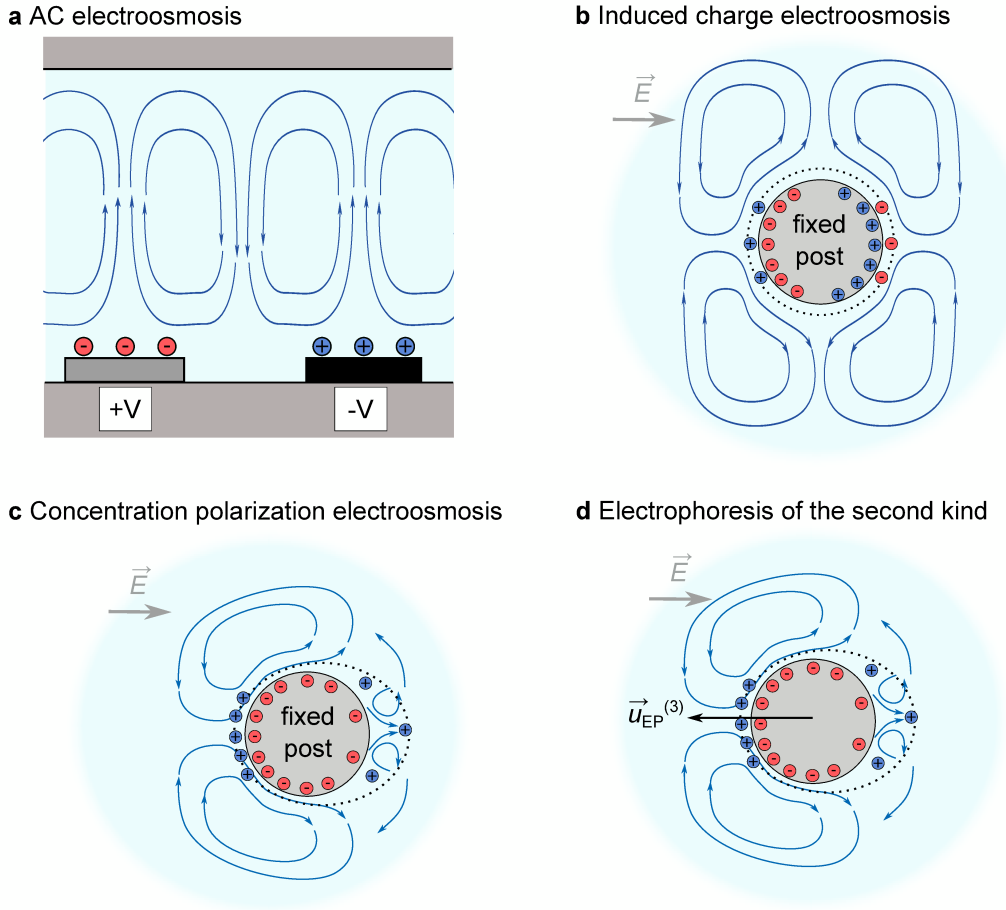

Fig. 2.9.: Electrokinetic phenomena. For illustration, only one polarity of the electrodes or one direction of the electric field are shown, which alternate with the AC field. a) Fluid flow due to AC electroosmosis in a closed microsystem. Two symmetrical flow rolls rise over the electrode edges (based on Ref. [Ram98]). b) Induced charge electroosmosis around a dielectric cylinder (based on Ref. [Cal21]). c) Concentration polarization induced fluid flow around a fixed cylinder. Here the case of a conducting object is shown (based on Ref. [Mis10]), for which stronger CPEO is expected than for insulators. d) Electrophoresis of the second kind for a dielectric particle.

2.3.8 Concentration polarization electroosmosis

Concentration polarization electroosmosis (CPEO) refers to fluid flows that result from the polarization of an EDL due to the action of an electric field [Lyk95, p. 3.206]. The difference to ICEO is that the charges around the particle are attracted by the surface charge of the object (as in standard EDL formation) and are not solely induced by the electric field (Fig. 2.9 c). Due to the effect of the applied electric field, the ion concentration within the EDL becomes asymmetric.

A normal flux of counter-ions balances the variation in the surface current. As a result, the double layer thickness depends on the position around the object. For an AC field, the zeta potential becomes an oscillating function, and the concentration gradients induce a rectified electric field, resulting in the formation of a quadrupolar electroosmotic flow around the object. [Cal21]

CPEO has the biggest impact for DC or low-frequency (< 1 kHz) AC fields. The maximum time-average CPEO slip velocity around a cylinder for an AC field with a frequency below the electrolyte relaxation frequency is [Cal21]

$$v_{\mathrm{slip}}^{\mathrm{CPEO}} = \frac{\varepsilon_{\mathrm{m}} r E_0^2}{2\eta_{\mathrm{m}}} Du \left[\frac{|\zeta_0|}{\phi_{\mathrm{therm}}} + 2\tanh(\frac{|\zeta_0|}{2\phi_{\mathrm{therm}}}) \right] . \tag{2.51}$$

Here, the Dukhin number Du is defined as $Du = K_{\mathrm{S}}/r\sigma$. r is the cylinder radius, ζ_0 the undisturbed zeta potential, and $\phi_{\mathrm{therm}} = k_{\mathrm{B}}T/e$ the thermal voltage. The Dukhin number describes the non-linearity of a system [Car20], as it reflects the competition between surface and bulk conductivity. At high Dukhin numbers $Du >> 0.1$ and low Peclet numbers $Pe < 1$, non-linear EK effects are significant and need to be considered [Rou16]. The Peclet number [Lap22] $Pe = (av_{\mathrm{EP}})/D$ characterizes the balance between convective and diffusive processes near the particle surface [Rou16] which influences the concentration polarization. This theory is only valid for weak electric fields where $E_0 l < k_{\mathrm{B}}T/e$ which $l \sim r(\sqrt{(D\omega^{-1})})^{-1}$ [Fer21]. CPEO is used to explain the flow around dielectric micropillars induced by AC electric fields [Cal21], or more recently the wall repulsion for dielectric microparticles [Fer23].

2.3.9 Electrothermal flow

In contrast to natural convection, in which buoyancy forces drive low density (hotter) parts of a fluid upward and colder parts downward, an electrothermal flow arises from electrical forces. If locally different temperatures occur in a medium, this results in differences in the permittivity and conductivity of the medium. This inhomogeneity of dielectric properties leads to net charge density fluctuations on which electrostatic body forces act, causing a fluid motion [Kir10, p.365]. In channels with a small length scale the natural convection is usually irrelevant in contrast to electrothermal flows [Cas03]. The temperature fluctuation can be generated by external heating sources (like a Peltier element) or by Joule heating as an internal source. As explained in Sec. 2.1.6, Joule heating occurs when an electric current flows through the medium and a portion of the electric energy is dissipated in the form of heat.

To get the temperature field in the fluid, the energy equation

$$\rho_m c_p \left[\frac{\partial T}{\partial t} + (\vec{u} \cdot \nabla)T \right] = k_f \nabla^2 T + \sigma \vec{E}^2 \tag{2.52}$$

has to be solved, with the thermal conductivity k_f, and the specific heat capacity of the fluid c_p [Cas03]. The last term incorporates Joule heating as a heat source.

Furthermore, the heat transport due to convection and diffusion, and the heat flux through the channel walls has to be considered.

The time-averaged electrothermal body force is given by

$$\langle f_e \rangle = \langle (\varepsilon_\mathrm{m}\varepsilon_\mathrm{r} \nabla \cdot \vec{E} + \alpha_\mathrm{therm}\varepsilon_0 \vec{E} \cdot \nabla T)\vec{E} - 0.5\alpha_\mathrm{therm}\varepsilon_0 \vec{E}^2 \nabla T \rangle \tag{2.53}$$

with a linear temperature coefficient of the fluid permittivity α_therm and temperature gradient ∇T [Sri11a]. The first term is generated by the Coulomb and the second by the dielectric force on the free charge. The electrothermal fluid flow can be numerically calculated by solving the coupled electric potential, temperature (energy equation), and flow field (Navier-Stokes) using the electrothermal body force term [Sri11a]. Descriptions of the electrothermal flow over interdigital microelectrodes can be found, for example, in Refs. [Ram98; Cas03; Wan05]. Less studies concentrate on Joule heating in insulator-based DEP devices, e.g. [Sri11a; Gal19; Mal21].

In general, the electrothermal fluid velocity due to external heat sources scales with the temperature rise and the electric potential to the power of 2. In case of Joule heating, it scales with the medium conductivity and the electric potential to the power of 4 (as $\nabla T \sim E^2$ and $\langle f_e \rangle \sim E^2 \nabla T$). Keeping the medium conductivity low ensures no strong influence of electrothermal fluid motion in most cases [Mor03, pp. 140-142]. The frequency of the applied electric field has only an influence on the Coulomb part of the electrothermal force. It decreases with increasing frequency, and becomes negligible for electrical charging times of $\tau = \varepsilon/\sigma >> 1/2\pi f$. The dielectric part is frequency-independent. [Hon11b]

2.3.10 Electrolysis

The following paragraph is mainly based on Ref. [Gen11]. A phenomenon that needs to be considered, which can have undesirable effects, is electrolysis of water (hydrolysis) at the electrodes. Here, water molecules are split at the electrode surface by Faradaic reactions. Ionic charges that migrate to the surface of the electrode can either accumulate at the interface (capacitive current) or go through redox reactions that convert them to electronic charges in the external circuit (Faradaic current)[Pri10]. The reactions at the electrodes change the pH value of the medium locally; $\mathrm{H^+}$ ions are formed at the anode and the pH value decreases

$$\mathrm{Anode} : 2\mathrm{H_2O} \rightleftarrows \mathrm{O_2\ (g)} + 4\mathrm{H^+} + 4\mathrm{e}\ , \tag{2.54}$$

$\mathrm{OH^-}$ ions are formed at the cathode and the pH value increases

$$\mathrm{Cathode} : 2\mathrm{H_2O} + 2\mathrm{e} \rightleftarrows \mathrm{H_2\ (g)} + 2\mathrm{OH^-}\ . \tag{2.55}$$

The influence of the pH value on dielectrophoresis has rarely been investigated. However, especially due to the small channel volume and electrode distances of most DEP devices, hydrolysis can lead to pH gradients across the channel. The

change of the pH value of the solution changes the properties of the EDL, which can result in alterations of the electroosmotic flows [Las04; Ram07; Gar09], particle polarization, and stability of the suspension (particle agglomeration due to lowered zeta potentials [Hug03, Sec. 3.8.4]).

Faradaic reactions arise not only from DC electric fields. Similarly, low frequency AC fields below the characteristic charging frequency of the electrode $\sigma_{\mathrm{m}}\lambda_D/(\varepsilon_{\mathrm{m}}L)$ can provide a potential drop across the EDL to drive Faradaic reactions, just like in the DC case. Here, L is a characteristic length for the electrode system. For the most part, electrolysis can be prevented by using AC fields with frequencies above the charge relaxation frequency [An15]. If a DC field is required for fluid transport (via electroosmosis) or if an unintended DC offset occurs when generating the AC field (no symmetric oscillation around zero current) [Pri10], effects of electrolysis reactions should be considered and the absolute applied voltage should be reduced if possible [Gen11]. AC Faradaic reactions, however, do not necessarily lead to the formation of bubbles. If insignificant amounts of gas are generated in each half cycle, the gas molecules can dissolve without nucleating macroscopic bubbles [Las04].

In addition to the pH value, hydrolysis also changes the ion concentration locally. This leads to conductivity gradients in the fluid and thus local gradients in the electric field. The ions are induced beyond the Debye length and furthermore can be of the same polarity as the electrode. At certain parameters, both can lead to stronger flows than those that occur due to other electrokinetic phenomena like ACEO and can cause a change in the direction of the flow patterns. [Gar09]

2.4 Retention of particles by DEP in fluids

In this chapter an overview of the phenomena contributing to the particle trapping in DEP devices used in this work is given. The chapter is divided in electrokinetic- and pressure-driven methods as both were applied. In both methods, particles can be retained by nDEP or pDEP. The locations of the trapping spots are different for nDEP and pDEP trapping. An inhomogeneous electric field can be generated by inserting insulating structures into an electric field (Fig. 2.10 a). For cylindrical posts, field maxima are created at the structure edges parallel and field minima perpendicular to the electric field. Particles showing pDEP are retained at field maxima if $\nabla|E|^2$ and the particle's effective polarizability are sufficiently high. Accordingly, particles exhibiting nDEP are repelled by the field maxima and can be retained in this way. The structure thus serves as a filter in which the particles are retained via DEP. Usually, the nDEP force on a particle is weaker than pDEP forces, making pDEP trapping more efficient. Considering the Clausius-Mossotti factor, it minimally reaches the value -0.5 at optimal conditions for nDEP, instead of +1 at optimal conditions for pDEP. Moreover, the field gradients at local field minima are several orders of magnitude smaller than at field maxima, which also leads to a significantly lower nDEP force [Lor20].

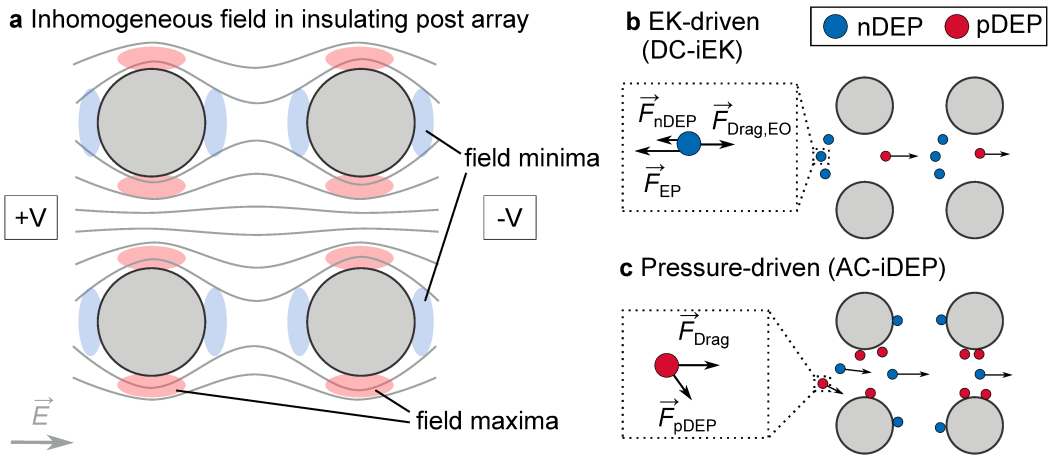

Fig. 2.10.: Retention of particles by DEP. For each subfigure only one electric field direction is shown as an example. a) Field inhomogeneties in an array of insulating posts. The field maxima are located at the posts surface parallel to the electric field. Field minima can be found perpendicular to the field. b) Forces on a negatively charged particle showing nDEP (blue) and trapping spots in electrokinetic-driven DEP methods. Particles showing nDEP are repelled from the field maxima and accumulate in so-called trapping bands in front of each line of posts. Particles showing weak pDEP (red) will be transported out of the filter by the electroosmotic flow (based on Ref. [Hil19]). c) Forces on the particle showing pDEP and trapping spots of pressure-driven methods. Particles experiencing strong pDEP are trapped at the field maxima. Particles showing nDEP pass the filter or may be trapped at the field minima if the nDEP force is very strong.

2.4.1 Electrokinetic-driven DEP

One electrokinetic-driven DEP method is DC insulator-based DEP (DC-iDEP), developed by Cummings and Singh, [Cum00]. Here, the electrokinetic (EK) motion of particles, i.e., electroosmosis (EO) and electrophoresis (EP), is used to carry particles with a steady and homogeneous velocity into trapping zones. If a particle experiences nDEP and it approaches the field maxima between two posts, the nDEP force counteracts the EK motion and the particle can get retained in the filter (Fig. 2.10 b). Recent studies [Car20; Col20] show that for high electric fields it is mainly non-linear electrophoresis – not nDEP – that is responsible for particle retention. The non-linear part (called EP of the second kind) results from a concentration polarization of the diffuse layer, the same phenomenon that causes CPEO (Fig. 2.9 d). Accordingly, the same dependencies on the Dukhin and Peclet number apply (further read Refs. [Rou16; Lap22]). The non-linear electrophoretic term should be considered if the voltage drop across a particle is comparable or larger than the thermal voltage ($\phi_{\mathrm{therm}} = k_{\mathrm{B}}T/e \approx 25$ mV) [Col20]. Note that for high frequencies (above the relaxation frequency) the EDL is not entirely formed and EP of the second kind is thus negligible [Squ04].

For a particle to be captured, the velocity due to DEP and EP of both kinds must overcome the EO motion (Fig. 2.10 b). Considering all phenomena contributing

to the particle velocity (without any additional pressure-driven flow), the trapping condition for DC and low-frequency (< 1 kHz) AC fields becomes [Col20]

$$\vec{v} = \vec{v}_{\mathrm{EP}} + \vec{v}_{\mathrm{EO}} + \vec{v}_{\mathrm{DEP}} = \mu_{\mathrm{EP}}^{(1)}\vec{E} + \mu_{\mathrm{EP}}^{(3)}|\vec{E}|^3\vec{i} + \mu_{\mathrm{EO}}\vec{E} + \mu_{\mathrm{DEP}}\nabla\vec{E}^2 = 0 \tag{2.56}$$

with unit vector $\vec{i}$ in the direction of the applied electric field. For negatively charged particles in a negatively charged channel, both electrophoretic mobilities are negative and counteract electroosmosis. $\mu_{\mathrm{EP}}^{(3)}$ is usually determined experimentally [Lap22] or can be estimated by a non-linear function that depends on several physical parameters, i.e., a modified Duhkin number and a dimensionless particle zeta potential (for details see Ref. [Car20]). Experimentally, it can be estimated by determining the EK velocity

$$\vec{v}_{\mathrm{EK}} = -\frac{\zeta_{\mathrm{wall}}\varepsilon_{\mathrm{m}}}{\eta_{\mathrm{m}}}\vec{E} + \frac{\zeta_{\mathrm{p}}\varepsilon_{\mathrm{m}}}{\eta_{\mathrm{m}}}\vec{E} + \mu_{\mathrm{EP}}^{(3)}|\vec{E}|^3\vec{i}, \tag{2.57}$$

if v_{DEP} is known or assumed to be negligible [Vag22].

2.4.2 Pressure-driven DEP

To retain and hold particles in trapping spots out of a pressure-driven flow, the DEP force must overcome hydrodynamic forces, Brownian Motion, and increasing diffusion. The Langevin equation describes the particle's motion

$$m\frac{dv}{dt} = \vec{F}_{\mathrm{deterministic}} + \vec{F}_{\mathrm{random}} - f_{\mathrm{P}}\vec{v}, \tag{2.58}$$

including random forces due to Brownian motion [Mor03, pp. 177, 178]. Although this equation can be solved numerically, in many cases some simplifications can be applied. For dilute suspensions, for example, particle-particle interactions and near-wall forces can be neglected, and for microparticles the Brownian motion does not need to be considered. For small density differences between medium and particle, buoyancy can be ignored. In many cases, it can be assumed that the particles move in the channel at their terminal velocity $\vec{v}_{\mathrm{T}}$. This leads to a less complex description of the particle motion

$$\vec{v}_{\mathrm{T}} = \frac{\vec{F}_{\mathrm{DEP}}}{f_{\mathrm{P}}} + \vec{u}. \tag{2.59}$$

If this particle velocity becomes zero in the channel, particles can be retained (Fig. 2.10 c). Afterwards, particles can be eluted by switching off the electric field or changing process parameters.

A simplified consideration of a critical trapping distance can be used to investigate different properties of insulating structures such as a post array as well [Pes17]. This is a perpendicular distance from the trapping spot where a particle with a certain diameter can start so that the DEP is strong enough to move it to the spot and retain it. This consideration can help to optimize the geometry and spacing of the filter structure.

A sorting of particles via DEP can be achieved if they show differences in sign and/or magnitude of their DEP forces, so that either the target particles or non-target particles are completely retained in the filter, while the others are flushed out of the filter by the fluid drag. For this the dielectrophoretic mobilities of the particles have to be sufficently different. Sorting is much easier to perform if the DEP force of the target and non-target particles acts in different directions. Since the dielectrophoretic mobility of the particles depends on the process parameters such as medium conductivity and electric field frequency, these parameters can be adjusted to obtain different signs of the mobilities for certain particle systems. Of course this is only possible within a technically feasible range and without causing other interfering physical phenomena (such as Joule heating at high medium conductivities) to overshadow the DEP effects.

Dielectrophoretic separation

3

Dielectrophoresis has already been used as an electrokinetic particle manipulation technology for several decades. First studies on the movement of particles [Poh51] and the separation of materials of different polarizability were performed by Pohl [Poh60]. To date, numerous methods have been developed to concentrate, precipitate, or sort particles with the help of DEP. In this chapter, the state of the art is presented, with a focus on high-throughput DEP devices, dielectrophoretic filtration, and separation based on different particle properties. At the beginning, however, basic concepts of DEP devices are described in order to illustrate the position of the following separation methods and DEP devices within the overall field of DEP research. Furthermore, fields of application of DEP methods are discussed. In the context of this work, the focus is on the concentration and, above all, the classification of particles. Therefore, topics like manipulation with the help of DEP or the separation of biological particles will not be covered in detail. Finally, parameters to characterize the performance of sorting devices are provided.

3.1 Concepts of DEP devices

DEP devices are used to align, capture, focus, concentrate, or separate particles, cells, or liquids in dielectric media [Qia14; Hen22]. The variety of DEP methods can be classified according to some basic concepts, which are introduced in this section. Regarding the most common distinction between insulator- or electrode-based methods, the advantages and disadvantages are discussed, and some example devices are presented.

3.1.1 Basic principles

The basic requirement for DEP motion is the difference in polarizability between particles and the surrounding dielectric medium. DEP processes can be distinguished on the basis of the suspending medium. This can be air, water, oils, or other dielectric fluids. Most common applications use water as a medium as it is highly polarizable, easy to handle, environmentally friendly and bio-compatible [Bal10].

A classification of particles can be achieved by selectively trapping particles via nDEP or pDEP in the device. Here, the DEP force must exceed other forces acting on the particles which should be retained. For a selective process, the other particles must experience DEP forces that are too weak or point in opposite directions so that they are not retained. Such techniques are classified as non-equilibrium methods because target and non-target particles do not experience a continuous equilibrium of forces throughout the whole device length [Gas14]. In equilibrium methods particles do not need to be retained in the device to be sorted. If the target and non-target particles differ sufficiently in their polarizabilities or volume, they can

also be separated in time or space by experiencing differently strong DEP forces. Particles can be separated in time by a DEP force influencing the migration speed within a channel, as in chromatographic processes [Was94]. Here, the DEP force is in equilibrium e.g. with the buoyancy and keeps particles at different heights in the channel. Due to the parabolic flow profile of laminar flows in microchannels, particles at different heights move with different velocities (Fig. 3.1 a1). This method is called dielectrophoretic field flow fractionation (FFF) and is operated batchwise [Dav86; Hua97; Gas09]. An example for a possible continuous separation mode is a spatial separation into multiple outlets. Particles are deflected to different degrees on the basis of their DEP force and are thus forced into different outlets (Fig. 3.1 a2) [Shi08; Abd13; Jon17].

One of the most common classification parameters of DEP processes is how the inhomogeneous field is generated. The inhomogeneous electric field can be either generated by asymmetric electrodes or their arrangement, electrode-based DEP (eDEP), or – as already mentioned – by insulating structures or channel constrictions distorting a homogeneous field (iDEP). Both variations are presented and compared in the next sections.

3.1.2 Electrode-based concepts

For eDEP, the most common electrode-structure is an array of planar, interdigitated electrodes at the bottom of microchannels (Fig. 3.1 a), but the earliest DEP devices with a wire electrode surrounded by a cylindrical counter electrode [Poh51; Poh58] belong to this category as well (Fig. 3.1 b). Since the progressive development of clean room technologies, electrode structures in the micrometer range have been predominantly used, apart from a few technical applications such as in Ref. [Du08]. This is due to the fact that smaller electrodes produce stronger inhomogeneous electric fields, which enables the devices to operate at lower voltages while still producing high DEP forces [Hug16]. The simultaneous use of microchannels also means short orthogonal distances to the electrodes. As the gradient of the electric field decreases rapidly with the distance to the electrode surface [Wan98], this helps to keep the particles within the area of a DEP influence.

First microelectrode-based channels were used by Price et al. [Pri88] to characterize the dielectrophoretic behaviour of cells. The first pDEP trapping of submicroparticles with interdigital, castellated microelectrodes was shown by Gascoyne et al. [Gas92]. The first eDEP continuous method as described above was presented by Markx and Pethig [Mar94] and was able to transport viable and non-viable cells to different outlets. A continuous principle with a spatial separation is also used in the commercial device ApoStream to separate circulating tumor cells from blood [Bal17]. A time-based separation, with a field flow fractionation method, was first introduced by Davis and Giddings [Dav86]. Here, nDEP forces are usually used to push particles away from the electrode array to varying extents. A special form of eDEP, which was also explored quite early, is traveling-wave dielectrophoresis. In this method

particles with different properties travel along the electrode array at different speeds or in different directions. The motion is caused by a lateral DEP force produced by a traveling electrical wave over the electrode array [Hua93; Goa97].

Recent studies continue to show a broad variety of different eDEP methods. Increasingly complex electrode geometries become possible through improvements in manufacturing processes [Hug16], such as 3D [Taj20], vertical sidewall [Wan07], or curved [Han09] electrodes. In addition to the further improvement of existing processes, new separation tasks are explored and hybrid processes developed [Hug16]. A rather new continuous, equilibrium technique combining multiple principles is, for example, isodielectric cell separation. Here, an angled electrode array and a conductivity gradient within the medium, normal to the fluid flow direction, are used to separate particles. Via a combination of DEP and hydrodynamic drag forces the cells are carried in the direction of decreasing conductivity across the channel width until the isodielectric point is reached [Vah08]. The isodielectric point is reached when the net polarization charge of the particle vanishes. A similar approach to classical DEP-FFF is dielectrophoretic particle chromatography (DPC), which also exploits the parabolic velocity profile, but does so by modeling the frequency to achieve multiple trap-and-release cycles of the particles to further increase the resolution [Gie19].

Typically, microfluidic eDEP setups can process sample volumes in the range of microliter to milliliter [Mar22]. Continuous processes like DEP-FFF achieve volume flows of around 100 mL h^{-1} [Wah21]. So far, only few studies exist on further upscaling of eDEP processes. Small throughputs are sufficient for highly valuable products, like carbon nanotubes, which are sorted by their conductivity [Shi08; Rab17], or if high selectivities are necessary, e.g., in the capture of circulating tumor cells out of blood samples [Moo11; Bal17]. One upscaling approach is to use interdigitated structures on PCB board, which can be fabricated with much less effort and cost than microelectrodes, and nowadays more accurate than it was possible in the 80s. Giesler et al. [Gie23] designed a device that achieves high separation efficiencies in volume flow ranges of around 360 mL h^{-1}.

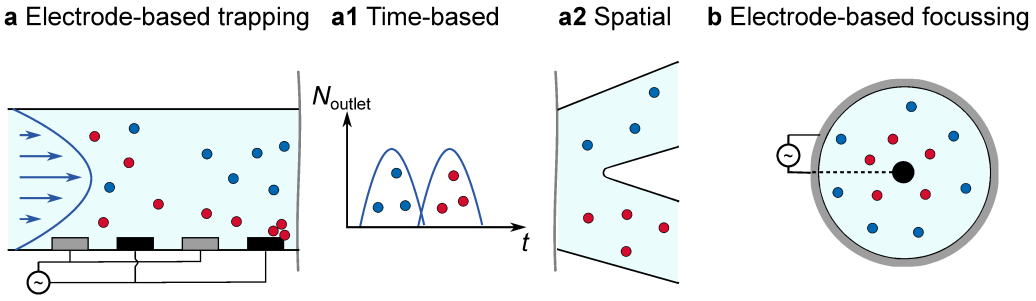

Fig. 3.1.: Overview of electrode-based DEP methods. a) Device with microelectrode array at the channel bottom which is capable of trapping particles at the electrode edges, a1) time-based separation or a2) spatial separation. b) Concentric macroscopic setup which focuses particles into the center or direction of the outer electrode-based on their DEP force.

3.1.3 Insulator-based concepts

Insulator-based concepts are also called electrodeless since the inhomogeneities of the electric field are not caused by the electrodes themselves but by dielectric interfaces within an (almost) homogeneous field. Typically, devices use insulating post structures or one or multiple constrictions of the channel between widely spaced electrodes to create an inhomogeneous electric field [Reg11]. The majority of iDEP or iEK methods are operated in microfluidic setups because higher voltages must be applied as the distance between the electrodes increases in order to generate sufficient field gradients. Approaches that can be considered macroscopic are described in more detail in Sec. 3.2.

A particularly commonly used method is DC-iDEP [Lap05; Cam12; Vag23], developed by Cummings and Singh [Cum00] and recently renamed to DC-iEK [Lap22]. As explained in Sec. 2.4.1, an electroosmotic flow is used to carry particles with a steady and homogeneous velocity into an array of insulating posts where they are retained by nDEP and mainly electrophoresis of the second kind that counteract the EO motion of the particles. To apply the electric field, for example, simple wire electrodes immersed in reservoirs at the inlet and outlet of the channel or embedded in the channel itself can be used. Various geometries were used for the insulating post structures, like diamond, square or circular shaped posts. The focus of some studies [LaL14; Sau15a; Pes16] has been the optimization of the geometry and arrangement of the posts to reduce the required voltage or increase the selectivity. A combination of post structures of different size scales has been investigated as well to capture small biomolecules such as DNA and proteins [Cam12]. For this order of particle sizes, streaming and no complete trapping is more likely [Cam12]. In case of streaming, the particles are focused into areas of high/low field strength where the concentration is significantly increased, depending on whether the particles show pDEP or nDEP. The latest discoveries of the changed contributions of the forces involved in DC-iEK facilitate the optimization of the channel and process parameters in a more targeted manner [Car20]. Before, to match simulated and experimental data, correction factors were used which were in the order of 100. The error was assumed to arise from unconsidered phenomena (which turned out to be correct) and measurement errors [Mon11]. Retention of particles via pDEP is also possible (Fig. 3.2 a) [Pes18b; Jen10; Cum03] but implemented less frequently. Cummings et al. [Cum03], for example, simulatively and experimentally investigated the transition from streaming to trapping in DC-iEK channels. Different post geometries were examined and a field strength of $250\ \mathrm{V\ cm^{-1}}$ was used. Carboxylated 200 nm latex spheres were concentrated in pDEP trapping spots near the sides of the posts. Pesch et al. [Pes18b] also showed pDEP trapping of 1 μm polystyrene particles in a post array, but used $(0.35\text{–}1.4)\ \mathrm{kV_{rms}\ cm^{-1}}$ AC electric fields with a frequency of 15 kHz. Separation efficiencies of up to 90% have been achieved.

Devices with constrictions are used less frequently. Methods that utilize only one constriction often separate spatially by differently strong deflection of particles into different outlets (Fig. 3.2 b) [Abd13; Jon17]. Channels with multiple constrictions [Jen09; Che09a; Cro17] mainly work in a streaming or trapping mode. The individual constrictions act as a kind of DEP gates. Selectively, particles cannot pass through these areas of high field inhomogeneity. An approach with progressively smaller distances between constrictions called gradient iDEP was developed by Hayes's group [Pys07; Che09a; Jon15; Din17]. Here, particles with different properties can pass through different numbers of gates before being retained and thus spatially separated.

Recent studies investigate further optimization or refinement of iDEP/iEK procedures. Crowther and Hayes [Cro17] propose a multi-length scale approach with small bulges on larger constrictions/posts to increase the resolution of iEK devices in general. The particles are forced on more similar pathlines due to high forces at the bulges and experience more uniform forces in the trapping zones which minimize extraneous trapping. In addition, procedures are combined, such as the deterministic lateral displacement (DLD) and electric fields [Cal19; Ho20]. In DLD channels, an array of micro-pillars is slightly tilted so that particles can or cannot follow the carrier fluid depending on their size. The superposition of an electric field can improve sorting [Cal19] or make the process sensitive to other particle properties such as zeta potential [Ho20].

In insulator-based devices DC fields [Cum00; Cam12] are used most frequently. Here, the electric field serves to transport and separate the particles. Less common are DC-biased AC [Gen14; Luo16; Lew18] and pure AC fields [Cho02; Lew14; Jon17]. In case of a pure AC-signal, a pressure-driven flow has to replace electroosmosis if the particles have to be transported through the channel. This can be applied either with the help of a pump [Ili07; Pes14] or via different filling levels of reservoirs [Jon17].

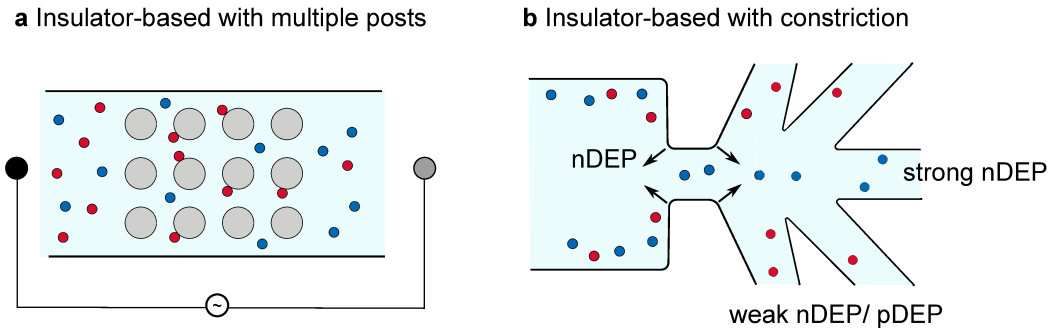

Fig. 3.2.: Overview of insulator-based DEP methods. a) Insulator-based DEP with multiple posts. A selective trapping of particles showing pDEP is shown. b) Continuous insulator-based sorter with a single constriction.

3.1.4 Comparison of electrode- and insulator-based methods

Insulator-based and electrode-based DEP processes are particularly suitable for certain tasks due to their respective advantages and disadvantages. In general, eDEP methods are not suitable to operate at low frequencies (below 1 kHz [Pet17a, p. 286]) as electrolysis and electrokinetic effects (e.g. ACEO) can compromise the processes [Pet17a, p. 285; Hug16; Cho02]. To separate particle or cell systems, the device must operate in a frequency range where sufficient differences in their dielectric properties occur. This requirement opens the main niche for iDEP/iEK procedures. Especially in the bioanalytical field, where differences in the cell membrane capacitance are to be exploited, iDEP/iEK methods are particularly suitable [Pet17a, p. 285]. Also to be mentioned in this context is the fact that high medium conductivities are less of a problem in iDEP/iEK setups [Hug16]. Thus, physiological conditions for cells can be better approached [Pet17b] and a wider process parameter window is available.

A further advantage of iDEP/iEK devices is that their fabrication is usually less costly because there is no need for complex electrode structures [Reg11; Sri11b]. The channels can be fabricated mechanically robust and chemically inert [Cho02]. The production and reproduction of the microfluidic channels can especially be kept simple if polymers, such as polydimethylsiloxane (PDMS), can be used as an insulating channel substrate material [Reg11; Sri11b; Lap19]. Furthermore, the particles do not usually come into contact with the electrode surface, which reduces the possibility of particle damage [Reg11; Lap19]. In addition, this also prevents electrode fouling, which is the deposition of, e.g., salts by electrochemical effects, or the accumulation of trapped biomolecules/particles on the electrode surfaces [Reg11] – both effects that can gradually reduce the trapping efficiency of a device. Finally, iDEP/iEK devices show constant field gradients over the full channel height [Reg11], which is not the case for standard eDEP devices.

However, iDEP/iEK procedures also have significant drawbacks compared to eDEP procedures. IDEP/iEK processes usually require much higher voltages to create sufficient field gradients [Pet17b]. EDEP processes can operate at low voltages (starting at around 10 V), while most iDEP/iEK methods need voltages in the kilovolt range [Hug16]. The high voltage demand can also restrict the range of field frequencies due to limitations of slew-rates of high-voltage equipment [Haw10]. Especially when electrokinetic effects are used for particle transport in iDEP/iEK methods, the throughput is significantly lower than that of eDEP processes [Pet17b]. Pethig [Pet17a, p. 290] thus describes iDEP as suitable for niche applications and summarizes: “An objective assessment of the capabilities of iDEP would suggest that it will not compete well against electrode-based and contactless DEP devices for applications that require high volumetric processing of samples, in combination with fine tuning of the frequency of the applied field to achieve sufficient dielectric discrimination between target and background cell”. However, this statement refers to iDEP/iEK methods that are not pressure-driven and use DC electric fields [Pet17a,

p. 290]. It should be clear by the end of this chapter that pressure-driven iDEP procedures are scalable as well.

3.1.5 Applications of DEP

DEP devices are used for different applications. They can achieve a purification of liquids, an enrichment of particles and cells, a capture for particle analysis, or the classification of different fractions [Cit15, p. 328]. Dielectrophoresis is mostly applied in the biomedical/biotechnological field [Pet10]. It is able to handle cells, subcellular entities (like cell organelles), as well as DNA, RNA, and proteins [Li21]. Numerous reviews provide a good overview of previous applications. Regarding applications in the biomedical/bioanalytical field, the reviews of Li et al. [Li21], Kim et al. [Kim19], and Lapizco-Encinas [Lap19] as well as Pethig's monography [Pet17a] should be mentioned. In the technical field, there are fewer reviews. An overview is given, for example, in Ref. [Cit15]. Pesch and Du [Pes21], on the other hand, summarized the application of DEP for non-biological particle systems. Examples for 'technical' particles handled in DEP devices are carbon nanotubes [Rab17], minerals [Bal10], gold [Du08], and plastic particles such as polystyrene [Zhu12; Pol18; Sau15b].

Recently, Ghomian and Hihath [Gho23] summarized requirements and goals for future DEP procedures which the author considers reasonable as well. The goals are: (1) operation at low voltages to prevent any unwanted effects of high electric fields or potentials and to make portable devices possible; (2) to offer a large electrochemical window to decrease electrochemical reactions between the electrodes and the samples in eDEP case; (3) inexpensive and straightforward fabrication processes; (4) manipulation of sufficiently high sample volumes for practical applications. To expand the applicability of DEP, further research is needed. Some applications and designs are presented in more detail in the next section. The focus here is on processes with a high throughput.

3.2 Concepts of high-throughput DEP devices

While the early DEP separators were already suitable for high throughputs, DEP techniques evolved over time more in the direction of highly selective and specific methods for (bio-)analytics with low throughputs. For analytical or medical procedures batchwise or low throughput methods are sufficient as resolution and reliability are crucial. For technical products, in contrast, an enrichment can already be an achievement and high throughputs are needed. The reason given for not implementing DEP more widely, though, is that there is still a lack of throughput [Mar22], especially with regard to selective processes. Different approaches exist for scaling DEP procedures. These can be macroscopic electrodes of different geometries, the continuous separation into multiple outlets, the use of 3D electrodes, or insulator-based DEP filtration methods.

The definition of high throughput is relative, but to give an order of magnitude, in the biomedical field a throughput above around 0.0001 L h^{-1} can already be considered high throughput [Li21]. For technical applications, Pohl's first concentric DEP device reached throughputs of around 0.75 L h^{-1} [Poh59], while Crissman and Fritsche [Cri77b] even describe throughputs of 18200 L h^{-1} in a packed bed DEP filter with glass beads. Pohl's separator retained rather big particles (130 μm average PVC particles), whereas Crissman's patent describes the retention of iron sulfide and iron oxide of less than 5 μm. However, these kinds of separators are not intended to be selective, and high DC voltages (up to 20 kV_{DC} $inch^{-1}$ [Cri77b]) or low frequency AC voltages (4 kV at 60 Hz [Poh59]) have to be applied. This is only applicable in no aqueous solutions like petroleum-based or other non-polar solvents (low current flows due to low conductivity and no electrolysis). Furthermore, high energy input can also give rise to detrimental effects such as Joule heating [Li21].

The electric field gradient scales proportionally to the voltage input and antiproportionally to the characteristic length [Li21]. Thus, in standard DEP devices with low voltage input the channel cross section is limited. Martinez-Duarte [Mar22] reviews fabrication methods for an asymmetrical scaling of DEP using 3D electrodes to increase the cross section in one dimension (height). Most fabrication processes of such devices are relatively complex and of high cost, which has restricted their large-scale preparation [Li21]. Semi-batch, microfluidic eDEP methods with interdigital electrodes reach around 0.03 L h^{-1} [Gad06]. Continuous methods, like the combination of DEP and DLD or FFF, can achieve higher fluxes but rely on a complex and rigorous design, which restricts the flexibility of particle manipulation [Li21]. For example, throughputs of 0.24 L h^{-1} can be reached with DEP-FFF [Wah21]. IDEP methods like DEP filtration, similar to the separators of the early days, were proposed to increase the throughput further; however, the devices are unlikely to reach the selectivity of state-of-the-art microfluidic DEP separators yet [Pes21]. Some DEP filtration methods are presented in more detail in the following section (Sec. 3.2.1). A combination of high throughput and selectivity has not been achieved so far, and one possible pathway to overcome the problems mentioned above in order to achieve this is presented within this work.

3.2.1 Dielectrophoretic filtration

Processes can be classified as dielectrophoretic filtration when a dielectric filter matrix develops a filtering effect by applying an electric field. The advantage over standard depth filtration is that the pores of the filter matrix can be significantly larger than the target particles. This means that the filters have significantly lower pressure losses and particles can be recovered without backwashing by switching off the electric field. In comparison to electrical filters, the particles do not need to be charged [Cit15, p. 389] or get charged (like corona discharge in electrostatic precipitators) [Miz00]. An overview of studies on DEP filtration can be found in the appendix (D).

Different kinds of filter matrix materials can be used. The selection should be made according to the characteristics of the particles to be separated. For example, the zeta potentials of the matrix and particle should have the same sign and preferably high magnitudes to achieve sufficient electrostatic repulsive forces and thus prevent adhesion. In general, however, high field gradients should be generated (smallest possible structures) and at the same time, the surface should be smooth so that the particles can be easily washed out of the filter [Cit15, p. 376]. In addition, the matrix should be chemically inert.

The most common form of filter matrix is a packed bed of insulating materials. Even before the first mention of insulator-based DEP in the early 2000s, numerous patents were filed under the term 'electrostatic filter' without naming the phenomenon that leads to the separation – dielectrophoresis. Common to all of them is the goal of removing microparticles from oils or other non-polar liquids to purify them by using high DC voltages (5–200 kV) [Obe77] applied to macroscopic electrodes in a vessel between which insulating materials are loosely packed. These filters can remove finest particles from the oils with low pressure losses, no clogging, and longer running times without cleaning compared to classic filters. In addition, cleaning is easier because the main force holding the particles in the filter matrix can be switched off. The patents describe a wide variety of fillers such as sand, gravel [Obe77], limestone, furnace slag, glass beads [Cri77a; Cri77b; Fri94; Hal00], crushed glass [Lan79], ceramics, palletized clay, plastic granules [Ham50], fibers (glass wool, plastic, nylon) [Shi68; Wat83; Ham51], polyurethane foams [Wat67] as well as their suitability for specific tasks. Additionally, different electrode arrangements and flow paths, the improvement of cleaning processes, or the design of replaceable filter packs [Wat67; Wat83] are described. Oberton [Obe77] proposed the usage of non-spheroidal configurations like crushed materials to increase the trapping efficiency without knowing the scientific explanation for the improvement. Applications range from petroleum processing, liquid silicones [Hal00], dry cleaning solvents [Ham51] to natural oils and (edible) fats [Obe77]. One commercial available device is the Gulftronic® electrostatic separator to remove catalyst fines from petroleum or crude oil, which is based on the patents [Cri77a; Cri77b; Fri94].

Early studies of Benguigui and Lin [Lin81; Ben82; Lin82b; Lin82a; Lin85] investigated the design of the Gulftronic filter with respect to its optimization potential, such as a multi-stage and a continuous variant as well as the use of AC fields. They already use the term 'dielectrophoretic filter'. Until today, further studies conducted by other groups have followed, using packed beds of glass or silica spheres [Sis95; Sue03; Wak03; Ili07; Lew18; Li19b; Li19a; Li20; Li23b; Li23a]. For the first time, nanoparticles (50 and 300 nm SiO_2) were separated from alcohols [Sis95] and live and dead cells (yeast) were sorted in aqueous media [Sue03; Ili07; Lew18; San20]. For separations in aqueous solutions comparably low AC voltages (15 to 600 V_{pp}) with 5 kHz to 1 MHz were used. Sankaranarayanan et al. [San20] recently investigated the application of such filters powered by low voltages (15 V, 1 MHz)

to filtrate foodborne pathogens out of water. No volume flow is given as the sample was circulated for 1.5 h in the filter unit.

Much less frequently, monolithic structures were used as filter media. To the best of the author's knowledge, sponges as a filter matrix were first mentioned in a patent by Waterman [Wat67]. Here, the use of polyurethane foams with 10 to 30 pores per inch was proposed, although in a filamentary form. Considerably later, Pesch and co-workers again utilized foams [Pes14] and sponges as filter material [Pes18b; Lor20]. They separated 300 nm nanocapsules from a highly conducting aqueous medium in a polyethylene monolithic foam with a pore size of 20 to 60 µm between to stainless steel plate electrodes [Pes14]. Lorenz et al. [Lor20] separated polystyrene (4.5 µm) and graphite microparticles (≈ 3 µm) in an alumina-mullite ceramic sponge (see Fig. 3.3 a) with a pore window diameter from 180 to 270 µm. The ceramic has high

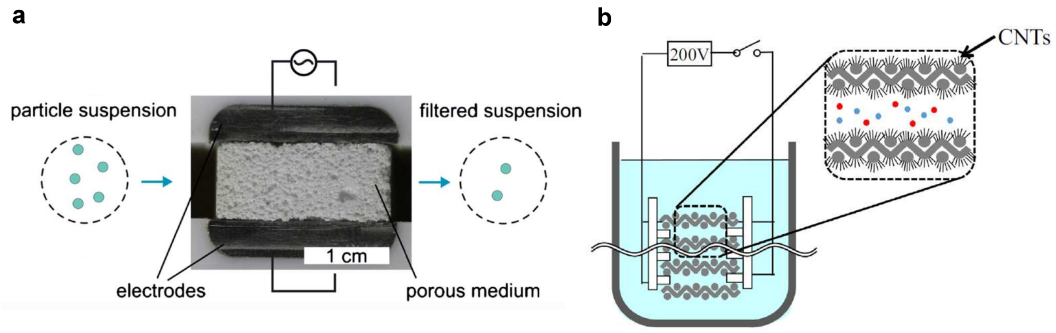

Fig. 3.3.: Examples of DEP separation devices. a) Macroscopic DEP filter with a porous ceramic filter medium (reprinted from [Lor20] published under CC BY 4.0 license). b) DEP separator with a stack of mesh electrodes and attached carbon nanotubes (CNT) to enhance trapping (reprinted with permission from [San16], copyright (2016) Elsevier).

open porosity and features numerous pore windows of different sizes with sharp thin edges. This leads to a mixing of the fluid and thus transport to the trapping zones and simultaneously high electric field gradients [Lor20]. In comparison to packed beds of beads, this can be beneficial to increase the trapping of particles (showing no strong sedimentation). A rather unusual low-cost variant was presented by Islam and Gagnon [Isl22], who used fiberglass paper as a filter matrix between electrodes of copper tape.

3.2.2 Mesh-based filters

Another possible filter material with high scaling potential are meshes. A list of studies using meshes in dielectrophoretic devices can be found in Tab. 3.1; it is by no means complete and aims to provide an overview. Mainly, woven meshes or cloth with metal wires were used as electrodes in 3D eDEP concepts. For example, Sano et al. [San12; San14] developed a filter consisting of stacked stainless steel mesh electrodes separated by spacers which were submerged to a particle suspension in a vessel. Later, they enhanced the electric field strength by attaching carbon nanotubes

directly on the electrode wires (see Fig. 3.3 b) and thereby achieved a selective capture of titanate nanotubes [San14]. Abidin et al. [Abi07] trapped yeast in a stacked flow-through filter made of metal wire electrodes woven into a polymer fabric. Iliescu et al. [Ili07] and Lewpiriyawong et al. [Lew18] separated viable and non-viable yeast in packed bed filters with 100 μm silica beads and mesh electrodes. Shen et al. [She11] introduced an oil filter out of two copper mesh electrodes with several layers of polymer meshes in between, using a dielectrophoretic gating concept. In the last two devices, the insulating fibers also act as additional field disturbers. More recently Nadzri, Abidin, and Salleh [Nad18] studied the influence of the wire diameter, yarns size, and wire configuration of wire cloth electrodes for DEP filters. They found that the electric field strength is highest when wire electrodes with a larger diameter (100 μm), insulator fibers with smaller yarns sizes (10 μm), and a double twisted wire configuration is used. Only the patent by Watson, Mayse, and Franse [Wat83] mentions the possibility of using nylon meshes wrapped in layers as an insulating filter matrix. However, to the author's knowledge, this has not been further investigated or technically implemented. In general, these mesh-based concepts have a great potential for scalability due to their simple design and 3D structure [San12]. In addition, low-cost and commercially available materials can be used as well. Therefore, in this thesis, a scalable mesh-based iDEP filter is conceptualized and technically implemented.

Tab. 3.1.: List of studies that used meshes in dielectrophoretic devices.

Reference	Filter matrix	Electrodes	Particle type	Process parameters	Comments
[Abi07]	Cloth made of stainless steel wires and polyester yarn	Wires in cloth (100 μm, 150 μm/170 μm distance)	Dead and live yeast cells	300 mL h^{-1}, 30 V_{pp}, 1 MHz	Propose straightforward scaling with a stack design
[Nad18]	Cloth made of stainless steel wires and polyester yarn	Wires in cloth (71 μm/100 μm, (40–200) μm distance)	Bacteria (E. coli cells)	20 V_{pp}, 1 MHz	Optimization of wire and yarn diameters as well as configuration
[San12]	Mesh-stacked electrodes with spacer	Wire-mesh-sheets (0.25 mm wire diameter, 0.5 mm distance)	Tungsten carbide from diatomite particles	90 V_{pp}, (50–800) kHz	In ethanol, batchwise input of the particles and collection of sample below the filter
[San14]	Mesh-stacked electrodes with spacer	Wire-mesh-sheets (0.29 mm wire diameter, 0.5 mm distance) with attached carbon nanotubes	Titanate nanotubes	200 V_{pp}, 40 kHz	Batchwise, capture of particles by immersion in bath and release in other vessel
[She11]	Winded filter out of woven metallic and insulating meshes	Copper wire-mesh (114 μm)	Glass beads, fused aluminum oxide powder, silicon metal powder	61.2×10^3 mL h^{-1}, (220–400) V_{rms}, 60 Hz	Continuous, from engine oil, low cost, easy scalable
[Ili07]	100 μm silica beads	Metall mesh electrodes, 1 mm distance	Live and dead yeast	150 V, (10–20) kHz, (3–12) mL h^{-1}	Batchwise, aqueous solution
[Lew18]	100 μm silica beads	Metall mesh electrodes, 1 mm distance	Live and dead yeast	600 V_{pp} (0.1–10) kHz +50 V_{DC}, (60–300) ml h^{-1}	Batchwise, aqueous solution

3.3 Research and studies on separation in respect of various properties

This chapter presents dielectrophoretic methods and studies that separate particles based on their properties. First, processes that address individual properties are presented, followed by multidimensional sorting. Here, only studies that separate particles and do not, for example, investigate the orientation or targeted accumulation on the basis of specific properties are discussed. In the chapter on multidimensional separation, methods aside from DEP are also described to highlight that multidimensional separation of microparticles is still a rarely explored task. Some parts in this section are based on Refs. [Wei19] and [Wei22].

3.3.1 Size-based separation

The separation by particle or cell size is one major unit operation, e.g., for the preparation for technical applications or in analytics. In many cases, the size of the particles determines their properties, like the catalytic activity [Zho10; Bis13], electrical resistance [Don20], light absorption [Kum10], or the drug delivery capability [Koh07]. In addition, size is a parameter to easily differentiate between cell types and alterations, like distinguishing between normal and leukemic cells [Gas92]. As has already been discussed in the introduction, separability in the nanometer and micrometer range is not always (economically) feasible by means of standard methods. Size-based separation using DEP was investigated in many studies, for example Refs. [Wan98; Kra06; Che09b; Sau16; Mod19; Cal19; Gie19; Gie23]. Since the DEP force scales with the particle radius to the power of three, separation is already possible based on small differences. For example, Calero et al. [Cal19] separated 500 nm, 1 μm, and 3 μm PS particles with a combination of DEP and DLD. They were able to classify more than two particle sizes by superimposing an AC field with low DC offset and were able to work with a DLD array, which is suitable for separating larger particles (critical diameters of 5 μm at which separation would occur).

3.3.2 Material- or charge-based separation

Only few studies concentrate on the material-selective separation of particles. A separation by the material has a special relevance in the technical field. For example, materials have to be gained from natural resources (e.g., rare earths from natural minerals [Che22]), products have to be separated from reactants, residues, or impurities (e.g., grinding media wear from ground products [Fla17]), or material mixtures have to be separated in recycling processes (e.g., metals and non-metals from electrical waste [Soh12; Hua09]). The possibility for sorting polystyrene and graphite particles in a DEP filtration setup was shown by Lorenz et al. [Lor20], and the potential of DEP to sort different minerals (like galena and quartz) was shown by Ballatyne and Holtham [Bal10]. Jia [Jia15] classified mixtures of 25 μm

gold-coated PS microparticles and native 10 μm PS microspheres, as well as 2.5 μm yeast cells and the same gold-coated PS in a continuous device with 3D electrodes spatially. Sano et al. [San14] purified titanate nanotubes by removing TiO_2 powder from which they were synthesized. Titanate nanotubes are used, for example, as photocatalysts or absorption media [San14]. The same group also separated tungsten-carbide particles, which are a waste product in machine tool production, from diatomite filter media particles [San12].

Significantly more often, charge-based separation of particles was investigated, e.g., in Refs. [Zhu12; Pol18; Len19; Hil20; Cal19; Pat13; Jel09; Vag22; Gie21]. Vaghef-Koodehi et al. [Vag22], for example, separated almost identical particles with a zeta potential difference of 3.6 mV in an iEK microfluidic channel. Rabbani et al. [Rab17] classified semiconducting carbon nanotubes by their zeta potential also using an insulator-based setup with low AC-frequencies. The separation of PS particles based on their surface functionalization and hence surface charge was shown, e.g., by Giesler et al. [Gie21] and Lentz et al. [Len19].

3.3.3 Shape-based separation

The separation by particle shape is even less frequently investigated than that by material, but it has received increasing attention. In particle synthesis, there are often variations in size and shape, and the subsequent classification according to shape in the microscale is still difficult to realize [Beh18]. For example, the use of non-spherical polystyrene particles is investigated in drug delivery [Bar13] and the shape influence of metal nanoparticles was recently studied for the use in photovoltaic cells [Cho17]. Several studies have shown that DEP is suitable for shape-selective separations [Bar94; Mon11; Val11; Ria11; Sau15b; DuB14]. One example is the classification of fibers according to their length by Baron et al. [Bar94]. They classified 8 μm to 31 μm chrysotile fibers by their length out of an aerosol in a macroscopic dielectrophoretic classifier. Effective separation based on length, independent of fiber diameter, could only be achieved with conductive fibers or at high humidities. The possibility of separating rod and cubic shaped ZnO particles was investigated by Riahifar et al. [Ria11]. They used an electrode array and low frequency AC-fields to deposit the rod shaped particles in the electrode gaps by DEP, while the cubic shaped particles follow ACEO vortices.

3.3.4 Multidimensional separation

In this work, multidimensional separation is understood as a purposeful separation based on more than one particle property [Buc23] in a single pass of the separation device. This can also be termed as multi-target [Kim08; Wu21] or multi-parameter separation or sorting [Cha22]. The term ‘multidimensional separation’ was originally introduced in the context of chromatography. Giddings [Gid84; Gid87] defined multidimensional separations as techniques where samples are separated in two or more displacement steps (mechanisms) according to different factors. A second

requirement for a technique to fit the definition is that the resolution reached in one step remains in the following steps [Gid87].

So far, complex multi-target separations can be realized by using label-based separation methods, which require rather complicated preparations and procedures, or by combining multiple label-free techniques on a single microfluidic chip [Wu21]. For example, Kim et al. [Kim09] used different DEP-tags that bind to specific target cells. These are separated in a dielectrophoretic spatial sorter according to the DEP properties of the tags. In this way, different target cells with their specific labels and also non-target cells can be sorted. There are a few examples of sequential systems using DEP. Derakhshan et al. [Der21] numerically investigated the combination of traveling surface acoustic waves and DEP to separate red blood cells, white blood cells, and breast cancer cells. These cell types differ in terms of both size and membrane capacitance. Ho et al. [Ho20] combined DLD and DEP to sort polystyrene particles and nano liposomes by their zeta potential and size. Four sequential microfluidic methods (DLD, DEP, bipolar electrode focusing, and acoustic separation) were used by Wu et al. [Wu21] to separate PS particles, oil droplets, and viable and non-viable yeast cells. More examples on hybrid dielectrophoretic devices can be found in a review of Al-Ali et al. [Al-22] and Cha et al. [Cha22].

One label-free method using only a single separation mechanism (DEP) is the frequency hopping method introduced by Modarres and Tabrizian [Mod19]. They use a continuous change between two frequencies to separate a multi-target particle mixture in a microchannel with interdigitated electrodes and achieved volume flows of around 40 µL h^{-1}. So far, they have only shown the multitarget aspect using three different particle sizes. A size-selective multi-target separation into several fractions was also shown by Lewpiriyawong and Yang [Lew14]. They spatially sort the particles into multiple outlets. B.I. et al. [BI20] simulatively investigated the parameter and design criteria for such spatial separation devices. The author believes that these methods offer potential to address separation based on other properties as well, but this has only been demonstrated using multiple target particles that vary in only one property. Other methods such as multi-step DEP [Ald06] or dielectrophoretic particle chromatography [Shi13; Was94; Gie19; Gie21] use a frequency or voltage modulation to achieve a time-based separation resulting from multiple trap-and-release cycles. These methods might also be suitable for multidimensional separation, as they can address multiple particle properties.

3.4 Selective release of particles

One approach to enable multidimensional separation might be the selective release of particles trapped by DEP. A few studies show the selective removal of single bioparticles which were isolated in individual controllable traps [Vol01; Thi20; Zhu12; Gen19]. For example, Geng et al. [Gen19] selectively detach particles by

applying an nDEP force at additional electrodes located at the trapping zones. These methods are suitable for analytical purposes.

A simple possibility to selectively release batches of particles is given in the case of DC-iEK. Since different particle types experience electrokinetic forces of different strengths, it is sufficient to reduce the DC voltage until the forces in the direction of the channel exit (EO) outweigh the restraining forces (EP and DEP) for one particle type. For example, this was shown for viable and non-viable bacteria, and PS-particles [Lap04; Mon10]. In pressure-driven devices, this can also be achieved by increasing the fluid velocity, which again releases particles with a lower restraining force. Since the magnitude of the pDEP force often exceeds that of an nDEP force, this enables, for example, particles to be selectively detached in a channel where different types of particles are retained by either nDEP or pDEP [Wan93].

Another method is to specifically pass the crossover frequency for only one particle type. This method takes advantage of the fact that different particle types show different dependencies of their effective polarizability on process parameters. For example, in a device in which particles are selectively retained by pDEP, reaching the point of transition to nDEP for one particle type can lead to selective remobilization. This can be realized either by gradually increasing the medium conductivity [Mar96], or by changing the frequency of the electric field [Bec94; Bec95; Kik18]. Becker et al. [Bec94; Bec95] achieved a separation of cancer cells from normal blood cells by alternating between two frequencies, whereby only the normal cells exhibit a negative effective polarization at one frequency. The separation of live and dead bacteria was shown by Kikkeri et al. [Kik18] by reducing the frequency once below the crossover point of the dead cells to release them selectively. To the best of the author's knowledge, selective remobilization has not been used for multidimensional separation of more than two properties before.

3.5 Parameters to describe filter/sorter performance

The performance of a separation or sorting process can be measured in terms of different aspects. Common factors include throughput, separation efficiency, purity of separated fractions, and reproducibility. Depending on the application, the importance of these aspects differs. For example, in many cases throughput and selectivity show opposite trends, and it must be weighed up which one is decisive for the application. Since the definition of performance parameters can be ambiguous or different across disciplines, the parameters used are presented in this chapter. This section is mainly based on Ref. [Pet17a, pp. 3, 4].

3.5.1 Throughput

The throughput of a device or plant is often expressed in terms of a volumetric flow rate (mL h^{-1}) or number/mass of product processed in a given time (g h^{-1}).

When developing separation methods, the first definition is often initially more applicable, which is why the term 'throughput' is used in this work as the realized volumetric flow rate of the separator.

3.5.2 Separation quality

When evaluating the performance of a separator, it is important to take into account which function is to be fulfilled. If only one type of particle (index a, target particle) should be unselectively filtered or immobilized, a simple specification of the trapping efficiency

$$\eta_a = \frac{\dot{n}_{a,\mathrm{in}} - \dot{n}_{a,\mathrm{out}}}{\dot{n}_{a,\mathrm{in}}} \tag{3.1}$$

is suitable, where $\dot{n}_{a,\mathrm{in}}$ is the particle flux into the channel (index in) and $\dot{n}_{a,\mathrm{out}}$ is the particle flux out of the channel (index out). If the time intervals and the unit area to which the fluxes are related are the same, the total number of particles N can be considered as well.

However, the aim may not only be to deplete particles in the filtrate, but also to increase the particle concentration in the retentate or remobilisate. The quality of a particle concentration can be characterized by the enrichment EN_a of the target species a

$$EN_a = \frac{N_{a,\mathrm{out}}}{N_{b,\mathrm{out}}} \frac{N_{b,\mathrm{in}}}{N_{a,\mathrm{in}}} \tag{3.2}$$

with all non-target species combined as b. Here, N_{out} is the number of particles collected at the outlet compared to the initial number in the suspension N_{in}.

If, on the other hand, the focus is on the selective separation of one particle type or even the sorting of several particle types, these parameters are not sufficient. As a quantification of the selectivity for one of the species a the parameter separation purity P can be considered:

$$P_a = \frac{N_{a,\mathrm{out}}}{N_{a,\mathrm{out}} + N_{b,\mathrm{out}}} \ . \tag{3.3}$$

In order to evaluate the sorting performance independently of any initial concentration differences of the original suspension, in this thesis, all particle numbers are normalized to their total/initial number. However, the purity can hardly be compared between processes without taking the yield into account. For example, a process may achieve a purity of 1, but may separate only a negligible fraction of the particle type. The yield indicates how large the proportion of the trapped and then released particle quantity is compared to the total quantity of processed particles of this fraction

$$Y_a = \frac{N_{a,out}}{N_{a,in}} \ . \tag{3.4}$$

Depending on the separation task, yield must be balanced against purity.

3.5.3 Recovery rate

A comparable parameter to the yield is the recovery rate. This parameter represents the ratio of released particles (index remob) to previously captured particles (index trap) of one type

$$R = \frac{N_{a,\mathrm{remob}}}{N_{a,\mathrm{trap}}} \,. \tag{3.5}$$

Compared to the yield, the recovery rate therefore does not consider the fraction that flows into the channel but is not retained (due to trapping efficiencies < 1). In the case of a DEP filter, the recovery rate is 1 if all previously trapped particles exit the channel after the electric field is switched off. If other non-specific interactions with the filter matrix outweigh fluid drag, such as van der Waals interactions, particles may remain in the filter.

3.5.4 Filter capacity

In classical depth filtration processes, the pressure drop of the filter matrix increases over the experimental time due to the accumulation of particles, which leads to a decrease in the flow rate at constant pressure [Ho07, p. 179]. To maintain a high flow rate, the filters must be back-flushed regularly. The filter performance can be characterized by the filter capacity. This is defined as the volume that can be processed before the flow rate falls below a specified value in the case of a pressure-driven flow [Ho07, p. 179].

No noticeable increase in pressure drop is expected with DEP filtration, as the particles are substantially smaller than the filter matrix pores. However, due to the accumulation of particles at trapping zones, the separation efficiency may decrease over the test period. Therefore, DEP filtration processes should also be tested for possible time dependencies of the separation efficiency and, if necessary, filter capacities should be defined.

Aim of this thesis

4

As described in the previous chapter, dielectrophoresis has been successfully applied to highly selectively separate or concentrate particles. It is also able to address different properties like size, shape, material, or surface properties, which has been shown especially in the bio-analytical area. However, many studies simultaneously varied multiple parameters by using different kinds of cells or particle materials instead of investigating the influence of a single property at a time and primarily aimed to solve specific separation tasks. On the other hand, this thesis intends to improve the general understanding of separation based on different particle characteristics by specifically investigating the influence of individual particle properties. The findings are intended to help realize a combination of selective remobilization from the filter structure and selective trapping.

Through the combination of selective retention and release of particles, an interconnection to a multidimensional sorting is conceivable. For example, a preclassification according to material or size could be realized by selective trapping. Subsequently, the retained particles could be additionally sorted via a selective remobilization step, e.g., based on their shape. In this way, a kind of semi-continuous operation mode could be realized to sort particles multidimensionally (see principle sketch in Fig. 4.1). By periodical injection of a particle mixture into a carrier flow, the purity of the remobilized fractions could be increased. During the inflow of the particle solution, particles would be selectively retained in the filter and a first fraction of not-trapped particles could be collected at the channel outlet (Step 1: Selective trapping). A subsequent change to a flushing solution as well as changes in the electric field properties (e.g. voltage U or f) could selectively remobilize types of particles that show no pDEP at the now applied parameters (Step 2: Selective remobilization 1). The procedure could be repeated with a different set of parameters to release another fraction of the particles (Step 3: Selective remobilization 2). By switching off the voltage, finally, the remaining particles could be eluted from the channel (Step 4: Recovery). Subsequently, a new particle pulse could be injected and the procedure repeated. In the following, the term 'remobilization' is used when particles are detached from the filter by a change in frequency, while 'recovery' is used when particles are detached by switching off the electric field.

The scope of this work is to lay the foundations of such a process. An overview of the content and workflow of this thesis is presented in Fig. 4.2. First, a model particle system is selected and its suitability tested using standard DEP/EK methods (chapter 5). For this, monodisperse, fluorescent polystyrene particles are used as a starting point as they offer almost homogeneous properties and facilitate in-situ observations of the particle motion, immobilization and release, which significantly

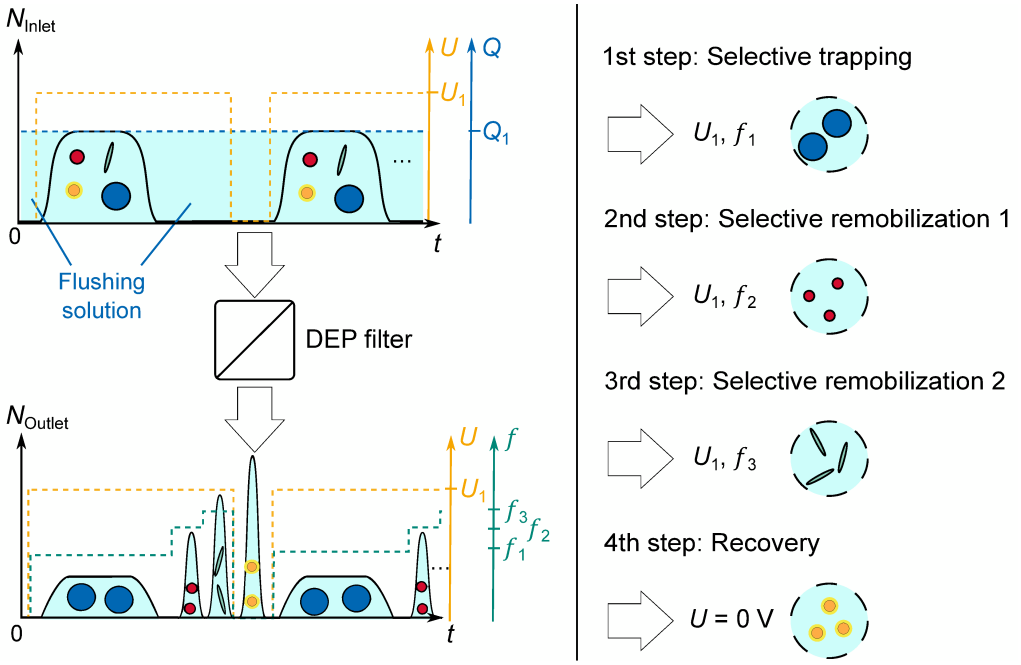

Fig. 4.1.: Principle sketch of a semi-continuous operation mode of a DEP filter which sorts according to several particle properties in one pass.

simplifies the investigation. Particles are altered by a coating and a stretching procedure to achieve differences in just one property at a time with respect to the base particle (conductivity and shape).

A second major task in this thesis is the conceptualization of a scalable DEP filter design with regular structures, its realization, and the testing of the prototype. The investigations of Pesch et al. [Pes18a] and Lorenz et al. [Lor21] aimed for deriving general design rules for insulator-based DEP filtration devices and for reaching higher throughputs. The focus was on increasing separation efficiencies and they made first steps towards selective trapping and an improvement of particle recovery. The DEP filter prototype in this thesis shall facilitate the experimental investigation of multidimensional separation by using ordered field disturbing structures (chapter 6). Furthermore, a concept for scaling shall be developed. The volumetric flow rates of the prototype realized in this thesis shall achieve throughput ranges that are sufficient for further off-line evaluation steps (such as particle size determination via scanning electron microscope (SEM) images), which are necessary for real particle mixtures in the near future. In order to compare the sorting performance of the developed DEP filter, the separation results of the standard DEP methods in microchannels serve as benchmarks. After the comparison of the microchannel and the upscaled version, the concept of multidimensional sorting will be examined (chapter 7). The aim is to realize one cycle of the semi-continuous process described at the beginning of this chapter.

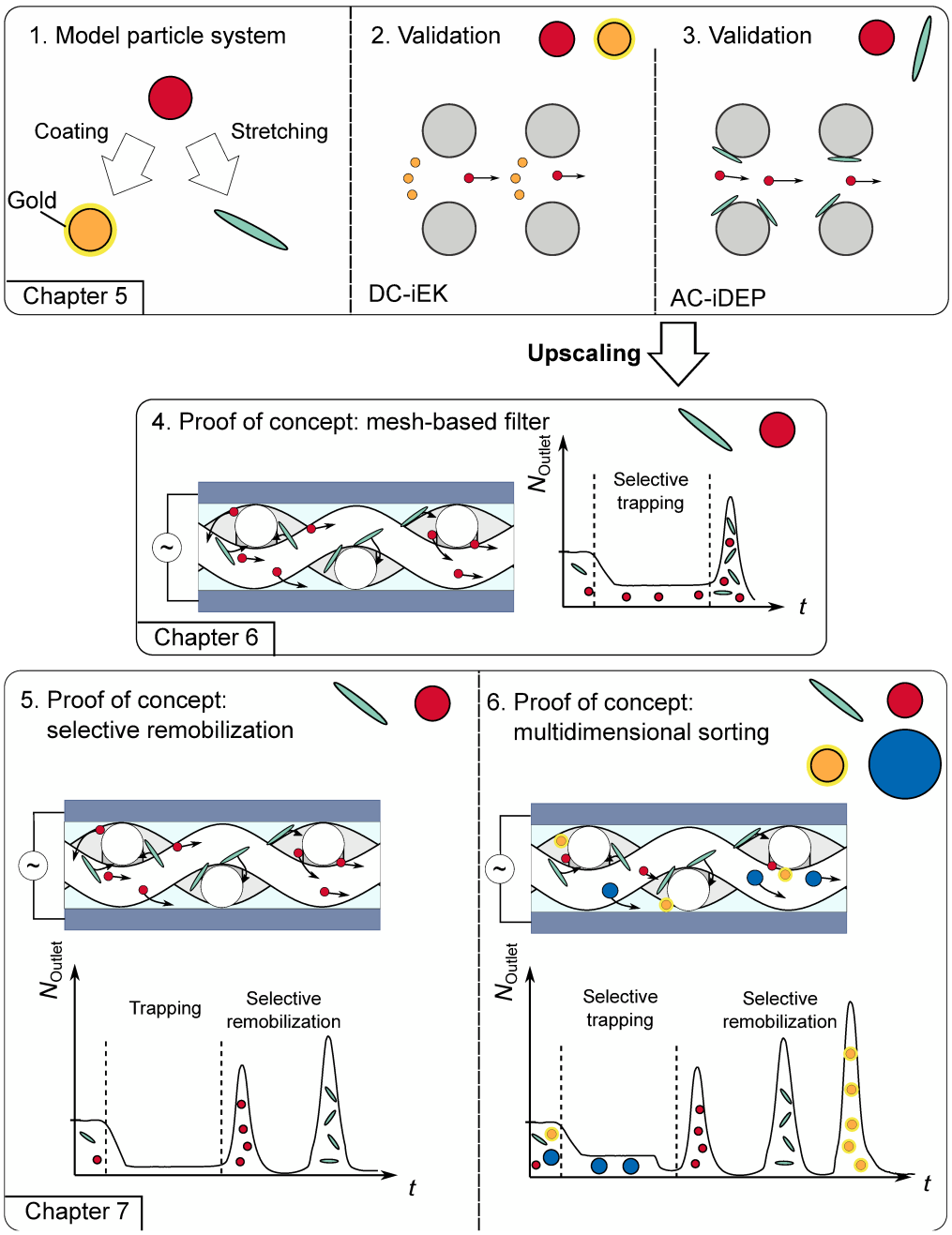

Fig. 4.2.: Graphical overview of the contents and approaches of this work. The particle retention methods used for the validation of the particle system, DC insulator-based electrokinetics (DC-iEK) and AC insulator-based dielectrophoresis (AC-iDEP), were explained in Sec. 2.4.

5 Development and validation of a model particle system

In order to investigate the capability of DEP setups to separate particles based on several properties simultaneously, a suitable particle system needs to be selected. This chapter presents the criteria that were set for the particle system in the context of this work and briefly describes the methods used for the alteration and characterization of particles. Furthermore, results of the particle alteration steps are shown and the dielectrophoretic behavior of the altered particles was evaluated with standard DEP methods. Two different iDEP/iEK methods are used for this. Initially a method well established in the literature was used. Subsequently, a pressure-driven method more suitable for non-biological particles with higher sample throughputs was available. More details are given in the individual subchapters (Secs. 5.4 and 5.5).

5.1 Criteria for and selection of a particle system

As explained before, each particle species of the model particle system should differ from the base particle in only one property at a time. For example, when varying the shape, the volume and material shall remain the same.

Effects apart from electrokinetic ones, such as sedimentation, should be reduced as far as possible to reduce complexity. Therefore, the density should generally be similar to that of the suspension medium, since otherwise the particles quickly sediment to the channel bottom or are driven up to the channel ceiling due to buoyancy. Similarly, particle agglomeration or non-specific interactions with the channel walls should be as minimal as possible, because these effects can alter the DEP response or hinder the release of the particles.

For process development, it is also helpful when the particles and processes in the channel are visually accessible. Fluorescence labeling of the particles does not only facilitate real-time observation in the channel via fluorescence imaging, but also simple and fast subsequent evaluation. This can be done by evaluating videos of fluorescence imaging or by using fluorescence spectroscopy. The choice of fluorescent labels of different colors additionally facilitates the easy discrimination of particles with different properties. For particles with distinct, non-distributed properties, no further analysis, e.g., chemical or optical, is required to evaluate the separation results.

One type of model particles widely used in DEP technology are polystyrene (PS) particles. They are available in similar sizes to cells and are characterized by standardized properties (size, dielectric properties) that make a comparison between different DEP methods straightforward [Che19]. PS particles are not only utilized as model particles, but they are also used, for example, in the drug delivery or cosmetic

industry [Kik20]. The general DEP behavior of PS particles is well described in the literature, and they show a single (Maxwell-Wagner) relaxation at frequencies below the MHz range when suspended in water [Mor03, p. 215]. Other advantages are that they have a high surface charge, which prevents agglomeration of particles and adhesion to the channel walls. Their density is very similar to water, which reduces buoyancy. In addition, PS particles are available in multiple fluorescence colors. PS micro- and nanoparticles can be produced in a very monodisperse manner so that the variation in chemical composition, size, and shape is as small as possible.

The listed properties make PS particles particularly suitable as base particles for various modifications to create a suitable particle system in the context of this work. There are several process routes to modify the PS particles. Their surface can be easily functionalized or further modified, e.g., coated [Mor03, p. 215]. The two modification methods that were used in this thesis will be introduced in the following. In this way, a particle system was generated in which the particles differ in only one property at a time compared to the base particle type.

5.2 Modification methods

The influence of particle size, shape, and material will be investigated in this work. Different sizes and also different functionalizations of the particle surface are commercially available. In addition, a gold-coating of PS particles (Sec. 5.2.1) was selected to investigate a material influence. The coating ensures a smaller density difference compared to solid metal spheres, while the dielectric behavior of coated particles agrees well with the theoretical behavior of solid conducting spheres [Gar12]. The coating procedure and obtained results have been published in Ref. [Wei19]. As a second alteration, the shape of PS particles can be changed via stretching processes (Sec. 5.2.2). A deformation into an ellipsoidal shape was chosen because this shape is very similar to the particle shapes found in engineering applications, such as fibers, tubes, or rods. The ellipsoidal particle generation section is based on Ref. [Wei22]. Here, the processes are only briefly summarized. Details can be found in the appendix A.1.

5.2.1 Gold-coated particles

Gold-coated polystyrene particles were prepared using a process based on the method described in Refs. [Lim08; Ren11; Gar12]. Fluorescent PS particles were used as initial particles (carboxylated PS in FluoGreen and FluoRed, microParticles GmbH, Berlin, Germany), thus no further fluorescent labeling is required. Details of the procedure can be found in the appendix (Sec. A.1.1). To give a brief summary, fluorescent PS particles will be seeded with gold nanoparticles and then coated by a reduction reaction of gold (I) sodium thiosulfate with ascorbic acid. The gold-coating process leads to a nearly homogeneous gold layer with a thickness in the nanometer range.

5.2.2 Ellipsoidal particles

Ellipsoidal polystyrene particles were prepared using a process based on a method by Ho et al. [Ho93]. This method produces prolate and rotationally symmetric ellipsoids where the two minor axes are equal. Moreover, the deformation is isochor [Coe14], which preserves their comparability with unstretched particles of the same volume. Monodisperse fluorescent polystyrene particles were used as initial particles (PS plain in FluoGreen, microParticles GmbH). The stretching process and materials used are described in detail in the appendix (Sec. A.1.2). Briefly, the particles are embedded into a polyvinyl alcohol (PVA) film that is stretched in an oil bath after hardening. The embedded particles are simultaneously deformed into an ellipsoidal shape and can be recovered by dissolving the film. To ensure comparability between ellipsoidal (stretched) and spherical (not stretched) particles, the same procedure (embedding in a PVA film, heating in an oil bath, dissolution of the film, and washing steps) except for the stretching step itself was also applied to the spherical reference particles. In the following, these particles are referred to as treated spheres. The treatment is necessary because PVA cannot be completely removed from the particle surface, thus changing the surface properties. This topic will be further discussed in Sec. 5.5.2.

5.3 Particle characterization methods

Particles were characterized in terms of their size, shape, and electrical charge (zeta potential or K_{S} value). This section provides an overview of the characterization methods used throughout this work. Parts of this chapter are published in Ref. [Wei19] or [Wei22].

5.3.1 Size and shape determination with SEM

The particle size and its standard deviation were determined from scanning electron microscopy (SEM) images with the help of ImageJ's (Fiji [Sch12], version 1.53c) measuring tool. In the same way, the dimensions of the ellipsoidal particles, major and minor axis diameters and their distribution, were evaluated. The ellipsoids were assumed to lie with their major axis on the SEM carrier and to have a prolate shape (both minor axes are the same). Approaches for an automatic segmentation and evaluation are described in appendix Sec. A.3.2, but so far have not been able to achieve sufficient accuracy. The layer thickness of the gold-coated particles was measured directly with the scanning electron microscope using a higher magnification.

5.3.2 Dielectrophoretic properties

The particles' zeta potential was characterized via single particle tracking (SPT) in microchannels (details in appendix A.3.3) for all particles used in the DC-iEK experiments (gold-coated and uncoated particles). The zeta potential of the particles is calculated from the electrokinetic mobility with which the particles move in the channel. The ellipsoidal and PVA-treated particles were only used in pressure-driven

setups. Therefore, the particle's zeta potential does not play a decisive role and instead the K_{S} value is necessary to estimate their effective polarizability.

For PVA-treated and original spherical as well as ellipsoidal particles, K_{S} values were obtained via fixed-frequency DPC experiments [Gie21]. Details of the K_{S} value determination can be found in the appendix (Sec. A.3.4). To give a brief summary, the crossover frequency of the particles is determined by comparing the residence time distribution in a microchannel with interdigitated electrodes at different frequencies of the applied electric field with that with no field. At the crossover frequency, the residence time distribution with and without an applied electric field match. Below and above the crossover frequency, the particles are pushed to slower streamlines at the channel bottom or ceiling due to DEP. With the determined crossover frequency, the K_{S} value can be calculated. For the calculation, the ellipsoids are assumed to be aligned to the electric field with their major axis (this assumption is explained in section 5.5.3), and the mean values for the axes radii after stretching are used.

5.4 Separability of gold-coated and uncoated particles

The dielectrophoretic behavior of the gold-coated particles and their separability from uncoated particles was shown in electroosmotic-driven DC-iEK microchannels. This method was chosen because it provides an established and highly selective standard procedure from the bioanalytical field. Thus, it can be verified whether the dielectrophoretic properties have been altered by the gold-coating to such an extent that separation from untreated particles is possible at all. This subsequently provides a benchmark for the scalable procedure developed in this work. Likewise, it can be easily tested whether the particles' dielectrophoretic behavior is in accordance with theory.

At the beginning of this section the DEP methods to validate the suitability of the material part of the particle system are described, then the results of the particle charaterization are given, and finally the results of the validation are shown and discussed. The chapter is based on Ref. [Wei19]. In addition, recent findings on the influence of non-linear EK phenomena are discussed.

5.4.1 Methods of electroosmotic-driven iEK

In this section, first the microchannel design and experimental setup of the electroosmotic-driven process is introduced. Then the experimental procedure is summarized. Details on the materials and setup, like which types of laboratory equipment were used, can be found in the appendix (Chap. A.4).

Setup

Insulator-based microchannels made out of polydimethylsiloxane (PDMS) were used

for the DC-iEK method. They were fabricated with a standard soft lithography technique (details can be found in the appendix A.2). The channels contained an array of insulating, cylindrical posts with a diameter of 200 µm and spacing of 20 µm at the channel center for particle separation (Fig. 5.1 a and b). Cylindrical posts were chosen because they provide a compromise between intensity and reach of DEP force [Pes16]. Two pipette tips serve as liquid reservoirs at the channel inlet and outlet. The electric field in the microchannels was applied with two platinum wire electrodes immersed in the reservoirs (Fig. 5.1c). Imaging of the microchannel was done with an inverted microscope.

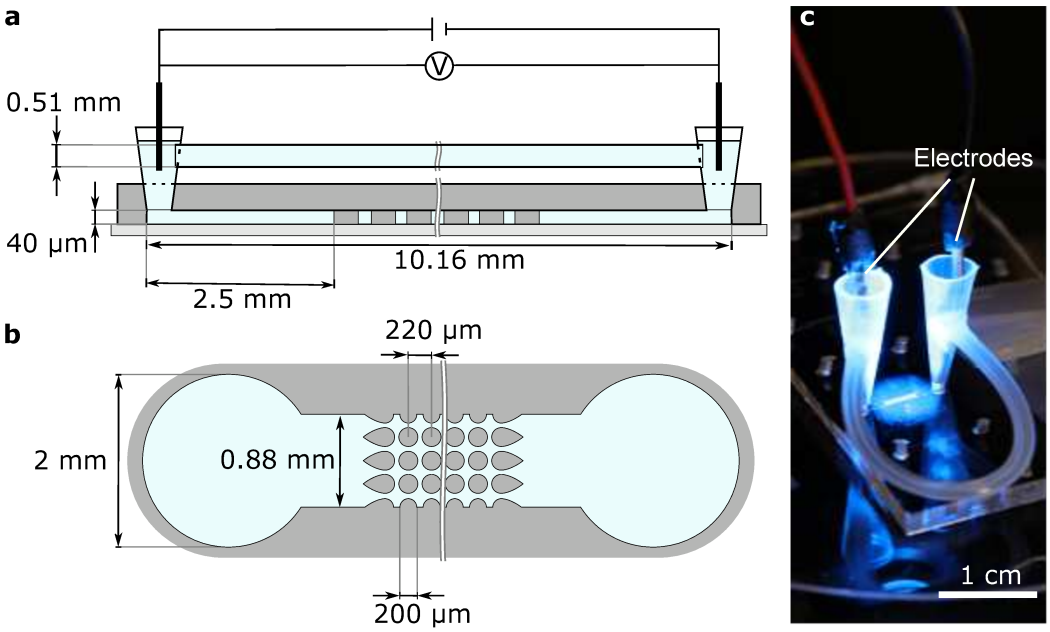

Fig. 5.1.: a) Schematic representation of a microchannel with post array (side view, not to scale). Two pipette tips were inserted into holes that were previously punched into the PDMS to serve as fluid reservoirs. The reservoirs were connected to each other by a tube in order to balance the static pressure that builds up in the reservoirs during experiments. An electric field is applied across the channel length by introducing two platinum wires into the reservoirs. b) Schematic sketch of the channel (top view, not to scale). The post array used consists of cylindrical insulating posts in a square array of 4×14 posts with 'dove-tail' geometry at the in- and outlet. c) Photo of the microchannel with reservoir connection tube and electrodes. (Based on [Wei19])

Alterations to standard channel design

A problem that arose in iEK separation experiments was a backpressure that builds up over time when the fluid is pumped to one side of the channel by EO and changes the reservoir filling level of the in- and outlet (see appendix B.2). The backpressure build-up gradually reduces the required trapping voltage since the flow through the channel decreases. This behaviour makes reliable reproducible iEK trapping difficult. To compensate pressure differences between both reservoirs, a silicone tube was used to connect the two reservoirs and balance their fluid level (see Fig. 5.1). The tube's cross section was chosen to be much bigger than the channel cross section

to act as a quick compensation of the reservoir's fluid levels. When a voltage is applied at the electrodes, an electric current also flows via this connection (the longer this connection is, the smaller this current becomes). The potential at the iEK channel, however, which is crucial for iEK separation, remains unchanged because both channels are in parallel. An influence of the bypass on the potential difference was excluded by measuring the output voltage during each experiment with and without reservoir connection. The measured output voltage remained the same and was unaffected by the changed load. It is assumed that EO pumping in the tube is negligible because the tube diameter is big enough so that the backflow dominates the fluid flow. With an increasing cross section, the influence of the flow due to the static backpressure increases [Yan07]. The reservoir connection successfully keeps the particles' EK movement nearly constant, as shown in Sec. B.2.

Experimental procedure

The experiments were performed for two different particle sizes, 2.4 μm and 4.5 μm, each with uncoated and coated particles. The particles were suspended in a 0.05 % v/v aqueous Tween 20 solution with an adjusted conductivity of 29.5 μS cm^{-1} and pH above 7 to prevent particle agglomeration. 1 μL of particle suspension (particle concentration 4×10^6 ml^{-1}) was injected into the inlet reservoir. The minimum voltage that was required to retain first particles in the post array was determined. This voltage provides information on when the DEP force and EP forces of both kinds start to match the EO force so that particles are trapped in the iEK device. For the separation experiments, a mixture of coated and uncoated particles of the same size was injected into the channel. A high voltage was applied (above the minimum voltages required for trapping for both particle types) until all particles injected into the system were retained within the first columns of the post array. Then, the voltage was reduced for 30 s to a value between and subsequently below the minimum trapping voltages of the two particle types. This first reduction releases all particles of one type (with a higher minimum trapping voltage) and then, at a lower voltage, all particles of the second type. Videos were recorded at the channel outlet to detect the particle release.

Evaluation

The videos were segmented according to the different fluorescence colors using a Matlab (MathWorks Inc.) routine and the fluorescence intensity was determined by integrating the gray values of each frame. The fluorescence intensity measured at the outlet of the channel plotted over the experimental time is called 'dielectropherogram' and was determined for both particle sizes. As a quantification of the selectivity the normalized purity (Eq. 3.3) and yield (Eq. 3.4) were considered, assuming that the fluorescence intensity I is proportional to the particle concentration c. When calculating the yield, it must be taken into account that the particles are transported

through the post array via EK at different velocities. Details on the calculation can be found in the appendix (Sec. A.4.3).

In all figures in this chapter, the green fluorescence of the uncoated particles is represented by a blue color, whereas the orange color of the Au-coated particles appears to be red to be colorblind friendly. Only in Fig. 5.4 the original colors are used, because these are the fluorescence microscopy images from the experiments.

If DEP is negligible, calculation of the EP mobility of the second kind is possible via Eq. 2.56 and the electric field strength which is necessary to retain all particles of one kind (as $\vec{v}_\mathrm{p}(E_\mathrm{trapping}) = 0$). Rearranging the equation for the mobility, we obtain [Vag22]:

$$\mu_\mathrm{EP}^{(3)} = -\frac{(\mu_\mathrm{EP}^{(1)} + \mu_\mathrm{EO})}{E_\mathrm{trapping}^2}. \tag{5.1}$$

However, only the minimum trapping voltage was determined here, which is why the EP mobility can just be estimated.

5.4.2 Characterization of the gold-coated particles

The Au-coating process leads to a nearly homogeneous gold layer with a thickness of approx. 100 to 300 nm (Fig. 5.2 b). The gold layer is sufficiently thin so that the fluorescence of the base particle is not completely shielded and is well visible with a conventional fluorescence microscopy. In contrast to the gold-seeded particle (Fig. 5.2 a), the coated particle has a coarse surface. An overview on the particle

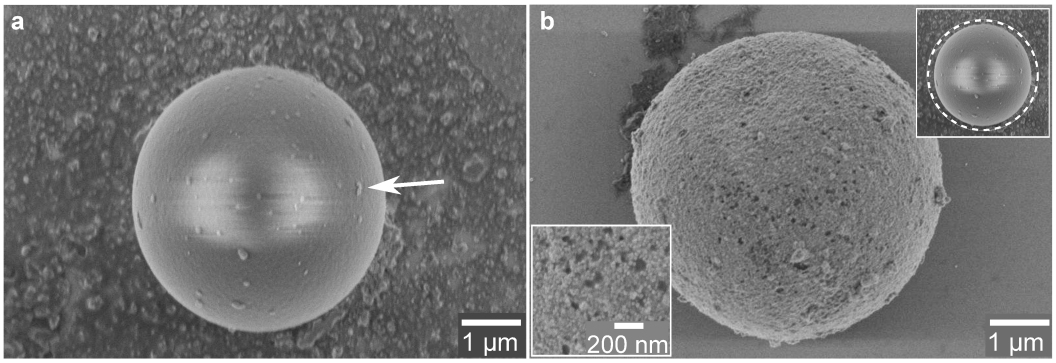

Fig. 5.2.: a) SEM image of a 4.5 µm particle after one day in gold colloid solution. Larger nanoparticle clusters attached to the surface are clearly visible and one is indicated by an arrow. b) SEM image of a 4.5 µm gold-coated particle after complete coating procedure. An almost closed layer of about hundreds of nanometers is formed on the particle surface, through which the fluorescence still can be detected. Upper Inset: illustration of particle size before coating in relation to the size after coating (dashed line); Lower Inset: close-up view of the gold surface structure. (Based on [Wei19])

diameters before and after the coating process can be found in Tab. 5.1.

All particles have a less negative zeta potential than the channel wall (with -70 mV, Fig. 5.3 a). The gold-coating increases the absolute value of the zeta potential and thus decreases the difference to the zeta potential of the channel wall. In addition

Tab. 5.1.: Properties of particle system. The diameter of the uncoated spheres are data from the manufacturer. The diameter of the Au-coated particles was measured with ImageJ's measuring tool ($n = 20$).

	Diameter in µm	Zeta potential in mV
PS sphere 2.4 µm	2.36 ± 0.04	-33 ± 3
PS sphere 4.5 µm	4.47 ± 0.01	-22 ± 5
Au sphere 2.4 µm	2.5 ± 0.1	-44 ± 4
Au sphere 4.5 µm	5.0 ± 0.3	-45 ± 5

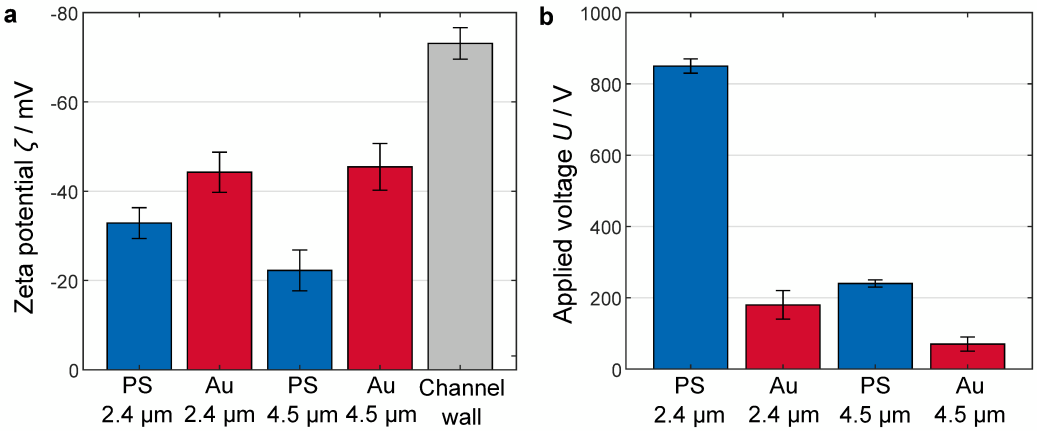

Fig. 5.3.: a) Zeta potentials of the particles and the PDMS microchannel. For the PS 2.4 µm particles, the ELS measured value and the associated standard deviation are given (pH 6.7, σ_m =29.5 µS cm^{-1}, $n = 3$). b) Minimum trapping voltage to retain particles in the post array $n = 3$. (Based on [Wei19])

to the material, the roughness of the surface also influences the zeta potential of a particle [Cho88]. Thus, it cannot be determined if the more negative zeta potential of the gold-coated particles is caused by the material gold itself or by an increase of the surface roughness due to the coating process.

5.4.3 Separation experiments with gold-coated particles

To find out if non-linear electrokinetic effects must be considered in the electroosmotic driven iEK experiments, the Peclet and Dukhin number were calculated for the particles and process parameters used (Tab. 5.2). The Dukhin number is strongly influenced by the K_S^S of the particles. Since this value had not been determined at the time when the separation experiments were performed, a value of 1 nS was assumed. This value is given in the literature as an order of magnitude, but is more in line with the maximum value measured for other PS particles used by our group. Especially for the uncoated particles, the Dukhin number should therefore also correspond to the maximum value. The Dukhin and Peclet numbers ($Du > 0.1$ and $Pe < 1$) indicate that already non-linear EK effects start to become relevant for all particles and that their EP velocities of the second kind are dependent on the cubed strength of the electric field and not on $E^{3/2}$ [Lap22]. However, these dependencies are particularly crucial when, for example, required trapping voltages are

Tab. 5.2.: The Dukhin and Peclet numbers were calculated as described in the appendix Sec. A.4.4, and for K_S^S a value of 1 nS was assumed. For the Peclet number the values at the highest electric fields (900 V cm^{-1} for 2.4 µm particles, 500 V cm^{-1} for 4.5 µm particles) are shown. The electrophoretic mobility of the second kind was calculated with Eq. 5.1 and the minimum trapping field strength given in this table. For the DEP mobility (Eq. 2.41) a CM factor of -0.5 was assumed.

	Du	Pe	Min. trapping field strength in V cm^{-1}	$\mu_{EP}^{(3)}$ in 10^{-19} m^4 V^{-3} s^{-1}	μ_{DEP} in 10^{-19} m^4 V^{-2} s^{-1}
PS sphere 2.4 µm	0.29	0.22	850 ± 20	-35	-0.4
PS sphere 4.5 µm	0.15	0.30	240 ± 10	-576	-2.9
Au sphere 2.4 µm	0.3	0.23	180 ± 40	-554	-0.8
Au sphere 4.5 µm	0.16	0.21	70 ± 20	-3524	-2.9

to be predicted. The estimated EP$^{(3)}$ mobility is several orders of magnitude larger than the DEP mobility, especially for the large and gold-coated particles (Tab. 5.2). Accordingly, depending on the magnitude of the electric field gradients, it can be assumed that the DEP force is not (solely) causing the retention of the particles in the DC-iEK experiments. This should be kept in mind when looking at the following results.

As explained in Sec. 2.4.1, EP of both kinds point in the opposite direction as EO for particles with the same sign of surface charge as the channel walls. The total particle velocity in the microchannel before the post array increases with increasing zeta potential difference between particle and channel walls (see Eq. 2.57). The same trend was observed with the particles used here. The minimum voltage for the trapping of the particles shows large differences for gold-coated and uncoated particles of the same size (Fig. 5.3 b), which is attributed to their zeta potential difference. The minimum voltage for iEK trapping increases with decreasing particle diameter when the material is the same. The DEP force is proportional to the volume of the particle, and EP of the second kind to the radius squared, while the linear EP force and counteracting EO are proportional to the hydrodynamic radius for laminar flows [Lap04; Sta06].

The retention of the 2.4 µm particles at two different applied voltages is shown in Fig. 5.4 a,b. At 1000 V_{DC} both particle types are retained and accumulate in front of the first post rows. In agreement with the literature [LaL14; Sau15b], the retained particles form curved trapping bands; at moderate to high voltages, the coated (orange) and uncoated (green) particles are trapped in two separate bands due to their difference in electrokinetic mobility (Fig. 5.4 a). The conductively coated particles are clearly not retained at typical pDEP trapping spots. It cannot be determined whether they actually show nDEP in DC electric fields due to the shielding of the double layer, or are retrained solely by strong EP forces of the second kind. When the voltage is decreased to 200 V_{DC}, only the gold-coated particles are retained and the pure PS particles can move through the post array (Fig. 5.4 b). The

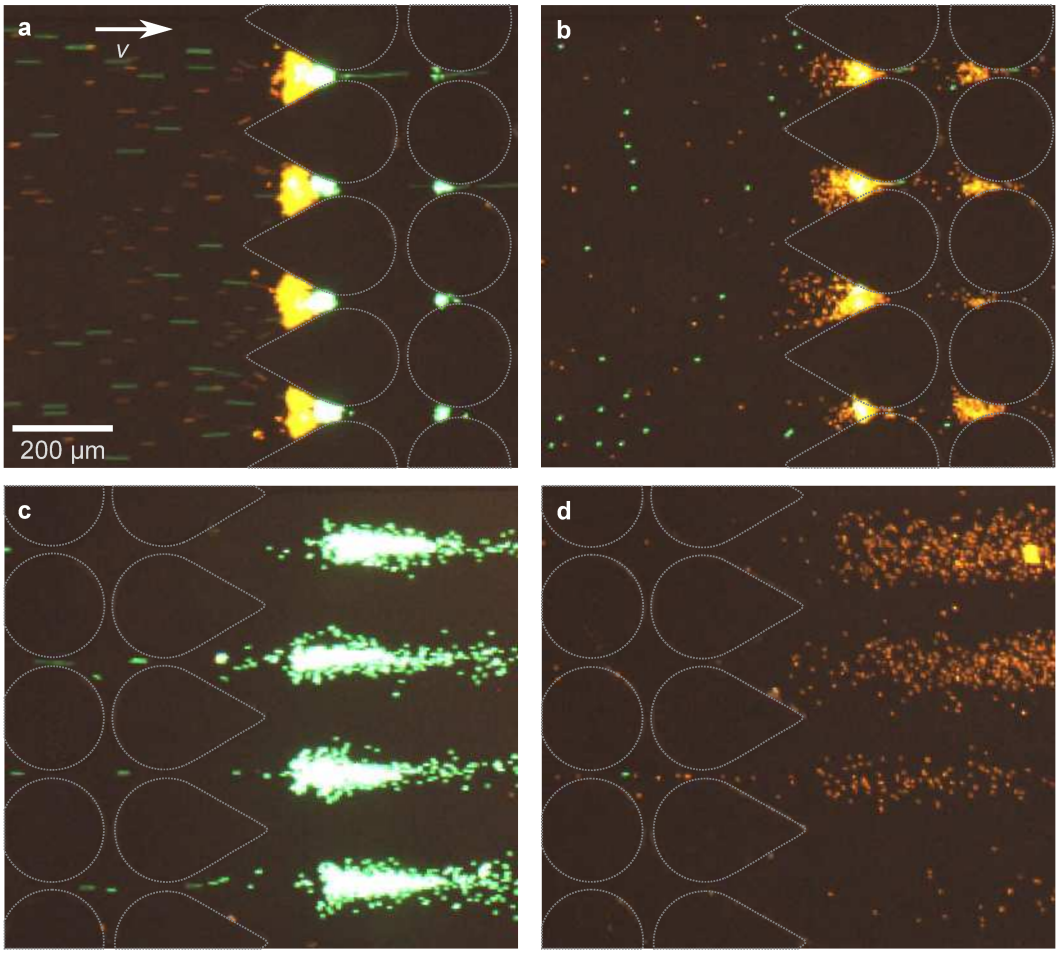

Fig. 5.4.: Fluorescence microscopy images of the particles in the microchannel. The real fluorescence color of the particles is shown. The post outlines have been redrawn for better visibility. a) Retention of both particle types with a diameter of 2.4 µm in front of the first rows of the post array at 1000 V_{DC}. b) Selective trapping of gold-coated particles (orange) at 200 V_{DC} (at the inlet of the post array). c) Selective release of PS particles (green) at the post array outlet at 200 V_{DC}. d) Release of gold-coated particles at 50 V_{DC} (at the outlet of the post array). (Based on [Wei19])

release at the outlet is shown in Fig. 5.4 c. A further reduction of the voltage to 50 V_{DC} finally lets the gold-coated particles pass the post array (Fig. 5.4 d). Only small agglomerates of few particles are visible, but these are small enough to pass through the post array (e.g., upper right corner in Fig. 5.4 d). Retention of both particle types and subsequent selective remobilization by reducing the trapping voltage is possible.

For the replicate particle separation experiments, in order to determine purity and yield, the trapping voltage was reduced slightly to 900 V_{DC} for the 2.4 µm and 500 V_{DC} for the 4.5 µm particles. At the trapping voltage, no fluorescence is detected at the outlet in either case, which means that complete retention has occurred (see 'dielectropherogram' Fig. 5.5 a and c). The following two-step voltage reduction mainly results in two narrow and clearly separated peaks for the uncoated

and coated particles. Smaller peaks in the PS particle curve (blue) after the second voltage reduction are due to small agglomerates of some PS particles, which are more easily retained due to their size and thus released at lower voltage. The reason for the broader peak of the gold-coated particles is the lower EK motion caused by the reduced applied voltage during this step. Consequently, the particles reach the field of observation delayed and remain in it longer. If the particles are collected at the

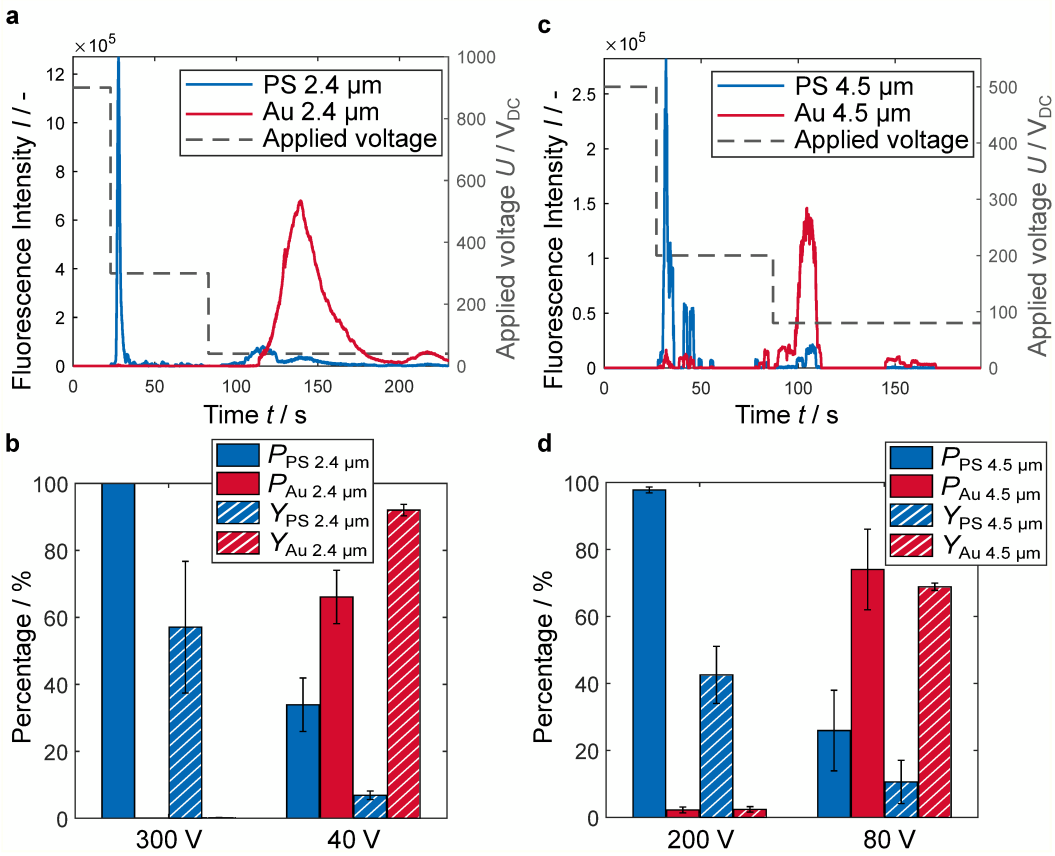

Fig. 5.5.: a)/c) Exemplary dielectropherograms of 2.4 µm/4.5 µm particles in adapted suspension (pH 7.05/pH 7.2, σ_m =29.5 µS cm^{-1}). The fluorescence intensity at the channel outlet is shown over the experimental period. Before recording, the particles were trapped for 60 s to 70 s at the inlet at highest voltage. With voltage reduction, the PS particles are released, followed by smaller PS agglomerates and then gold-coated particles (based on [Wei19]). b)/d) Corresponding calculated normalized purity and yield of separation process ($n = 3$).

outlet directly after the first voltage reduction, a normalized purity of $(99.94 \pm 0.01)\%$ is obtained for the 2.4 µm PS particles and a normalized purity of $(97.8 \pm 0.9)\%$ for the larger particles (Fig. 5.5 b/d). The yield is between $(57 \pm 20)\%$ and $(43 \pm 9)\%$ with a high standard deviation. Looking at the videos of the separation, especially in the case of the high standard deviation of the 2.4 µm particles, it is noticeable that in one experiment more particles are agglomerated and therefore remobilized at the second voltage reduction. This has a high impact because of the relatively low sample throughput of the experiments. The agglomeration of particles, which remained in some repetitions despite pH adjustment, also leads to lower purities

and stronger deviations during the second voltage reduction and collection of the Au-coated fraction. Nevertheless, for the 2.4 μm Au-coated particles a normalized purity of $(66 \pm 8)\%$ and in the case of 4.5 μm of $(74 \pm 12)\%$ can be achieved. When looking at the dielectropherograms, the different particle velocities must be taken into account. The first remobilization peak is much narrower due to the significantly higher particle velocity. Also, the small proportions of gold-coated particles released in the first fractions are only noticeable in the calculated yield.

It is expected that a further increase in purity and reproducibility can be achieved with this method by reducing the array length because the electric field gradient at each post line increased. This approach has already been investigated in Ref. [Per18] and leads to lower required trapping voltages. It is expected that this would reduce the probability of particle agglomeration. Since the zeta potential magnitude after the pH adjustment should be sufficient to prevent agglomeration, it is assumed that the remaining agglomeration is caused by collisions between particles already retained in the trapping zones and particles transported at a high speed toward these areas. The higher the applied DC voltage that is required for trapping, the higher is the particles' velocity.

5.5 Separability of ellipsoids and spheres

The dielectrophoretic behavior of the ellipsoidal particles and their separability from spherical particles of the same volume was shown in pressure-driven AC-iDEP microchannels. The method for validation was changed, since at this stage the use of pressure-driven DEP methods had become established in our working group. The advantages of these methods compared to DC-iEK are that the sample quantity is not limited to a few μL, no DC voltage has to be used for the transport of the particles (e.g., avoidance of electrolysis, which can influence the results), and the experiments are easier to perform. Furthermore, the pressure-driven approach facilitates an easier upscaling, which is investigated in the following Chap. 6. Again, the results of the microchannel experiments provide benchmark separation results for the scalable device. As explained before, in the pressure-driven method particles will be separated by trapping one kind with a stronger pDEP force on the post array, while the others showing nDEP or weak pDEP go through the filter.

At the beginning of this section, the methods used to validate the suitability of the shape part of the particle system are described and the results of the validation are shown and discussed. This chapter is based on Ref. [Wei22].

5.5.1 Methods of pressure-driven iDEP

In this section, first the microchannel design and experimental setup of the pressure-driven process is introduced and are alterations described. Then the experimental procedure is summarized.

Setup

The microchannels used for the pressure-driven experiments were also fabricated using a standard soft lithography technique (Fig. 5.6 a and b). A post array of insulating posts with a diameter h_S of 260 µm and a distance d of 360 µm is located in the center of the microchannel. An electric field can be applied by using two platinum wire electrodes placed $d_E = 9$ mm apart. The electrodes were inserted into the channel via punched holes in the PDMS substrate. The particle suspension was pumped into the microchannel with a syringe pump. Imaging of the microchannels was done with an upright microscope.

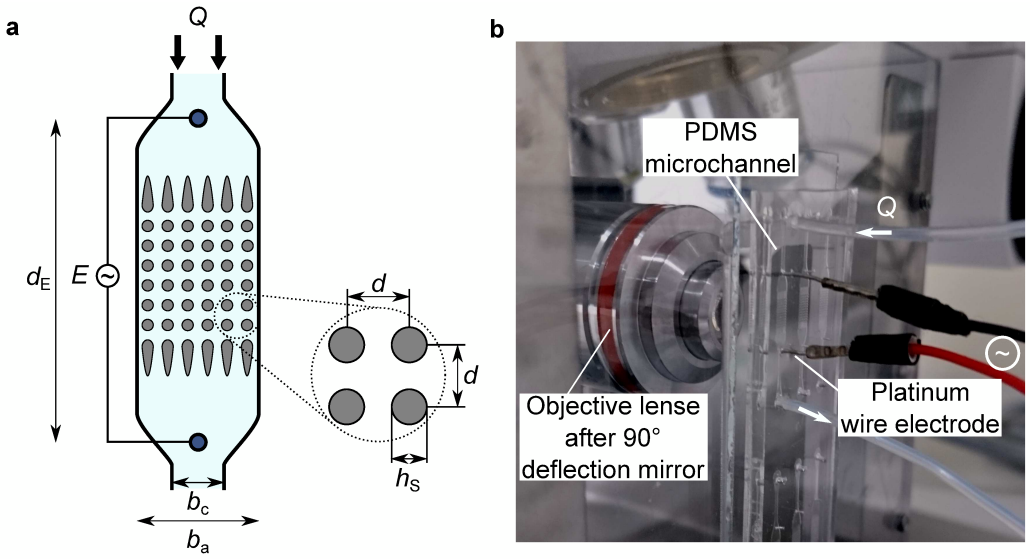

Fig. 5.6.: a) Scheme of microchannel (not to scale). The microchannels have a height (out of plane) of 79 µm and a width b_a of 2.5 mm. A 10 by 7 array of insulating posts with a diameter h_S of 260 µm, a distance d of 360 µm, and with a 'dove-tail' geometry at each side is located in the center of the microchannel. An electric field E can be applied by using two platinum wire electrodes placed $d_E = 11$ mm apart. Before and after the electrodes, the channel narrows to a width b_c of 0.7 mm. b) Photo of vertical mounted microchannel. The channel is flowed through in the direction of gravitation supplied by a syringe pump. The microscope objective is mounted behind a deflection mirror so that the particles in the microchannel can still be observed. Adapted from Ref. [Wei22], published under CC BY 4.0 license.

Alterations to standard channel design and setup

To increase the reproducibility of the microchannel experiments, two major alterations were made to the established channel design (from DC-iDEP/iEK methods and the pressure-driven process of Ref. [Pes18b]). Firstly, the channel width was changed. In contrast to the common design, the channel narrows to a width b_c of 0.7 mm before and after the electrodes. In iDEP microchannels like the ones used in Ref. [Pes18b], a formation of vortex flows on the millimeter scale around the electrodes is observable, which is assumed to be caused by a combination of nonlinear electrokinetic effects. The vortex formation will be discussed in more detail in the appendix Sec. C. The vortices occur over a wide range of process parameters

starting at a field strength of around 1 kV_{pp} cm^{-1}. To reduce vortex formation at the electrodes, microchannels that narrow significantly before and after the post array were designed (Fig. 5.6 a and photo Fig. 5.6 b) in order to accelerate the fluid flow near the electrodes and to slow it down in the trapping zone. This reduces the influence of the vortices on the laminar flow in the post array, thereby increasing the separation efficiency and reducing fluctuations due to slightly differing electrode placements. The reproducibility of the experiments could be significantly increased compared to channels with a constant width (see appendix B.4).

Secondly, the assembled channel was mounted vertically to prevent any sedimentation of particles. In order to maintain a visual access, a 90° deflection mirror was installed between the nose piece of the microscope and the objective lense. The additional deflection and the distance that a light beam must travel has no effect on the working distance of the objective due to the infinity-corrected microscope optics. The syringe holder/delivery unit of the syringe pump was also mounted vertically above the set-up using a laboratory stand, and the particle suspension was mixed inside the syringe with a magnetic stirrer for the entire duration of the experiment. In this way, even large microparticles, or materials with high densities, can be used in microchannel experiments.

Experimental procedure

All experiments were conducted using ultrapure water containing 0.005 vol% Tween20 to reduce particle–wall interactions, 6 μM potassium hydroxide to adjust pH, and 0.25 μM potassium chloride to adjust the electrical conductivity to the desired value (1.1 μS cm^{-1}). Green fluorescent particles were used as initial particles for the ellipsoids, while the spheres exhibit red fluorescence. The total particle concentration in all experiments was 2.5×10^5 mL^{-1}. All separation experiments in the microchannels were carried out with a binary particle mixture. To choose a suitable trapping frequency, the Re(f_{CM}) factors of the particles were calculated using the determined K_S value ranges in Eq. (2.18) and Eq. (2.19) respectively, and are accordingly also given as ranges. A volume flow of 0.1 mL h^{-1} and an electric field of 2.5 kV_{pp} cm^{-1} at 15 kHz was used for the separation experiments. Three experiments were performed in different PDMS microchannels (with the same geometry). For each datapoint, three recordings of inlet and outlet were made and averaged.

Evaluation

The separation efficiency was calculated according to Eq. 3.1. The average value of an evaluation period of 20 s immediately before the voltage was turned off was taken in order to get the particle fluxes for each fluorescence color. For this, an in-house MATLAB programm in combination with the TrackMate Plugin of Fiji was used. Details of the tracking procedure are again described in the appendix (Sec. A.4.3). The purity was calculated with Eq. 3.3. Since the channel in these validation experiments is flushed with the particle suspension for the entire experimental time

and no particle peak is separated, no calculation of a yield is meaningful for these validation experiments.

5.5.2 Characterization of the stretched particles

The manufacturer's data and the SEM image of the PVA-treated spherical particles show that they are highly monodisperse and 2.5 µm in size (Tab. 5.3 and inset Fig. 5.7 a). The stretching process deforms the particles into a noticeably ellipsoidal shape (Fig. 5.7 a). The determined mean diameter of the major axis is (4.0 ± 1.6) µm and of the minor axis (1.8 ± 0.3) µm. In other studies [Ho93; Fló10], the stretching

Tab. 5.3.: Mean dimensions of particles and their K_S values. The mean dimensions of the axes $\bar{a}_1$ and $\bar{a}_2$ of the ellipsoids and treated spheres were determined from SEM images (Treated spheres $n = 100$, ellipsoids $n = 600$). For the untreated spherical particles, dimensions are taken from the manufacturer's datasheet. The K_S value ranges were obtained via fixed-frequency dielectrophoretic particle chromatography (DPC) experiments (details in appendix). From Ref. [Wei22], published under CC BY 4.0 license.

	Major axis $\bar{a}_1$ in µm	Minor axis $\bar{a}_2$ in µm	Crossover frequency range in kHz	Calculated K_S range in nS
Untreated sphere	2.47 ± 0.04	2.47 ± 0.04	250	0.9
Treated sphere	2.5 ± 0.2	2.5 ± 0.2	20–30	0.09–0.12
Ellipsoid	4.0 ± 1.6	1.8 ± 0.3	40–60	0.13–0.21

method obtained very narrow distributions of the aspect ratios of the ellipsoids by dividing the stretched film into sections of different draw ratios before dissolving. Since wide draw ratios of the stretched film were summarized into one fraction in this work, the distribution of the aspect ratios of the particles (Fig. 5.7 b) is broad compared to those in the literature. The width of the fraction was chosen in this way because large quantities of the fluorescent particles were needed for the experiments with increased throughputs.

The polarizability of polystyrene particles depends on their size and shape, but also on their surface conductance (K_S value), since its contribution to the particle conductivity dominates due to the low bulk conductivity [Mor99]. The determined crossover frequencies and calculated K_S values are given in Tab. 5.3. Ranges are shown because a determination at such low crossover frequencies is not precise with the setup used. Therefore, the determined lower and upper limits of the crossover frequencies were used to calculate K_S value ranges and estimate the particles' polarizabilities. The indicated decimal digits result from the calculation and do not correspond to the accuracy of the measurement method. The previously described treatment of the particles reduces the K_S value by almost one order of magnitude. The loss of surface conductance is caused by the embedding of the particles in polyvinyl alcohol (PVA) for the stretching. Presumably, a residual amount of PVA remains on the surface of the particles after the dissolution of the PVA film. Residual amounts of PVA on particle surfaces were also described in literature [Flo12;

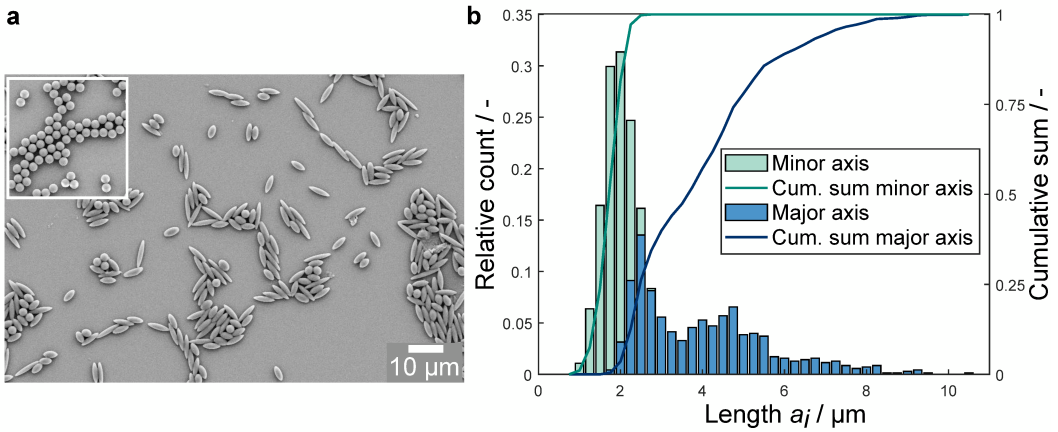

Fig. 5.7.: a) SEM image of PS particles after treatment without stretching step (inset) and after whole stretching process. The majority of the particles have a distinct ellipsoidal shape. b) Distribution and cumulative sum of the diameters a_i after the stretching process. The stretching process caused a significant lengthening of the major axis and shortening of the minor axis. The major axis length is distributed broadly. Adapted from Ref. [Wei22], published under CC BY 4.0 license.

Coe14], and PVA is known for its reduction of zeta potential (making it less negative) [Gar76]. Accordingly, a reduction in the K_S value is to be expected. As comparability was ensured by treating both particles similarly, this was not investigated further. It has to be noted, though, that the determined K_S value ranges of the different shaped particles with the same treatment differ slightly. The stretched particles have a higher K_S value. This can probably be attributed to the fact that the mean value of the aspect ratio of the ellipsoids was used for the calculation of the K_S range. It was not taken into account that the aspect ratio distribution also affects the particular K_S value. Accordingly, the specified K_S range is also to be understood as an average for the ellipsoidal particles.

5.5.3 Separation experiments with ellipsoidal particles

As explained in Sec. 2.4.2, particle sorting in a pressure-driven iDEP process should be possible if the DEP behavior of the particles is sufficiently different, which can be influenced by the process parameters. The graphs of the real part of the CM factor (Fig. 5.8 a) of both particle shapes were used to select suitable frequencies for sorting the particles in a DEP channel. It must be taken into account that ellipsoids that were hardly deformed may be more likely to have a $\mathrm{Re}(f_\mathrm{CM})$ near the range of the spheres. Likewise, particles stretched more than the average axis diameter can have a much higher value than the displayed ranges. Furthermore, for the ellipsoids, the values for the major axis were used to predict their DEP behavior, as the orientation of this axis is assumed to point in the direction of the electric field.

The alignment of non-spherical particles in an electric field by dielectrophoresis can be estimated using the real part of the CM factor of the individual axes. The axis with the higher CM factor aligns with the x-component of the electric field [Tor18].

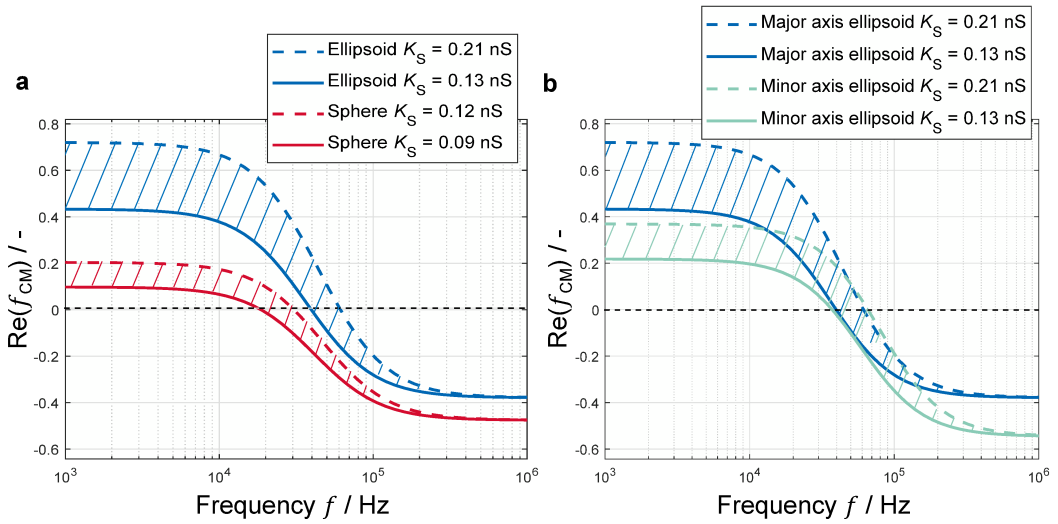

Fig. 5.8.: a) Calculated range of the real part of the Clausius-Mossotti factor Re(f_{CM}) of ellipsoids and spheres as a function of frequency f at $\sigma_m = 1.1$ µS cm^{-1}. The dashed areas indicate the possible range, depending on the variation of the K_{S} value of the particles. For the ellipsoidal particles, the value range for the major axis is shown and no length variation is considered. b) Real part of the Clausius-Mossotti factor Re(f_{CM}) for the major and minor axis of the ellipsoids over frequency f. Adapted from Ref. [Wei22], published under CC BY 4.0 license.

Figure 5.8 b) shows the CM factor ranges for the major and minor axis separately. The factors of the major axis are almost in every case higher than those of the minor axis (at the same K_{S} value), which is why the longer axis will align with the electric field. Only for the maximum K_{S} value the orientation of the ellipsoids would change approximately between 45 and 100 kHz. However, in this range, the magnitude of the CM factor of both axes is comparable and thus also the DEP force acting on the particles.

At a frequency below 20 kHz, both particle shapes reliably show pDEP (Fig. 5.8 a). In this frequency range, the magnitude of the real part of the CM factor is significantly lower for the spherical particles than for the ellipsoidal particles. The crossover to nDEP also occurs at lower frequencies for the spherical particles. In former studies, it was described that the double layer polarization should be more pronounced for non-spherical particles compared to spheres due to their anisotropic shape [Ria11]. Therefore, at high polarizabilities (high K_{S} value) the influence of the shape becomes stronger. This dependence is already visible in the Re(f_{CM}) factors over the determined K_{S} range. The difference between the values of the ellipsoids and the spheres at high K_{S} values (dashed lines in Fig. 5.8 a) is larger than the difference at low K_{S} values (solid lines). Accordingly, the reduction of the K_{S} value due to embedding the particles in PVA during the stretching process decreases the shape-based separability of the particles compared to if they had kept their original K_{S} value. A possibility to maintain a high K_{S} value or to increase it afterward would

improve the separability of this model particle system. However, this is rather an academic problem inherent to this specific particle modification method.

For the selective trapping step, a frequency of 15 kHz was chosen at which the spheres should show only weak pDEP, while the ellipsoids should show strong pDEP. A higher trapping frequency would lead to a decrease of the elliposoids' trapping efficiency as well. The measured trapping efficiency of the ellipsoidal particles at 2.5 $\mathrm{kV_{pp}}$ $\mathrm{cm^{-1}}$ is significantly higher than that of the spherical particles (Fig. 5.9 a). The differences in trapping result from the unequal polarizabilities (magnitude of

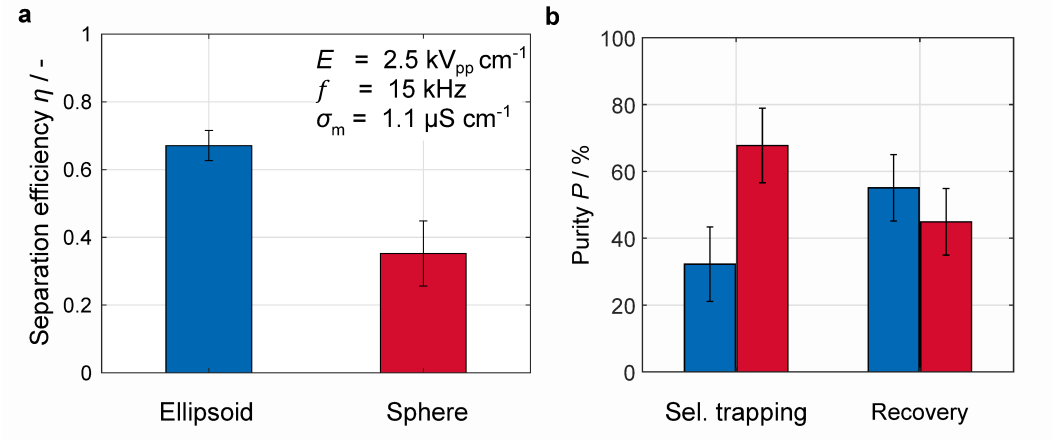

Fig. 5.9.: a) Measured shape influence on separation efficiency η in microchannels at $\sigma_\mathrm{m} = 1.1$ µS $\mathrm{cm^{-1}}$ and at a volume flow of $Q = 0.1$ mL $\mathrm{h^{-1}}$. Data were determined at a frequency of 15 kHz and an electric field of 2.5 $\mathrm{kV_{pp}}$ $\mathrm{cm^{-1}}$ from a binary mixture. Standard deviation is shown as error bars ($n = 3$). Adapted from Ref. [Wei22], published under CC BY 4.0 license. b) Purity for the filtrate during the selective trapping step and the recovery step.

$\mathrm{Re}(f_\mathrm{CM})$) of the particle shapes and therefore differently strong DEP forces. The higher polarizability of elongated particles was already exploited by Riahifar et al. for a shape-dependent deposition of zinc oxide rods and cubic particles [Ria11] as well as by Moncada-Hernandez et al. for sorting *S. cerevisiae* and *E. coli* cells [Mon11]. Note that for the ellipsoids, a slightly higher K_S value was measured than for the spherical particles (see Tab. 5.3). This difference cannot solely be the cause for the higher polarizability of the ellipsoidal particles. To illustrate this, the real part of the CM factor for both particle shapes with exactly the same K_S value range can be found in the appendix (Fig. B.6). There is still a clear difference in polarizability due to the particles' shapes. Accordingly, the experiments indicate an increased trapping of the ellipsoids compared to the spheres. During this selective trapping step, the concentration of spheres (non-captured) in the filtrate is increased. The purity is increased to $(68 \pm 11)\%$ (Fig. 5.9 b). Since the channel in these validation experiments is flushed with the particle suspension for the entire experimental time and no particle peak is separated, the achieved purity of the recovery step is low. Only a slight increase of the ellipsoids' concentration can be detected.

5.6 Conclusion

The experiments in the microchannels show, on a scale established in DEP, that the single parts of the particle system are suitable for studying material- and shape-dependent separation. For both particle modifications, an altered DEP/EK behavior could be detected, which makes a concentration of the particle species in different fractions possible. The experiments in the microchannels also provide general insights into particle-particle interactions. The high purity and well-defined peaks achieved in the DC-iEK sorting of the gold-coated and uncoated particles show that material-dependent separation is possible with a DEP standard method. Shape-dependent sorting in the AC-iDEP microchannels, on the other hand, achieves lower purities. However, a direct comparison to those achieved in the DC-iEK process is not possible because the differences in dielectrophoretic properties between the coated and uncoated particles are much higher than those between the two particle shapes and, moreover, the particle stretching rate has a wide distribution. Nevertheless, a different DEP behavior of the particles could be shown in the validation.

A few alterations on the standard procedures or channel designs were made to facilitate a higher reproducibility of the sorting processes. On the one hand, an adjustment of the pH of the experimental suspension was found to reduce the agglomeration of particles during the separation process and unspecific adhesion on the channel walls. Particle agglomeration was especially observed for the DC-iEK experiments, as the particle concentrations in the trapping zones was high and the particles had low absolute zeta potentials. The agglomeration was identified as a decisive parameter for limiting selectivity and reproducibility. In the pressure-driven experiments the adjustment of the pH value was maintained and almost no particle agglomerations were observed during or after the separation process. On the other hand, some changes of the device designs were made. In order to extend the duration of the DC-iEK experiments, a possibility was developed to prevent a static back pressure that builds up in classical approaches. The classic design was extended by a reservoir connection which balances out the reservoir levels for this purpose. For the pressure-driven method, the channel design was modified to reduce the influence of a vortex formation at the electrode. By selectively increasing the flow velocity at the electrodes, the presumed electrokinetic turbulence was superimposed and an increase in the reproducibility and separation efficiency of the experiments was achieved. In addition, a vertical arrangement counteracted effects due to particle sedimentation.

In summary, a change in DEP properties was observed due to both coating and stretching of the particles. In combination with a size-selective sorting – which has been demonstrated in several publications – DEP processes are suitable to exploit differences in one of these properties to concentrate fractions. A mixture of the two subsystems with the addition of commercially available particles of a different

volume should therefore be suitable for investigating the extent to which it is possible to separate particles specifically on the basis of individual properties.

6 Development of a scalable prototype

In the past, macroscopic filter matrices such as packed beds of glass spheres [Sue03; Wak03; Ili07] or porous alumina sponges [Pes18b; Lor20] were proposed to increase the throughput of DEP filtration processes. However, such devices are unlikely to reach the selectivity of state-of-the-art microfluidic DEP/iEK separators [Pes21]. In this work, it was investigated if a high throughput of DEP filtration could be maintained while improving the selectivity by using regular, ordered filter structures. The development of and experiments with a mesh-based DEP filter prototype are described in this chapter. To evaluate its capabilities, the separation of a binary mixture by selectively trapping was performed first. A comparison is made to a porous ceramic filter structure in terms of the strength of nDEP trapping. An occurrence of nDEP trapping reduces the selectivity of DEP filtration and should be addressed by the novel mesh-based approach. Parts of this chapter are published in Ref. [Wei22].

6.1 Criteria for the channel design

The goal of this thesis is to develop a macroscopic DEP filter concept with an ordered filter matrix in which high throughputs comparable to those reported by Lorenz et al. [Lor20] are maintained. The prototype should at least be able to process a volumetric flow rate of 60 mL h^{-1}. This is intended to ensure that sufficient sample volumes can be generated within a reasonable amount of time to make subsequent analytical procedures (like material analysis) possible. In particular, this point will be valuable for testing particle mixtures apart from fluorescently labeled model particles in the future. Furthermore, a concept for the scaling of the prototype shall be developed.

The disadvantage of porous structures like the ones used in Ref. [Lor20] is the limitation of the predictability of the local field perturbation associated with the irregular structure. The distributed size of the pores lead to high separation efficiencies even at high volume flows, but make sorting with high selectivity and based on multiple properties difficult. An ordered structure of the field disturbers should avoid ‘dead zones’ with very low field gradients, which can be the cause for the unwanted retention of particles with nDEP properties and thus reduced selectivities. In this work, meshes with an ordered grid were tested as field disturbers. The mesh makes this approach a direct upscaling of the highly ordered post arrays used in microfluidics. A slightly increased probability of nDEP trapping is expected, but the selectivity should still be much higher compared to irregular porous filter structures. This could open up the possibility for multidimensional sorting.

Optical accessibility is helpful for a prototype which is intended to verify that the basic relationships observed in the microchannels also apply to mesh structures. For this purpose, indium tin oxide (ITO)-coated glass substrates are suitable for the use as electrodes. The ITO coating is electrically conductive yet transparent and facilitates the observation of the filter via microscopy. This can be helpful in order to understand the motion of the particles within the filter. Visually differentiating between nDEP and pDEP trapping as well as observing if vortices form or particles adhere irreversibly in the filter medium should be possible.

Further requirements for the filter are that it remains highly permeable and electrically switchable. Therefore, the particle retention must be caused mainly by DEP forces and not by mechanical or electrostatic interactions of mesh and particles. To generate sufficient field gradients for particle retention, a critical issue is that sufficient voltages can be applied over a wide range of frequencies. Only in this way it is possible to transfer the separabilty of the particles achieved in the microchannels and the generated knowledge to the large scale filter.

6.2 Mesh-based DEP filter

In this work, a DEP filter was developed in which a mesh serves as an insulating structure sandwiched between two flat transparent electrodes. By using one layer of mesh, the electrode distance is small and comparatively low voltages are necessary to generate a sufficient electric field strength. A regular porous medium, such as this mesh, is expected to show higher selectivity with regard to pDEP trapping compared to sponges or packed beds, which will be examined in this chapter.

6.2.1 Methods

This section contains a brief summary of the materials and methods used, which facilitate a discussion of the results. The appendix contains more information (Sec. A.6).

Channel fabrication

The mesh-based DEP filter prototype (see Fig. 6.1 a and b) consists of a polypropylene (PP) fabric with a mesh width of 500 µm and a fiber diameter of 340 µm as an electrically insulating material. Transparent ITO-coated glass slides with a sheet resistance of 10 – 15 Ω sq^{-1} were used as electrodes. The channel sides and the connection to the 3D printed fluid distributors were sealed with a polymer glue. The distance between the ITO electrodes varies due to the adhesive connection between 0.6 mm and 0.8 mm. A new channel was used for each experiment to account for manufacturing variations in the reproducibility of the results.

Experimental procedure

All experiments were conducted using the same composition of the suspending medium: Ultrapure water containing a volume fraction of 0.005% Tween 20 to reduce particle–particle and particle-wall interactions, potassium hydroxide to adjust

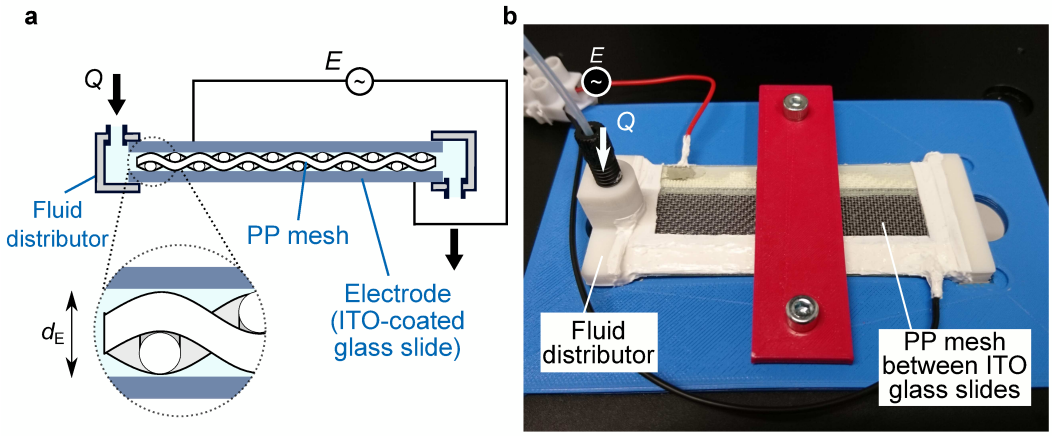

Fig. 6.1.: a) Scheme of mesh-based filter (not to scale). The particle suspension flows into the channel ($Q = 120$ mL h^{-1}) from above through a distributor structure, then flows through the polypropylene mesh from left to right, and leaves the channel on the underside through a second distributor. The ITO-coated microscope slide electrodes with a distance of $d_E = 0.6 - 0.8$ mm are connected to an amplifier. b) Photo of a mesh-based DEP filter. Adapted from Ref. [Wei22], published under CC BY 4.0 license.

pH, and potassium chloride to adjust the electrical conductivity to the desired value. The total particle concentration in all experiments was around 2.5×10^5 mL^{-1}. The separation and release processes in the mesh filter were observed using an inverted microscope with a triple bandpass filter. Since the entire cross section of the filter cannot be recorded due to its size, the evaluation method used in the microchannel experiments cannot be transferred. Instead, the fluorescence intensity in the filter outlet stream was measured in-line by a spectrometer (see Fig. 6.2). A wavelength range between 190 and 1110 nm can be recorded. Fluid input was realized using a piston pump. The fluorescence intensity was recorded using a LABVIEW program and evaluated via an in-house MATLAB script. Experiments were started when a stable intensity value was reached and the steady-state intensity signal (corresponds to flow with concentration c_0) was recorded.

To test the performance of the mesh filter, the selective separation experiments of the binary ellipsoids and spheres mixture from the pressure-driven AC-iDEP experiments were repeated. For this purpose, experiments were performed with the same field strength, frequency, and medium conductivity in the mesh filter. The particles were trapped in the filter for 170 s and 3 repetitions were performed. To compare the results between the device scales, the fluid velocity in the channel and the superficial velocity u_s within the "pores" of the structures

$$u_s = \frac{Q}{A_c \Phi_P} \tag{6.1}$$

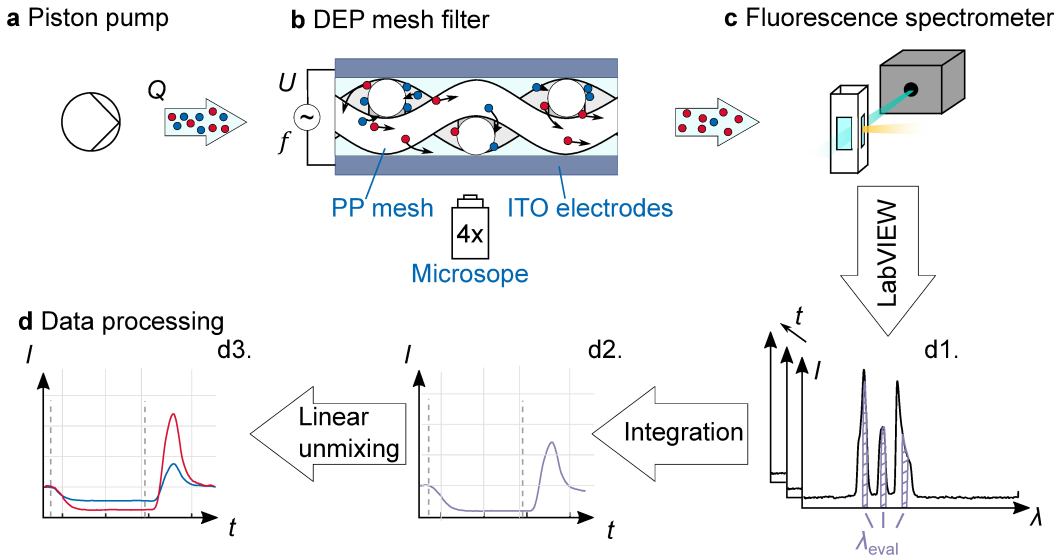

Fig. 6.2.: Scheme of mesh-based DEP filter and route of data processing. a) A binary particle suspension is constantly pumped with flow rate Q into the DEP filter using a piston pump. b) The filter consists of two ITO-coated microscope slides and a PP mesh as an electrically insulating structure. The processes in the filter can be observed with a microscope thanks to the transparency of the ITO electrodes. An AC signal with voltage U and frequency f is applied to the electrodes of the DEP mesh filter. Particles experiencing strong pDEP forces are retained in the filter. c) Behind the filter outlet, the fluorescence signal is recorded using a spectrometer and intensity values are obtained for each time step over the full wavelength range of 190 to 1110 nm (d1.). d) The signal I over time (d2.) is determined by integrating selected wavelength ranges λ_{eval} which lie in the range of the transmission maxima of the emission filter used. The total fluorescence intensity signal is divided into the components of the particles' fluorescence colors by linear unmixing (d3.). Adapted from Ref. [Wei22], published under CC BY 4.0 license.

were considered. For this purpose, the porosity Φ_{P} was calculated via

$$\Phi_{\mathrm{P}} = \frac{V_{\mathrm{open}}}{V_{\mathrm{total}}} \leq 1 \tag{6.2}$$

in which the permeable volume (index open) is related to the total volume of the channel section containing the porous structure (mesh or post array, index total).

To check the strength of nDEP trapping in the DEP filter and compare it with the values of a porous ceramic filter medium, experiments by Lorenz [Lor21] were repeated. Here, 4.5 µm PS particles were retained in the DEP filter at different medium conductivities and the separation efficiency was determined. Due to their size, these particles are expected to be easily retained via DEP forces and show early crossover to nDEP. The field strength was adopted from the experiments with the porous ceramic filter, but the volume flow rate was halved in order to be able to measure sufficient particle retention in the mesh-based filter. If sufficient pDEP trapping is already not possible at low conductivities, it can be expected that even at a minimum CM factor, no nDEP trapping will occur. The superficial velocities were calculated so that the results could still be compared. For each conductivity,

the experiments were repeated three times.

Evaluation

A full wavelength (λ) spectrum at an exemplary point of time is shown in Fig. 6.2 d1. In the case of binary particle suspensions, this is composed of the fluorescence spectra of the different particles. To obtain the constituent parts of each particle type, a linear unmixing of the spectrum was performed (described in detail in Sec. A.6.3). Prior to unmixing, the data were integrated in specific wavelength ranges to speed up the algorithm (Fig. 6.2 d2).

Using the curves determined over the measurement time for each particle type (Fig. 6.2 d3), the separation efficiency can be calculated with an equation similar to Eq. (3.1) with the fluorescence intensities of the suspension after passing through the filtration cell without (corresponds to c_0) and with an applied electric field. The purity was calculated for the filtrate during the trapping step, whereas for the 'retentate' during the particle concentration peak of the recovery step. As has been mentioned, the channel in these validation experiments is flushed with the particle suspension for the entire experimental time and therefore no yield was calculated.

6.2.2 Results and discussion

Trapping of the ellipsoidal and spherical microparticles with high separation efficiencies is achievable in the mesh-based filter (Fig. 6.3 a). At comparable field strength, frequency, and medium conductivity and despite a 16 times higher superficial velocity in the filter medium/post array (15 times in the empty channel), a higher separation efficiency of both particles can be achieved. $(94 \pm 5)\%$ of the ellipsoids and $(51 \pm 8)\%$ of the spheres could be retained in the mesh compared to $(67 \pm 5)\%$ and $(35 \pm 10)\%$ in the microchannel. This is despite the fact that the field disturbers are slightly larger than the post diameters (340 µm compared to 260 µm) and a lower voltage must be applied due to the reduced electrode spacing. One possible reason for the higher separation efficiency in the macroscopic filter could be that the electrodes introduce the electric field over the entire channel length and perpendicular to the flow direction. Thus, the field maxima are not only located at areas where maximum flow velocities are expected (between the posts, compare Fig. 6.4 a and b). The upscaling can therefore be declared successful.

Just as in the AC-iDEP experiments in the microchannels, in the mesh-based DEP filter the ellipsoidal particles are trapped more than the spherical particles of the same volume. A slightly higher purity of filtrate fractions with respect to spherical particles can be achieved for the selective trapping step, (74 ± 8)% in the mesh-based filter compared to $(68 \pm 11)\%$ in the microchannel (Fig. 6.3 b). Again, for completeness, the purity of the recovery step is also shown, but a high purity of the ellipsoidal fraction can only be expected if the particle suspension is replaced by a flushing solution prior to remobilization.

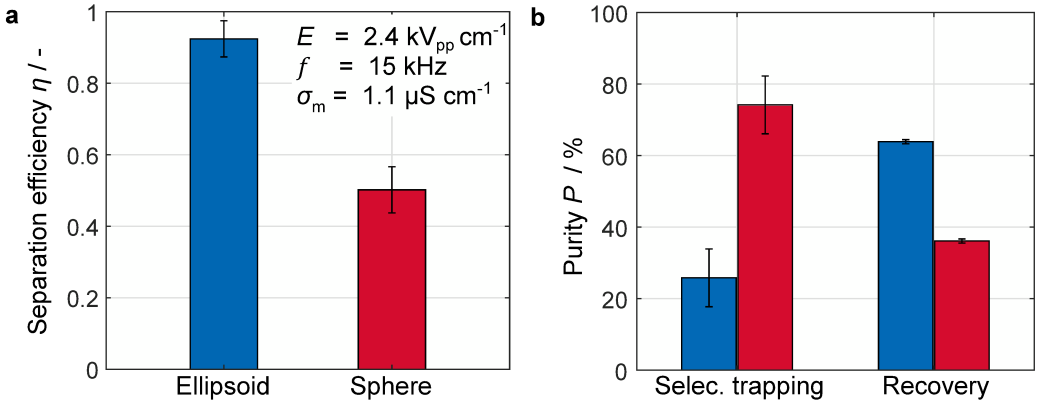

Fig. 6.3.: a) Measured shape influence on separation efficiency η in mesh-based filter at $\sigma_\mathrm{m} = 1.1$ µS cm^{-1} and at a volume flow of $Q = 120$ mL h^{-1}. Data were determined at a frequency of 15 kHz and an electric field of 2.4 kV$_\mathrm{pp}$ cm^{-1} of a binary mixture $n = 3$. b) Associated calculated normalized purities of the fractions.

To quantify the amount of nDEP trapping compared to existing approaches, experiments with 4.5 µm PS particles were conducted. The separation efficiencies for different medium conductivities were determined at a comparable electric field strength and frequency used in experiments with an open porous ceramic medium (Fig. 6.5). As the mesh is characterized by ordered field disturbing structures, it is expected to show little nDEP trapping. Below 5 µS cm^{-1}, the trapping efficiencies of the ceramic and mesh filter medium are comparable in trend and magnitude. Despite the higher flow rate used in the ceramic filter experiments, the superficial velocity of the mesh-based filter is 11 times higher (7 times for the empty channel) because its cross section is smaller. Therefore, higher separation efficiencies are expected at the same superficial velocities in the mesh as the viscous drag on the particles is reduced at lower flow rates. Similar to the porous ceramic material, the particles are likely to pass by the pDEP trapping zones (field maxima, see Fig. 6.4 b and c). However, the higher separation efficiency could be due to the increased length of the filter media and the more evenly distributed trapping spots in the mesh.

While for the ceramic filter the separation efficiency passes through a minimum with increasing medium conductivities (calculated crossover at about 4.3 µS cm^{-1} for 15 kHz and $K_\mathrm{S} = 0.46$ nS) and then rises again slightly, it drops to around zero for the mesh-based filter at higher conductivities. Slightly negative values measured for the mesh-based filter can be explained by minor fluctuations of the intensity signal. This indicates negligble nDEP trapping in the mesh-based setup and an enhancement compared to the porous ceramic filter where over 20% trapping were observed at high conductivities, which limits its selectivity. The increased selectivity can be explained by the defined and regular spacing between the fibers, resulting in more uniform fluid velocities and less disturbance to the laminar flow ($Re \approx 1.42$ for flow around mesh fiber) compared to irregular structures such as the ceramic filters. The possibility of particles being transported to nDEP trapping spots or exposed to

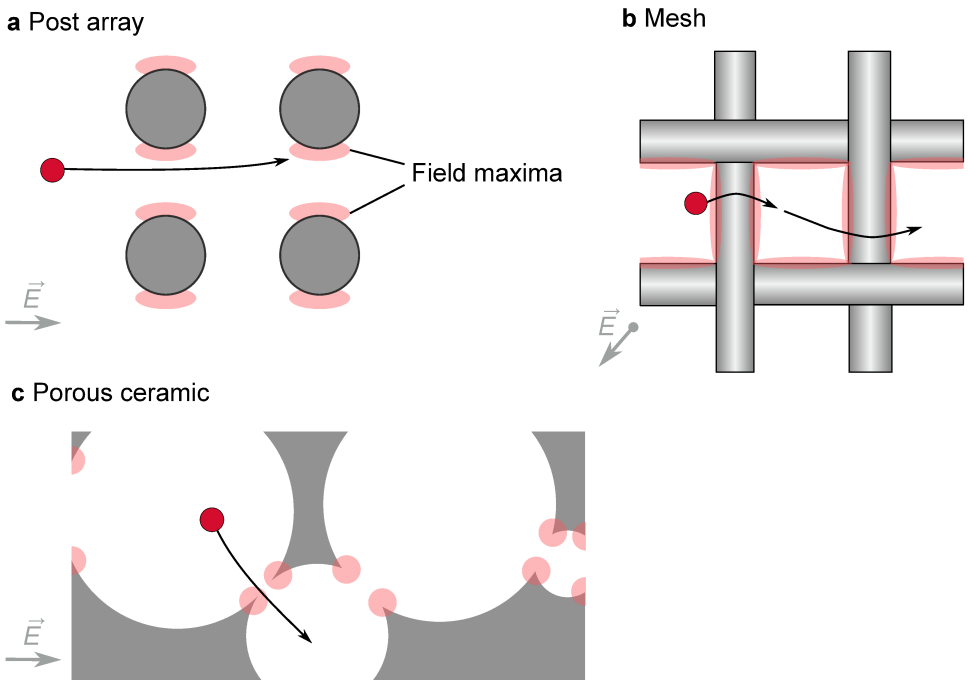

Fig. 6.4.: Schematic comparision of the geometry (top view) and field maxima in a post array a), a mesh material b), and a porous ceramic filter matrix c) (extended and adapted from Ref. [Lor21]).

lower drag forces is more likely in a porous medium with distributed pore sizes (as for the ceramic filter). Likewise, zones with lower field gradients can be expected in the irregular structure.

6.3 Concept for scaling

The mesh-based DEP filter prototype described in this chapter can be scaled by further increasing its cross section. For the DEP force, the electrode spacing is crucial, so the enlargement must be balanced with an increase in voltage to produce sufficient field gradients. Widening the cross section, on the other hand, is possible without this limitation. While an increase in electrode distance requires higher voltages to ensure a sufficient field strength (V m^{-1}), larger electrode surfaces facilitate maintaining the voltage but at cost of an increased current. As the current is around 20 mA at 15 kHz and 80 mA at 150 kHz for the prototype, this is not considered as a substantial limitation. An important aspect is that a uniform fluid supply must be ensured, e.g., by means of a suitable distribution system. One possible limitation to be considered is the dissipation of heat generated by joule heating. Especially for a stack system, a cooling mechanism should be considered.

Analogous to membrane technology or plate heat exchangers, higher throughputs can also be generated by an easily scalable stack system. An alternation of plastic fabrics and (bipolar) electrode plates in a kind of sandwich is considered. The optical accessibility is helpful for the research on the phenomena, but not necessary for

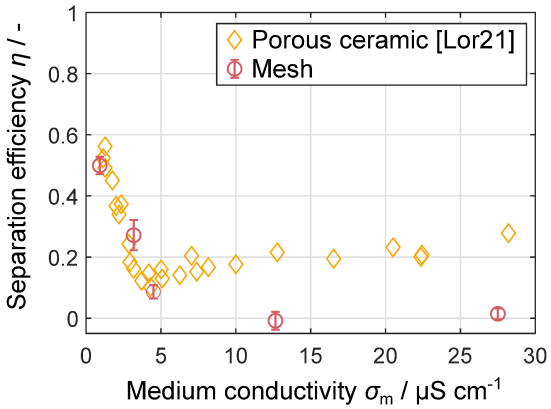

Fig. 6.5.: Separation efficiency over medium conductivity for trapping in a ceramic and mesh-based DEP filter. Experiments were done with 4.5 µm PS particles at the same electric field strength $E = 1060\ \mathrm{V_{pp}\ cm^{-1}}$, frequency $f = 15$ kHz, but different flow rates, 120 mL $\mathrm{h^{-1}}$ in the mesh-based ($n = 3$) and 240 mL $\mathrm{h^{-1}}$ in the ceramic medium filter. Data was extracted from Ref. [Lor21] of a filter with a hydraulic diameter of $d_\mathrm{h} = 222$ µm.

the operation of the filter. It is conceivable to switch to lower-cost, commercially available materials such as graphite or stainless steel plates as electrodes.

6.4 Conclusion

In this chapter, the functionality of a macroscopic filter with ordered field disturbing structures was illustrated by means of a shape-based selective separation. The prototype DEP filter used facilitated the observation of the particles in-situ and achieved separation at volume flows of 120 mL $\mathrm{h^{-1}}$, which is 1000 times higher than the throughput which can be reached in the AC-iDEP microchannels at similar separation efficiencies. For the superficial velocities in the corresponding filter structure 'pores', this leads to a 16 times higher value. Here, even a reduction of the necessary voltage is achievable by reducing the distance between the electrodes from about 1 cm in the microchannels to below 0.1 cm. This is possible due to the electrodes being parallel to the direction of flow along the entire length of the channel. The increase in volume flow is attainable because of the macroscopic width of the channel. A concept for further scaling of the throughput by widening the channel cross section and stacking multiple filter units was also introduced.

In addition, an in-line measurement of fluorescence intensity using a spectrometer could be implemented and thus parameters to describe the separation quality could be derived. This is also possible for particle mixtures with different fluorescence colors by splitting the total fluorescence signal into the respective contributions of the particles by a linear unmixing method.

Using the selective trapping of ellipsoids and spheres of the same volume as an example, it was shown that the mesh-based filter can achieve similar purities of the fractions as an AC-iDEP microchannel. Furthermore, as expected, the filter

with regular structures shows negligible nDEP trapping of particles in contrast to a filter with an irregular porous medium. Thus, it meets the requirements of both throughput and selectivity for the prototype and in a next step, the separation based on multiple particle properties can be investigated.

7 Multidimensional separation with DEP filters

In this chapter, it will be investigated if a separation of particles regarding multiple properties is possible in one pass of a DEP filter. The mesh-based DEP filter and the particle system consisting of differently sized spherical PS particels, PS ellipsoids, and Au-coated PS spheres will be used for the evaluation. To sort particles according to multiple properties in one filter pass, the aim is not only to selectively trap but also selectively remobilize particles. A size-selective trapping via nDEP/pDEP differences of particles was already shown in some studies [San16; Mod19; Lor20], reaching high purities. The feasibility of selective remobilization has not yet been investigated for DEP filtration devices. Therefore, a binary mixture of differently shaped particles was first used to validate the transferability of the method. After showing the possibility of selectively remobilizing particles from the mesh-based DEP filter, selective trapping and multiple selective remobilization steps will be combined to sort a mixture of the whole particle system.

7.1 Concept adaption: selective remobilization for multidimensional separation

As has been previously shown in several studies and in the DC-iEK experiments, particles can be selectively remobilized by reducing the voltage until the force acting on one particle species is too small to retain it. For this, however, the particle types must exhibit sufficient differences in their effective polarizability, which is not always the case, especially when the particle volume is similar. In this case, it should be exploited that particles show different variations of the Clausius-Mossotti factor over the frequency of the applied electric field. By selecting a frequency, both the magnitude and the direction of the force acting on a particle can be changed and differences enhanced. Selective remobilization via a frequency change has been used to separate different cells in the context of previous research, as mentioned earlier. However, this concept has not yet been applied to DEP filtration or used to sort based on multiple properties. An initial sorting, for example based on particle size (volume), can be achieved via selective trapping (Fig. 7.1 a and b at frequency f_1). The retained particle species can then be further sorted by selective remobilization (e.g., addressing the shape or material) and lastly by switching off the voltage. For this, the frequency is increased stepwise to exceed the crossover to nDEP of one particle type at a time. A higher purity of the fractions from the remobilization steps can be achieved by switching to a flushing solution after the trapping step.

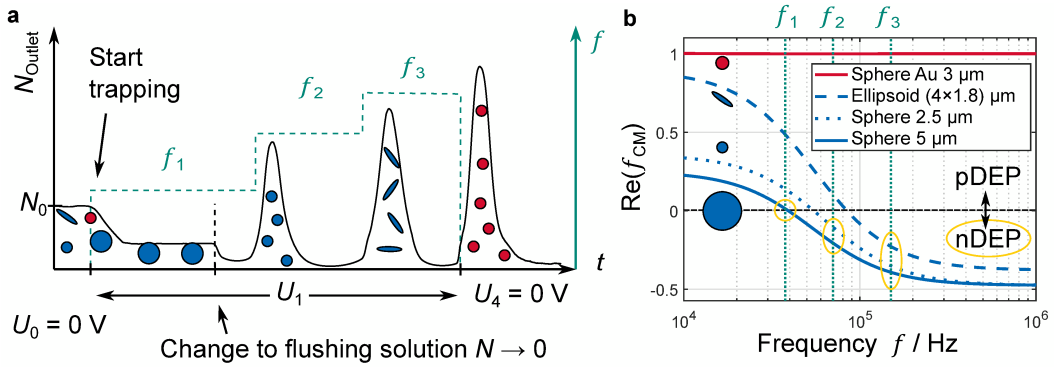

Fig. 7.1.: Principle sketch of transferring the selective remobilization method to multidimensional sorting of particles. a) Dielectropherogram of the combination of selective trapping and selective remobilization. First, particle types are selectively retained in the filter, afterward the particle solution is replaced by a flushing solution, and then particles are selectively remobilized based on different properties. b) Clausius-Mossotti factor of the model particle species over the frequency. For simplicity, only the upper CM boundary for the maximum determined K_S value is shown for all uncoated particles. A frequency is selected for the selective trapping step so that one particle type already shows nDEP (frequency f_1, U_1). All other particles are retained in the filter via pDEP. Then, the frequency is increased stepwise so that one particle type changes to nDEP in each remobilization step (release of small spheres at frequency f_2, release of ellipsoids at frequency f_3). Particle materials for which no change to nDEP is possible in the feasible frequency range (Au-coated particles) can be released from the filter by switching off the voltage ($U_4 = 0$ V). For the individual CM courses, it is marked in yellow at which frequencies the particles show nDEP and thus are not trapped/remobilized.

7.2 Selective remobilization in scalable filters

Before examining whether DEP can be used to sort multidimensionally, it must be verified that selective remobilization by changing the frequency of the applied electric field also works in the mesh-based DEP filter. In the case of the binary mixture of the ellipsoidal and spherical particles, both shapes are initially trapped in the filter at a frequency at which they exhibit pDEP when using a sufficiently high voltage. Then, the frequency is increased so that only the spheres show nDEP and consequently detach from the filter. Finally, the ellipsoids can be recovered from the filter by switching off the voltage. The hypothesis is that particles will be immediately released from the mesh if their crossover to nDEP is exceeded, as the mesh-based filter shows a high selectivity with regard to pDEP trapping. This section is based on Ref. [Wei22].

7.2.1 Methods

The channel fabrication and experimental procedure was carried out mostly in accordance with Sec. 6.2.1. Suitable frequencies for the trapping and remobilization steps were estimated using Clausius–Mossotti factor calculations and were selected via preliminary experiments (see Sec. 7.2.2). For this, the recovery rate of the particles (calculated according to Eq. 3.5) was compared. Both particle types were

trapped in the mesh for 4 min (at 10 kHz) and remobilized for 3 to 4 min at different higher frequencies.

After the selection of a suitable remobilization frequency, the experiments were repeated for the chosen parameter set. Here, initially a change to a flushing solution is not made in order to prevent possible slight parameter changes due to the suspension replacement, which could influence the remobilization. The normalized purity P for each species was evaluated for the release peak of the selective remobilization and recovery step ($U = 0$).

Due to the limited amount of particles in a batch, experiments were done with a) particles of only one shape and with b) binary mixtures. Therefore, the number of repetitions is different for both particle shapes; it is indicated in each respective figure caption. The comparability was verified by plotting the intensity curves obtained from pure and binary particle systems against each other; no difference was found.

7.2.2 Preliminary experiments for the selection of the remobilization frequency

Due to the axis length distribution of the ellipsoids, one specific crossover frequency to choose a suitable remobilization frequency for the experiments does not exist. Therefore, preliminary experiments were performed at different frequencies and the recovery rates of both types of particles were determined (Fig. 7.2). First, both particles (ellipsoids and spheres) were trapped in the filter medium at

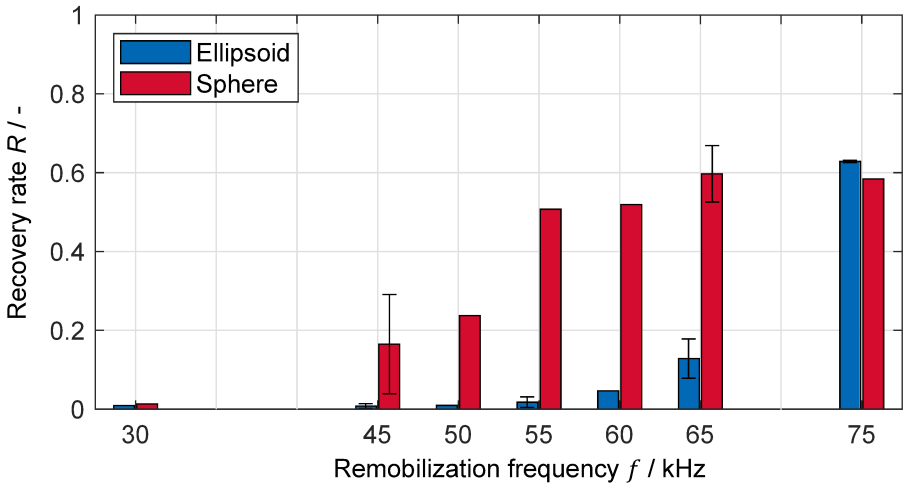

Fig. 7.2.: Recovery rate R of ellipsoids and spheres of the remobilization step at different frequencies f, $E = 2.2\ \mathrm{kV_{pp}\ cm^{-1}}$, $\sigma_\mathrm{m} = 1.1\ \mu\mathrm{S\ cm^{-1}}$, and $Q = 120\ \mathrm{mL\ h^{-1}}$. Selected experiments were performed several times and the standard deviation is given as error bars (45 kHz both n = 2; 55 kHz ellipsoids $n = 2$/spheres $n = 1$; 65 kHz ellipsoids $n = 4$/spheres $n = 2$; 75 kHz ellipsoids $n = 2$/spheres $n = 1$). Adapted from Ref. [Wei22], published under CC BY 4.0 license.

10 kHz and then remobilized at frequencies in the range from 30 kHz to 75 kHz. Below 10 kHz, a slightly higher DEP force for both particle types is expected, but

the influence of electrokinetic phenomena besides DEP is likely to increase. Since the medium conductivity is low, electrothermal effects are less likely than ICEO or CPEO. The recovery rate of the spheres increases rapidly with increasing frequency and reaches its maximum at about 65 kHz. The ellipsoids are hardly remobilized below 60 kHz (below 10%). Only at 75 kHz, a drastic increase can be observed. A selective remobilization of the spheres is possible in the range between 55 – 65 kHz. The selection of a suitable remobilization frequency must be made depending on the purity requirements of the separation task. As a model system is used here, a compromise for high purity of both particle types as target particles was selected and a remobilization frequency of 65 kHz was chosen.

7.2.3 Shape-based selective remobilization

For the main selective remobilization experiments, the parameter set selected by the preliminary experiments is considered in detail. A typical normalized intensity curve (Fig. 7.3) decreases from the initial intensity value (corresponds to c_0) for both particle types and reaches a stable low value after applying an electric field of 2.2 kV_{pp} cm^{-1}. When the frequency is increased to the remobilization frequency

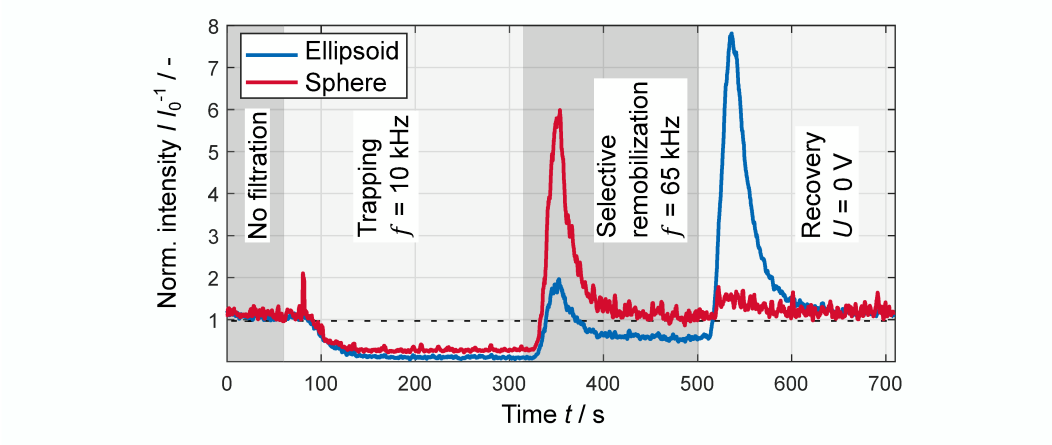

Fig. 7.3.: Typical curve of the normalized intensity II_0^{-1} over the experimental time t. Trapping of both particle types is performed at 10 kHz and 2.2 kV_{pp} cm^{-1} for 240 s at $\sigma_m = 1.1$ µS cm^{-1} and $Q = 120$ mL h^{-1}. At 300 s the frequency f is increased to the remobilization frequency, in this case 65 kHz. Adapted from Ref. [Wei22], published under CC BY 4.0 license.

(65 kHz) at 300 s, both particle types are remobilized in different amounts. The intensity curve rises with a time delay, which results from the distance between the filter cell to the flow-through cuvette. In the example shown, the spherical particles are remobilized to a much higher extent than the ellipsoidal particles. About 100 s after changing the frequency, a stable intensity value is reached again ($t \approx 400$ s), for the spheres nearly similar to the initial concentration and for the ellipsoids significantly below it because they continue to be trapped. When the voltage supply is switched off at 480 s, a strong increase in the fluorescence intensity can be observed. This time, the amount of ellipsoidal particles recovered is substantially

higher. Again, after about 100 s ($t \approx 600$ s), the intensity drops to the initial level for both particle types, as the original particle inflow is re-established.

The results of the entire series of experiments (Fig. 7.4 a) show that both the trapping step and the remobilization steps can be performed reproducibly. At the trapping

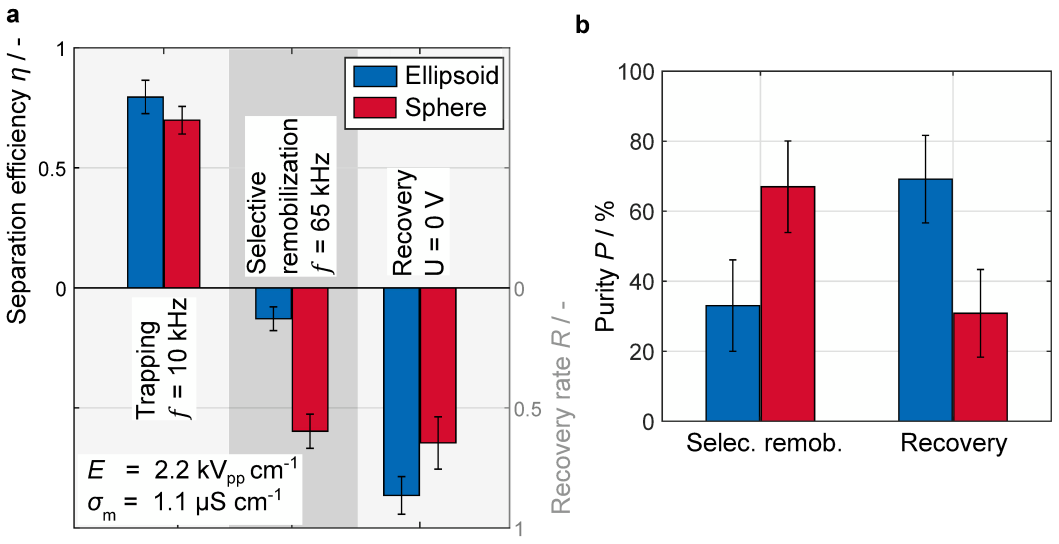

Fig. 7.4.: a) Mean separation efficiency at 10 kHz, recovery rate for selective remobilization step at 65 kHz, and total recovery rate. Experiments were performed at a volume flow of $Q = 120$ mL h^{-1}, a medium conductivity of $\sigma_m = 1.1$ µS cm^{-1}, and an electric field strength of $E = 2.2$ kV$_{pp}$ cm^{-1}. Standard deviation is shown as error bars (ellipsoids $n = 13$/spheres $n = 9$ for trapping and recovery, ellipsoids $n = 4$/spheres $n = 2$ for remobilization at 65 kHz). Adapted from Ref. [Wei22], published under CC BY 4.0 license. b) Normalized purity for the selective remobilization and recovery step.

frequency and at 2.2 kV$_{pp}$ cm^{-1}, both types of particles are trapped in the mesh filter with a high separation efficiency, for the spherical particles $\eta_{10\mathrm{kHz}} = (70 \pm 6)\%$ and for the ellipsoidal particles $\eta_{10\mathrm{kHz}} = (79 \pm 7)\%$. At the remobilization frequency, the spherical particles show a recovery rate of $R_{65\mathrm{kHz}} = (60 \pm 7)\%$. In comparision, the recovery rate of ellipsoids is $R_{65\mathrm{kHz}} = (13 \pm 5)\%$, which shows the suitability of the selected remobilization frequency, as it is significantly different to that of the spheres. There is a significant enrichment of spherical particles in the suspension during this first remobilization step. The crossover frequency of the ellipsoids was found to be (40 – 60) kHz (Chap. 5.5.2, and Fig. 5.8). Yet most particles remain attached to the filter during remobilization. This is because of the distributed sizes of the stretched particles and thus distributed crossover frequencies. A large part of the ellipsoids is stretched more strongly (Fig. 5.7 b), thus has a higher crossover frequency and still shows pDEP at 65 kHz. Consequently, a portion of the ellipsoids show nDEP, but the majority still shows pDEP and thus stays trapped.

In the subsequent recovery step, the remaining spheres and ellipsoids are detached from the filter. For the recovery step, the total recovery rate is given, which means the percentage of previously trapped particles released from the filter during the

first selective remobilization peak and second recovery peak. When looking at the proportion of particles that were recovered in total, a difference between the spheres and the ellipsoids becomes apparent. $R_{\mathrm{total}} = (86 \pm 8)\%$ of the ellipsoids, but only $R_{\mathrm{total}} = (65 \pm 11)\%$ of the spheres were released from the mesh. A possible reason for this could be the particle shape as well. The ellipsoidal particles may be attached to the mesh structures in such a way that a larger part protrudes into the fluid flow compared to the spheres, and they are therefore more easily detached by the drag force. When increasing the flow rate while flushing the channels after each experiment, both particle shapes are detached from the filter by almost 100%. Even after several experiments, there is no strong irreversible accumulation of particles in the mesh.

A normalized purity of $(67 \pm 13)\%$ is obtained for the spherical particles in the selective remobilization step and of $(69 \pm 13)\%$ for the ellipsoidal particles in the recovery step (Fig. 7.4 b). The purity of the individual fractions can be increased further by changing the particle suspension to a solution without particles after the trapping step has been completed.

For the selection of the remobilization frequency it is helpful to know the Clausius-Mossotti factor over the frequency of the individual particles. However, remobilization via a change in frequency is only suitable for particle systems for which a change between pDEP and nDEP is possible in a technically applicable frequency range. Here, the mesh-based approach is helpful, since low voltages compared to the pressure-driven iDEP microchannels or other DEP setups with large electrode spacing are needed to generate sufficient field gradients. High required voltage is considered the primary limiting factor with respect to the applicable frequencies, as the slew rate of the amplifiers is finite. If no transition to nDEP or significant reduction in effective polarizability is possible for any of the species, material- or shape-dependent sorting is difficult to achieve. In this case, it can be attempted to exploit differences in the magnitude of the DEP force by selecting voltages just high enough to trap one type of particle.

To conclude, the results show that selective remobilization of particles in DEP filters utilizing a frequency shift can be realized. Here, the selectivity of the regular mesh structure with respect to pDEP trapping is essential, because otherwise particles will not be efficiently remobilized upon transition to nDEP.

7.3 Multi-step sorting in scalable filters

In this section, selective trapping and selective remobilization are combined. As a particle system for the multidimensional sorting the individual particle alterations and commercially available particles with a higher volume are used. Once again, the multi-step process is investigated using the optically accessible mesh-based DEP filter prototype.

7.3.1 Methods

The same methodology was used as was described in Sec. 7.2. To increase the purity of the subsequent remobilization fractions, the particle mixture was replaced with a flushing solution without particles after the trapping step. For the particle system, this time 2.5 μm plain PS (FluoRed), PS ellipsoids initially 2.5 μm in size (FluoGreen), Au-coated 3 μm PS (Nilered [orange in figures]), and 5 μm plain PS (FluoBlue) were mixed. Again, all uncoated PS particles were treated the same (PVA treatment). To increase the K_{S} value of the particles by removing more PVA from the surface, a double cleaning method was used (described in Sec. A.1.2). Consequently, the crossover frequency of the particles increased by about 40 kHz, which corresponds to an increase of the K_{S} value by around 0.2 nS (compared to the values given in Tab. 5.3).

The splitting of the fluorescence intensity signal using linear unmixing produced good results for mixtures of two (see Fig. 7.3 in previous section) and three particles (not shown in this thesis) with different fluorescence colors. When unmixing four different fluorescence colors and especially two very similar spectra like NileRed and FluoRed, the reliability of the unmixing method is low. Therefore, for these experiments, the particle fractions of the individual trapping and remobilization steps were collected and the samples evaluated via SEM images. Once again, the characteristics of the particles were evaluated using the ImageJ measurement tool and the achievable purity of the fractions was determined. The slightly larger size of the initial particles used for the gold-coating was helpful in order to distinguish between coated and uncoated spheres (3 μm instead of 2.5 μm). Due to their larger size, a crossover to nDEP would be expected at lower frequencies compared to 2.5 μm PS particles. However, the gold-coating should result in no crossover within the realizable frequency range of the amplifier due to the increased particle conductivity. Thus, for the overall process, there should be no difference between 2.5 μm or 3 μm gold-coated particles. In order to obtain sufficient particle concentrations for the evaluation of the SEM images, samples from three replicate experiments were collected together and concentrated via centrifugation and decantation. This facilitates obtaining information about the average value of the purities for the replicates, but no information regarding the standard deviation can be obtained.

Since the particle concentration strongly depends on the wetted area during the loading and drying of the SEM samples, it cannot be determined via the SEM images. If the SEM images are considered exclusively, no statement on separation efficiency and yield is possible. Therefore, the course of the particle concentration over the experimental time was recorded and evaluated via measurements of the singular or binary particle mixtures. Transferability can be assumed, since no particle interaction or other mixing effects were detected for binary and ternary particle mixtures which are diluted suspensions at the selected concentration.

The initial particle concentration was recorded for 60 s. Then, an electric field of 2.9 kV_{pp} cm^{-1} was applied at a frequency of 30 kHz for 390 s to selectively trap particles. Starting from 210 s on, the suspension was switched to the flushing solution to flush all untrapped particles out of the filter and measurement setup. Between 390 s and 510 s the applied frequency was increased to 77 kHz for the first and from 510 s – 640 s to 150 kHz for the second selective remobilization step. Lastly, the voltage was turned off and the recovery was recorded for another 200 s.

The fractions were collected as illustrated in Fig. 7.5 a–e and for three repetitions of the experiment. The normalized purity of each fraction was determined with respect to the different particle species. The total number of particles evaluated depends on the individual SEM images and is therefore given in the caption of Fig. 7.6. The sample of the selective trapping step is called 'filtrate' in the following, the sample of the remobilization steps 'remob 1' and 'remob 2', and the fraction of the recovery step 'recovery'. The yield was determined at the same time intervals as the purity using the intensity curves of the individual measurements, which were also repeated three times.

7.3.2 Results and discussion

The intensity curve over the experimental time of the individual experiments (Fig. 7.6 a) showed negligible trapping for the large 5 µm PS particles, whereas the signal decreased significantly for the other particles. Consequently, a fraction of the 5 µm particles with high purity elutes from the channel during the selective trapping (selectively not trapped). The signal decreased most for the ellipsoidal and gold-coated particles, which can be attributed to their strong effective polarizability. The trapping efficiencies at 30 kHz were $\eta_{\mathrm{PS\ 2.5\ \mu m}} = 0.81 \pm 0.01$, $\eta_{\mathrm{Ellipsoid}} = 0.92 \pm 0.00$, $\eta_{\mathrm{Au\ \ 3\ \mu m}} = 0.87 \pm 0.05$, and on the other hand $\eta_{\mathrm{PS\ 5\ \mu m}} = 0.21 \pm 0.07$. Compared to the selective remobilization experiments of the ellipsoids and spheres in Sec. 7.2.3 a higher trapping frequency could be used, as the particles' crossovers were shifted to higher frequencies by the double cleaning method. Collecting the fraction flowing out of the filter at the selective trapping step leads to a normalized purity of $P_{\mathrm{PS\ 5\ \mu m}} = 67\%$ (Fig. 7.6 b) with a yield of $Y_{\mathrm{PS\ 5\ \mu m}} = (22 \pm 2)\%$ (Fig. 7.6 c). The change of the flushing solution (medium without particles) led to a further decrease of the fluorescence intensity at the outlet because not-trapped particles and therefore mainly 5 µm PS particles were flushed out of the channel. The subsequent frequency increase caused clear individual intensity peaks for each particle type. At around 400 s, mainly the 2.5 µm spheres were remobilized, although a small fraction of ellipsoids was also detected in this step. On the other hand, a small fraction of spheres remobilized at around 500 s with the main peak being ellipsoids. This is because of the different crossover frequencies and the distributed aspect ratio of the ellipsoids which were measured before (see Sec. 5.5.2). For the spherical 2.5 µm particles a normalized purity of $P_{\mathrm{PS\ 2.5\ \mu m}} = 67\%$ at a yield of $Y_{\mathrm{PS\ 2.5\ \mu m}} = (31 \pm 4)\%$ was reached in the first remobilization step; afterward the initial 2.5 µm ellipsoids

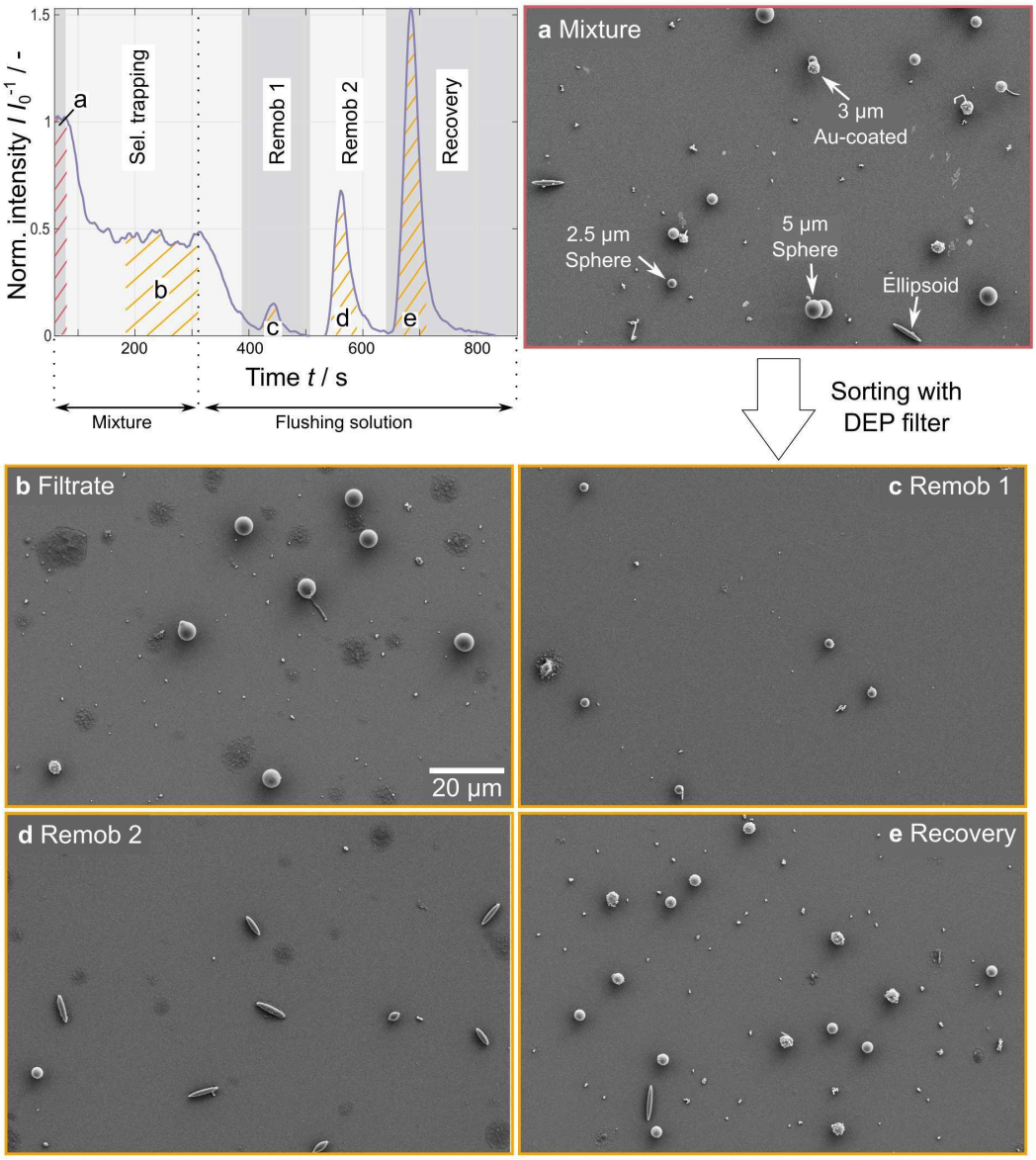

Fig. 7.5.: Exemplary SEM images of a) the particle suspension before sorting (mixture) containing spherical particles of two sizes (2.5 µm and 5 µm), ellipsoids (same volume as 2.5 µm sphere), and gold-coated particles (3 µm) and b) to e) single fractions after sorting. In the upper left corner, the intensity curve (total normalized signal without separation based on the fluorescence colors) of an experiment shows at which times the individual fractions were collected. Experiments were performed at a volume flow of $Q = 120\ \mathrm{mL\ h^{-1}}$, a medium conductivity of $\sigma_\mathrm{m} = 1.1\ \mu\mathrm{S\ cm^{-1}}$, and an electric field strength of $E = 2.9\ \mathrm{kV_{pp}\ cm^{-1}}$.

could be remobilized with a normalized purity of $P_{\mathrm{Ellipsoid}} = 67\%$ at a yield of $Y_{\mathrm{Ellipsoid}} = (43 \pm 6)\%$ at the second step. Compared to the selective remobilization experiments in Sec. 7.2.3 a similar purity could be achieved for the ellipsoidal fraction despite the more complex separation task, because the medium was changed to a flushing solution. The purity of the sphere, on the other hand, is slightly lower, which is due to the fact that not all 5 µm particles have been rinsed out of the channel before remobilization was started. An extension of the amount of time between the change to the flushing solution and the first remobilization step is necessary. After these two remobilization steps, only the gold-coated particles should remain in the channel. The gold-coated particles can be recovered by switching off the voltage at around 600 s (with $P_{\mathrm{Au\ 3\ \mu m}} = 55\%$ and $Y_{\mathrm{Au\ 3\ \mu m}} = (62 \pm 7)\%$). During this step, smaller yet not negligible peaks of all particles are visible, causing a lower purity of this fraction compared to the others. At this point, the two spherical PS particles (2.5 µm and 5 µm) should already be completely remobilized, as they should show nDEP in the previous steps (see Fig. 7.1 b). This means that a small fraction can only be remobilized when the voltage is switched off. Inspecting the videos from the channel for the 2.5 µm spheres shows no change in trapping position on the mesh fibers between the selective trapping step at which they should show pDEP and the subsequent higher frequency steps at which they should show nDEP. Since nDEP trapping was excluded by the experiments in Chap. 6.2.2 and no change in trapping position is evident, it is assumed that other (electrokinetic) forces are responsible for the remaining retention of the 2.5 µm and 5 µm spheres. The cause could not be found. It should be noted that the particles are eluded after the voltage is switched off which favors the theory of an electrokinetic effect. However, for the ellipsoids, a higher remobilization frequency would likely reduce the number of particles still trapped in the filter after the second remobilization step. A higher CM factor is expected for more elongated particles than the mean, which are not remobilized at 150 kHz. For the gold-coated particles, on the other hand, no crossover in the kHz range is expected. Consequently, increasing the frequency should not lead to increased remobilization of these particles in the second remobilization step. Accordingly, the purity of the last two fractions could be improved by selecting a higher second remobilization frequency. However, higher frequencies are not applicable with the amplifier used. A further increase of the frequency while maintaining the high voltage leads to a distorted AC sine signal which results in a DC offset. If the DC current exceeds 0.5 A, discoloration of the ITO layer can be seen, which indicates electrochemical degradation that reduces the ITO's conductivity. A further increase of the frequency would only be possible by changing the amplifier to one with a higher slew rate.

Nevertheless, the exemplary SEM images of the particle mixture (Fig. 7.5 a) and the collected fractions over the experimental time (Fig. 7.5 b to e) illustrate the multidimensional separation success. In each fraction, mainly the particle type that was expected based on its determined crossover can be seen. Non-spherical objects

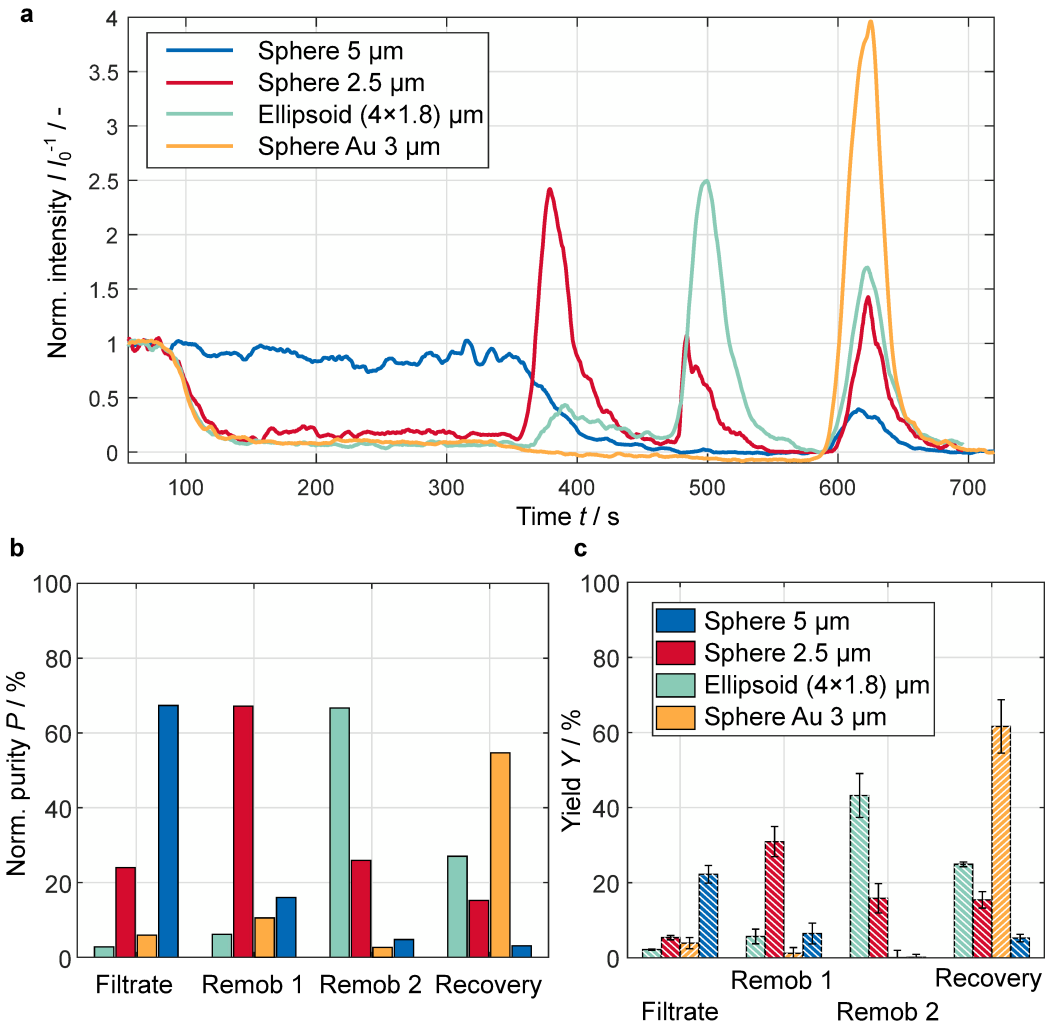

Fig. 7.6.: a) Exemplary normalized intensity curves for a multi-step sorting process with a DEP filter from monodisperse suspensions. Experiments were performed at a volume flow of $Q = 120\ \mathrm{mL\ h^{-1}}$, a medium conductivity of $\sigma_\mathrm{m} = 1.1\ \mu\mathrm{S\ cm^{-1}}$ and an electric field strength of $E = 2.9\ \mathrm{kV_{pp}\ cm^{-1}}$. b) Purity (sample collected for $n = 3$, 50 – 240 particles counted per fraction) and c) yield (n =3) for fractions.

that are significantly smaller than the smallest particles (< 2.5 μm, see Fig. 7.5 a, b, and e) are presumably smaller pieces of gold that were created during the coating process or chipped off from particles. This assumption can be supported by the fact that these particles either mainly appear in the recovery fraction and are therefore strongly retained despite their small size, or – in case of those who are of an even smaller size – are not retained at all and directly leave the channel (filtrate). Both indicate a conductive material that is either retained independently of the frequency or not at all due to its small size. Although the presence of these particles in the mixture was not by choice, the separation experiments should not be influenced.

7.3.3 Conclusion

In this chapter, the combination of selective trapping and selective remobilization for sorting based on multiple particle properties was demonstrated in one pass of the DEP filter. As an example, the particle system developed in this work consisting of polystyrene particles of different size, shape, and with or without conductive coating was used. In contrast to the semi-continuous operation mode introduced in Chap. 4, only one sorting cycle was shown in this thesis and the voltage was switched on after the particle suspension had been fed into the channel. This makes a calculation of the separation efficiencies of the selective trapping step possible, for which a c_0 concentration must be determined. Nevertheless, the concept of a semi-continuous process is considered to be realizable in a mesh-based electrically switchable DEP filter. A clear increase in purity was shown for the individual particle types in the collected fractions.

Conclusion and outlook

8

Dielectrophoresis is known for its high selectivity and ability to precisely manipulate particles. The versatility and functionality of DEP has been proven numerous times especially in the (bio-)analytical field. This thesis demonstrates a new field of application for the DEP filtration technique, namely sorting particles based on multiple properties with a combination of selective trapping and remobilization. Separation methods that exploit multiple properties of microparticles simultaneously and, above all, in a scalable process have rarely been considered. This is where dielectrophoresis as a label-free method with the ability to address multiple properties becomes attractive. Although the DEP force scales with the particle volume, different dependencies of the effective polarizability on the frequency of the applied electric field can be present, which in turn depend on the shape, size, and material/surface functionalization of the particles. In this thesis, this was exploited to sort particles multidimensionally. The complexity of the investigation was reduced by examining a model particle system of particles that differ in one property at a time. The separability of the model particle system components was verified using established DEP methods (DC-iEK and AC-iDEP in microchannels) and was then examined in a scalable filter prototype that had been developed within the context of this work. To enable multidimensional sorting in one filter run, the concept of selective remobilization was transferred to the filter. For this purpose, the filter structure had to retain particles exclusively via pDEP and not nDEP, and it needed to have high recovery rates. Finally, a mixture of particles was sorted based on their particle size, shape, and coating with a combination of selective trapping and selective remobilization. The frequency was increased stepwise, resulting in a parameter-dependent crossover to nDEP.

With the development of multi-step DEP sorting processes, complex interconnections of several separation methods or multiple passes through a DEP filter could be avoided. The method presented here thus offers the possibility to work cost- and time-effectively and can be used to generate highly specific particle systems. The knowledge gained can also be transferred to the bioanalytical field for sorting cells by several properties simultaneously. In addition, the separation of particle systems showing multidimensionally distributed properties is also conceivable. One major drawback of the remobilization concept, however, is that the change in direction of the DEP force is not achievable for all materials. Especially for highly conductive or insulating materials a crossover is not attainable with the existing equipment, but it is realizable for some semiconductors or dielectric particles with surface charges that form a double layer in aqueous media, such as polystyrene. Increasing the applicable frequency range by suitable equipment or adapting the setup can increase

the range of possible particle systems that can be sorted via pDEP/nDEP transitions. Alternatively, it is possible to work with the smaller difference resulting from the unequal DEP force magnitudes of the particles.

The development of a scalable DEP filter is essential for the transition to industrial separation processes of non-biological particles, but it is equally useful in the biological field as long as high selectivity is maintained. Exactly this aspect is reviewed within this work, namely a scalable DEP filter that maintains a high selectivity. The highly ordered post array structures in frequently used microchannels to create well predictable and consistent field inhomogeneities are mimicked as far as possible by a coarsely woven mesh. For this kind of filter cell, a concept for further scaling was elaborated. Increasing the cross section of the filter without changing the electrode distance can raise the throughput without decreasing the field gradients and corresponding DEP force within the filter. In addition, a stacking of alternating electrodes and filter mesh is conceivable. A possible limitation to be considered could be the dissipation of heat generated by joule heating. The extent to which heat is generated and how a possible cooling system could be integrated is beyond the scope of this work and could be part of future studies. Since this work aims primarily for proof of concepts, the actual interconnection to a semi-continuous process as described in Chap. 4 was not shown. Such an operation mode can be enabled by using two pumps to alternately feed the filter with a flushing solution and a particle mixture, and an automatic valve switching system. For a further scalability and a better handling, a transition to an easily demountable filter design is important. Switching to less expensive electrode materials, such as stainless steel, is conceivable, as the optical accessibility is especially helpful for process development. The prototype presented in this thesis achieves separations at volume flows of 120 mL h^{-1}, which is 1000 times higher than the throughput that could be reached in the AC-iDEP microchannels used in Chap. 5.5 at similar separation efficiencies for particles in the micrometer range. To enable the separation of smaller particle size scales, future studies could address the variation of mesh parameters such as pore size and fiber diameter. This may expand its spectrum of use in order to tackle interesting separation problems, such as sorting nanoparticles, e.g., carbon nanotubes.

It is the author's belief that DEP filtration in macroscopic filter materials is one valuable addition to the repertoire of dielectrophoresis methods. The concept of DEP filtration with regular field disturbing structures offers the chance to increase throughput while achieving sufficient selectivity for several separation tasks. DEP filtration in scalable devices brings us one step closer to industrial-scales for the processing of non-biological particles and a broader use of DEP. Furthermore, the possibility to combine selective trapping and remobilization may enable us to solve more complex separation tasks in the future.

Experimental details

A

The methods presented here have been published in Refs. [Wei19] and [Wei22].

A.1 Details on model particle generation

A.1.1 Gold-coating procedure

Gold-coated polystyrene particles were prepared using a process based on the method described in Ref. [Lim08; Ren11; Gar12]. Unlike the original process, here fluorescent gold-coated particles are directly produced, and thus no further fluorescent labeling is required. For this purpose, 45 µL suspension of fluorescent polystyrene particles (weight/volume fraction of 2.5%, PS plain or COOH, microParticles GmbH, Berlin, Germany) with a diameter of 2.4 µm and 3 µm or 80 µL of an equally concentrated suspension using 4.5 µm particles are mixed with 1.8 mL of 20 nm gold nanoparticles suspension (BBI Solutions, Crumlin, UK) for one day (Fig. A.1). Via van der Waals forces, some nanoparticles adsorb on the particle surface and serve as a nucleation site for the subsequent gold plating [Ren11]. The seeded beads are washed twice in deionized (DI) water (adjust to pH 7 by adding KOH) via centrifugation and decantation, and the supernatant is replaced with 1 mL of a gold plating solution [570 mM L-ascorbic acid (Carl Roth GmbH + Co. KG, Karlsruhe, Germany) and 340 mM gold (I) sodium thiosulfate (Alfa Aesar, Ward Hill, Massachusetts, USA)]. The gold-seeded microparticles are left in the gold plating solution for 4 days, continuously mixed on a shaker (ThermoMixer C, Eppendorf SE, Hamburg, Germany) at 1000 rpm. The suspension was subsequently washed 3 times with DI water to remove the reagents.

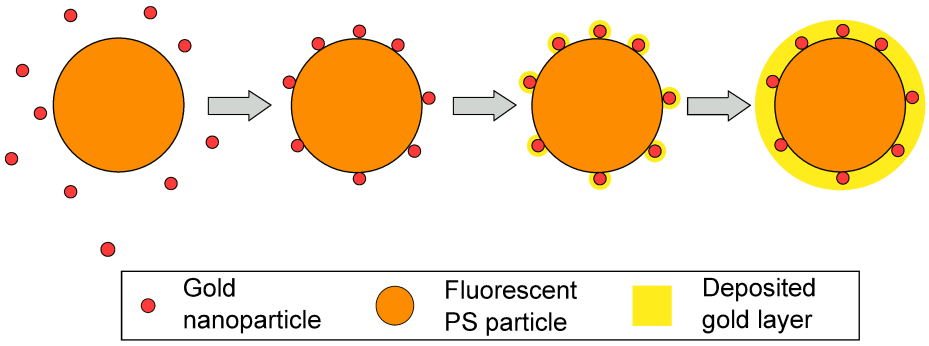

Fig. A.1.: Gold-coating process of fluorescent polystyrene particles. Polystyrene spheres are dispersed in a gold colloid. Nanoparticles adsorb onto the surface and serve as nucleation sites for reductive deposition of gold (based on Ref. [Wei19], original Ref. [Gar12])

A.1.2 Stretching procedure

The particle stretching process is based on Ref. [Ho93]. To generate the ellipsoidal particles, 75 mL of a PVA solution with a mass fraction of 8% was prepared, and 500 µL of fluorescent particles (weight/volume fraction of 2.5%) were added. The mixture was poured into a 95 mm$\times 135$ mm mold and dried over 72 h at room temperature (Fig. A.2). From the resulting film, 30 mm$\times 90$ mm strips were cut, each marked with a defined grid structure, and inserted into a manual stretching device. In a 120 °C hot oil bath, the films were first heated for 30 s and then stretched slowly for 60 s. Based on the change in the dimensions of the grid structure on the stretched films, the draw ratio was determined. Only the film sections whose grid dimensions had elongated less than 1.5 times the initial length were sorted out. This ensures that most of the particles have a noticeably elongated shape. All other film sections (stretched 1.5 to 4 times) were dissolved together in a (7:3 v/v) water-isopropanol mixture. The suspension was heated for 1 h at 40 °C to speed up the dissolution process. The particle suspension was then washed 4 times via centrifugation and decantation.

When processing fluorescent particles, the choice of the molecular weight (MW) of the PVA, which is used for the film formation, seems to be critical. A loss of fluorescence was observed when the stretched film had to be dissolved for a long time at high temperatures. When using PVA with a low MW that is highly soluble in water, the stretched film dissolves within a few hours, even at room temperature, which reduces the fluorescence loss of the particles. Good results were obtained using Parteck COAT (Merck KGaA, Darmstadt, Germany) with an average MW of 40000 g mol^{-1}. The particles had a sufficient fluorescence signal for the measurement methods used in the thesis. A PVA with a MW of 125000 g mol^{-1}, Mowiol 20-98 (Sigma-Aldrich Chemie GmbH, Taufkirchen, Germany), which is closer to the PVA used in the original procedure (with 115000 g mol^{-1}) worked well only for non-fluorescent particles.

To ensure comparability between ellipsoidal (stretched) and spherical (not stretched) particles, the same procedure (embedding in a PVA film, heating in an oil bath, dissolution of the film, and washing steps) except for the stretching step itself was also applied to the spherical reference particles. This is required as the K_S value of the particles was significantly reduced after the stretching process. A total of two batches of ellipsoids and treated spheres were used for the experiments. Care was taken to select comparable batches with respect to K_S values and aspect ratios.

Double-cleaning procedure

For the multidimensional experiments (Chap. 7.3), a double-cleaning method based on Ref. [Coe14] was tried out to remove more PVA from the particles' surfaces. After the normal washing cycle with ultrapure water, an additional heating step to 50 °C is performed with subsequent ultrasonication for 30 min. Measurements showed an increase of the K_S value by around 0.2 nS (corresponds to a higher crossover of

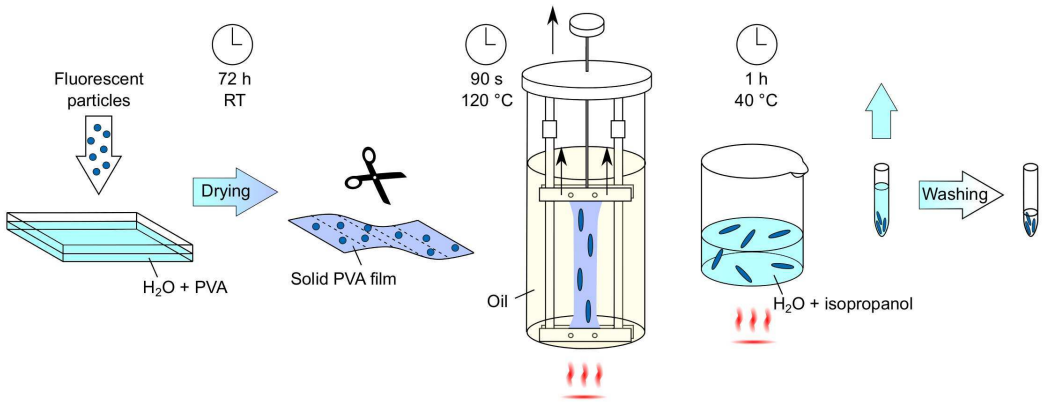

Fig. A.2.: Process schematic of stretching process and used parameters. The fluorescent PS particles are embedded with the help of a water-soluble PVA in a film, which after drying at room temperature, is cut into strips and stretched in a defined manner in an oil bath at 120 °C. The film with the stretched particles is then dissolved in a mixture of water and isopropanol, and the ellipsoidal particles are purified via washing steps. (Adapted from Ref. [Wei22], published under CC BY 4.0 license, parts of the figure originally are based on [Ho93])

around 40 kHz). Increasing the K_S value leads to an increase in polarizability for PS particles and, likewise their crossover, making the particles still trappable at higher frequencies via pDEP. The increase in the CM factor of the particles also results in a higher DEP force magnitude.

A.2 Details on the channel production

A.2.1 Microchannels

A standard soft lithography technique was used for the PDMS microchannel fabrication. The master molds for the soft lithography steps were produced using standard photolithography with printed transparency masks and SU8 3050. To produce the PDMS microchannel, Sylgard 184 (Dow Corning, Midland, Michigan, USA) basis and curing agent are mixed (10 to 1) and degassed for 40 minutes in a vacuum bell (≈ 70 mbar) before and after pouring onto the mold. Afterward, the channel is cured for 1 h at 80 °C in an oven. After curing, the channel is peeled off the mold, and holes are cut into the PDMS with a biopsy punch (Rapid-Core, World Precision Instruments, Inc., Sarasota, Florida, USA) that form the inlet and outlet of the channel. For the electroosmotic-driven DC-iEK channels, a PDMS-coated glass wafer was used as the channel bottom, so that the surface properties are the same throughout the whole channel. For this, 1 mL of PDMS is applied to a glass wafer (100 mm diameter) using a spin coater WS-650-23 B (Laurell Technologies Corporation, Lansdale, Pennsylvania, USA) at 4000 rpm for 200 s and cured in the same way as the channel [Wei19]. For the pressure-driven AC-iDEP channels, uncoated glass slides were used. To generate a closed channel, both PDMS surfaces, respectively the microscope glass slide, are then treated with a corona

plasma treater (Corona SB BD-20ACV, Electro-Technic Products, Chicago, Illinois, USA) for 20 to 40 s and placed on top of each other. Annealing takes place at 40 °C for 4 h.

The produced DC-iEK channels of 0.88 mm×10.16 mm (width, length) were either empty (post-free), to measure the particle zeta potential with single particle tracking (SPT), or contained an array of insulating posts at the channel center for particle separation. The post array consisted of cylindrical insulating posts (200 μm in diameter) in a square array of 4×14 posts. One row with a 'dove-tail' structure before (and after the post array) has been established in the DEP microfluidic to prevent clogging. Two 1000 μL pipette tips serve as liquid reservoirs at the channel inlet and outlet. They were cut to a length that the syringes (Terumo U-40 1 ml) fit into them to fill and flush the channels with fluid. To compensate for pressure differences between both reservoirs, a silicone tube with an inner diameter of 0.51 mm was used to connect the two reservoirs and balance their fluid level. The tube was glued into holes that were melted into the reservoirs (one hole per reservoir) to prevent leaking. The connection via the tube can be closed with a clamp while rinsing the channel so that the liquid must flow through the post array (for example, to remove particles that were attached to the channel surface after experiments).

The microchannels used for the pressure-driven AC-iDEP experiments have a height of 79 μm and a width b_a of 2.5 mm. A 10 by 7 array of insulating posts with a diameter h_s of 260 μm, and a distance d of 360 μm is located in the center of the microchannel. A 'dove-tail' geometry is located at each side of the array. PTFE capillaries with an inner diameter of 250 μm were used for fluid supply. To introduce the electric field, two additional holes (500 μm) were punched into the PDMS, and the slightly bigger platinum rod electrodes (diameter of 600 μm) were inserted.

A.2.2 Mesh-based filter

For the large scale mesh-based channels, fluid distributors were 3D printed (Elegoo Mars, Shenzhen, China) using an epoxy resin (Elegoo ABS-Like Photopolymer Resin, Shenzhen, China). As an electrically insulating material, a polypropylene fabric with a mesh width of 500 μm, a fiber diameter of 340 μm, and a fabric thickness of 610 μm (PP-500/36, Franz Eckert GmbH, Waldkirch, Germany) is used. Transparent ITO-coated glass slides (Biotain Crystal Co., Ltd., Fujian, China) with a film thickness of 135 nm and a sheet resistance of 10 – 15 Ω sq^{-1} were used as electrodes. Wires were attached with a conductive glue to connect the electrodes to the voltage source (Elecolit 323, Panacol-Elosol GmbH, Steinbach, Germany). To seal the channel sides and the connection to the distributors, a glue based on a modified-silane polymer DEKAsyl MS-2 (Dekalin, Ranstadt, Germany) was used, which offers a good compromise between adhesive and sealant. The distance between the ITO electrodes varies due to the adhesive connection between 0.6 mm and 0.8 mm.

A.3 Experimental details on particle characterization methods (Chapter 5)

A.3.1 Determination of particle size and shape with SEM images

The particle size and its standard deviation, as well as the particle shape, were determined from scanning electron microscopy (SEM) images. For SEM imaging, the particle or filtrate samples were concentrated via centrifugation and decantation if necessary, then transferred to silicon carriers and dried via freeze-drying (Alpha 1-2 LD plus, Martin Christ Gefriertrocknungsanlagen GmbH, Osterode, Germany). This type of drying made the distribution of the particles on the carrier more uniform. When dried at room temperature, circular bands with high particle concentration often formed due to the slow evaporation of the sample suspension. The SEM images were evaluated with the help of ImageJ (Fiji [Sch12], version 1.53c). For this, the individual spheres and ellipsoids were selected using the elliptical selection tool and added to a region of interest (ROI) manager. Using the measure command in the ROI manager, the major and minor diameters of the particles can be output. The means and standard deviations of the data were determined in Matlab.

Besides this manual evaluation, some (semi-)automatic methods were tried (overview in the next section). No satisfactory results could be achieved at the state of the thesis, which is why the more time-consuming but more accurate manual evaluation was used.

A.3.2 Automatic image analysis to determine particle properties

For a (semi-)automatic determination of particle sizes and shapes from SEM images, in most methods, a segmentation of the particles from the background is necessary. This was difficult due to several aspects:

- An uneven brightness of the background due to deposits from the DEP suspension
- Difficult edge detection of individual particles when they are closely adjacent or partially overlap each other
- Shadows cast by the particles on the background
- The edge of the particles appearing brighter than the particle center.

Some of these aspects can be seen, for example, on the SEM images in Fig. 7.5. The following approaches were tested:

- Thresholding in ImageJ, with different pre-processing steps (e.g., Gaussian blur, denoising, and background subtraction with a rolling-ball algorithm)

and splitting binary structure with watershed algorithm [Vin91], 'Ellipse Split' Plugin [Wag17], or Matlab programs that can handle overlapping particles [Zou21]

- Ridge detection plugin in ImageJ [Ste98]
- Trainable segmentation plugin of ImageJ ('Trainable WEKA segmentation') [Arg17]
- Deep learning-based method 'DeepParticleNet' (inspired by Mask R-CNN) [Fre20].

Due to the aspects described above, simple thresholding is not suitable even after several preprocessing steps. The same applies to edge detection or the trainable WEKA segmentation. If the binary images generated using these methods are not accurate, e.g., because the darker particle centers are not recognized as belonging to the particle, the following methods that can handle overlapping particles may also fail to provide satisfactory results. For example, the methods presented in Ref. [Zou21] for splitting overlapping ellipsoids in Matlab were able to subdivide smaller sections of the image well, but they could not handle objects that were not based on ellipsoidal shapes, e.g., deposits from solution in the background of SEM images or edgy particles.

The most promising is the evaluation via Deep Learning algorithms. However, training is necessary based on numerous manually segmented images, which justifies the effort only for a high number of images to be evaluated. In the context of this work, the total number of images to be evaluated was less than the number of images required just to train the algorithm adequately.

A.3.3 Particle zeta potential determination via SPT

The particle zeta potential was determined by single particle tracking in a microchannel without posts. SPT is an image analysis method to determine particle velocities. Particles are segmented from images and their trajectories are tracked across multiple images by assigning an identity to each object. To determine the zeta potentials of the particles, the EK velocities of particles are analyzed for different applied DC potentials. For the velocity measurements, low voltages were used. Therefore, no influence of electrophoresis of the second kind is expected. The EK particle velocity $\vec{v}_{\mathrm{EK}}$ in empty channels (homogeneous field strength) results from the superposition of EO motion that is exerted via drag by the fluid and EP motion of the particle itself and is given by

$$\vec{v}_{\mathrm{EK}} = \mu_{\mathrm{EK}}\vec{E} = \mu_{\mathrm{EO}}\vec{E} + \mu_{\mathrm{EP}}\vec{E}. \tag{A.1}$$

The electrokinetic mobility becomes

$$\mu_{\mathrm{EK}} = (\zeta_{\mathrm{p}} - \zeta_{\mathrm{wall}})\frac{\varepsilon_{\mathrm{m}}}{\eta_{\mathrm{m}}}. \tag{A.2}$$

To determine the zeta potential of the channel wall, the zeta potential of the 2.4 μm PS COOH particles was measured by electrophoretic light scattering (ELS) with a Delsa Nano C Particle Analyser (Beckman Coulter Inc., Brea, California, USA). With the ELS measured zeta potential of the 2.4 μm PS COOH particles, $\zeta_{\text{PS 2.4 }\mu\text{m}} = (-32.86 \pm 3.45)$ mV, and their SPT determined EK mobility the wall zeta potential was calculated using Eq. (A.2), $\zeta_{\text{wall}} = (-73.1 \pm 3.5)$ mV. All further particle zeta potentials were calculated using Eq. (A.2) and ζ_{wall}. This method was chosen because the determination of the zeta potential using ELS is not suitable for high-density particles such as gold-coated particles, and this approach allows particle characterization in the same conditions in which they will be separated [Hid19].

For the SPT, a DC-EK microchannel (without posts) was filled with the standard DEP solution used in this work and about 5 μL of particle suspension (particle concentration 1×10^6 ml^{-1}) was added with a 10 μL pipette into a reservoir directly at the channel inlet. The electrodes were immersed in both reservoirs and it was made sure that the particles were entering the channel due to an initial static pressure. Subsequently, the bypass tubing was opened to let the static pressure in both reservoirs equalize and all particles came to a stop. For measurement, a voltage was applied, and a video was captured for 15 s. Three to four different voltages between 25 and 150 V were applied for each of the four particles examined with the DC-iEK method, and experiments were repeated at least three times per data point. The average EK velocity of the particles was determined from the recorded videos by using the ImageJ plugin TrackMate (Fiji) with the 'linear Motion' tracking algorithm (which is further described in Sec. A.4.3).

A.3.4 Fixed-frequency dielectrophoretic particle chromatography experiments

The particles' K_{S} values were determined by fixed frequency dielectrophoretic particle chromatography (DPC) experiments [Gie21]. In DPC, a particle peak is released into a microchannel with an interdigitated electrode array at the channel bottom. When applying an electric field, the particles experience dielectrophoresis and are moved via pDEP or nDEP in low velocity streamlines at the channel bottom or top (Fig. A.3). There is hardly any delay of the particle peak if the particles have only a negligible polarization (Re(f_{CM})≈ 0 at crossover). By comparing the elution profiles of the particles with and without voltage application at different frequencies, the crossover frequency can be determined. A 25 μm high microchannel with an interdigitated electrode array (electrode distance and width of 50 μm) was used. 1.6 mL h^{-1} was selected as the volume flow and 10 V_{pp} as the applied voltage. The suspension used consists of the same components as those in the main experiments. The conductivity was set to 1.1 μS cm^{-1} and a particle concentration

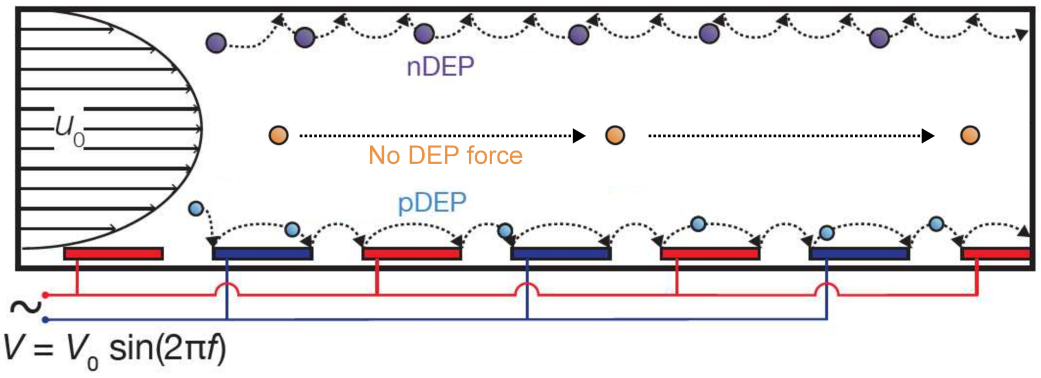

Fig. A.3.: Possible particle trajectories depending on its DEP behavior in fixed-frequency DPC experiments. If the frequency f is close to the crossover of the particle, it is not deflected from its original streamline. If the particles show nDEP or pDEP, they are moved on streamlines of slower fluid velocity. Accordingly, a particle peak, with particles starting distributed over the channel height, is delayed on average. Adapted from Ref. [Gie19], published under CC BY license.

of approximately 5.1×10^6 mL^{-1} was used. With the determined crossover frequency, the K_S for a spherical particle is calculated as [Che19]

$$K_\mathrm{S} = \frac{r_\mathrm{p}}{4}\left(-\sigma_\mathrm{m} + \sqrt{9\sigma_\mathrm{m}^2 - 4(\varepsilon_\mathrm{p} - \varepsilon_\mathrm{m})(\varepsilon_\mathrm{p} + 2\varepsilon_\mathrm{m})(2\pi f_\mathrm{CO})^2}\right) . \tag{A.3}$$

For the ellipsoidal particles, Eq. (A.4) was obtained by substituting σ_p (Eq. (2.24)) in Eq. (2.19) and setting Re(f_CM)$= 0$

$$K_\mathrm{S} = \frac{a_2}{4L_{a_1}}\Big(\sigma_\mathrm{m}(2L_{a_1} - 1) + \sqrt{\sigma_\mathrm{m}^2 - 4L_{a_1}(\varepsilon_\mathrm{p} - \varepsilon_\mathrm{m})(L_{a_1}(\varepsilon_\mathrm{p} - \varepsilon_\mathrm{m}) + \varepsilon_\mathrm{m})(2\pi f_\mathrm{CO})^2}\Big) . \tag{A.4}$$

A.4 Experimental details on DC insulator-based electrokinetics (DC-iEK, Chapter 5)

A.4.1 Setup

The electric field in the DC-iEK microchannels was applied with two platinum wire electrodes (0.6 mm diameter) that were immersed in the reservoirs. The electric potential was controlled by a signal generator (DG-4062, Rigol Technologies EU GmbH, Puchheim, Germany) and amplified by a power amplifier (PZD700A, TREK Inc., Lockport, New York, USA). Imaging of the microchannel was done with an inverted microscope Eclipse Ts2R-FL (Nikon Corporation, Tokyo, Japan) with a 4× or 10× lens, a DAPI/FITC/TRITC triple bandpass filter (Semroc Inc., Rochester, New York, USA) and a Grasshopper3 color camera (FLIR Systems Inc., Wilsonville,

Oregon, USA).

A.4.2 Methods

The channels were conditioned with vacuum-degassed DI water (to reduce gas bubbles in the channel) for several hours before experiments. This increased the hydrophilicity of the PDMS surface and made it easier to remove all air from the channels when they were filled with the suspension used for experiments. Before the experiments, the particles were stored for at least 12 hours in the medium that was later used in the experiments. This prevented the medium in which the particles were stored from affecting the experimental conditions. Directly before experiments, all particles were sonicated for at least 2 minutes to break aggregates. A 0.05% v/v Tween 20 solution with an adjusted conductivity of 29.5 μS cm^{-1} and a pH of 7.05 was used for 2.4 μm particles and pH 7.2 for 4.5 μm particles. The pH was adjusted by adding KOH. A higher pH was necessary for the bigger particles to prevent agglomeration, as the uncoated PS particles had a lower zeta potential (less negative).

Determination of minimum trapping voltage

The minimum voltage that was required to retain the first particles by iEK was determined in the microchannel design with the post array. Fluid and particles were injected into the channel in the same way as for the zeta potential measurements and the static pressure was equalized by opening the tube. Voltage was applied and stepwise increased until the first particle trapping was observed. For all particles, three measurements were done and the average value was determined.

Separation experiments

For the separation experiments, a mixture of coated and uncoated particles of the same size was injected into the channel. A high voltage was applied (above the minimum voltages required for trapping for both particle types) until all particles in the system were retained within the first columns of the post array. Then the voltage was reduced in time steps of at least 30 s so that first all particles of one kind and then at a lower voltage all particles of the second kind were released. Videos were recorded at the channel outlet to detect the particle release.

A.4.3 Evaluation: Tracking and counting particles

SPT data

For the evaluation of the SPT videos from the microchannels, a Matlab script was used, which accesses the TrackMate function [Tin17] of Fiji. Initially, the script converted the videos to 8-bit grayscale. With the TrackMate function, the particles were detected in the observation window (1224 px$\times$1024 px, 1 px corresponds to 1 μm for the 10x objective used; recorded in the middle of the empty (SPT) channel) and their trajectories were determined. A threshold for the grayscale value and the minimum particle radius was defined for particle detection. The 'linear motion

LAP tracker' (relies on a Kalman filter) was selected as a tracking algorithm and gave good results because the particle motion (velocity and direction) was almost constant. The parameters 'linking max distance', 'Kalman search radius', and 'gap closing max frame gap' with the values 40 μm, 40 μm, and 4 frames were passed to the function for determining the trajectories. The individual particle positions at each point were stored for each frame as XML files, and in another Matlab script, the average velocities of the particles at the individual applied voltages were determined.

Separation experiments

The videos of the separation experiments were segmented according to the different fluorescence colors used with a Matlab (MathWorks Inc., Portola Valley, California, USA) routine. The segmentation step of the in-house developed evaluation program is based on segmentation in the CIELAB color space [Inc23]. In this color space, colors are represented by two parameters a^* and b^* that uniquely define the color and a perceptual lightness L^*. This makes it easier to classify different exposure conditions of the same color into one group. After segmentation, the fluorescence intensity was determined by integrating the gray values of each frame. The fluorescence intensity measured at the channel outlet plotted over the experimental time is called 'dielectropherogram' and was determined for each particle type.

As a quantification of the selectivity, the purity and yield were considered, assuming that fluorescence intensity I is proportional to particle concentration c. The values for particle trapping at the outlet were calculated for the 2.4 μm particles during the first remobilization peak for approx. 5 s and during the second for 70 s. For the 4.5 μm particles for approx. 6 and 20 s. The number of particles of each species flowing in and out of the channel was determined by integrating the intensity at these time intervals and the parameters were calculated with Eqs. 3.3 and 3.4. For the determination of the yield, the different EK transport velocities of the particles must be taken into account in the integration. Accordingly, the corresponding determined areas were multiplied by a velocity factor.

A.4.4 Calculation of Dukhin and Peclet number

The Dukhin and Peclet numbers facilitate the assessment of whether non-linear electrophoresis of particles has relevant effects on particle retention in DC-iEK experiments. The Dukhin number was calculated with [Hug03, Gl. 3.19]

$$Du = \frac{K_{\mathrm{S}}^{\mathrm{D}}}{r\sigma_{\mathrm{m}}} + \frac{K_{\mathrm{S}}^{\mathrm{S}}}{r\sigma_{\mathrm{m}}} \,. \tag{A.5}$$

The surface conductance of the stern layer $K_{\mathrm{S}}^{\mathrm{S}}$ was assumed to be 1 nS as no measurements were performed to be able to determine the value. The surface conductance of the diffuse layer can be approximated by

$$K_{\mathrm{S}}^{\mathrm{D}} = \frac{4F^2cz^2D^{\mathrm{D}}(1+3M/z^2)}{RT\kappa}\left(\cosh[\frac{ze\zeta_{\mathrm{P}}}{2k_BT}]-1\right) \tag{A.6}$$

with dimensionless parameter M [Hug03, Gl. 11.8 and 11.9]

$$M = \left(\frac{RT}{F}\right)^2 \frac{2\epsilon_\mathrm{m}\epsilon_0}{3\eta_\mathrm{m} D^\mathrm{D}} \,. \tag{A.7}$$

Here, D^D is the ion diffusion coefficient for the counterions in the diffuse layer ($D^\mathrm{D}_{\mathrm{K}^+} = 1.94 \times 10^{-9}$ m^2 s^{-1}), c the electrolyte concentration (in mol m^{-3}), and η_m the dynamic viscosity of the medium.

To calculate the Peclet number, the particle velocity at the maximum applied voltage at the inlet of the channel was determined with ImageJ's TrackMate tool and was used in

$$Pe = \frac{v_\mathrm{EK} r}{D^\mathrm{D}} \,. \tag{A.8}$$

The parameters for the particles used in the DC-iEK experiments are given in Tab. A.1.

Tab. A.1.: Properties and calculated dimensionless parameters for the particles used in iEK experiments.

	K_S^S in nS	K_S^D in nS	Du	E in V cm^{-1} for estimation of v_EK	v_EK in µm s^{-1}	Pe
PS 2.4 µm	1	0.04	0.29	900	362.2	0.22
PS 4.5 µm	1	0.02	0.15	500	255.6	0.30
Au 2.4 µm	1	0.08	0.30	900	375.7	0.23
Au 4.5 µm	1	0.08	0.16	500	177.6	0.21

A.5 Experimental details on AC insulator-based dielectrophoresis (AC-iDEP, Chapter 5)

A.5.1 Setup

In the AC-iDEP experiments, the particle suspension was pumped with a syringe pump (TJA-3A, Longer Precision Pump Co., Ltd., Hebei, China) into the microchannel. The electrodes were connected to a voltage amplifier (PZD2000A, TREK, Inc., Lockport, New York, USA) controlled by a signal generator (Rigol DG4062, Rigol Technologies EU GmbH, Puchheim, Germany). Imaging of the microchannels was done with a Zeiss Axio Scope A1 (Carl Zeiss Microscopy Deutschland GmbH, Oberkochen, Germany) with a 5×/0.13 EC Epiplan lens, a DAPI/FITC/TRITC triple bandpass filter (Semrock, IDEX Health & Science, LLC, Rochester, New York, USA), and a Grasshopper3 color camera (FLIR Systems, Inc., Wilsonville, Oregon, USA). In order to maintain visual access for the vertically mounted channel, a 90° deflection mirror (CCM1-E02/M dielectric turning mirror, Thorlabs, Inc., Newton, New Jersey, USA) was installed between the nose piece of the microscope and the objective lens.

A.5.2 Experimental procedure

All experiments were conducted using ultrapure water (Omniatap 6 UV/UF, stakpure GmbH, Niederahr, Germany) containing 0.005 vol% Tween20 (Sigma-Aldrich, Steinheim, Germany) to reduce particle–wall interactions, 6 μM potassium hydroxide to adjust pH, and 0.25 μM potassium chloride to adjust the electrical conductivity to the desired value (1.1 μS cm^{-1}). Green fluorescent particles were used as initial particles for the ellipsoids (PS-FluoGreen plain, microParticles GmbH, Berlin, Germany). The spheres exhibit red fluorescence (PS-FluoRed plain, microParticles GmbH, Berlin, Germany). The total particle concentration in all experiments was 2.5×10^5 mL^{-1}. For the ellipsoidal particles and PVA-treated spheres, the initial particle concentration after the modification process was determined for one batch by counting in a Thoma counting chamber (Paul Marienfeld GmbH & Co. KG, Lauda Königshofen, Germany). This value was used as a reference value for the subsequent batches.

All separation experiments in the microchannels were carried out with a binary particle mixture. Before the experiments, the channel was completely wetted with ethanol. The channel was then flushed with the particle suspension at 1 mL h^{-1} for 30 min. Before each experiment, any adhering particles were loosened at 10 mL h^{-1} for 10 s. The flow was allowed to become stationary at 0.1 mL h^{-1} for 1 min, and then the particle flux was recorded for 10 s. The electric field (2.5 kV_{pp} cm^{-1} at 15 kHz) was then turned on for 170 s which causes trapping of the particles in the post array structure.

A.5.3 Evaluation

Separation efficiency

The TrackMate-based script was also used for the determination of the particle fluxes to calculate separation efficiencies, purities, and yields for the pressure-driven AC-iDEP experiments. Before using the tracking script, the videos of the inlet and outlet were cropped so that only the free channel and, thus, neither electrodes nor post structures were in the image. The videos were then segmented based on the fluorescence colors, as explained in the last section. The TrackMate script was applied to the videos of each particle type. In the *.xlm files, which are produced by TrackMate, the particle positions and their course over the experimental time (trajectories) are given. A Matlab script was developed to count how many particles flow through the channel based on the particle trajectories. By this, it can be determined how many particles of one type flow into the filter and leave it again at the outlet. For the separation efficiency, the time period between 160 s and 180 s was evaluated right before switching off the voltage for recovery. The purity was calculated for the selective trapping step in the same interval. For the recovery step, the range of 188 s to 200 s was evaluated.

A.6 Experimental details on AC-iDEP in mesh-based filters (Chapters 6 and 7)

A.6.1 Setup

The separation processes in the large mesh filter were observed using an inverted microscope (Eclipse Ts2R-FL, Nikon Corporation, Tokyo, Japan) with a 4×/0.13 Plan Fluor lens, a DAPI/FITC/TRITC triple bandpass filter (Semroc Inc., Rochester, New York, USA), and a Grasshopper3 color camera (FLIR Systems Inc., Wilsonville, Oregon, USA). The spectrometer setup to record the fluorescence intensity over the experimental time consisted of a 110 µL flow-through cuvette (176-765-85-40, Hellma GmbH, Müllheim, Germany), a cuvette holder with four light ports (CVH100, Thorlabs Inc., Newton, New Jersey, USA), an EXFO X-Cite 120 PC Q light source (EXFO Inc., Richardson, Texas, USA), and a spectrometer (SILVER-Nova, StellarNet Inc., Tampa, Florida, USA). A wavelength range between 190 and 1110 nm can be recorded. For the fluorescent particles, the light source and spectrometer were placed at a 90° angle to each other. Again, a DAPI/FITC/TRITC emission filter was used in front of the spectrometer. The electrodes were connected to a voltage amplifier (A400, FLC Electronics, Göteborg, Sweden) supplied by a signal generator (Rigol DG4062, Rigol Technologies EU GmbH, Puchheim, Germany). Fluid input was realized using an Ismatec MCP-CPF IP65 piston pump with the pump head FMI 202 QP.Q0.SSY (Cole-Parmer GmbH, Wertheim, Germany).

A.6.2 Experimental procedure

The same medium composition was used as for the AC-iDEP experiments. Additionally, the particle suspension was degassed for 5 min in a vacuum vessel at 70 mbar. This step reduces the gas bubble formation within the capillaries, the mesh filter, and the flow-through cuvette at high flow rates. Before each experiment, the channel was completely wetted with ethanol, rinsed for 15 min with a medium without fluorescent particles, and the background signal was recorded. The channel was then flushed with the particle suspension for at least 15 min at a flow rate of 240 mL h^{-1}. Before each recording, the flow rate was increased to 600 mL h^{-1} for 30 s and then allowed to settle to 120 mL h^{-1} for another minute. Experiments were started when a stable intensity value was reached. The steady-state particle flux was recorded for 1 min.

A.6.3 Evaluation

The fluorescence intensity was recorded using a LABVIEW program and evaluated via an in-house MATLAB script. The signal I over time was determined by integrating specific wavelength ranges to speed up the algorithm. The intervals were selected on the basis of the characteristic values of the emission filter used. The total fluorescence intensity signal is divided into the components of the particles' fluorescence colors by a linear unmixing algorithm. It is assumed that the fluorescence intensity

depends linearly on the particle concentration (with proportion A_i) and that the total spectrum is a linear combination of the spectra of all individual fluorophores I_i,

$$I(\lambda) = \sum_{i=1}^{N_{\mathrm{ref}}} A_i I_i(\lambda), \tag{A.9}$$

where N_{ref} is the total number of reference spectra [Dic01]. Reference spectra were acquired for each fluorescent particle, and the best matching combination of particle proportions was calculated using a genetic algorithm (GA) (from the global optimization toolbox version 4.4) with non-negativity constraints. The validation of the linear unmixing algorithm can be found in Sec. B.5. Using the intensity curves determined over the experimental time, the separation efficiency can be calculated analogously to Eq. (3.1) with the fluorescence intensities of the suspension after passing through the filtration cell without applied (corresponds to the particle number going into the channel) and with an electric field (particle number going out of the channel). For this, the fluorescence intensities before switching on the electric field and 20 s directly before the first remobilization were averaged (see Fig. A.4, orange-colored areas). Here, it is assumed that the number of particles flowing out without an applied field at the channel outlet corresponds to the number flowing into the channel since hardly any non-specific and irreversible trapping was detected.

The recovery rate represents the ratio of released particles (index remob) to previously captured particles (index trap). Since a linear relationship between the measured fluorescence intensity and the particle concentration in the cuvette is assumed and the values are always set in relation to others for which the same proportionality applies, here, calculations are made with the measured intensities instead of absolute particle numbers. The calculation of the recovery rate is further simplified by dividing the surface area (between the curve and the x-axis) with a positive sign after subtracting I_0 (particle detachment) by those with a negative sign (particle trapping, see Fig. A.4, hatched areas)

$$I_{\mathrm{remob}}(t) = \begin{cases} I(t) - I_0 & \text{if } I(t) > I_0 \\ 0 & \text{if } I(t) \leq I_0 \end{cases} \tag{A.10}$$

$$I_{\mathrm{trap}}(t) = \begin{cases} 0 & \text{if } I(t) > I_0 \\ I(t) - I_0 & \text{if } I(t) \leq I_0 \end{cases} \tag{A.11}$$

$$R = \frac{\int_{t=0}^{t_{\mathrm{remob,end}}} I_{\mathrm{remob}}(t)dt}{\left|\int_{t=0}^{t_{\mathrm{remob,end}}} I_{\mathrm{trap}}(t)dt\right|}. \tag{A.12}$$

For the selective remobilization step, the entire time spans up to the point $t_{\mathrm{remob,end}}$ at which the intensity signal falls below the signal of I_0 after the beginning of the remobilization was evaluated. To make the detection method robust against

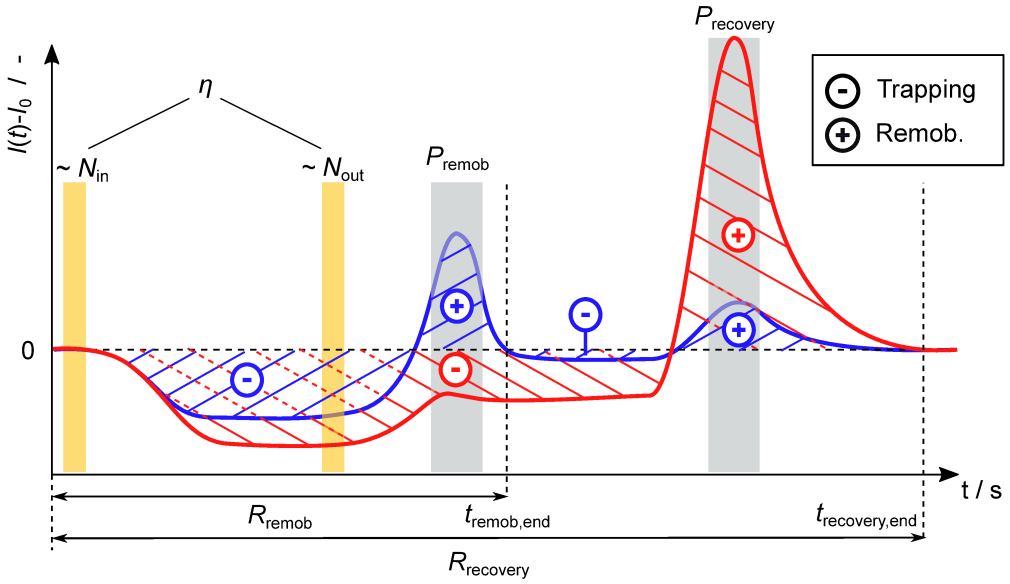

Fig. A.4.: Evaluation intervals on the example of a selective remobilization experiment with a binary particle mixture (red particles - selectively remobilized and blue particles- not remobilized till recovery).

outliers, the intensity signal was smoothed beforehand using a moving average method. To determine the end of the recovery step, a similar procedure was chosen. This recovery rate describes the total number of particles recovered in the whole experiment. Therefore, the time span up to the point $t_{\text{recovery,end}}$ was evaluated.

The purity (and yield for the multidimensional experiments) was calculated for 50 s around the maximum of the individual remobilization/recovery peaks (see Fig. A.4, gray colored areas). The particle number ($\propto I_{\text{out}}$) going out of the channel during the remobilization steps is related to the particle number going in ($\propto I_{\text{in}}$) until the end of the time period ($t_{\text{purity,end}}$, end of first gray area) in the case of yield

$$Y_i = \frac{\int_{t_{\text{purity,start}}}^{t_{\text{purity,end}}} I_{i,\text{out}} dt}{\int_{t=0}^{t_{\text{purity,end}}} I_{i,\text{in}} dt}. \tag{A.13}$$

In the case of the purity, the outgoing flux of each species is related to the total amount of particles leaving the filter of both species i and k

$$P_i = \frac{\frac{\int_{t_{\text{purity,start}}}^{t_{\text{purity,end}}} I_{i,\text{out}} dt}{\int_{t=0}^{t_{\text{purity,end}}} I_{i,\text{in}} dt}}{\frac{\int_{t_{\text{purity,start}}}^{t_{\text{purity,end}}} I_{i,\text{out}} dt}{\int_{t=0}^{t_{\text{purity,end}}} I_{i,\text{in}} dt} + \frac{\int_{t_{\text{purity,start}}}^{t_{\text{purity,end}}} I_{k,\text{out}} dt}{\int_{t=0}^{t_{\text{purity,end}}} I_{k,\text{in}} dt}}. \tag{A.14}$$

In Eq. (A.14), the amount of particles going out is normalized to the amount going in of the individual species to include any differences in the initial concentration.

Additional information and plots

B

B.1 Agglomeration of particles in DC-iEK experiments

Figure B.1 shows the blocking of the microchannel inlet by particle agglomerates that occurs during separation without the pH adjustment of the solution. The agglomerates cannot be dissolved after formation or flushed out of the channel.

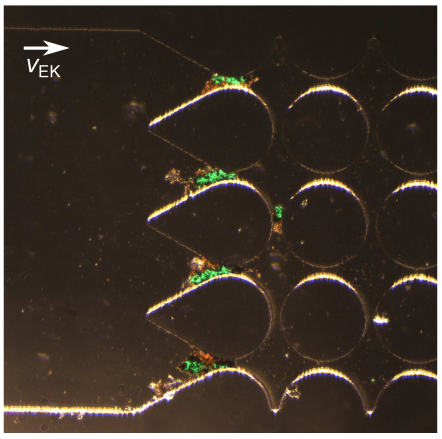

Fig. B.1.: Image of particle agglomerations blocking the inlet of the post array. Based on [Wei19].

B.2 Influence of reservoir connection on the backpressure build-up in DC-EK experiments

The backpressure, which increases with the duration of the experiments, leads to reduced averaged electrokinetic particle velocities during SPT experiments (Fig. B.2 a) with a standard iEK setup without reservoir connection. The electrokinetic velocity decreases by about 20% within a few seconds. In comparison, if the reservoir connection is used, no significant reduction (less than 5%) in the electrokinetic velocity was detected (Fig. B.2 b). As both channels, microchannel and bypass, are in parallel in the equivalent circuit diagram (Fig. B.2 c) the introduction of reservoir connection does not have any influence on the applied voltage as long as there is no load-dependent behavior of the amplifier. As the same applied voltages were measured with and without a reservoir connection, this can be excluded.

B.3 Details of single particle tracking results

In accordance with the theory, the EK velocity increases linearly with the applied electric field for all particle types (Fig. B.3). The slope that represents the EK mobility

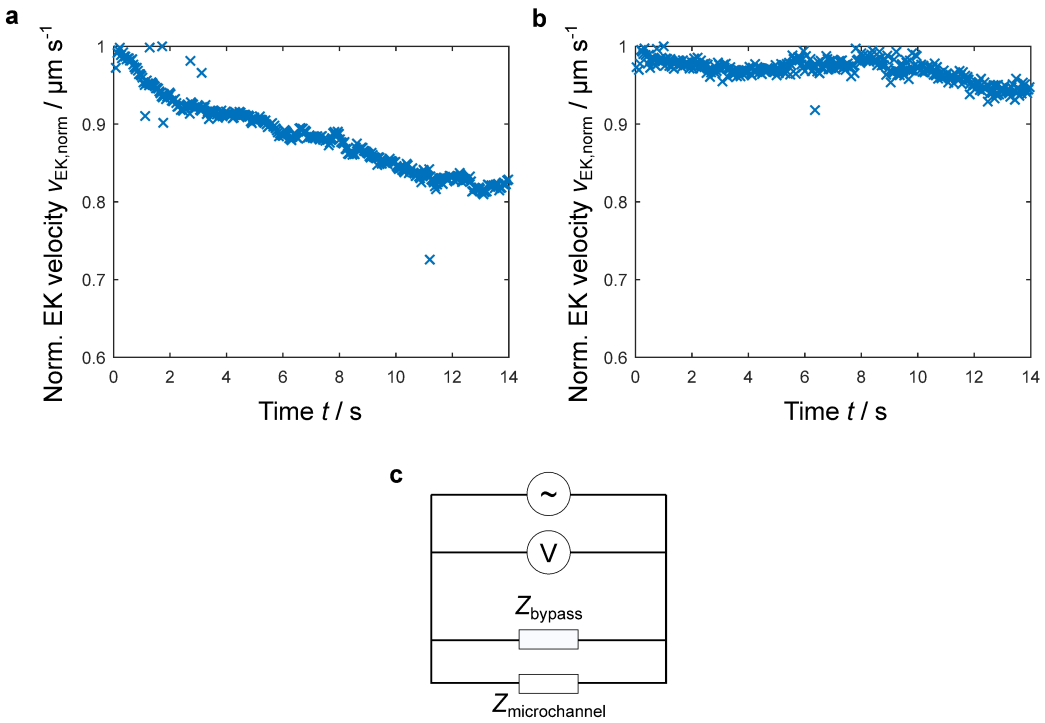

Fig. B.2.: a) Electrokinetic velocity of 2.4 µm PS particles over time at 100 V_{DC} in characterization suspension (pH 6.7) without reservoir connection. b) Same conditions with reservoir connection. c) Equivalent circuit diagram of the channel with reservoir connection. Due to the cross section differences of the capillaries, it is assumed that impedances $Z_{\text{bypass}} << Z_{\text{microchannel}}$. Based on Ref. [Wei19].

of the gold-coated particles is smaller than that of the uncoated particles. The

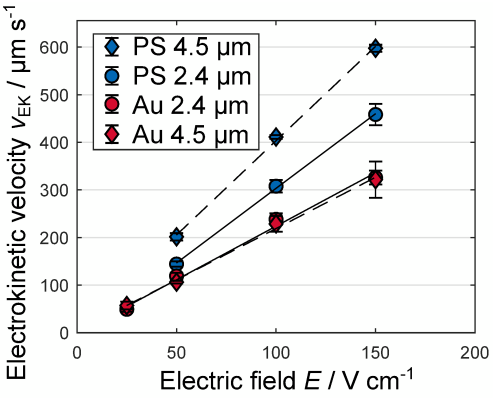

Fig. B.3.: Measured electrokinetic velocities of the different particle types as a function of the applied electric field determined by SPT. The electrokinetic mobility of the particles was determined from linear regression that is shown as solid lines for 2.4 µm particle diameter and dashed lines for 4.5 µm diameter. Linear regressions for EK velocity measurements are included in Tab. B.1. Based on Ref. [Wei19].

electrokinetic mobilities μ_{EK} that were determined from linear regression for each particle type, including the y-intercept y_{inter} and the coefficients of determination R^2 are shown in Tab. B.1. R^2 is almost one for all cases implying nearly perfect

agreement between measurements and linear fitting. In theory, the regression line should cut the origin, i.e., $y_{\text{inter}} = 0$. When the uncertainty of y_{inter} is considered, it shows that this requirement is met in all cases.

Tab. B.1.: Experimentally determined electrokinetic mobility of the particle types and parameters of linear regressions. The general form of the linear regression equations is $v_{\text{EK}} = \mu_{\text{EK}}\, E + y_{\text{inter}}$.

Type	d / µm	y_{inter} / µm s^{-1}	Electrokinetic mobility μ_{EK} / 10^{-8} m^2 (s V)$^{-1}$	R^2
PS COOH	2.4	-10 ± 31	3.14 ± 0.28	0.99
PS COOH	4.5	$+7 \pm 18$	3.96 ± 0.17	1.00
PS Au	2.4	-1 ± 13	2.25 ± 0.15	0.99
PS Au	4.5	$+3 \pm 25$	2.15 ± 0.27	0.97

B.4 Influence AC-iDEP channel design on reproducibility

Figure B.4 shows the reproducibility of the standard iDEP microchannel design with a constant channel width compared to the altered design with narrowing at the beginning and end of the channel. The standard deviation is significantly higher for the 'normal' design. The absolute height of the separation efficiencies of both experiments is not comparable, as the particles and their surface functionalization are different. The slightly bigger particles (2.4 µm plain instead of 2 µm carboxylated) used in the narrowing design show much higher separation efficiencies.

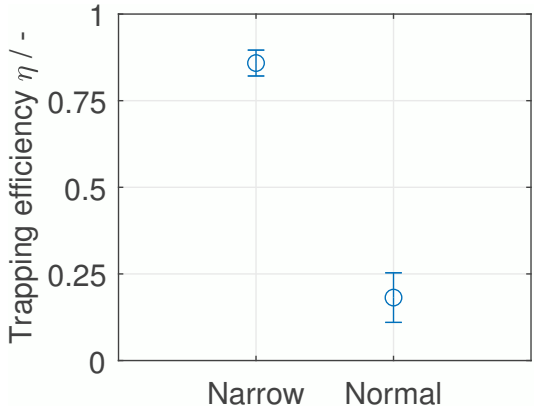

Fig. B.4.: Comparison of the reproducibility of microchannel experiments in the standard channel design with the same channel width and the altered design with narrowing at the beginning and end $n = 3$. 2.4 µm PS plain particles were used in the narrowing and 2 µm PS COOH in the normal design.

B.5 Validation of the linear unmixing algorithm

For the evaluation of the spectrometer data, it was assumed that the fluorescence intensity is directly correlated with the particle concentration in the concentration

range used. To verify the linear unmixing algorithm, measurements of different mixing ratios of both particle fluorescence colors were made. The concentration of the particles after the stretching/treatment process was estimated but not precisely determined, which is why slight deviations could occur. Subsequently, the fluorescence signal was divided into the components of both particle colors using the linear unmixing script, and the calculated and selected concentration ratio was compared (Fig. B.5). The calculated values deviate by 6% on average.

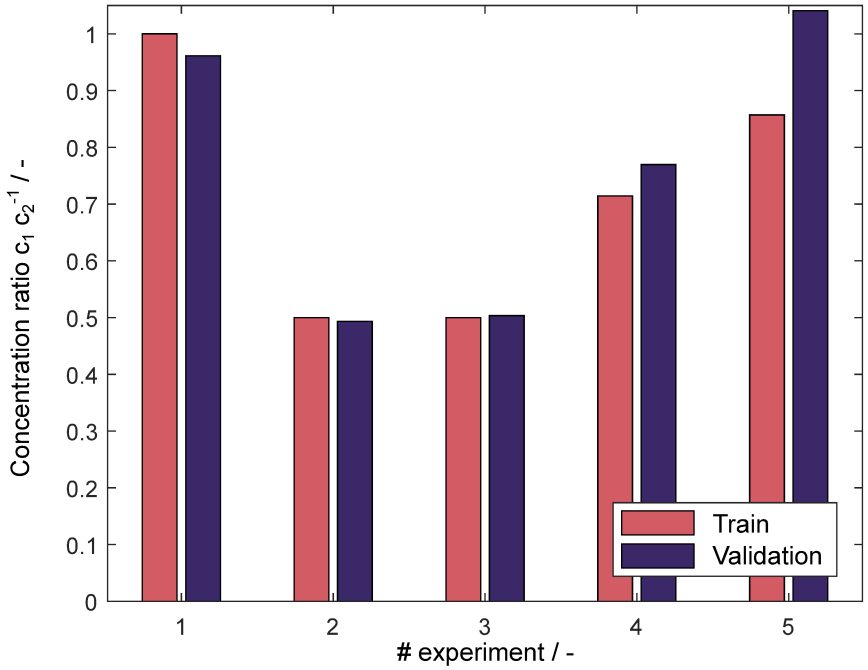

Fig. B.5.: Validation of linear unmixing algorithm. The chosen concentration ratio $c_1 c_2^{-1}$ (train) was compared with the calculated one (validation). Adapted from Ref. [Wei22], published under CC BY 4.0 license.

B.6 Shape influence

Figure B.6 illustrates the CM factor for an ellipsoid and a sphere with identical K_{S} values (lower and upper bounds). The figure shows the significant difference of the $\mathrm{Re}(f_{\mathrm{CM}})$ due to the particle shape.

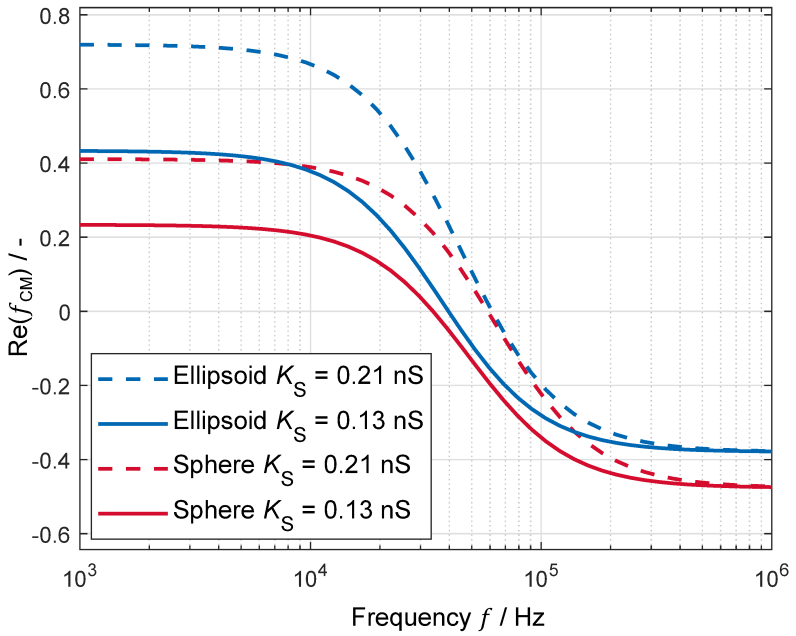

Fig. B.6.: Real part of the Clausius-Mossotti factor $\mathrm{Re}(f_{\mathrm{CM}})$ for ellipsoids and spheres over frequency f, if the K_{S} range of both particle shapes were equal. Adapted from Ref. [Wei22], published under CC BY 4.0 license.

C On the vortex formation in microchannels

In the AC-iDEP microchannel experiments, vortices are formed at the electrodes. The source could not be determined; however, numerous experiments were conducted to identify their origin. The results and conclusions drawn from these experiments are presented within this chapter in order to provide a starting point for other researchers. First some general observations are described, possibly involved phenomena are named, and then experiments are listed which were undertaken to identify the source of the vortices. At the end of this chapter, a short conclusion is drawn and some ideas for further experiments are given. In the main part of this work, the effect of the vortices on the experiments was reduced as much as possible by changing the channel geometry. Since reproducible results could thus be obtained and no such effects occurred in the mesh-based channels, the investigation of the cause was not pursued further.

C.1 General observations

The vortex formation starts at a field strength of about 1 kV_{pp} cm^{-1}. The size of the vortices varies between the experiments and channels used, although the process parameters such as field strength, frequency, and medium conductivity are the same, and care was taken to ensure the same electrode positioning in the microchannel. A noteworthy aspect is that the vortices are not of the same size at both electrodes. In the experiments, one electrode provides the AC signal ($\pm U$, in the following called 'live' electrode) and the other is grounded. The vortex size is larger at the live electrode for all experiments regardless if it is positioned before or after the post array. The vortices are visible both by tracing particle trajectories (Fig. C.1 a) or by introducing a dye pulse into the system and tracking how the dye behaves (Fig. C.1 b). No time dependence could be detected. When the voltage is switched on, the vortices appear almost instantaneously and do not change their size noticeably over the experimental time.

In contrast, no vortex formation is observed in the mesh-based DEP filter. The reason for this is presumably the higher flow velocities in the DEP filter structure and generally the higher fluid volume, which may allow concentration gradients to be compensated more quickly or the pressure-driven flow to dominate over electrokinetic effects.

C.2 Possible involved phenomena

Some phenomena have been reported in the literature that can cause vortex structures in microchannels used for DEP. Literature references and a description

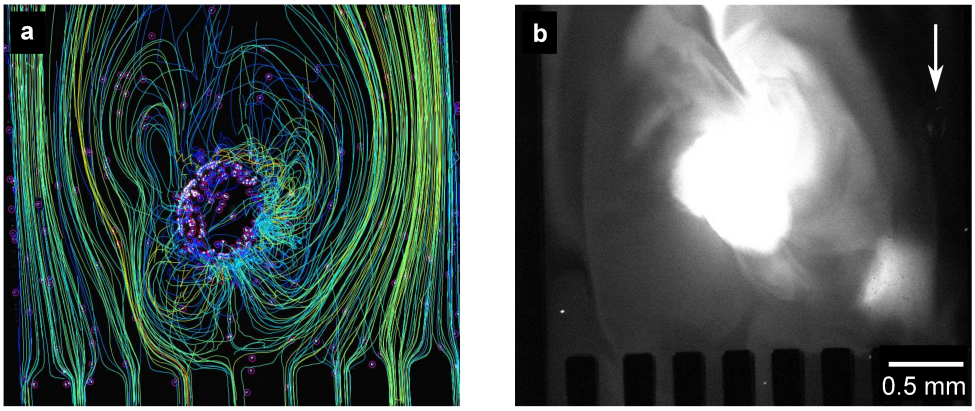

Fig. C.1.: Vortex at live electrode at 2.75 kV_{pp} cm^{-1}, 15 kHz and 10 µS cm^{-1}. The direction of the pressure-driven laminar flow is indicated by an arrow. a) Particle trajectories determined with SPT. b) Effect of vortices on a fluorescent dye pulse (Fluorescein).

of the theoretical background can be found in Chap. 2.3. A distinction must be made here between whether the effects occur at, for example, constrictions or posts or, as in this case, at the electrodes. Since in iDEP microchannels with post arrays the electrodes are located in widely spaced reservoirs, no vortex formation around electrodes has been reported in the literature. Only the vortex formation at the posts structure/constrictions due to electrothermal or electrokinetic effects (ICEO and CPEO) were reported for iDEP methods. Both are caused by high electric field gradients and it can be assumed that these can also take place at the electrodes. Direct contact between medium and electrodes and the resulting vortex formation is more familiar from electrode-based DEP methods. Electrothermal vortex structures caused by Joule heating are described for eDEP methods as well as fluid motion due to ACEO. Furthermore, the illumination can cause temperature gradients which –like Joule heating –can cause vortex formation [Gre00]. An effect that is rarely considered is Faradaic reactions at the electrodes. Under DC (-offset) or low frequency AC electric fields, water can be electrolyzed and concentration gradients can arise that can cause fluid movement. In the AC-iDEP method used here, high frequencies are applied. At first glance, electrolysis is therefore not likely. Hydrodynamic vortex formation (wake) due to the flow around the cylindrical posts can be excluded as the flow is in the creeping flow regime ($Re << 1$) [Pan13, p. 352]. An overview of the possible effects and the expected dependencies over changed process parameters (medium conductivity and frequency) is shown in Tab. C.1.

C.3 Experiments

The vortex formation was qualitatively assessed by observing particle trajectories (1 µm PS particles). Tracking (via ImageJ's TrackMate) and subsequent quantitative assessment of the vortex size or particle acceleration proved to be difficult. Since the particle acceleration is non-uniform and the trajectories are chaotic, the

Tab. C.1.: Overview of the parameter influence on different phenomena which could be source of the vortex formation at the electrodes. In addition, a tendency observed in the experiments is also given.

Phenomenon	**Medium conductivity ↑**	**Frequency ↑**	**Electric field ↑**
Electrothermal flow	↑ linear	↓	↑ squared
ACEO	↓	↓	↑ linear
ICEO	↓	Maximum at $\sigma/(2\pi\varepsilon_\mathrm{m}) = 25$ kHz	↑ squared
CPEO	↓	↓	↑ squared
Electrolysis	↑	↑ as DC offset increases	↑ with ϕ
Observation of vortex size	↓	Only slight influence between (10–130) kHz, maximum at around 20 kHz	↑ with ϕ and E

tracking algorithm had problems to determine the particle trajectories. In addition to experiments with microparticles, experiments with multiple fluorescence dyes (Rhodamine B, Rhodamine 6G, and Fluorescein) were conducted, each with a molar concentration of 10^{-5} M.

Exclusion of individual suspension components

A fluorescent dye (Fluorescein) was injected into the fluid as a pulse. This was done to examine whether the vortex formation is possibly only caused by forces that affect only the particles and not the medium or whether the medium is also influenced. A laminar flow of the dye puls and the characteristic residence time distribution can be observed in the microchannel without a voltage supply. Clear vortices can be seen when an electric field is applied. Accordingly, it can be excluded that only the particles are affected, e.g., by DEP or other EK effects.

One of the medium components (Tween 20, KOH, KCl) being the cause of the vortices was excluded by omitting one of these components at a time from the experiments. In any case, the vortices occurred with comparable intensity. The same applies to pure water. However, when using pure ethanol as the suspending medium, no vortices are visible, but also PS particles are not trappable via pDEP as the influence of the EDL is missing. Both conductivity and permittivity of ethanol are substantially lower compared to the aqueous DEP medium, which reduces the power dissipated in the channel. This indicates that either water as a substance is participating in the formation of the vortices, or that the vortices are related to a specific power dissipation.

Influence of process or design parameters

The medium conductivity (and thus KCl concentration) had an influence on the vortex size. It decreases slightly with increasing medium conductivity and then rises by a hardly noticable extent. This is an argument against the hypothesis that the vortices are caused by electrothermal effects like Joule heating which should increase linearly with medium conductivity. The frequency influence could be examined up to 130 kHz at the necessary voltage for the microchannel experiments. Only a slight influence of the frequency with a maximum at around 20 kHz was found in this tested range.

Instead of a monopolar amplifier with one live and one grounded electrode, a bipolar amplifier was tested and the same voltage with opposite signs was applied to both electrodes. At both electrodes, vortices of approximately the same size were observed, but they were smaller compared to the live electrode of the monopolar amplifier. This suggests that not only the electric field strength is decisive but also the absolute potential of the electrode. To test this hypothesis, the electrode spacing [(11–19) mm] and the length of the post array were varied [(4–12) mm]. The field strength was kept constant and the applied potential was increased in relation to the increasing electrode spacing. In the selected range, there is no clear trend detectable.

Different numbers of electrodes (only the live electrode Fig. C.2 a, standard case with two b –e and three electrodes f/g) and arrangements (b/c symmetric around post array and d/e asymmetric) were tested to investigate the effects on vortex formation. An overview is shown in Fig. C.2. It is striking that a current measurement which was connected in series before the grounded or before the live electrode shows deviating values. It must be noted, however, that with the measuring device used, it was only possible to measure at a lower voltage (max. 1 kV_{pp}, Precision Power Analyser LMG670, ZES ZIMMER Electronic Systems GmbH, Oberursel, Germany). Before the live electrode, the values were around 6 times higher. This is surprising as current conservation must hold. Even with only the live electrodes and not the ground electrode inserted in the channel (Fig. C.2 a), vortices are formed around it. A reason for the imbalance in the experiments could be a leakage current to ground. The only possibility that could be supposed is a grounding via the capillaries and syringe pump, as the vortex size and current flowing is higher when the live electrode is closer to the channel outlet (Fig. C.2 d). The insertion of a second live electrode at the outlet supplying this potential drop so that the potential at the normally positioned live electrode dropped across the channel (Fig. C.2 f) showed a decreased trapping in the channel and only a slight redistribution of vortices. However, the capillaries as a potential sink could be excluded by an experiment with reservoirs as in the DC-iEK microchannels. No explanation for this observation was found since all other components of the channel or its vicinity (PDMS, microscope slide as channel bottom, and microscope holder) are made of non-conductive materials.

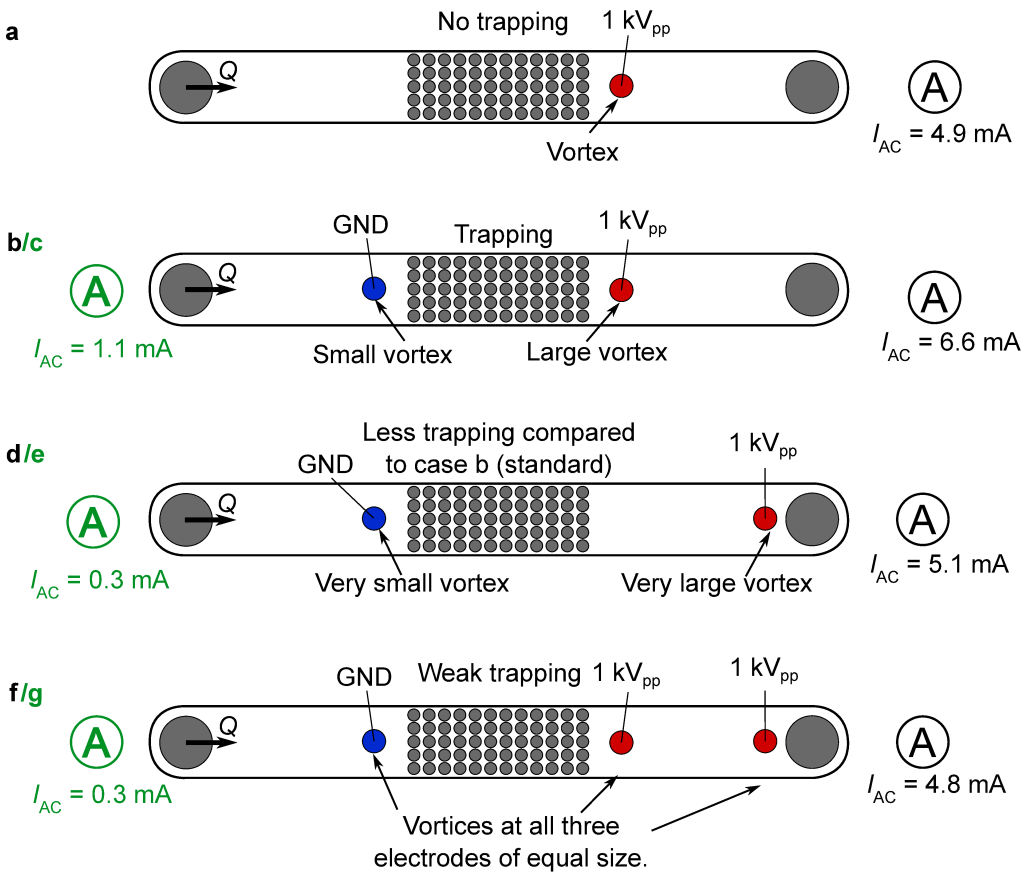

Fig. C.2.: Overview of current measurements and observations for different numbers of electrodes and arrangements in the AC-iDEP microchannels. GND stands for grounded electrode, and the symbol A marks the position of the current measurement. At the live electrode 1 kV_{pp} and 15 kHz were applied in each case due to limitations of the measuring device.

At 1 kV_{pp} applied voltage, a DC offset of about 0.8 V caused by the amplifier is measurable. Accordingly, a significantly higher DC offset is expected for the 2.75 kV_{pp} applied in the AC-iDEP experiments. However, it must be kept in mind that not the whole potential is available for Faradaic reactions. Accordingly, only low reaction rates are expected, if Faradaic reactions take place at all. A DC offset can be prevented by connecting a capacitor in series. Using capacitors with capacitances from 1 nF–1 µF indeed reduces the measurable DC offset (at 1 kV_{pp}), but no influence on the vortex formation (at 2.75 kV_{pp}) could be observed. At higher field strength, compensation by manually adding a DC offset via the signal generator with a different sign but the same magnitude reduces the measurable DC offset as well while reducing the vortex formation slightly. The experiments suggest that vortex formation could be due to electrolysis at the electrodes caused by a DC offset. However, it cannot be explained why a capacitor connected in series does not affect the vortex formation. Furthermore, applying a pure DC voltage causes only a slight vortex to form above a voltage of 20 V. A further increase, on the other hand, does not lead to any further amplification of the vortices but results in a directed

electroosmotic fluid movement from one electrode to the other. Accordingly, the DC offset cannot cause the vortex formation alone.

The geometry of the electrodes also seems to have no influence. Avoiding the 'sharp' edge at the bottom of the electrode, where significantly increased field gradients may occur (Fig. C.3 a), did not result in any change. For this purpose,

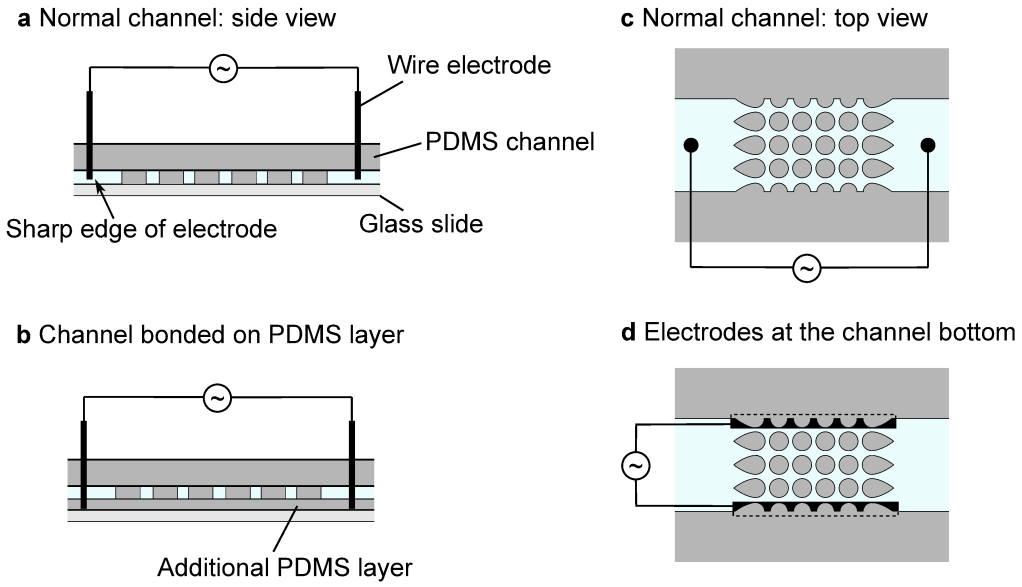

Fig. C.3.: Different electrode arrangements. a) side view and c) top view of normal electrode positions. The wire electrodes only protrude into the channel and the cutting edge of the wire forms a sharp edge. b) The channel was bonded to an additional PDMS layer instead of the glass substrate so that the electrode edge protrudes into the PDMS layer instead of the region through which the fluid flows. d) Arrangement of electrodes sputtered onto the glass slide (channel bottom). The dashed line shows the shape of the electrodes below the patterned PDMS structure.

the PDMS channel was bonded to a PDMS layer instead of a glass slide, and the electrode was inserted protruding into the lower PDMS plate (Fig. C.3 b). Instead of platinum wires, gold electrodes at the bottom of the channel, arranged laterally to the post array, were tested (similar to interdigital electrodes, see Fig. C.3 d). Again, strong vortices emerged, unfavorably located within the post array, which almost completely inhibits the trapping of the particles. No effect on the vortex formation was found when the electrode thickness was changed.

Fluorescence dye experiments

Various fluorescent dyes are used in microfluidics to optically determine medium properties like temperature or pH in the channel. Here, three different dyes were used. The channel was flushed with a solution containing one of the fluorescence dyes at a time with a molar concentration of 10^{-5} M. An overview of the results can be found in Tab. C.2. Rhodamine 6G is a dye with a single positive charge that dissociates completely in water. It indicates local changes in ionic strength

Tab. C.2.: Changes in fluorescence intensity when applying an electric field.

Dye	Live electrode	Grounded electrode	Possible conclusion
Rhodamine 6G	little brighter	much darker	ions are generated at the live electrode
Fluorescein	much darker	much brighter	pH decreases on live electrode
Rhodamine B	little darker	no change	no strong change in temperature

[Gar09; Lei04]; the higher the ionic strength, the stronger the fluorescence. With an increasing medium conductivity, it was observed that the fluorescence increases at the live electrode and decreases at the grounded electrode. From this it can be concluded that the ionic strength at the live electrode increases, e.g., due to the production of ions by electrolysis, and this effect is enhanced with the conductivity of the medium.

Fluorescein is weakly acidic and does not dissociate completely in water. Only the deprotonated form is fluorescent; accordingly, fluorescence increases with increasing pH [Gar09; Fie95]. The fluorescence intensity increases at the grounded electrode and decreases at the live electrode, which also suggests proton production at the live electrode. This effect again increases with the conductivity of the medium. The experiments suggest that electrolysis occurs at the electrodes due to a DC offset. When a bipolar amplifier is used, a reduction in the effects is observed, but vortex-like changes in fluorescence intensity are still clearly visible. The use of capacitors does not lead to any improvement. The vortices could be originated by the electrochemical reactions (Faradaic reactions) at the electrodes. Therefore, one experiment was done with methanol, which cannot be electrolyzed in the absence of water. Also, for methanol, vortex structures from areas where fluorescence intensity decreases or increases were clearly visible and of a similar magnitude as in an aqueous solution. From this, it can be concluded that the color change of fluorescein in the channel is not caused by pH changes due to Faradaic reactions at the electrodes, as assumed. One explanation could be accumulation/depletion of the dye molecules in the liquid.

Rhodamine B is uncharged at pH between 5 and 10 and is therefore used as a neutral current marker [Von96; Gea74; Mil12]. The strength of the fluorescence decreases with increasing temperature. With voltage applied (Fig. C.4, on after 10 s, off after 60 s), a slight decrease in fluorescence intensity at the live electrode and the surrounding medium is observable. A part that can be assumed to be linear is caused by heat input from the illumination (orange line, and its linear regression yellow line). The fluorescence intensity was normalized to the initial intensity (without voltage) and corrected for the photobleaching effect (purple line). The intensity is not calibrated to the temperature change, but Ross et al. [Ros01] gives an order of magnitude of 10%/5 °C between 10 and 40 °C. In this case, a maximum decrease in fluorescence intensity of 0.3%, i.e., about +0.15 °C, can be detected. Without

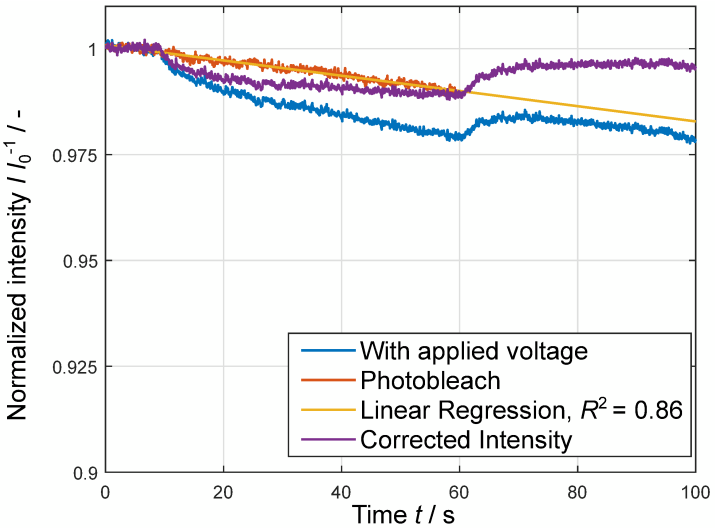

Fig. C.4.: Change of normalized fluorescence intensity with applied electric field and effect of the light source. Here, the case of a non-flowing RhodamineB solution is shown.

pumping the suspension through the channel, it is about 1.2%, which corresponds to a temperature increase of about 0.6 °C. The heat input from the light source appears to be greater than that from Joule Heating. Thus it is assumed that the vortices are not caused by temperature differences.

Coating of the channel

One possible way to reduce electroosmotic flows is the coating of the surfaces with Polyvinylpyrrolidone (PVP) [Mil12]. PVP suppresses electroosmotic flow by adsorbing onto the channel walls and reducing the zeta potential. For the experiments, a 2% w/w PVP (40.000 MW) solution was used to flush the channel for 5 min. After changing to the normal aqueous DEP medium, there should be a residual amount of PVP on all surfaces of the channel and electrodes, which prevents electroosmotic fluid movement. No influence on the vortex size was observable. It can be assumed that the effect due to a thin PVP layer is insufficient to completely prevent electroosmosis, and it is not clear whether a layer also forms on the platinum electrode surface.

C.4 Conclusion

The cause of the vortex formation at the electrodes could not be conclusively determined. The observations and parameter influences do not clearly fit one of the phenomena. Therefore, it is assumed that it could be a combination of several effects and that the dominant effect may change within certain parameter ranges. The observed influence of medium conductivity, frequency, and electric field is most similar to electroosmotic phenomena. For example, a combination of ICEO/CPEO and Faradaic reactions could be possible. A simulation of CPEO could shed light on whether these effects can also appear at electrodes and are sufficiently strong to

dominate the superimposed pressure-driven fluid flow [Cal21]. The asymmetry of the resulting vortices at the live and grounded electrode as well as the experiments with fluorescein could indicate a contribution of Faradaic reactions caused by a DC offset. In this case, a more specific selection of a capacitor via a simulation of an electrical equivalent circuit representing the microchannel could help. Furthermore, the influence of the electrode material on the vortex formation has not yet been investigated. For example, the zeta potential or electronegativity could be relevant here. The zeta potential influences the double layer thickness and thus electroosmotic effects, whereas the electronegativity influences possible Faradaic reactions.

Overview on dielectrophoretic filtration

D

Table starts on the next page due to space limitations.

Tab. D.1.: List of studies investigating DEP filtration (Concept based on Ref. [Pes18a])

Reference	Method	Filter matrix	Electrodes	Particle type	Process parameters	Comments
[Ben82; Lin81; Lin82a; Lin85; Lin82b]	Packed bed	500 μm glass beads	Concentric	Metal oxide powder (50 μm)	60 L h^{-1}, 6 kV_{DC}	Oil, Gulftronic
[Wak03]	Packed bed	500 μm glass beads		PVC (28 μm mean diameter), Test dust (1–100 μm)	180 L h^{-1}, 6–12 kV_{DC}	Oil
[Sis95]	Packed bed	1 mm glass beads	Stainless steel wire mesh at both ends	50 nm and 300 nm SiO_2	6.5–8.5 mL min^{-1} 0–25 kV DC	Tert-amyl alcohol
[Ili07]	Packed bed	100 μm silica beads	Metall mesh electrodes, 1 mm distance	Live and dead yeast	150 V, 10–20 kHz, 0.05–0.2 mL min^{-1}	Aqueous solution, 90% separation
[Sue03]	Packed bed	200 μm glass beads	Parallel plate electrodes	Live and dead yeast	50–140 Vpp, 10 kHz–1 MHz 60–100 mL h^{-1}	Aqueous solution, 100% separation

Reference	Method	Filter matrix	Electrodes	Particle type	Process parameters	Comments
[Lew18]	Packed bed	100 μm silica beads	Metall mesh electrodes, 1 mm distance	Live and dead yeast	600 Vpp, 0.1–10 kHz +50 V_{DC}, 1–5 ml min^{-1}	Aqueous solution, 77% separation
[Li19a]	Packed bed	1.5–4 mm glass beads	Ring shaped copper sheet and bar	Catalyst particles, 3–26 μm	0–10 kV_{DC}	oil
[Isl22]	"Mesh"	Synthetic fiber paper	Copper tape electrodes, 1 mm gap	1 μm PS	Pulsed 2–10 V_{DC} in 100 kHz, 4 μL min^{-1}	Mini, aqueous solution
[San20]	Packed bed	tiny glass beads of borosilicate with 2 mm	Copper electrode sheets 2 mm	Food borne pathogens	5–15 V, 300 kHz–1 MHz, circulated	
[Pes14]	Deep-bed filtration	20–60 μm pore size, Polyethylene filter	Stainless steel plate, 20 mm apart	Polyelectrolyte nanocapsules (300 nm)	200 V, 210 kHz, 30–120 mL h^{-1}	Aqueous solution, 65% separation
[Pes18b; Lor20]	Deep-bed filtration	Monolithic foams (83% porosity, 230 μm $d_{50,3}$)	Stainless steel plate at sides, 8 mm distance	PS particles (4.5 μm), yeast, graphite (3 μm)	1–9 mL min^{-1}, 150–600 V_{rms}, 1–15 kHz	Aqueous solution, 95% separation

Patents						
Reference	Method	Filter matrix	Electrodes	Particle type	Process parameters	Comments
[Cri77a; Cri77b; Fri94]	Packed bed	Glass beads 1/8 inch	central tubular and cylindrical outer electrode	<5 μm, iron sulfide, and oxide	5–20 kV inch^{-1}, 80 gallons min^{-1}	hot refinery streams, radial flow pattern, 90% separation, Backflushing
[Hal00]	Packed bed	Glass beads 2–4 mm	Ring shaped tube	0.01–100 μm particles	2–50 kV inch^{-1}	Liquid silicon
[Ham50]	Packed bed	Vessel with Anion active resin granular material	Platinum electrode	Copper compounds	8 mL min^{-1}, 100–2000 V_{DC}	Liquid hydrocarbon
[Ham51]	Packed bed	Vessel with loosely packed glass, hard rubber or plastic, glass wool fibers		Dirt particles	10–15 kV_{DC}, 10 gallons min^{-1} (2300 L h^{-1})	Dry Cleaning solvent, explanation was unknown

Reference	Method	Filter matrix	Electrodes	Particle type	Process parameters	Comments
[Obe77]	Packed bed	1–13 mm, crushed flint 2.5 mm, marine sand, river gravel	Zigzag path of closely spaced electrodes	Hydrogenation catalysts (nickel)	20–40 kV inch^{-1}, 9 gallons min^{-1} (2000 L h^{-1})	Non-petroleum organic liquids (fats, edible oils ...), prevent abraded material in oil
[Wat67]	Packed bed	Multilayer-filling, filamentary polyurethane foam 1/8 inch	Plate electrodes, small distance	Iron oxide, road dust, filamentary material, Also < 5 μm–100 μm	15 kV, 81 inches min^{-1}	Oil, flow parallel to electrode, replaceable pack
[Wat83]	Packed bed	Polyurethane foam, nylon mesh wrapped in layers or voids	Planar horizontal electrodes, floating electrodes	Fe_2O_3, dust, air filter test dust	1–60 kV_{DC}	Removal filter pack, jet fuels, absorption oils
[Lan79]	Packed bed	flint, garnet, granite and fused quartz, crushed to provide non-spheroidal configurations	Vertically elongated metal tubes	Solid, moisture, and soaps		Non-petroleum organic oils

Reference	Method	Filter matrix	Electrodes	Particle type	Process parameters	Comments
[Shi68]	Packed bed	Wool or fibers, no foam			-20 kV_{DC}	

Bibliography

[Abd13] Bahige G. Abdallah, Tzu-Chiao Chao, Christopher Kupitz, Petra Fromme, and Alexandra Ros. „Dielectrophoretic Sorting of Membrane Protein Nanocrystals“. *ACS Nano* 7.10 (2013), pp. 9129–9137.

[Abi07] Zurina Z. Abidin, Les Downes, and Gerard H. Markx. „Novel Electrode Structures for Large Scale Dielectrophoretic Separations Based on Textile Technology“. *Journal of Biotechnology* 130.2 (2007), pp. 183–187.

[Al-22] Abdulla Al-Ali, Waqas Waheed, Eiyad Abu-Nada, and Anas Alazzam. „A Review of Active and Passive Hybrid Systems Based on Dielectrophoresis for the Manipulation of Microparticles“. *Journal of Chromatography A* 1676 (2022), p. 463268.

[Ald06] Fredrik Aldaeus, Yuan Lin, Gustav Amberg, and Johan Roeraade. „Multi-Step Dielectrophoresis for Separation of Particles“. *Journal of Chromatography A* 1131.1-2 (2006), pp. 261–266.

[Ali18] Elaheh Alidoosti and Hui Zhao. „On the Impact of Electrostatic Correlations on the Double-Layer Polarization of a Spherical Particle in an Alternating Current Field“. *Langmuir* 34.19 (2018), pp. 5592–5599.

[An15] Ran An. „ELECTROCHEMICAL PROCESSES IN MICROFLUIDICS SYSTEMS UNDER AC ELECTRIC FIELDS“. Doctor of Philosophy in Chemical Engineering. Houghton, Michigan: Michigan Technological University, 2015.

[Arg17] Ignacio Arganda-Carreras, Verena Kaynig, Curtis Rueden, Kevin W Eliceiri, Johannes Schindelin, Albert Cardona, and H Sebastian Seung. „Trainable Weka Segmentation: A Machine Learning Tool for Microscopy Pixel Classification“. *Bioinformatics* 33.15 (2017). Ed. by Robert Murphy, pp. 2424–2426.

[Bal10] G.R. Ballantyne and P.N. Holtham. „Application of Dielectrophoresis for the Separation of Minerals“. *Minerals Engineering* 23.4 (2010), pp. 350–358.

[Bal17] Priya Balasubramanian, Robert J. Kinders, Shivaani Kummar, Vishal Gupta, David Hasegawa, Anoop Menachery, Scott M. Lawrence, Lihua Wang, Katherine Ferry-Galow, Darren Davis, Ralph E. Parchment, Joseph E. Tomaszewski, and James H. Doroshow. „Antibody-Independent Capture of Circulating Tumor Cells of Non-Epithelial Origin with the ApoStream® System“. *PLOS ONE* 12.4 (2017), e0175414.

[Bar13] Sutapa Barua, Jin-Wook Yoo, Poornima Kolhar, Aditya Wakankar, Yatin R. Gokarn, and Samir Mitragotri. „Particle Shape Enhances Specificity of Antibody-Displaying Nanoparticles“. *Proceedings of the National Academy of Sciences* 110.9 (2013), pp. 3270–3275.

[Bar94] P. A. Baron, G. J. Deye, and J. Fernback. „Length Separation of Fibers“. *Aerosol Science and Technology* 21.2 (1994), pp. 179–192.

[Baz04] Martin Z. Bazant and Todd M. Squires. „Induced-Charge Electrokinetic Phenomena: Theory and Microfluidic Applications“. *Physical Review Letters* 92.6 (2004), p. 066101.

[Baz11a] Martin Z. Bazant. „Induced-Charge Electrokinetic Phenomena“. *Electrokinetics and Electrohydrodynamics in Microsystems*. Ed. by Antonio Ramos. Vienna: Springer Vienna, 2011, pp. 221–297.

[Baz11b] Martin Z. Bazant, Brian D. Storey, and Alexei A. Kornyshev. „Double Layer in Ionic Liquids: Overscreening versus Crowding“. *Physical Review Letters* 106.4 (2011), p. 046102.

[Bec94] F F Becker, X -B Wang, Y Huang, R Pethig, J Vykoukal, and P R C Gascoyne. „The Removal of Human Leukaemia Cells from Blood Using Interdigitated Microelectrodes“. *Journal of Physics D: Applied Physics* 27.12 (1994), pp. 2659–2662.

[Bec95] F F Becker, X B Wang, Y Huang, R Pethig, J Vykoukal, and P R Gascoyne. „Separation of Human Breast Cancer Cells from Blood by Differential Dielectric Affinity.“ *Proceedings of the National Academy of Sciences* 92.3 (1995), pp. 860–864.

[Beh18] Behrouz Behdani, Saman Monjezi, Mason J. Carey, Curtis G. Weldon, Jie Zhang, Cheng Wang, and Joontaek Park. „Shape-Based Separation of Micro-/Nanoparticles in Liquid Phases“. *Biomicrofluidics* 12.5 (2018), p. 051503.

[Ben82] L. Benguigui and I. J. Lin. „Dielectrophoretic Filtration of Nonconductive Liquids“. *Separation Science and Technology* 17.8 (1982), pp. 1003–1017.

[BI20] Mohamed Zackria Ansar B.I., Vineet Tirth, Caffiyar Mohamed Yousuff, Neeraj Kumar Shukla, Saiful Islam, Kashif Irshad, and K. O. Mohammed Aarif. „Simulation Guided Microfluidic Design for Multitarget Separation Using Dielectrophoretic Principle“. *BioChip Journal* 14.4 (2020), pp. 390–404.

[Bis13] Abhijit Biswas, Alice Corani, Arunkumar Kathiravan, Yingyot Infahsaeng, Arkady Yartsev, Villy Sundstrom, and Swati De. „Control of the Size and Shape of TiO_2 Nanoparticles in Restricted Media“. *Nanotechnology* 24.19 (2013), p. 195601.

[Buc23] Thomas Buchwald, Ralf Ditscherlein, and Urs A. Peuker. „Beschreibung von Trennoperationen mit mehrdimensionalen Partikeleigenschaftsverteilungen“. *Chemie Ingenieur Technik* 95.1-2 (2023), pp. 199–209.

[Cal19] Victor Calero, Pablo Garcia-Sanchez, Antonio Ramos, and Hywel Morgan. „Combining DC and AC Electric Fields with Deterministic Lateral Displacement for Micro- and Nano-Particle Separation“. *Biomicrofluidics* 13.5 (2019), p. 054110.

[Cal21] Víctor Calero, Raúl Fernández-Mateo, Hywel Morgan, Pablo García-Sánchez, and Antonio Ramos. „Stationary Electro-osmotic Flow Driven by Ac Fields around Insulators“. *Physical Review Applied* 15.1 (2021), p. 014047.

[Cam12] Fernanda Camacho-Alanis, Lin Gan, and Alexandra Ros. „Transitioning Streaming to Trapping in DC Insulator-Based Dielectrophoresis for Biomolecules“. *Sensors and Actuators B: Chemical* 173 (2012), pp. 668–675.

[Car20] Braulio Cardenas-Benitez, Binny Jind, Roberto C. Gallo-Villanueva, Sergio O. Martinez-Chapa, Blanca H. Lapizco-Encinas, and Victor H. Perez-Gonzalez. „Direct Current Electrokinetic Particle Trapping in Insulator-Based Microfluidics: Theory and Experiments“. *Analytical Chemistry* 92.19 (2020), pp. 12871–12879.

[Cas03] A. Castellanos, A. Ramos, A. González, N. G. Green, and H. Morgan. „Electrohydrodynamics and Dielectrophoresis in Microsystems: Scaling Laws“. *Journal of Physics D: Applied Physics* 36.20 (2003), pp. 2584–2597.

[Cha13] David Leonard Chapman. „LI. *A Contribution to the Theory of Electrocapillarity*“. *The London, Edinburgh, and Dublin Philosophical Magazine and Journal of Science* 25.148 (1913), pp. 475–481.

[Cha22] Haotian Cha, Hedieh Fallahi, Yuchen Dai, Dan Yuan, Hongjie An, Nam-Trung Nguyen, and Jun Zhang. „Multiphysics Microfluidics for Cell Manipulation and Separation: A Review“. *Lab on a Chip* 22.3 (2022), pp. 423–444.

[Che09a] Kang Ping Chen, Jose Rafael Pacheco, Mark. A. Hayes, and Sarah J. R. Staton. „Insulator-Based Dielectrophoretic Separation of Small Particles in a Sawtooth Channel“. *ELECTROPHORESIS* 30.9 (2009), pp. 1441–1448.

[Che09b] I-Fang Cheng, Victoria E. Froude, Yingxi Zhu, Hsueh-Chia Chang, and Hsien-Chang Chang. „A Continuous High-Throughput Bioparticle Sorter Based on 3D Traveling-Wave Dielectrophoresis“. *Lab on a Chip* 9.22 (2009), p. 3193.

[Che19] Qiaoying Chen and Yong J. Yuan. „A Review of Polystyrene Bead Manipulation by Dielectrophoresis“. *RSC Advances* 9.9 (2019), pp. 4963–4981.

[Che22] Ziying Chen, Zhan Li, Jia Chen, Parashuram Kallem, Fawzi Banat, and Hongdeng Qiu. „Recent Advances in Selective Separation Technologies of Rare Earth Elements: A Review“. *Journal of Environmental Chemical Engineering* 10.1 (2022), p. 107104.

[Cho02] Chia-Fu Chou, Jonas O. Tegenfeldt, Olgica Bakajin, Shirley S. Chan, Edward C. Cox, Nicholas Darnton, Thomas Duke, and Robert H. Austin. „Electrodeless Dielectrophoresis of Single- and Double-Stranded DNA“. *Biophysical Journal* 83.4 (2002), pp. 2170–2179.

[Cho17] Saniat Ahmed Choudhury, Nuzhat Nawshin, and Mustafa Habib Chowdhury. „Influence of Particle Shape on the Efficacy of Plasmonic Metal Nanoparticles to Enhance the Energy Conversion Efficiency of Thin-Film Solar Cells“. *TENCON 2017 - 2017 IEEE Region 10 Conference*. Penang: IEEE, 2017, pp. 2393–2398.

[Cho88] Ross S Chow and Koichi Takamura. „Effects of Surface Roughness (Hairiness) of Latex Particles on Their Electrokinetic Potentials“. *Journal of Colloid and Interface Science* 125.1 (1988), pp. 226–236.

[Cit15] Morgane Citeau, Olivier Larue, and Eugene Vorobiev. „Electric (Electro/Dielectro-Phoretic)—Force Field Assisted Separators“. *Progress in Filtration and Separation*. Elsevier, 2015, pp. 325–397.

[Coe14] Stijn Coertjens, Paula Moldenaers, Jan Vermant, and Lucio Isa. „Contact Angles of Microellipsoids at Fluid Interfaces“. *Langmuir : the ACS journal of surfaces and colloids* 30.15 (2014), pp. 4289–4300.

[Col20] Adriana Coll De Peña, Abbi Miller, Cody J. Lentz, Nicole Hill, Anutthaman Parthasarathy, André O. Hudson, and Blanca H. Lapizco-Encinas. „Creation of an Electrokinetic Characterization Library for the Detection and Identification of Biological Cells“. *Analytical and Bioanalytical Chemistry* 412.16 (2020), pp. 3935–3945.

[Con17] Catia Contado. „Field Flow Fractionation Techniques to Explore the “Nano-World”“. *Analytical and Bioanalytical Chemistry* 409.10 (2017), pp. 2501–2518.

[Cri77a] James H. Crissman and Ray G. Fritsche. „Filtering Process“. 4009089. 1977.

[Cri77b] James H. Crissman, Ray G. Fritsche, Frederick B. Hamel, and Lloyd W. Hilty. „Radial Flow Electrostatic Filter“. 4059498. 1977.

[Cro17] Claire V. Crowther and Mark A. Hayes. „Refinement of Insulator-Based Dielectrophoresis“. *The Analyst* 142.9 (2017), pp. 1608–1618.

[Cum00] Eric B. Cummings and Anup K. Singh. „Dielectrophoretic Trapping without Embedded Electrodes“. *Conference on Microfluidic Devices and Systems III*. Ed. by Carlos H. Mastrangelo and Holger Becker. Vol. 4177. Santa Clara CA: International Society for Optics and Photonics, 2000, pp. 164–173.

[Cum03] Eric B. Cummings and Anup K. Singh. „Dielectrophoresis in Microchips Containing Arrays of Insulating Posts: Theoretical and Experimental Results“. *Analytical Chemistry* 75.18 (2003), pp. 4724–4731.

[Dav86] Joe M. Davis and J. Calvin Giddings. „Feasibility Study of Dielectrical Field-Flow Fractionation“. *Separation Science and Technology* 21.9 (1986), pp. 969–989.

[Deb23] P. Debye and E. Hückel. „Zur Theorie Der Elektrolyte. I. Gefrierpunktserniedrigung Und Verwandte Erscheinungen“. *Physikal. Zeitschr.* 24.185 (1923), p. 305.

[Del07] A.V. Delgado, F. González-Caballero, R.J. Hunter, L.K. Koopal, and J. Lyklema. „Measurement and Interpretation of Electrokinetic Phenomena“. *Journal of Colloid and Interface Science* 309.2 (2007), pp. 194–224.

[Der21] Reza Derakhshan, Arash Mahboubidoust, and Abas Ramiar. „Design of a Novel Optimized Microfluidic Channel for CTCs Separation Utilizing a Combination of TSAWs and DEP Methods“. *Chemical Engineering and Processing - Process Intensification* 167 (2021), p. 108544.

[Dic01] M.E. Dickinson, G. Bearman, S. Tille, R. Lansford, and S.E. Fraser. „Multi-Spectral Imaging and Linear Unmixing Add a Whole New Dimension to Laser Scanning Fluorescence Microscopy“. *BioTechniques* 31.6 (2001), pp. 1272–1278.

[Din17] Jie Ding, Christine Woolley, and Mark A. Hayes. „Biofluid Pretreatment Using Gradient Insulator-Based Dielectrophoresis: Separating Cells from Biomarkers“. *Analytical and Bioanalytical Chemistry* 409.27 (2017), pp. 6405–6414.

[Don20] Qiaoqiao Dong, Yuchang Su, Yanzi Liu, Jing Zhang, Hongzhi Zhang, and Congcong Shi. „Effects of Particle Size on the Electrical Properties of NdFeO3 Nanoparticles“. *Journal of Materials Science: Materials in Electronics* 31.24 (2020), pp. 21913–21922.

[Du08] F. Du, M. Baune, A. Kück, and J. Thöming. „Dielectrophoretic Gold Particle Separation“. *Separation Science and Technology* 43.15 (2008), pp. 3842–3855.

[DuB14] John DuBose, Xinyu Lu, Saurin Patel, Shizhi Qian, Sang Woo Joo, and Xiangchun Xuan. „Microfluidic Electrical Sorting of Particles Based on Shape in a Spiral Microchannel“. *Biomicrofluidics* 8.1 (2014), p. 014101.

[Erm05] Irina Ermolina and Hywel Morgan. „The Electrokinetic Properties of Latex Particles: Comparison of Electrophoresis and Dielectrophoresis“. *Journal of Colloid and Interface Science* 285.1 (2005), pp. 419–428.

[Fan06] D. L. Fan, F. Q. Zhu, R. C. Cammarata, and C. L. Chien. „Efficiency of Assembling of Nanowires in Suspension by Ac Electric Fields“. *Applied Physics Letters* 89.22 (2006), p. 223115.

[Fer21] Raúl Fernández-Mateo, Pablo García-Sánchez, Víctor Calero, Hywel Morgan, and Antonio Ramos. „Stationary Electro-Osmotic Flow Driven by AC Fields around Charged Dielectric Spheres“. *Journal of Fluid Mechanics* 924 (2021), R2.

[Fer23] Raúl Fernández-Mateo, Hywel Morgan, Antonio Ramos, and Pablo García-Sánchez. „Wall Repulsion during Electrophoresis: Testing the Theory of Concen-Tration-Polarization Electro-Osmosis“. *Physics of Fluids* 35.1 (2023), p. 012019.

[Fie95] Stefan. Fiedler, Rolf. Hagedorn, Thomas. Schnelle, Ekkehard. Richter, Bernd. Wagner, and Guenter. Fuhr. „Diffusional Electrotitration: Generation of pH Gradients over Arrays of Ultramicroelectrodes Detected by Fluorescence“. *Analytical Chemistry* 67.5 (1995), pp. 820–828.

[Fla17] F. Flach, S. Breitung-Faes, and A. Kwade. „Grinding Media Wear Induced Agglomeration of Electrosteric Stabilized Particles“. *Colloids and Surfaces A: Physicochemical and Engineering Aspects* 522 (2017), pp. 140–151.

[Fló10] Laura V. Flórez. „Uptake of Ellipsoidal Polystyrene Nanoparticles in Human“. PhD thesis. Universidad de Los Andes Bogotá, Colombia, 2010.

[Flo12] Laura V. Florez, Christine Herrmann, Jens M. Cramer, Christoph P. Hauser, Kaloian Koynov, Katharina Landfester, Daniel Crespy, and Volker Mailänder. „How Shape Influences Uptake: Interactions of Anisotropic Polymer Nanoparticles and Human Mesenchymal Stem Cells“. *Small* 8.14 (2012), pp. 2222–2230.

[Fre20] M. Frei and F.E. Kruis. „Image-Based Size Analysis of Agglomerated and Partially Sintered Particles via Convolutional Neural Networks“. *Powder Technology* 360 (2020), pp. 324–336.

[Fri00] Sheldon K. Friedlander. *Smoke, Dust, and Haze: Fundamentals of Aerosol Dynamics*. 2nd ed. Topics in Chemical Engineering. New York: Oxford University Press, 2000.

[Fri94] Ray G. Fritsche, Roko S. Bujas V, and Giovanni C. Caprioglio. „Electrostatic Separator Using a Bead Bed“. 5308586. 1994.

[Gad06] Nitzan Gadish and Joel Voldman. „High-Throughput Positive-Dielectrophoretic Bioparticle Microconcentrator“. *Analytical Chemistry* 78.22 (2006), pp. 7870–7876.

[Gal19] Roberto C. Gallo-Villanueva, Victor H. Perez-Gonzalez, Braulio Cardenas-Benitez, Binny Jind, Sergio O. Martinez-Chapa, and Blanca H. Lapizco-Encinas. „Joule Heating Effects in Optimized Insulator-based Dielectrophoretic Devices: An Interplay between Post Geometry and Temperature Rise“. *ELECTROPHORESIS* 40.10 (2019), pp. 1408–1416.

[Gam86] N. I. Gamayunov, V. A. Murtsovkin, and A. S. Dukhin. „Pair Interaction of Particles in Electric Field. 1. Features of Hydrodynamic Interaction of Polarized Particles“. *Colloid J. USSR (Engl. Transl.)* 48:2 (1986).

[Gar09] P. García-Sánchez, A. Ramos, A. González, N. G. Green, and H. Morgan. „Flow Reversal in Traveling-Wave Electrokinetics: An Analysis of Forces Due to Ionic Concentration Gradients“. *Langmuir* 25.9 (2009), pp. 4988–4997.

[Gar12] Pablo García-Sánchez, Yukun Ren, Juan J. Arcenegui, Hywel Morgan, and Antonio Ramos. „Alternating Current Electrokinetic Properties of Gold-Coated Microspheres“. *Langmuir* 28.39 (2012), pp. 13861–13870.

[Gar76] M. J. Garvey, Th F. Tadros, and B. Vincent. „A Comparison of the Adsorbed Layer Thickness Obtained by Several Techniques of Various Molecular Weight Fractions of Poly(Vinyl Alcohol) on Aqueous Polystyrene Latex Particles“. *Journal of Colloid And Interface Science* 55.2 (1976), pp. 440–453.

[Gas02] Peter R. C. Gascoyne and Jody Vykoukal. „Particle Separation by Dielectrophoresis“. *ELECTROPHORESIS* 23.13 (2002), p. 1973.

[Gas09] Peter R. C. Gascoyne, Jamileh Noshari, Thomas J. Anderson, and Frederick F. Becker. „Isolation of Rare Cells from Cell Mixtures by Dielectrophoresis“. *ELECTROPHORESIS* 30.8 (2009), pp. 1388–1398.

[Gas14] Peter Gascoyne and Sangjo Shim. „Isolation of Circulating Tumor Cells by Dielectrophoresis“. *Cancers* 6.1 (2014), pp. 545–579.

[Gas92] P R C Gascoyne, Ying Huang, R Pethig, J Vykoukal, and F F Becker. „Dielectrophoretic Separation of Mammalian Cells Studied by Computerized Image Analysis“. *Measurement Science and Technology* 3.5 (1992), pp. 439–445.

[Gea74] Adrian R.L. Gear. „Rhodamine 6G“. *Journal of Biological Chemistry* 249.11 (1974), pp. 3628–3637.

[Gen11] Aytug Gencoglu, Fernanda Camacho-Alanis, Vi Thanh Nguyen, Asuka Nakano, Alexandra Ros, and Adrienne R. Minerick. „Quantification of pH Gradients and Implications in Insulator-Based Dielectrophoresis of Biomolecules“. *Electrophoresis* 32.18 (2011), pp. 2436–2447.

[Gen14] Aytug Gencoglu, David Olney, Alexandra LaLonde, Karuna S. Koppula, and Blanca H. Lapizco-Encinas. „Dynamic Microparticle Manipulation with an Electroosmotic Flow Gradient in Low-Frequency Alternating Current Dielectrophoresis: Microfluidics and Miniaturization“. *ELECTROPHORESIS* 35.2-3 (2014), pp. 362–373.

[Gen19] Yangye Geng, Zhen Zhu, Yingying Wang, Yiyun Wang, Shuiping Ouyang, Ke Zheng, Wenbo Ye, Yimin Fan, Zixin Wang, and Dejing Pan. „Multiplexing Microelectrodes for Dielectrophoretic Manipulation and Electrical Impedance Measurement of Single Particles and Cells in a Microfluidic Device“. *ELECTROPHORESIS* 40.10 (2019), pp. 1436–1445.

[Gho23] Taher Ghomian and Joshua Hihath. „Review of Dielectrophoretic Manipulation of Micro and Nanomaterials: Fundamentals, Recent Developments, and Challenges“. *IEEE Transactions on Biomedical Engineering* 70.1 (2023), pp. 27–41.

[Gid84] J. Calvin Giddings. „Giddings, J. Calvin. "Two-dimensional Separations: Concept and Promise."“ *Analytical chemistry* 56.12 (1984), 1258A–1270A.

[Gid87] J. C. Giddings. „Concepts and Comparisons in Multidimensional Separation“. *Journal of High Resolution Chromatography* 10.5 (1987), pp. 319–323.

[Gie19] Jasper Giesler, Georg R. Pesch, Laura Weirauch, Marc-Peter Schmidt, Jorg Thöming, and Michael Baune. „Polarizability-Dependent Sorting of Microparticles Using Continuous-Flow Dielectrophoretic Chromatography with a Frequency Modulation Method“. *Micromachines* 11.1 (2019), p. 38.

[Gie21] Jasper Giesler, Laura Weirauch, Jorg Thöming, Michael Baune, and Georg R. Pesch. „Separating Microparticles by Material and Size Using Dielectrophoretic Chromatography with Frequency Modulation“. *Scientific Reports* 11.1 (2021), p. 16861.

[Gie23] Jasper Giesler, Laura Weirauch, Jorg Thöming, Michael Baune, and Georg R. Pesch. „High-throughput Dielectrophoretic Separator Based on Printed Circuit Boards“. *ELECTROPHORESIS* 44.1-2 (2023), pp. 72–81.

[Goa97] Andrew D Goater, Julian P H Burt, and Ronald Pethig. „A Combined Travelling Wave Dielectrophoresis and Electrorotation Device: Applied to the Concentration and Viability Determination of *Cryptosporidium*“. *Journal of Physics D: Applied Physics* 30.18 (1997), pp. L65–L69.

[Gou10] M. Gouy. „Sur la constitution de la charge électrique à la surface d'un électrolyte“. *Journal de Physique Théorique et Appliquée* 9.1 (1910), pp. 457–468.

[Gre00] Nicolas G Green, Antonio Ramos, Antonio González, Antonio Castellanos, and Hywel Morgan. „Electric Field Induced Fluid Flow on Microelectrodes: The Effect of Illumination“. *Journal of Physics D: Applied Physics* 33.2 (2000), pp. L13–L17.

[Gre99] Nicolas G. Green and Hywel Morgan. „Dielectrophoresis of Submicrometer Latex Spheres. 1. Experimental Results“. *The Journal of Physical Chemistry B* 103.1 (1999), pp. 41–50.

[Guo22] Wenshang Guo, Ye Tao, Weiyu Liu, Chunlei Song, Jian Zhou, Hongyuan Jiang, and Yukun Ren. „A Visual Portable Microfluidic Experimental Device with Multiple Electric Field Regulation Functions“. *Lab on a Chip* 22.8 (2022), pp. 1556–1564.

[Hal00] Roland Lee Halm and Keith Quentin Hayes II. „Method for Removing Particulate from a Liquid Silicon Containing Compound“. 6126803. 2000.

[Ham50] Garnet Philip Ham and Robert Bowling Barnes. „Process of Purifying Hydrocarbon Liquids“. 2534907. 1950.

[Ham51] Frederick Henry Hamlin. „Electrical Precipitation Method“. 2573967. 1951.

[Han09] Ki-Ho Han, Song-I Han, and A. Bruno Frazier. „Lateral Displacement as a Function of Particle Size Using a Piecewise Curved Planar Interdigitated Electrode Array“. *Lab on a Chip* 9.20 (2009), p. 2958.

[Haw10] Benjamin G. Hawkins and Brian J. Kirby. „Electrothermal Flow Effects in Insulating (Electrodeless) Dielectrophoresis Systems“. *ELECTROPHORESIS* 31.22 (2010), pp. 3622–3633.

[Hel53] H. Helmholtz. „Ueber einige Gesetze der Vertheilung elektrischer Ströme in körperlichen Leitern mit Anwendung auf die thierisch-elektrischen Versuche“. *Annalen der Physik und Chemie* 165.6 (1853), pp. 211–233.

[Hen22] Anders Henriksson, Peter Neubauer, and Mario Birkholz. „Dielectrophoresis: An Approach to Increase Sensitivity, Reduce Response Time and to Suppress Nonspecific Binding in Biosensors?“ *Biosensors* 12.10 (2022), p. 784.

[Hid19] Samuel Hidalgo-Caballero, Cody Justice Lentz, and Blanca H. Lapizco-Encinas. „Assessment of Submicron Particle Zeta Potential in Simple Electrokinetic Microdevices“. *Electrophoresis* 40.10 (2019), pp. 1395–1399.

[Hil19] Nicole Hill and Blanca H. Lapizco-Encinas. „On the Use of Correction Factors for the Mathematical Modeling of Insulator Based Dielectrophoretic Devices“. *ELECTROPHORESIS* 40.18-19 (2019), pp. 2541–2552.

[Hil20] Nicole Hill and Blanca H. Lapizco-Encinas. „Continuous Flow Separation of Particles with Insulator-Based Dielectrophoresis Chromatography“. *Analytical and Bioanalytical Chemistry* 412.16 (2020), pp. 3891–3902.

[Ho07] Chia-Chi Ho. „Chapter 7 - Membranes for Bioseparations“. *Bioprocessing for Value-Added Products from Renewable Resources*. Ed. by Shang-Tian Yang. Amsterdam: Elsevier, 2007, pp. 163–183.

[Ho20] Bao Ho, Jason Beech, and Jonas Tegenfeldt. „Charge-Based Separation of Micro- and Nanoparticles“. *Micromachines* 11.11 (2020), p. 1014.

[Ho93] C. C. Ho, A. Keller, J. A. Odell, and R. H. Ottewill. „Preparation of Monodisperse Ellipsoidal Polystyrene Particles“. *Colloid & Polymer Science* 271.5 (1993), pp. 469–479.

[Hon11a] T. Honegger, K. Berton, E. Picard, and D. Peyrade. „Determination of Clausius–Mossotti Factors and Surface Capacitances for Colloidal Particles“. *Applied Physics Letters* 98.18 (2011), p. 181906.

[Hon11b] F.J. Hong, J. Cao, and P. Cheng. „A Parametric Study of AC Electrothermal Flow in Microchannels with Asymmetrical Interdigitated Electrodes“. *International Communications in Heat and Mass Transfer* 38.3 (2011), pp. 275–279.

[Hua09] Kui Huang, Jie Guo, and Zhenming Xu. „Recycling of Waste Printed Circuit Boards: A Review of Current Technologies and Treatment Status in China“. *Journal of Hazardous Materials* 164.2-3 (2009), pp. 399–408.

[Hua93] Y Huang, X -B Wang, J A Tame, and R Pethig. „Electrokinetic Behaviour of Colloidal Particles in Travelling Electric Fields: Studies Using Yeast Cells“. *Journal of Physics D: Applied Physics* 26.9 (1993), pp. 1528–1535.

[Hua97] Y. Huang, X.B. Wang, F.F. Becker, and P.R. Gascoyne. „Introducing Dielectrophoresis as a New Force Field for Field-Flow Fractionation“. *Biophysical Journal* 73.2 (1997), pp. 1118–1129.

[Hug03] Michael P. Hughes. *Nanoelectromechanics in Engineering and Biology*. Nano- and Microscience, Engineering, Technology, and Medicine Series. Boca Raton: CRC Press, 2003.

[Hug16] Michael P. Hughes. „Fifty Years of Dielectrophoretic Cell Separation Technology“. *Biomicrofluidics* 10.3 (2016), p. 032801.

[Hug99] Michael P. Hughes, Hywel Morgan, and Mary F. Flynn. „The Dielectrophoretic Behavior of Submicron Latex Spheres: Influence of Surface Conductance“. *Journal of Colloid and Interface Science* 220.2 (1999), pp. 454–457.

[Ili07] Ciprian Iliescu, Guo Lin Xu, Poh Lam Ong, and Kwong Joo Leck. „Dielectrophoretic Separation of Biological Samples in a 3D Filtering Chip“. *Journal of Micromechanics and Microengineering* 17.7 (2007), S128–S136.

[Inc16] Polysciences Inc. *Technical Data Sheet 788: Polybead® Microspheres*. 2016.

[Inc18] Polysciences Inc. *Technical Data Sheet 1002: Functionalized Polybead® and Fluoresbrite® Microspheres*. 2018.

[Inc23] The MathWorks Inc. *Color-Based Segmentation Using the L*a*b* Color Space - MATLAB & Simulink - MathWorks Deutschland*. https://de.mathworks.com/help/images/color-based-segmentation-using-the-l-a-b-color-space.html. 2023.

[Isl22] Md Nazibul Islam and Zachary Gagnon. *Dielectrophoretic Trapping in Paper: Paper-based Electric Field Gradients for High-Throughput Particle Trapping*. Preprint. 2022.

[Jel09] L. C. Jellema, T. Mey, S. Koster, and E. Verpoorte. „Charge-Based Particle Separation in Microfluidic Devices Using Combined Hydrodynamic and Electrokinetic Effects“. *Lab on a Chip* 9.13 (2009), p. 1914.

[Jen09] Chun-Ping Jen and Teng-Wen Chen. „Selective Trapping of Live and Dead Mammalian Cells Using Insulator-Based Dielectrophoresis within Open-Top Microstructures“. *Biomedical Microdevices* 11.3 (2009), pp. 597–607.

[Jen10] Chun-Ping Jen, Ching-Te Huang, and Hsin-Yuan Shih. „Hydrodynamic Separation of Cells Utilizing Insulator-Based Dielectrophoresis“. *Microsystem Technologies* 16.7 (2010), pp. 1097–1104.

[Jia15] Yankai Jia, Yukun Ren, and Hongyuan Jiang. „Continuous Dielectrophoretic Particle Separation Using a Microfluidic Device with 3D Electrodes and Vaulted Obstacles: Microfluidics and Miniaturization“. *ELECTROPHORESIS* 36.15 (2015), pp. 1744–1753.

[Jon15] Paul V. Jones and Mark A. Hayes. „Development of the Resolution Theory for Gradient Insulator-Based Dielectrophoresis: General“. *ELECTROPHORESIS* 36.9-10 (2015), pp. 1098–1106.

[Jon17] Paul V. Jones, Gabriel L. Salmon, and Alexandra Ros. „Continuous Separation of DNA Molecules by Size Using Insulator-Based Dielectrophoresis“. *Analytical Chemistry* 89.3 (2017), pp. 1531–1539.

[Jon79] Thomas B. Jones. „Dielectrophoretic Force Calculation“. *Journal of Electrostatics* 6.1 (1979), pp. 69–82.

[Jon95] Thomas B. Jones. „Orientation of Nonspherical Particles“. *Electromechanics of Particles*. Cambridge: Cambridge University Press, 1995, pp. 110–138.

[Jon96] Thomas B. Jones and Masao Washizu. „Multipolar Dielectrophoretic and Electrorotation Theory“. *Journal of Electrostatics* 37.1-2 (1996), pp. 121–134.

[Kik18] Kruthika Kikkeri, Maria Virginia Riquelme Breazeal, Xiang Ren, Amy Pruden, and Masoud Agah. „A Monolithic Dielectrophoresis Chip With Impedimetric Sensing for Assessment of Pathogen Viability“. *Journal of Microelectromechanical Systems* 27.5 (2018), pp. 810–817.

[Kik20] Kinga Kik, Bożena Bukowska, and Paulina Sicińska. „Polystyrene Nanoparticles: Sources, Occurrence in the Environment, Distribution in Tissues, Accumulation and Toxicity to Various Organisms“. *Environmental Pollution* 262 (2020), p. 114297.

[Kim08] Unyoung Kim, Jiangrong Qian, Sophia A. Kenrick, Patrick S. Daugherty, and H. Tom Soh. „Multitarget Dielectrophoresis Activated Cell Sorter“. *Analytical Chemistry* 80.22 (2008), pp. 8656–8661.

[Kim09] Unyoung Kim and H. Tom Soh. „Simultaneous Sorting of Multiple Bacterial Targets Using Integrated Dielectrophoretic–Magnetic Activated Cell Sorter“. *Lab on a Chip* 9.16 (2009), p. 2313.

[Kim19] Daihyun Kim, Mukul Sonker, and Alexandra Ros. „Dielectrophoresis: From Molecular to Micrometer-Scale Analytes“. *Analytical Chemistry* 91.1 (2019), pp. 277–295.

[Kir10] Brian J. Kirby. *Micro- and Nanoscale Fluid Mechanics: Transport in Microfluidic Devices*. New York: Cambridge University Press, 2010.

[Koh07] Daniel S. Kohane. „Microparticles and Nanoparticles for Drug Delivery“. *Biotechnology and Bioengineering* 96.2 (2007), pp. 203–209.

[Kor07] Alexei A. Kornyshev. „Double-Layer in Ionic Liquids: Paradigm Change?“ *The Journal of Physical Chemistry B* 111.20 (2007), pp. 5545–5557.

[Kra06] Jason G. Kralj, Michael T. W. Lis, Martin A. Schmidt, and Klavs F. Jensen. „Continuous Dielectrophoretic Size-Based Particle Sorting“. *Analytical Chemistry* 78.14 (2006), pp. 5019–5025.

[Kum10] Latha Kumari, W.Z. Li, Charles H. Vannoy, Roger M. Leblanc, and D.Z. Wang. „Zinc Oxide Micro- and Nanoparticles: Synthesis, Structure and Optical Properties“. *Materials Research Bulletin* 45.2 (2010), pp. 190–196.

[LaL14] Alexandra LaLonde, Aytug Gencoglu, Maria F. Romero-Creel, Karuna S. Koppula, and Blanca H. Lapizco-Encinas. „Effect of Insulating Posts Geometry on Particle Manipulation in Insulator Based Dielectrophoretic Devices“. *Journal of Chromatography A* 1344 (2014), pp. 99–108.

[Lan79] Joel V. Landis. „Quality Improvement Process for Organic Liquid“. 4155924. 1979.

[Lap04] Blanca H. Lapizco-Encinas, Blake A. Simmons, Eric B. Cummings, and Yolanda Fintschenko. „Insulator-Based Dielectrophoresis for the Selective Concentration and Separation of Live Bacteria in Water“. *Electrophoresis* 25.1011 (2004), pp. 1695–1704.

[Lap05] Blanca H. Lapizco-Encinas, Rafael V. Davalos, Blake A. Simmons, Eric B. Cummings, and Yolanda Fintschenko. „An Insulator-Based (Electrodeless) Dielectrophoretic Concentrator for Microbes in Water“. *Journal of Microbiological Methods* 62.3 (2005), pp. 317–326.

[Lap19] Blanca H. Lapizco-Encinas. „On the Recent Developments of Insulator-based Dielectrophoresis: A Review“. *ELECTROPHORESIS* 40.3 (2019), pp. 358–375.

[Lap22] Blanca H. Lapizco-Encinas. „The Latest Advances on Nonlinear Insulator-Based Electrokinetic Microsystems under Direct Current and Low-Frequency Alternating Current Fields: A Review“. *Analytical and Bioanalytical Chemistry* 414.2 (2022), pp. 885–905.

[Las04] Dmitri Lastochkin, Ronghui Zhou, Ping Wang, Yuxing Ben, and Hsueh-Chia Chang. „Electrokinetic Micropump and Micromixer Design Based on Ac Faradaic Polarization“. *Journal of Applied Physics* 96.3 (2004), pp. 1730–1733.

[Lei04] Felix C. Leinweber and Ulrich Tallarek. „Nonequilibrium Electrokinetic Effects in Beds of Ion-Permselective Particles“. *Langmuir* 20.26 (2004), pp. 11637–11648.

[Len19] Cody J. Lentz, Samuel Hidalgo-Caballero, and Blanca H. Lapizco-Encinas. „Low Frequency Cyclical Potentials for Fine Tuning Insulator-Based Dielectrophoretic Separations“. *Biomicrofluidics* 13.4 (2019), p. 044114.

[Lev05] Jeremy A. Levitan, Shankar Devasenathipathy, Vincent Studer, Yuxing Ben, Todd Thorsen, Todd M. Squires, and Martin Z. Bazant. „Experimental Observation of Induced-Charge Electro-Osmosis around a Metal Wire in a Microchannel“. *Colloids and Surfaces A: Physicochemical and Engineering Aspects* 267.1-3 (2005), pp. 122–132.

[Lew14] Nuttawut Lewpiriyawong and Chun Yang. „Continuous Separation of Multiple Particles by Negative and Positive Dielectrophoresis in a Modified H-filter: Microfluidics and Miniaturization“. *ELECTROPHORESIS* 35.5 (2014), pp. 714–720.

[Lew18] Nuttawut Lewpiriyawong, Guolin Xu, and Chun Yang. „Enhanced Cell Trapping Throughput Using DC-biased AC Electric Field in a Dielectrophoresis-Based Fluidic Device with Densely Packed Silica Beads“. *ELECTROPHORESIS* 39.5-6 (2018), pp. 878–886.

[Li19a] Qiang Li, Zhijun Wu, Zhe Zhang, Zhenbo Wang, Linfei Guo, and Anmeng Li. „Experimental Study on the Removal of FCCS Catalyst Particles by Electrostatic Separation“. *Energy Sources, Part A: Recovery, Utilization, and Environmental Effects* (2019), pp. 1–13.

[Li19b] Qiang Li, Zhe Zhang, Zhijun Wu, Zhenbo Wang, and Linfei Guo. „Effects of Electrostatic Field and Operating Parameters on Removing Catalytic Particles from FCCS“. *Powder Technology* 342 (2019), pp. 817–828.

[Li20] Qiang Li, Anmeng Li, Linfei Guo, Hao Cao, Weiwei Xu, and Zhenbo Wang. „Microscopic Mechanistic Study on the Removal of Catalyst Particles in FCCS by an Electrostatic Field“. *Powder Technology* 363 (2020), pp. 500–508.

[Li21] Yalin Li, Yan Wang, Keming Wan, Mingxue Wu, Lei Guo, Xiaomin Liu, and Gang Wei. „On the Design, Functions, and Biomedical Applications of High-Throughput Dielectrophoretic Micro-/Nanoplatforms: A Review“. *Nanoscale* 13.8 (2021), pp. 4330–4358.

[Li23a] Qiang Li, Hao Cao, Qingzhu Qiu, Linfei Guo, Anmeng Li, Weiwei Xu, and Zhenbo Wang. „Experimental Study on the Removal of FCCS Catalyst Particles by the Coupling Interaction of the Electrostatic Field and Flow Field“. *Petroleum Science and Technology* 41.4 (2023), pp. 457–476.

[Li23b] Qiang Li, Qing-Zhu Qiu, Hao Cao, Hui-Zhen Yang, Wei-Wei Xu, and Zhao-Zeng Liu. „Effects of the Properties of FCCS on the Removing of Catalyst Particles from FCCS under a DC Electrostatic Field“. *Petroleum Science* 20.3 (2023), pp. 1885–1894.

[Lim08] Jit Kang Lim, Alexander Eggeman, Frederick Lanni, Robert D. Tilton, and Sara A. Majetich. „Synthesis and Single-Particle Optical Detection of Low-Polydispersity Plasmonic-Superparamagnetic Nanoparticles“. *Advanced Materials* 20.9 (2008), pp. 1721–1726.

[Lin81] I. J. Lin and L. Benguigui. „Dielectrophoretic Filtration and Separation: General Outlook“. *Separation and Purification Methods* 10.1 (1981), pp. 53–72.

[Lin82a] I. J. Lin and L. Benguigui. „Dielectrophoretic Filtration of Liquids. II. Conducting Liquids“. *Separation Science and Technology* 17.5 (1982), pp. 645–654.

[Lin82b] I.J. Lin and L. Benguigui. „High-Intensity, High-Gradient Electric Separation and Dielectric Filtration of Particulate and Granular Materials“. *Journal of Electrostatics* 13.3 (1982), pp. 257–278.

[Lin85] I. J. Lin and L. Benguigui. „Dielectrophoretic Filtration in Time-Dependent Fields“. *Separation Science and Technology* 20.5-6 (1985), pp. 359–376.

[Liu19] Linbo Liu, Ke Chen, Nan Xiang, and Zhonghua Ni. „Dielectrophoretic Manipulation of Nanomaterials: A Review“. *Electrophoresis* 40.6 (2019), pp. 873–889.

[Lor20] Malte Lorenz, Daniel Malangré, Fei Du, Michael Baune, Jorg Thöming, and Georg R. Pesch. „High-Throughput Dielectrophoretic Filtration of Sub-Micron and Micro Particles in Macroscopic Porous Materials“. *Analytical and Bioanalytical Chemistry* 412.16 (2020), pp. 3903–3914.

[Lor21] Malte Lorenz. „Dielectrophoretic Filtration of Particles in Porous Media: Concept, Design, and Selectivity“. PhD thesis. Universität Bremen, 2021.

[Luo16] Jinghui Luo, Katherine A. Muratore, Edgar A. Arriaga, and Alexandra Ros. „Deterministic Absolute Negative Mobility for Micro- and Submicrometer Particles Induced in a Microfluidic Device“. *Analytical Chemistry* 88.11 (2016), pp. 5920–5927.

[Lyk95] J. Lyklema. *Fundamentals of Interface and Colloid Science Vol. II: Solid-liquid Interfaces*. London: Academic Press, 1995.

[Mal21] Amirreza Malekanfard, Zhijian Liu, Le Song, Akshay Kale, Cheng Zhang, Liandong Yu, Yongxin Song, and Xiangchun Xuan. „Joule Heating-enabled Electrothermal Enrichment of Nanoparticles in Insulator-based Dielectrophoretic Microdevices“. *ELECTROPHORESIS* 42.5 (2021), pp. 626–634.

[Mar22] Rodrigo Martinez-Duarte. „A Critical Review on the Fabrication Techniques That Can Enable Higher Throughput in Dielectrophoresis Devices“. *ELECTROPHORESIS* 43.1-2 (2022), pp. 232–248.

[Mar94] Gerard H. Markx, Mark S. Talary, and Ronald Pethig. „Separation of Viable and Non-Viable Yeast Using Dielectrophoresis“. *Journal of Biotechnology* 32.1 (1994), pp. 29–37.

[Mar96] Gerard H. Markx, Penelope A. Dyda, and Ronald Pethig. „Dielectrophoretic Separation of Bacteria Using a Conductivity Gradient“. *Journal of Biotechnology* 51.2 (1996), pp. 175–180.

[Mas06] Jacob H. Masliyah and Subir Bhattacharjee. *Electrokinetic and Colloid Transport Phenomena*. Hoboken, N.J: Wiley-Interscience, 2006.

[Mil12] Denitsa Milanova, Robert D. Chambers, Supreet S. Bahga, and Juan G. Santiago. „Effect of PVP on the Electroosmotic Mobility of Wet-Etched Glass Microchannels: Microfluidics and Miniaturization". *ELECTROPHORESIS* 33.21 (2012), pp. 3259–3262.

[Mis10] Nataliya A. Mishchuk. „Concentration Polarization of Interface and Non-Linear Electrokinetic Phenomena". *Advances in Colloid and Interface Science* 160.1-2 (2010), pp. 16–39.

[Miz00] A. Mizuno. „Electrostatic Precipitation". *IEEE Transactions on Dielectrics and Electrical Insulation* 7.5 (2000), pp. 615–624.

[Mod19] Paresa Modarres and Maryam Tabrizian. „Frequency Hopping Dielectrophoresis as a New Approach for Microscale Particle and Cell Enrichment". *Sensors and Actuators B: Chemical* 286 (2019), pp. 493–500.

[Mon10] Héctor Moncada-Hernández and Blanca H. Lapizco-Encinas. „Simultaneous Concentration and Separation of Microorganisms: Insulator-Based Dielectrophoretic Approach". *Analytical and Bioanalytical Chemistry* 396.5 (2010), pp. 1805–1816.

[Mon11] Hector Moncada-Hernandez, Javier L. Baylon-Cardiel, Victor H. Pérez-González, and Blanca H. Lapizco-Encinas. „Insulator-Based Dielectrophoresis of Microorganisms: Theoretical and Experimental Results". *ELECTROPHORESIS* 32.18 (2011), pp. 2502–2511.

[Moo11] Hui-Sung Moon, Kiho Kwon, Seung-Il Kim, Hyunju Han, Joohyuk Sohn, Soohyeon Lee, and Hyo-Il Jung. „Continuous Separation of Breast Cancer Cells from Blood Samples Using Multi-Orifice Flow Fractionation (MOFF) and Dielectrophoresis (DEP)". *Lab on a Chip* 11.6 (2011), p. 1118.

[Mor03] Hywel Morgan and Nicolas G. Green. *AC Electrokinetics: Colloids and Nanoparticles*. Microtechnologies and Microsystems Series 2. Baldock: Research Studies Press, 2003.

[Mor97] Hywel Morgan and Nicolas G. Green. „Dielectrophoretic Manipulation of Rod-Shaped Viral Particles". *Journal of Electrostatics* 42.3 (1997), pp. 279–293.

[Mor99] Hywel Morgan, Michael P. Hughes, and Nicolas G. Green. „Separation of Submicron Bioparticles by Dielectrophoresis". *Biophysical Journal* 77.1 (1999), pp. 516–525.

[Mur11] Jane S. Murray and Peter Politzer. „The Electrostatic Potential: An Overview". *WIREs Computational Molecular Science* 1.2 (2011), pp. 153–163.

[Nad18] Fadhila Nadzri, Zurina Zainal Abidin, and Jamil Mohd Salleh. „Effects of Wire Diameter, Yarns Size and Wire Configuration to Wire Cloth Electrode Produced from Textile Technology for Dielectrophoresis Application". *IOP Conference Series: Materials Science and Engineering* 458 (2018), p. 012035.

[Nil11] H. Nili, T. Sun, and N. G. Green. „Higher Order Dielectrophoretic Force Characterisation of Non-Spherical Particles". *Journal of Physics: Conference Series* 301 (2011), p. 012061.

[Obe77] Serafin Bess Oberton. „Electrofiltration Process for Purifying Organic Liquids“. 4040926. 1977.

[OKo60] Chester T. O'Konski. „ELECTRIC PROPERTIES OF MACRORIIOLECULES. V. THEORY OF IOSIC POLARIZATIOS IS POLYELECTROLYTES“. *The Journal of Physical Chemistry* 64.5 (1960), pp. 605–619.

[Pan13] Ronald L. Panton. *Incompressible Flow*. Fourth edition. Hoboken, New Jersey: John Wiley and Sons, Inc, 2013.

[Pat13] Saurin Patel, Shizhi Qian, and Xiangchun Xuan. „Reservoir-Based Dielectrophoresis for Microfluidic Particle Separation by Charge: Microfluidics and Miniaturization“. *ELECTROPHORESIS* 34.7 (2013), pp. 961–968.

[Per18] Victor H. Perez-Gonzalez, Roberto C. Gallo-Villanueva, Braulio Cardenas-Benitez, Sergio O. Martinez-Chapa, and Blanca H. Lapizco-Encinas. „Simple Approach to Reducing Particle Trapping Voltage in Insulator-Based Dielectrophoretic Systems“. *Analytical Chemistry* 90.7 (2018), pp. 4310–4315.

[Pes14] Georg R. Pesch, Fei Du, Udo Schwientek, Caspar Gehrmeyer, Alexander Maurer, Jorg Thöming, and Michael Baune. „Recovery of Submicron Particles Using High-Throughput Dielectrophoretically Switchable Filtration“. *Separation and Purification Technology* 132 (2014), pp. 728–735.

[Pes16] Georg R. Pesch, Lars Kiewidt, Fei Du, Michael Baune, and Jorg Thöming. „Electrodeless Dielectrophoresis: Impact of Geometry and Material on Obstacle Polarization: General“. *ELECTROPHORESIS* 37.2 (2016), pp. 291–301.

[Pes17] Georg R. Pesch, Fei Du, Michael Baune, and Jorg Thöming. „Influence of Geometry and Material of Insulating Posts on Particle Trapping Using Positive Dielectrophoresis“. *Journal of Chromatography A* 1483 (2017), pp. 127–137.

[Pes18a] Georg R. Pesch. „On the Dielectrophoretic Particle Retention in Porous Media“. PhD thesis. Universität Bremen, 2018.

[Pes18b] Georg R. Pesch, Malte Lorenz, Shaurya Sachdev, Samir Salameh, Fei Du, Michael Baune, Pouyan E. Boukany, and Jorg Thöming. „Bridging the Scales in High-Throughput Dielectrophoretic (Bio-)Particle Separation in Porous Media“. *Scientific Reports* 8.1 (2018), p. 10480.

[Pes21] Georg R. Pesch and Fei Du. „A Review of Dielectrophoretic Separation and Classification of Non-biological Particles“. *ELECTROPHORESIS* 42.1-2 (2021), pp. 134–152.

[Pet10] Ronald Pethig. „Review Article—Dielectrophoresis: Status of the Theory, Technology, and Applications“. *Biomicrofluidics* 4.2 (2010), p. 022811.

[Pet17a] Ronald Pethig. *Dielectrophoresis: Theory, Methodology, and Biological Applications*. Hoboken, NJ: John Wiley & Sons, Inc, 2017.

[Pet17b] Ronald Pethig. „Review—Where Is Dielectrophoresis (DEP) Going?“ *Journal of The Electrochemical Society* 164.5 (2017), B3049–B3055.

[Poh51] Herbert A. Pohl. „The Motion and Precipitation of Suspensoids in Divergent Electric Fields“. *Journal of Applied Physics* 22.7 (1951), pp. 869–871.

[Poh58] Herbert A. Pohl. „Some Effects of Nonuniform Fields on Dielectrics“. *Journal of Applied Physics* 29.8 (1958), pp. 1182–1188.

[Poh59] Herbert A. Pohl and J. P. Schwar. „Factors Affecting Separations of Suspensions in Nonuniform Electric Fields“. *Journal of Applied Physics* 30.1 (1959), pp. 69–73.

[Poh60] Herbert A. Pohl and Charles E. Plymale. „Continuous Separations of Suspensions by Nonuniform Electric Fields in Liquid Dielectrics“. *Journal of The Electrochemical Society* 107.5 (1960), p. 390.

[Poh78] Herbert A. Pohl, K. Pollock, and J. S. Crane. „Dielectrophoretic Force: A Comparison of Theory and Experiment“. *Journal of Biological Physics* 6.3-4 (1978), pp. 133–160.

[Pol18] Danielle V. Polniak, Eric Goodrich, Nicole Hill, and Blanca H. Lapizco-Encinas. „Separating Large Microscale Particles by Exploiting Charge Differences with Dielectrophoresis“. *Journal of Chromatography A* 1545 (2018), pp. 84–92.

[Pre12] Volker Presser, Christopher R. Dennison, Jonathan Campos, Kevin W. Knehr, Emin C. Kumbur, and Yury Gogotsi. „The Electrochemical Flow Capacitor: A New Concept for Rapid Energy Storage and Recovery“. *Advanced Energy Materials* 2.7 (2012), pp. 895–902.

[Pri10] Dennis C. Prieve, Paul J. Sides, and Christopher L. Wirth. „2-D Assembly of Colloidal Particles on a Planar Electrode“. *Current Opinion in Colloid & Interface Science* 15.3 (2010), pp. 160–174.

[Pri88] Jonathan A.R. Price, Julian P.H. Burt, and Ronald Pethig. „Applications of a New Optical Technique for Measuring the Dielectrophoretic Behaviour of Micro-Organisms“. *Biochimica et Biophysica Acta (BBA) - General Subjects* 964.2 (1988), pp. 221–230.

[Pur13] Edward M. Purcell and David J. Morin. *Electricity and Magnetism:* 3rd ed. Cambridge University Press, 2013.

[Pys07] Michele D. Pysher and Mark A. Hayes. „Electrophoretic and Dielectrophoretic Field Gradient Technique for Separating Bioparticles“. *Analytical Chemistry* 79.12 (2007), pp. 4552–4557.

[Qia14] Cheng Qian, Haibo Huang, Liguo Chen, Xiangpeng Li, Zunbiao Ge, Tao Chen, Zhan Yang, and Lining Sun. „Dielectrophoresis for Bioparticle Manipulation“. *International Journal of Molecular Sciences* 15.10 (2014), pp. 18281–18309.

[Rab17] Mohammad Towshif Rabbani, Christoph F. Schmidt, and Alexandra Ros. „Single-Walled Carbon Nanotubes Probed with Insulator-Based Dielectrophoresis“. *Analytical Chemistry* 89.24 (2017), pp. 13235–13244.

[Ram07] Antonio Ramos, Antonio González, Pablo García-Sánchez, and Antonio Castellanos. „A Linear Analysis of the Effect of Faradaic Currents on Traveling-Wave Electroosmosis“. *Journal of Colloid and Interface Science* 309.2 (2007), pp. 323–331.

[Ram16] Antonio Ramos, Pablo García-Sánchez, and Hywel Morgan. „AC Electrokinetics of Conducting Microparticles: A Review“. *Current Opinion in Colloid & Interface Science* 24 (2016), pp. 79–90.

[Ram98] A Ramos, H Morgan, N G Green, and A Castellanos. „Ac Electrokinetics: A Review of Forces in Microelectrode Structures“. *Journal of Physics D: Applied Physics* 31.18 (1998), pp. 2338–2353.

[Reg11] Jan Regtmeier, Ralf Eichhorn, Martina Viefhues, Lukas Bogunovic, and Dario Anselmetti. „Electrodeless Dielectrophoresis for Bioanalysis: Theory, Devices and Applications“. *ELECTROPHORESIS* 32.17 (2011), pp. 2253–2273.

[Ren11] Yu K. Ren, Diego Morganti, Hong Y. Jiang, Antonio Ramos, and Hywel Morgan. „Electrorotation of Metallic Microspheres“. *Langmuir : the ACS journal of surfaces and colloids* 27.6 (2011), pp. 2128–2131.

[Ria11] Reza Riahifar, Ehsan Marzbanrad, Babak Raissi, Cyrus Zamani, Mahmood Kazemzad, and Alireza Aghaei. „Sorting ZnO Particles of Different Shapes with Low Frequency AC Electric Fields“. *Materials Letters* 65.4 (2011), pp. 632–635.

[Ros01] David Ross, Michael Gaitan, and Laurie E. Locascio. „Temperature Measurement in Microfluidic Systems Using a Temperature-Dependent Fluorescent Dye“. *Analytical Chemistry* 73.17 (2001), pp. 4117–4123.

[Rou16] Mehrnaz Rouhi Youssefi and Francisco Javier Diez. „Ultrafast Electrokinetics: General“. *ELECTROPHORESIS* 37.5-6 (2016), pp. 692–698.

[San12] Noriaki Sano, Bui Matsukura, Yusuke Ikeyama, and Hajime Tamon. „Dielectrophoretic Particle Separator Using Mesh Stacked Electrodes and Simplified Model for Multistage Separation“. *Chemical Engineering Science* 84 (2012), pp. 345–350.

[San14] Noriaki Sano, Satoru Matsuoka, and Hajime Tamon. „Purification of Titanate Nanotubes Using a Mesh-Stacked Dielectrophoretic Separator Equipped with Carbon Nanotube Electrodes“. *Chemical Engineering Science* 108 (2014), pp. 188–193.

[San16] Noriaki Sano, Yuta Tanemori, and Hajime Tamon. „A Selective Dielectrophoretic Particle Separator Using Flat Electrodes Covered with Vertically Aligned Carbon Nanotubes“. *Chemical Engineering Science* 144 (2016), pp. 321–325.

[San20] A. Sankaranarayanan, Mangukiya Dishaben Parsottambhai, K.M. Prabusankarlal, and Ankit Adesara. „Filtration and Removal of Artificially Contaminated Food Borne Pathogens Using Dielectrophoresis“. *Materials Today: Proceedings* 26 (2020), pp. 3564–3568.

[Sau15a] M.A. Saucedo-Espinosa and B.H. Lapizco-Encinas. „Design of Insulator-Based Dielectrophoretic Devices: Effect of Insulator Posts Characteristics“. *Journal of Chromatography A* 1422 (2015), pp. 325–333.

[Sau15b] Mario A. Saucedo-Espinosa and Blanca H. Lapizco-Encinas. „Experimental and Theoretical Study of Dielectrophoretic Particle Trapping in Arrays of Insulating Structures: Effect of Particle Size and Shape: Microfluidics and Miniaturization“. *ELECTROPHORESIS* 36.9-10 (2015), pp. 1086–1097.

[Sau16] Mario A. Saucedo-Espinosa, Mallory M. Rauch, Alexandra LaLonde, and Blanca H. Lapizco-Encinas. „Polarization Behavior of Polystyrene Particles under Direct Current and Low-Frequency (<1 kHz) Electric Fields in Dielectrophoretic Systems: Microfluidics and Miniaturization“. *ELECTROPHORESIS* 37.4 (2016), pp. 635–644.

[Sau85] Friedrich A. Sauer and Reinhard W. Schlögl. „Torques Exerted on Cylinders and Spheres by External Electromagnetic Fields. A Contribution to the Theory of Field-Induced Cell Rotation“. *Interactions between Electromagnetic Fields and Cells*. Ed. by A. Chiabrera, C. Nicolini, and Schwan. New York: Plenum, 1985.

[Sch12] Johannes Schindelin, Ignacio Arganda-Carreras, Erwin Frise, Verena Kaynig, Mark Longair, Tobias Pietzsch, Stephan Preibisch, Curtis Rueden, Stephan Saalfeld, Benjamin Schmid, Jean Yves Tinevez, Daniel James White, Volker Hartenstein, Kevin Eliceiri, Pavel Tomancak, and Albert Cardona. „Fiji: An Open-Source Platform for Biological-Image Analysis“. *Nature Methods* 9.7 (2012), pp. 676–682.

[She11] Yueyang Shen, Ezinwa Elele, and Boris Khusid. „A Novel Concept of Dielectrophoretic Engine Oil Filter“. *ELECTROPHORESIS* 32.18 (2011), pp. 2559–2568.

[Shi08] Dong Hun Shin, Ji-Eun Kim, Hyung Cheoul Shim, Jin-Won Song, Ju-Hyung Yoon, Joondong Kim, Sohee Jeong, Junmo Kang, Seunghyun Baik, and Chang-Soo Han. „Continuous Extraction of Highly Pure Metallic Single-Walled Carbon Nanotubes in a Microfluidic Channel“. *Nano Letters* 8.12 (2008), pp. 4380–4385.

[Shi13] Sangjo Shim, Katherine Stemke-Hale, Jamileh Noshari, Frederick F. Becker, and Peter R. C. Gascoyne. „Dielectrophoresis Has Broad Applicability to Marker-Free Isolation of Tumor Cells from Blood by Microfluidic Systems“. *Biomicrofluidics* 7.1 (2013), p. 011808.

[Shi68] William L. Shirley. „Method and Apparatus for Unloading Filters“. 3394067. 1968.

[Sis95] Warren G. Sisson, Ronald R. Brunson, Timothy C. Scott, Michael T. Harris, and Jee Loon Look. „Removal of Submicron Silica Particles from *Tert* -Amyl Alcohol by Dielectric/Electric Packed Bed Filtration“. *Separation Science and Technology* 30.7-9 (1995), pp. 1421–1434.

[Soh12] Johan Sohaili, Shantha Kumari Muniyandi, and Siti Suhaila Mohamad. „A Review on Printed Circuit Boards Waste Recycling Technologies and Reuse of Recovered Nonmetallic Materials“. *International Journal of Scientific & Engineering Research* 3.2 (2012), pp. 1–7.

[Squ04] Todd M. Squires and Martin Z. Bazant. „Induced-Charge Electro-Osmosis“. *Journal of Fluid Mechanics* 509 (2004), pp. 217–252.

[Sri11a] Sriram Sridharan, Junjie Zhu, Guoqing Hu, and Xiangchun Xuan. „Joule Heating Effects on Electroosmotic Flow in Insulator-Based Dielectrophoresis“. *ELECTROPHORESIS* 32.17 (2011), pp. 2274–2281.

[Sri11b] Soumya K. Srivastava, Aytug Gencoglu, and Adrienne R. Minerick. „DC Insulator Dielectrophoretic Applications in Microdevice Technology: A Review“. *Analytical and Bioanalytical Chemistry* 399.1 (2011), pp. 301–321.

[Sta06] A.M. Stalcup. „Chiral Separations by Capillary Electrophoresis“. *Chiral Analysis* (2006), pp. 241–275.

[Ste24] Otto Stern. „ZUR THEORIE DER ELEKTROLYTISCHEN DOPPELSCHICHT“. *Zeitschrift für Elektrochemie und angewandte physikalische Chemie* 30.21-22 (1924), pp. 508–516.

[Ste98] C. Steger. „An Unbiased Detector of Curvilinear Structures“. *IEEE Transactions on Pattern Analysis and Machine Intelligence* 20.2 (1998), pp. 113–125.

[Str07] Julius Adams Stratton. *Electromagnetic Theory*. John Wiley & Sons, 2007.

[Sue03] J. Suehiro, Guangbin Zhou, M. Imamura, and M. Hara. „Dielectrophoretic Filter for Separation and Recovery of Biological Cells in Water“. *IEEE Transactions on Industry Applications* 39.5 (2003), pp. 1514–1521.

[Taj20] Parham Tajik, Mohammad Said Saidi, Navid Kashaninejad, and Nam-Trung Nguyen. „Simple, Cost-Effective, and Continuous 3D Dielectrophoretic Microchip for Concentration and Separation of Bioparticles“. *Industrial & Engineering Chemistry Research* 59.9 (2020), pp. 3772–3783.

[Tha02] Sunil Kumar Thamida and Hsueh-Chia Chang. „Nonlinear Electrokinetic Ejection and Entrainment Due to Polarization at Nearly Insulated Wedges“. *Physics of Fluids* 14.12 (2002), pp. 4315–4328.

[Thi20] Pierre-Emmanuel Thiriet, Joern Pezoldt, Gabriele Gambardella, Kevin Keim, Bart Deplancke, and Carlotta Guiducci. „Selective Retrieval of Individual Cells from Microfluidic Arrays Combining Dielectrophoretic Force and Directed Hydrodynamic Flow“. *Micromachines* 11.3 (2020), p. 322.

[Tin17] Jean-Yves Tinevez, Nick Perry, Johannes Schindelin, Genevieve M. Hoopes, Gregory D. Reynolds, Emmanuel Laplantine, Sebastian Y. Bednarek, Spencer L. Shorte, and Kevin W. Eliceiri. „TrackMate: An Open and Extensible Platform for Single-Particle Tracking“. *Methods* 115 (2017), pp. 80–90.

[Tor18] Isaac Torres-Díaz, Bradley Rupp, Yuguang Yang, and Michael A. Bevan. „Energy Landscapes for Ellipsoids in Non-Uniform AC Electric Fields“. *Soft Matter* 14.6 (2018), pp. 934–944.

[Tun12] A. Tuncuk, V. Stazi, A. Akcil, E.Y. Yazici, and H. Deveci. „Aqueous Metal Recovery Techniques from E-Scrap: Hydrometallurgy in Recycling“. *Minerals Engineering* 25.1 (2012), pp. 28–37.

[Vag22] Alaleh Vaghef-Koodehi, Curran Dillis, and Blanca H. Lapizco-Encinas. „High-Resolution Charge-Based Electrokinetic Separation of Almost Identical Microparticles“. *Analytical Chemistry* 94.17 (2022), pp. 6451–6456.

[Vag23] Alaleh Vaghef-Koodehi, Olivia D. Ernst, and Blanca H. Lapizco-Encinas. „Separation of Cells and Microparticles in Insulator-Based Electrokinetic Systems“. *Analytical Chemistry* 95.2 (2023), pp. 1409–1418.

[Vah08] M. D. Vahey and J. Voldman. „An Equilibrium Method for Continuous-Flow Cell Sorting Using Dielectrophoresis“. *Analytical Chemistry* 80.9 (2008), pp. 3135–3143.

[Val11] Ana Valero, Thomas Braschler, Alex Rauch, Nicolas Demierre, Yves Barral, and Philippe Renaud. „Tracking and Synchronization of the Yeast Cell Cycle Using Dielectrophoretic Opacity“. *Lab on a Chip* 11.10 (2011), p. 1754.

[Vin91] L. Vincent and P. Soille. „Watersheds in Digital Spaces: An Efficient Algorithm Based on Immersion Simulations“. *IEEE Transactions on Pattern Analysis and Machine Intelligence* 13.6 (1991), pp. 583–598.

[Vol01] Joel Voldman, Mehmet Toner, Martha L. Gray, and Martin A. Schmidt. „A Dielectrophoresis-based Array Cytometer“. *Transducers '01 Eurosensors XV*. Ed. by Ernst Obermeier. Berlin, Heidelberg: Springer Berlin Heidelberg, 2001, pp. 322–325.

[Von96] F. V. Von Steyern, J O Josefsson, and S Tågerud. „Rhodamine B, a Fluorescent Probe for Acidic Organelles in Denervated Skeletal Muscle.“ *Journal of Histochemistry & Cytochemistry* 44.3 (1996), pp. 267–274.

[Wag17] Thorsten Wagner and Jan Eglinger. *Thorstenwagner/Ij-Ellipsesplit: EllipseSplit 0.6.0 SNAPSHOT*. Zenodo. 2017.

[Wah21] Waqas Waheed, Omar Z. Sharaf, Anas Alazzam, and Eiyad Abu-Nada. „Dielectrophoresis-Field Flow Fractionation for Separation of Particles: A Critical Review“. *Journal of Chromatography A* 1637 (2021), p. 461799.

[Wak03] R.J. Wakeman and G. Butt. „An Investigation of High Gradient Dielectrophoretic Filtration“. *Chemical Engineering Research and Design* 81.8 (2003), pp. 924–935.

[Wal14] Johannes Walter, Konrad Löhr, Engin Karabudak, Wieland Reis, Jules Mikhael, Wolfgang Peukert, Wendel Wohlleben, and Helmut Cölfen. „Multidimensional Analysis of Nanoparticles with Highly Disperse Properties Using Multiwavelength Analytical Ultracentrifugation“. *ACS Nano* 8.9 (2014), pp. 8871–8886.

[Wan05] Dazhi Wang, Marin Sigurdson, and Carl D. Meinhart. „Experimental Analysis of Particle and Fluid Motion in Ac Electrokinetics“. *Experiments in Fluids* 38.1 (2005), pp. 1–10.

[Wan07] Lisen Wang, Lisa Flanagan, and Abraham P. Lee. „Side-Wall Vertical Electrodes for Lateral Field Microfluidic Applications“. *Journal of Microelectromechanical Systems* 16.2 (2007), pp. 454–461.

[Wan93] X -B Wang, Y Huang, J P H Burt, G H Markx, and R Pethig. „Selective Dielectrophoretic Confinement of Bioparticles in Potential Energy Wells“. *Journal of Physics D: Applied Physics* 26.8 (1993), pp. 1278–1285.

[Wan97] Xujing Wang, Xiao-Bo Wang, and Peter R.C. Gascoyne. „General Expressions for Dielectrophoretic Force and Electrorotational Torque Derived Using the Maxwell Stress Tensor Method“. *Journal of Electrostatics* 39.4 (1997), pp. 277–295.

[Wan98] Xiao-Bo Wang, Jody Vykoukal, Frederick F. Becker, and Peter R.C. Gascoyne. „Separation of Polystyrene Microbeads Using Dielectrophoretic/Gravitational Field-Flow-Fractionation“. *Biophysical Journal* 74.5 (1998), pp. 2689–2701.

[Was93] Masao Washizu. „Precise Calculation of Dielectrophoretic Force in Arbitrary Field“. *Journal of Electrostatics* 29.2 (1993), pp. 177–188.

[Was94] M. Washizu, S. Suzuki, O. Kurosawa, T. Nishizaka, and T. Shinohara. „Molecular Dielectrophoresis of Biopolymers“. *IEEE Transactions on Industry Applications* 30.4 (1994), pp. 835–843.

[Wat67] Logan C. Waterman and Albert D. Franse. „Electric Filter“. 3324026. 1967.

[Wat83] Frederick D. Watson, Weldon D. Mayse, and Albert D. Franse. „Radial Flow Electrofilter“. 4372837. 1983.

[Wei19] Laura Weirauch, Malte Lorenz, Nicole Hill, Blanca H. Lapizco-Encinas, Michael Baune, Georg R. Pesch, and Jorg Thöming. „Material-Selective Separation of Mixed Microparticles via Insulator-Based Dielectrophoresis“. *Biomicrofluidics* 13.6 (2019), p. 064112.

[Wei22] Laura Weirauch, Jasper Giesler, Michael Baune, Georg R. Pesch, and Jorg Thöming. „Shape-Selective Remobilization of Microparticles in a Mesh-Based DEP Filter at High Throughput“. *Separation and Purification Technology* 300 (2022), p. 121792.

[Wil15] Barry A. Wills and Tim Napier-Munn. *Wills' Mineral Processing Technology*. Elsevier Science, 2015.

[Wu21] Yupan Wu, Rajarshi Chattaraj, Yukun Ren, Hongyuan Jiang, and Daeyeon Lee. „Label-Free Multitarget Separation of Particles and Cells under Flow Using Acoustic, Electrophoretic, and Hydrodynamic Forces“. *Analytical Chemistry* 93.21 (2021), pp. 7635–7646.

[Yan07] D. G. Yan, C. Yang, and X. Y. Huang. „Effect of Finite Reservoir Size on Electroosmotic Flow in Microchannels“. *Microfluidics and Nanofluidics* 3.3 (2007), pp. 333–340.

[Yos06] G. Yossifon, I. Frankel, and T. Miloh. „On Electro-Osmotic Flows through Microchannel Junctions“. *Physics of Fluids* 18.11 (2006), p. 117108.

[Zha09] Hui Zhao and Haim H. Bau. „The Polarization of a Nanoparticle Surrounded by a Thick Electric Double Layer“. *Journal of Colloid and Interface Science* 333.2 (2009), pp. 663–671.

[Zha11] Hui Zhao. „Double-Layer Polarization of a Non-Conducting Particle in an Alternating Current Field with Applications to Dielectrophoresis“. *Electrophoresis* 32.17 (2011), pp. 2232–2244.

[Zha17] Yu Zhao, Jozef Brcka, Jacques Faguet, and Guigen Zhang. „Elucidating the DEP Phenomena Using a Volumetric Polarization Approach with Consideration of the Electric Double Layer“. *Biomicrofluidics* 11.2 (2017), p. 024106.

[Zhe03] Lifeng Zheng, Shengdong Li, P.J. Burke, and J.P. Brody. „Towards Single Molecule Manipulation with Dielectrophoresis Using Nanoelectrodes“. *2003 Third IEEE Conference on Nanotechnology, 2003. IEEE-NANO 2003.* Vol. 2. San Francisco, CA, USA: IEEE, 2003, pp. 437–440.

[Zho10] Xiaochun Zhou, Weilin Xu, Guokun Liu, Debashis Panda, and Peng Chen. „Size-Dependent Catalytic Activity and Dynamics of Gold Nanoparticles at the Single-Molecule Level“. *Journal of the American Chemical Society* 132.1 (2010), pp. 138–146.

[Zho21] Jian Zhou, Ye Tao, Weiyu Liu, Haizhen Sun, Wenlong Wu, Chunlei Song, Rui Xue, Tianyi Jiang, Hongyuan Jiang, and Yukun Ren. „Self-Powered AC Electrokinetic Microfluidic System Based on Triboelectric Nanogenerator“. *Nano Energy* 89 (2021), p. 106451.

[Zhu12] Zhen Zhu, Olivier Frey, Diana Silvia Ottoz, Fabian Rudolf, and Andreas Hierlemann. „Microfluidic Single-Cell Cultivation Chip with Controllable Immobilization and Selective Release of Yeast Cells“. *Lab Chip* 12.5 (2012), pp. 906–915.

[Zou21] Tong Zou, Tianyu Pan, Michael Taylor, and Hal Stern. „Recognition of Overlapping Elliptical Objects in a Binary Image“. *Pattern Analysis and Applications* 24.3 (2021), pp. 1193–1206.

List of symbols

Symbol	Description	Unit
Roman		
a	half axis	m
A	weight (in linear unmixing)	–
A_c	cross section of flow area	m^2
b	slip length	m
b_a	channel width	m
b_c	width of constriction	m
B	factor Eq. 2.20	–
c	concentration	$\mathrm{g\ L}^{-1}$
c_p	specific heat capacity	$\mathrm{J\ (kg\ K)}^{-1}$
d	distance	m
d_h	hydraulic diameter	m
$\vec{d}$	vector distance	m
D	coefficient of diffusion	$\mathrm{m}^2\ \mathrm{s}^{-1}$
$\vec{D}$	displacement current	A
Du	Dukhin number	–
E	electric field strength	$\mathrm{V\ m}^{-1}$
EN	enrichment	–
$\vec{E}$	electric field vector	$\mathrm{V\ m}^{-1}$
f	frequency	Hz
f_P	friction factor	–
$\tilde{f}_\mathrm{CM}$	Clausius-Mossotti factor	–
$\vec{f}$	body forces	N
$\vec{F}$	force	N
$\vec{g}$	gravitational acceleration	$\mathrm{m\ s}^{-2}$
h	characteristic length of channel	m
h_S	post diameter	m
i, j, k	running index	–
$\vec{i}$	unit vector	–
I	fluorescence intensity	–
I_AC	current	A
j	imaginary unit	–
$\vec{J}$	electric current density	$\mathrm{A\ m}^{-2}$
k_f	thermal conductivity	$\mathrm{J\ (s\ m\ K)}^{-1}$
K_S	surface conductance	S
l_0 , L	characteristic length	m
L_a	depolarization factor	–

Symbol	Description	Unit
m	mass	kg
M	dimensionless parameter Eq. A.6	–
n	number of experiments	–
$\dot{n}$	particle flux	s^{-1} m^{-2}
n_0	number density of ions	m^{-3}
N	number	–
p	pressure	Pa
$\vec{p}$	dipole moment	C m
P	purity	–
Pe	Peclet number	–
q	charge	C
q_{therm}	thermal energy	J
Q	flow rate	L h^{-1}
Q_{e}	total charge	C
r	radius	m
$\vec{r}_e$	unit vector between two points	–
R	recovery rate	–
Re	Reynolds number	–
s	arbitrary distance Eq. 2.20	m
t	time	s
T_{e}	torque	N m
T	absolute temperature	K
$\vec{u}$	fluid velocity	m s^{-1}
u_{S}	superficial velocity	m s^{-1}
U	voltage	V
$\vec{v}$	particle velocity	m s^{-1}
V	volume	m^3
$\dot{V}$	volume flow	L h^{-1}
W	electrical power	W
WE	weighted enrichment	–
$\bar{x}$	mean displacement	m
x, y, z	coordinate directions	–
y_{inter}	y-axis intersection B.1	m s^{-1}
Y	yield	–
z	ion valence	–
Z	impedance	Ω
Greek		
α	effective polarizability	C m^2 V^{-1}
α_{therm}	temperature coefficient	K^{-1}
δ	eccentricity	–
ε_{r}	relative permittivity	–
ζ	zeta potential	V
η	separation efficiency	–
η_{m}	fluid viscosity	Pa s
κ	Debye Hückel parameter	m^{-1}
λ_D	Debye length	m
μ	mobility	varies
ρ	electric charge density	C m^{-3}
ρ_{f}	free volumetric charge density	C m^{-3}
ρ_{m}	mass density	kg m^{-3}

Symbol	Description	Unit
σ	electrical conductivity	S m^{-1}
τ	relaxation time	s
τ_a	accelaration time	s
ϕ	electric potential	V
ϕ_0	surface potential	V
Φ_P	porosity	–
ω	angular frequency	s^{-1}
Ω	dimensionless frequency Eq. 2.25	–
Re	real part of complex number	–
Δ	mathematical operator Delta	–
∇	mathematical operator Nabla	–

Index	Meaning
a	target particle
b	non-target particle
body	inside body
CO	crossover
dielec	dielectricum
drag	drag force
D	diffuse
DEP	dielectrophretic
e	electric
E	electrode
EK	electrokinetic
EO	electroosmotic
EP	electrophoretic
MW	Maxwell-Wagner
m	medium
n	normal
p	particle
ref	reference
rel	relative
remob	remobilization
S	surface
t	tangential
therm	thermal
trap	trapping
T	terminal

Subscripts	Meaning
CPEO	concentration polarization electroosmosis
D	diffuse layer
ICEO	induced-charge electroosmosis
S	Stern layer

Constants			
Symbol	**Quantity**	**Value**	**Unit**
k_B	Boltzmann constant	1.381×10^{-23}	J K^{-1}
k_e	Coulomb constant	8.988×10^{9}	N m^2 C^{-2}
e	elementary charge	1.602×10^{-19}	C
F	Faraday constant	9.6485×10^{4}	C mol^{-1}
ε_0	permittivity of free space	8.85×10^{-12}	A s $(V\ m)^{-1}$
π	mathematical constant pi	3.14159	–

Abbreviations	
AC	alternating current
CM	Clausius-Mossotti
CNT	carbon nanotube
CP	concentration polarization
DC	direct current
DEP	dielectrophoresis
DLD	deterministic lateral displacement
EDL	electric double layer
EK	electrokinetic
EO	electroosmosis
EP	electrophoresis
FFF	field flow fractionation
IC	induced charge
PS	polystyrene
PVA	polyvinyl alcohol
PVP	polyvinylpyrrolidone
SEM	scanning electron microscope
SPT	single particle tracking

Students's work

In this thesis, the results from the supervision of the following students' works are included:

Andrey Guzev, "Gleichförmige Streckung von Polystyrol-Mikropartikeln zur Untersuchung des Einflusses vom Aspektverhältnis auf die Dielektrophorese", *B. Sc. Thesis*, March 2021

Paul Jonas Meyer, "Conjugation of the glycoprotein fetuin to polystyrene microparticles and its influence for separation by dielectrophoresis", *M. Sc. Thesis*, November 2021

Colophon

This thesis was typeset with LaTeX 2_ε. It uses the *Clean Thesis* style developed by Ricardo Langner. The design of the *Clean Thesis* style is inspired by user guide documents from Apple Inc.

Download the *Clean Thesis* style at `http://cleanthesis.der-ric.de/`.